ALBERT–LUDWIG–UNIVERSITÄT FREIBURG

Fakultät für Physik

Measurement of Single W Production and Triple Gauge Boson Couplings in e^+e^- Collisions at $\sqrt{s}$ =161–189 GeV

Marco Verzocchi

Abstract

Single W production in the $e^+e^- \to q\overline{q}'e^-\overline{\nu}_e$ reaction has been studied using a data sample with an integrated luminosity of 251 pb^{-1} collected between 1996 and 1998 with the OPAL detector at LEP2. A sample of 92 events is selected in the data, for a Monte Carlo prediction of (87.6 ± 3.7) events. The selected events are used to measure the parameters describing the triple gauge boson vertex γW^+W^-: $\kappa_\gamma = 1.15^{+0.18}_{-0.20}$ and $\lambda_\gamma = -0.47^{+0.39}_{-0.27}$, where the errors include both statistical and systematic uncertainties and each parameter is determined setting the other to its Standard Model value. The cross section σ for the $e^+e^- \to q\overline{q}'e^-\overline{\nu}_e$ process proceeding through t–channel diagrams is measured in the kinematic region $m_{q\overline{q}'} > 40$ GeV/c^2 at $\sqrt{s} = 189$ GeV to be $\sigma = (615^{+150}_{-135} \pm 60)$ fb, where the first error is statistical and the second systematic. All measurements are consistent with the Standard Model predictions.

Post Address:
Hermann–Herder–Straße 3
D–79104 Freiburg i. Br., Germany

Universität Freiburg
Fakultät für Physik
January 2000

Messung der Produktion von einzelnen W–Bosonen und der Selbstkopplungen von Eichbosonen in der e^+e^-–Streuung bei $\sqrt{s}$ =161–189 GeV

INAUGURAL–DISSERTATION
zur
Erlangung des Doktorgrades
der
Fakultät für Physik
der
Albert–Ludwigs–Universität in Freiburg im Breisgau

vorgelegt von
Marco Verzocchi
aus
Rom, Italien

Januar 2000

Dekan	Prof. Dr. K. Königsmann
Leiter der Arbeit	Prof. Dr. G. Herten
Referent	Prof. Dr. G. Herten
Koreferent	Prof. Dr. A. Bamberger

Tag der Verkündung des Prüfungsergebnisses: 24. Februar 2000

Introduction

The subject of this thesis is the measurement of single W production in e^+e^- collisions at $\sqrt{s} = 161$–189 GeV using data collected with the OPAL detector at LEP2 between 1996 and 1998, for a total integrated luminosity of 251 pb^{-1}. Single W production is studied through its hadronic decay channel. The selected events are used to measure the *t*–channel cross section for the $e^+e^- \to q\overline{q}'e^-\overline{\nu}_e$ process and the κ_γ and λ_γ parameters describing the γW^+W^- vertex.

One of the least well tested sectors of the electroweak theory is that of the couplings among the electroweak bosons, in striking contrast with the precision reached in measurements of the couplings between bosons and fermions. Due to the non–Abelian nature of the gauge group which describes the electroweak interactions, it is predicted that the weak gauge bosons interact among themselves, giving rise to vertices with three or four gauge bosons. Each vertex has a set of corresponding dimensionless couplings assigned, commonly denoted as TGCs or QGCs (triple or quartic gauge couplings). The form and the strength of these couplings is obtained in the Standard Model ($\mathcal{SM}$) applying the principle of gauge symmetry. Higher order corrections cause deviations in the couplings of $\mathcal{O}(10^{-3})$ relative to $\mathcal{SM}$ tree level values. Possibly larger deviations of the couplings from the these values might arise if the $\mathcal{SM}$ is the low energy limit of a larger theory. In this way the measurement of the gauge couplings does not only establish another stringent test of the electroweak theory, but also probes possible extensions in the bosonic sector.

Prior to the measurements performed at LEP2 evidence for the existence of the self–interaction of electroweak gauge bosons and indirect limits on possible deviations of the couplings from the $\mathcal{SM}$ values have been obtained mainly from the study of pair production of gauge bosons in $p\overline{p}$ collisions and of radiative corrections to electroweak observables at LEP1. The direct measurements performed at the Tevatron give 95% confidence level (CL) limits on the deviations of the gauge couplings of $\mathcal{O}(1)$. The estimation of the couplings from radiative corrections requires additional assumptions about the possible contribution from other extension of the $\mathcal{SM}$: depending on the underlying hypotheses the obtained 95% CL limits vary between $\mathcal{O}(0.1)$ and $\mathcal{O}(1)$, to be compared with the $\mathcal{O}(10^{-3})$ deviations expected from radiative corrections. Due to the strong dependence on the underlying assumptions there is a general consensus that indirect limits cannot substitute direct measurements.

At LEP2 measurements of the couplings with a precision of $\mathcal{O}(0.05)$ are obtained from the study of the $e^+e^- \to W^+W^-$ reaction, with the drawback that one cannot separate the contributions from the couplings at the γW^+W^- and at the $Z^0W^+W^-$ vertices. This ambiguity can be solved measuring the rate of the single W production process, $e^+e^- \to W^+e^-\overline{\nu}_e$. This process proceeds mainly through two diagrams involving the *t*–channel exchange of a photon with a small momentum transfer. The first diagram corre-

sponds to Bhabha scattering followed by radiation of a real W boson from one of the two final state electrons. The second diagram describes the $\gamma W^* \to W$ fusion process, where the flux of virtual photons is provided by one of the beam electrons. This second diagram introduces the dependence on the structure of the $\gamma W^+ W^-$ coupling.

In the case of the hadronic decay of the W boson, the final state is characterised by a pair of acoplanar jets and missing transverse momentum due to the neutrino. Due to the small momentum transfer at the interaction, the electron is scattered at small angles in the beam pipe and therefore it is not detected. For leptonic decays of the W, the only particle visible in the detector is a high energy lepton, or its decay product(s) in the case of $W \to \tau\nu_\tau$. These topologies are often ascribed to the production of new particles which are foreseen in extensions of the $\mathcal{SM}$. The measurement of the single W production cross section provides therefore a useful check of the Monte Carlo programs used to estimate the backgrounds to the possible signals of production of new particles.

Outline of the thesis

This thesis starts with a theoretical introduction on gauge boson couplings in chapter 1, showing how self–interactions of bosons arise as a consequence of the non–Abelian nature of the gauge group used to describe the electroweak interactions. The theoretical frameworks for the description of anomalous gauge couplings which may arise in extensions of the $\mathcal{SM}$ are discussed next, also in relation with the symmetry breaking mechanism. Direct measurements of the gauge couplings performed at LEP2 and at Tevatron are reviewed in chapter 2, together with the estimates obtained from the study of effects of radiative correction on quantities which have been precisely measured at the Z^0 peak and at lower energies. The theory of single W boson production in e^+e^- collisions is discussed in chapter 3, with emphasis on the differences between this process and the double resonant production of W bosons. The OPAL detector used to perform the measurement discussed in this thesis is described briefly in chapter 4. Details are given on the procedures used for energy and momentum measurements, for lepton identification and for calibration, which are relevant for the analysis.

The original part of this thesis starts in chapter 5 with idealised Monte Carlo studies performed using various event generators to assess the sensitivity of the $e^+e^- \to W^+e^-\overline{\nu}_e$ process to the gauge couplings and to establish the best strategy for their measurement. For the first time in this channel the differential distributions of the selected events are used to improve the measurement of the gauge couplings. The selection of events which are kinematically compatible with the production of W bosons in the $e^+e^- \to W^+e^-\overline{\nu}_e$ reaction is the subject of chapter 6. A discussion of systematic errors arising from theoretical uncertainties, from fragmentation, experimental methods and backgrounds is given in chapter 7. The final measurements of the *t*–channel cross section for the $e^+e^- \to q\overline{q}'e^-\overline{\nu}_e$ process and of the κ_γ and λ_γ couplings are finally given in chapters 8 and 9.

Contents

1 Gauge boson couplings

The purpose of this chapter is to situate the measurement presented in this thesis in the context of current theoretical models. The general framework used for the description of particle physics phenomena, the Standard Model ($\mathcal{SM}$), is the subject of section 1.1. More details on the bosonic part of the electroweak Lagrangian, which are relevant for this thesis, are given in section 1.2. One of the least well tested sector of the $\mathcal{SM}$ is that of the couplings among electroweak bosons. These are introduced in section 1.3 starting from the electroweak Lagrangian. Possible extensions of the gauge boson interaction part of the Lagrangian are then discussed, starting in section 1.4 with the most general Lagrangian for triple gauge boson vertices, derived requiring only Lorentz–invariance. Two different models for introducing new interactions among vector bosons are then discussed in sections 1.5 and 1.6. The first model is based on the existence of a light Higgs boson, whereas the second one is more suited to the description of a strongly interacting Higgs sector. The chapter ends in section 1.7 with the estimates of the possible size of new effects which might be visible in the interactions of gauge bosons.

1.1 Gauge boson couplings in the Standard Model

The Standard Model ($\mathcal{SM}$) [1] provides the theoretical framework for describing almost all phenomena observed in particle physics, with the notable exception of the recent observation of neutrino oscillations [2]. This framework is the result of more than 50 years of experiments and theoretical improvements [3]. Predictions of the $\mathcal{SM}$ have received crucial verification in many experiments, starting with the discovery of neutral currents [4] in 1973, followed by the first direct observation of the $W^{\pm}$ and Z^0 bosons by the UA1 and UA2 collaborations [5] in 1983, and ending with the discovery of the top quark at the Tevatron collider [6] and with the observation of direct violation of charge and parity conservation ($\mathcal{CP}$) in the neutral K [7] and B [8] systems. Of all the constituents foreseen in the $\mathcal{SM}$ only the Higgs boson has yet to be observed and only a lower limit on its mass m_{H} is currently available [9].

With the start of the physics program at the LEP and SLC colliders tests of the $\mathcal{SM}$ have entered the precision phase. The theory [10] predicts relations among experimentally measurable quantities: any observable, like the mass of vector bosons, can be predicted in terms of a finite number of parameters determined in previous experiments. New measurements are compared with predictions and if agreement is found within errors they can be used to constrain further the input parameters. Non–agreement would indicate inconsistency of the theoretical framework and new physics. The high precision experiments performed with e^+e^- collisions at LEP and SLC have tested the electroweak theory to a

level comparable to the $g-2$ experiments which were performed to test quantum electrodynamics [11]. The accurate measurements of the mass, width and branching ratios of the Z^0 boson and of the asymmetries in its production and decay [12] have allowed for the first time quantitative tests of the electroweak theory beyond the tree level prediction. Using these measurements constraints have been obtained in the course of the early 90's on the mass of the top quark, which in the end turned out to be compatible with the first direct observation of the top quark at the Tevatron collider [6]. The latest indirect bounds on the mass of the top quark $m_t = (161.1^{+8.2}_{-7.1})$ GeV/c^2 [13] are in very good agreement with the value obtained from direct measurements by the CDF and DØ collaborations $m_t = (174.3 \pm 5.1)$ GeV/c^2 [14].

These tests of the $\mathcal{SM}$ at the level of the first order electroweak radiative corrections provide the first indication of gauge–boson contributions through loops (either in the propagator or at the Z^0 decay vertex) constituting therefore an indirect evidence for bosonic self–interactions [15]. These interactions among bosons are a direct consequence of the non–Abelian structure of the gauge group of the $\mathcal{SM}$. The investigation of the coupling among the gauge bosons of the electroweak force is together with the precision measurement of the W mass, m_W, one of the main goals of the LEP2 physics program [16] started in 1996. Improvements in the knowledge of m_W obtained from measurements performed at LEP2 and at the Tevatron collider [17] allow to put further constraints on radiative corrections in the electroweak theory and to reduce the allowed range for the mass of the Higgs boson, m_H. The current level of consistency of the $\mathcal{SM}$ is usually shown by the plot of figure 1.1a, where indirect bounds on m_t and m_W obtained from radiative corrections are compared with direct measurements. If these direct measurements are then included in a global fit of the $\mathcal{SM}$ parameters weak limits can be derived on m_H (the Higgs boson contributes only a logarithmic term in m_H to the radiative corrections), which are compared in figure 1.1b with the current direct searches performed at LEP2 [9].

One of the least well tested sectors of the electroweak theory is that of the couplings among the electroweak bosons, in striking contrast with the precision reached in measurements of the couplings between bosons and fermions. Due to the non–Abelian nature of the gauge group which describes the electroweak interactions it is predicted that gauge bosons interact among themselves, giving rise to three or four gauge bosons vertices. The gauge boson part of the electroweak Lagrangian, written in terms of the physical fields, contains two triple gauge boson vertices, γW^+W^- and $Z^0W^+W^-$, and four quartic gauge boson vertices, $\gamma\gamma W^+W^-$, $\gamma Z^0W^+W^-$, $Z^0Z^0W^+W^-$ and $W^+W^-W^+W^-$. One interesting feature of the Lagrangian is that the coupling in the triple gauge boson vertex, g_W, is the same as that in the vertex between the weak bosons and fermions and that the coupling in the quartic gauge boson vertices is g_W^2. This equality is shown schematically in figure 1.2.

The equality of the quark and lepton couplings to weak bosons has been demonstrated experimentally to high accuracy, and provides the strongest experimental evidence so far that the weak bosons are the gauge bosons of the $\mathcal{SM}$. The equality between the weak boson self–coupling and the coupling to fermions is the ultimate test of gauge symmetry. It provides, for example, the gauge cancellations which are necessary to avoid unitarity violation in the $e^+e^- \to W^+W^-$ cross section at high energies and for the renormalisability of the electroweak theory. Unitarity violation in the scattering of longitudinally polarised electroweak bosons is prevented from the relation between the triple and quartic gauge couplings and the existence of the Higgs field. The study of the self–interactions of weak

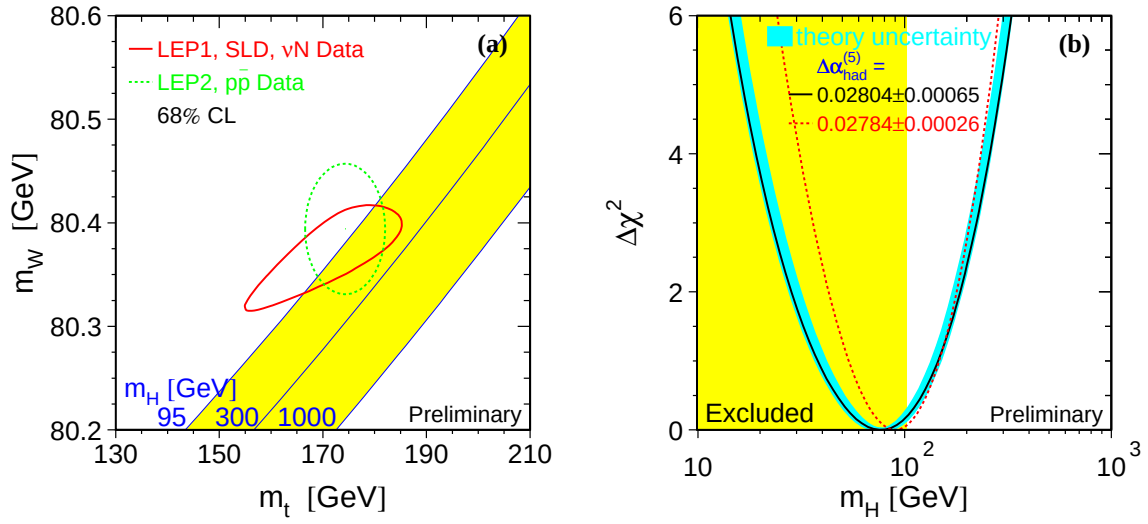

Figure 1.1: In (*a*) the direct measurements of m_{W} and m_t (Tevatron and LEP2 data) are compared with indirect measurements obtained from a fit to the LEP1, SLD and neutrino scattering data. In both cases the 68% CL contours are plotted. Also shown is the $\mathcal{SM}$ relation between the two masses as a function of the Higgs mass. In (*b*) the $\Delta\chi^2 = \chi^2 - \chi^2_{min}$ is shown as a function of m_{H}. The line is the result of the fit using all data, the band represents an estimate of the theoretical error due to missing higher order corrections ($\Delta\alpha$ indicates the contribution to the running of α_{em} from hadronic final states in the low energy region). The vertical band shows the 95% CL exclusion limit on m_{H} from the direct search.

bosons can therefore provide some insight also on the symmetry breaking mechanism.

Deviations of the triple and quartic gauge couplings (which sometimes are called anomalous gauge couplings) from the values predicted by the gauge symmetry principle might arise if the $\mathcal{SM}$ is only the low energy limit of a larger theory. In this way the measurement of the gauge couplings does not only establish another stringent test of the electroweak theory, but also probe for possible extensions in the bosonic sector. Such contributions have been studied so far only through the corrections (usually called oblique corrections) to the weak boson propagators, which contribute universally to all processes with external quarks and leptons. This has given evidence that self–couplings of vector bosons exist, but leaves ambiguities concerning the exact terms of the electroweak La-

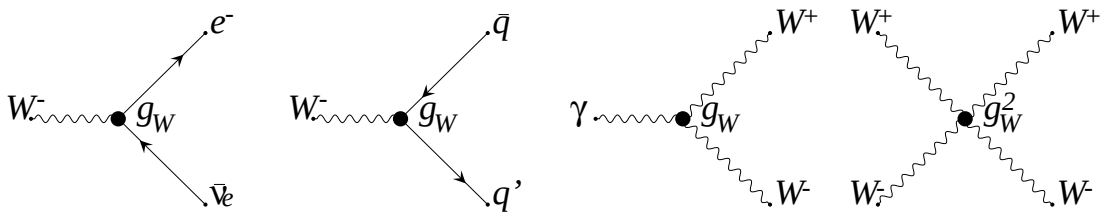

Figure 1.2: Universality of the weak gauge boson couplings.

grangian.

1.2 The electroweak Lagrangian and the Higgs mechanism

The electroweak part of the $\mathcal{SM}$ can be described mathematically with the gauge group SU(2) $\otimes$ U(1). The Lagrangian $\mathcal{L}$ obtained requiring local gauge invariance contains three massless bosons, $\mathcal{W}^i$ (i = 1,2,3), associated with the gauge group SU(2) and one massless boson, $\mathcal{B}$, associated with the U(1) gauge group. Introducing the field strength tensors of the SU(2) gauge field $\mathcal{W}^i$ and the U(1) gauge field $\mathcal{B}$,

$$\begin{aligned} \mathcal{W}^i_{\mu\nu} &= \delta_\mu \mathcal{W}^i_\nu - \delta_\nu \mathcal{W}^i_\mu - g_W \epsilon^{ijk} \mathcal{W}^j_\mu \mathcal{W}^k_\nu \\ \mathcal{B}_{\mu\nu} &= \delta_\mu \mathcal{B}_\nu - \delta_\nu \mathcal{B}_\mu, \end{aligned}$$

where g_W is the SU(2) gauge coupling and $\mu, \nu = 0, \ldots, 3$ are indices for the space–time coordinates, the Lagrangian of the gauge bosons can be written as:

$$\mathcal{L} = -\frac{1}{4} \mathcal{W}^{i\mu\nu} \mathcal{W}^i_{\mu\nu} - \frac{1}{4} \mathcal{B}^{\mu\nu} \mathcal{B}_{\mu\nu}.$$

This Lagrangian describes four massless vector bosons forming a singlet ($\mathcal{B}$) and a triplet ($W^\pm = \mathcal{W}^1 \pm i\mathcal{W}^2, \mathcal{W}^3$) under weak isospin. Self–interactions among the $\mathcal{W}^i$ vector bosons are generated by the $g_W \epsilon^{ijk} \mathcal{W}^j_\mu \mathcal{W}^k_\nu$ term of the field strength tensor, which is necessary to ensure gauge invariance for fields having a non–Abelian symmetry group.

The coupling of gauge fields to fermionic matter fields is implemented using the covariant derivative

$$D^\mu = \delta_{ij} \delta^\mu + i g_W (T \cdot \mathcal{W}^\mu)_{ij} + i Y \delta_{ij} g'_W \mathcal{B}^\mu$$

where g'_W is the U(1) gauge coupling. The matrices T are a representation of the SU(2) weak isospin algebra and the U(1) charge Y is called the weak hypercharge. To specify the coupling to fermions each matter field must be assigned to a representation T of SU(2) and to a charge Y for the gauge group U(1). The weak hypercharge Y satisfies the relation $Q = T^3 + Y$, so that the conserved quantum number Q coincides with the electric charge. The fermionic part of the Lagrangian will not be discussed further, as this is not relevant for the remainder of the thesis.

This model cannot describe the real world because there is only one massless boson observed in nature, the photon. The addition of explicit mass terms for three of the bosons would violate local gauge invariance and spoil the renormalisability of the theory. It is necessary to implement a mechanism of symmetry breaking which gives mass to three of the vector bosons and retain one conserved charge, the electric charge. This is achieved through the Higgs mechanism [18]. Three generators of the SU(2) $\otimes$ U(1) group are spontaneously broken and this should lead to the existence of three Goldstone bosons. However the Goldstone theorem does not apply if the theory contains long–range vector fields which have the same quantum numbers as the Goldstone bosons. The massless Goldstone bosons provide in this case the extra longitudinal degrees of freedom which are necessary to change the quanta of the vector fields from massless to massive bosons. The two neutral fields $\mathcal{W}^3_\mu$ and $\mathcal{B}_\mu$ are replaced by two new fields Z_μ and A_μ corresponding respectively to

the Z^0 boson and the photon. Through the Higgs mechanism the W and Z bosons acquire masses given by:

$$\begin{aligned} m_{\mathrm{W}} &= \frac{1}{2} v g_W \\ m_{\mathrm{Z}^0} &= \frac{1}{2} v \sqrt{g_W^2 + {g'}_W^2} = \frac{m_{\mathrm{W}}}{\cos\theta_W}, \end{aligned}$$

where the weak mixing θ_W is fixed by the relative strengths of the coupling constants:

$$\sin^2\theta_W = \frac{{g'}_W^2}{{g'}_W^2 + g_W^2}.$$

Writing the covariant derivative in terms of the physical fields the conserved operator $Q = T^3 + Y$ and the field A_μ, which remains massless, can be identified respectively with the electric charge and the photon, obtaining thus the following relation between the electric charge e and the weak SU(2) charge: $e = g_W \sin\theta_W$.

One particularly important constraint present in the $\mathcal{SM}$ model is that the ρ parameter [19] defined as $\rho = {m_{\mathrm{W}}}^2 / m_{\mathrm{Z}^0}^2 \cos^2\theta_W$ is equal to 1 at the tree level, a prediction which is very well verified using the latest measurements [12, 17]: $\rho = 1.0116 \pm 0.0011$. The deviation from the tree level value is caused by higher order corrections involving top quark loops, which give a contribution to $\Delta\rho = \rho - 1 = 3\mathrm{G_F} {m_t}^2 / 8\sqrt{2}\pi^2 \approx 0.01$. The constraint $\rho = 1$ is not a consequence of the spontaneous symmetry breaking mechanism, but rather of the form of the Higgs potential. After the symmetry breaking mechanism the global SU(2) $\otimes$ SU(2) symmetry of the Higgs potential is broken down to a residual SU(2) symmetry which ensures that $\rho = 1$ [20]. This symmetry is often called custodial and will be relevant in the following, since it helps in building models which account for anomalous couplings between the gauge bosons, without spoiling the $\rho = 1$ relation.

1.3 Interactions of gauge bosons

The part of the electroweak Lagrangian responsible for the self–interaction of gauge bosons, expressed in terms of the physical fields $W_\mu^\pm$, Z_μ and A_μ, is

$$\begin{aligned} \mathcal{L}_{int} = & -ig_W[W^{\mu\nu-}W_\mu^+ - W^{\mu\nu+}W_\mu^-](\cos\theta_W Z_\nu + \sin\theta_W A_\nu) \\ & -ig_W(\cos\theta_W Z^{\mu\nu} + \sin\theta_W A^{\mu\nu})[W_\mu^- W_\nu^+ - W_\mu^+ W_\nu^-] \\ & +g_W^2 \sin^2\theta_W A_\nu (A_\mu W^{+\nu} W^{-\mu} - A^\nu W_\mu^+ W^{-\mu}) \\ & +g_W^2 \cos\theta_W \sin\theta_W [W^{+\nu} W^{-\mu}(Z_\mu A_\nu + Z_\nu A_\mu) - W_\mu^+ W^{-\mu}(Z_\nu A^\nu + A_\nu Z^\nu)] \\ & +g_W^2 \cos^2\theta_W Z_\nu (Z_\mu W^{+\nu} W^{-\mu} - Z^\nu W_\mu^+ W^{-\mu}) \\ & +g_W^2 W_\nu^- W_\mu^+ (W^{-\nu} W^{+\mu} - W^{-\mu} W^{+\nu})/2, \end{aligned}$$

where $V^{\mu\nu} = \delta^\mu V^\nu - \delta^\nu V^\mu$ for $V = W^\pm, Z, A$. The first two lines of this part of the Lagrangian describe the two triple gauge boson vertices $\gamma\mathrm{W}^+\mathrm{W}^-$ and $\mathrm{Z}^0\mathrm{W}^+\mathrm{W}^-$, while the remaining four lines describe the quartic vertices $\gamma\gamma\mathrm{W}^+\mathrm{W}^-$, $\gamma\mathrm{Z}^0\mathrm{W}^+\mathrm{W}^-$, $\mathrm{Z}^0\mathrm{Z}^0\mathrm{W}^+\mathrm{W}^-$ and $\mathrm{W}^+\mathrm{W}^-\mathrm{W}^+\mathrm{W}^-$. This $\mathcal{SM}$ Lagrangian contains only operators that are invariant under the

charge conjugation ($\mathcal{C}$) and parity ($\mathcal{P}$) operators. The triple gauge boson vertices have a coupling strength g_W, whereas the quartic ones are proportional to g_W^2. This is consistent with the fact that tree level contribution to processes with four vector bosons (like in the scattering $W^+W^- \to W^+W^-$) come at the first order in perturbation theory for the quartic vertices and at second order in perturbation theory for the triple ones. Despite some recent theoretical [21] and experimental [22] interest in the field of quartic gauge couplings this subject will not be treated further in this thesis. Triple gauge couplings (TGC's) will instead be studied more in detail. The Feynman rule for the triple gauge boson vertices corresponding to the $\mathcal{SM}$ electroweak Lagrangian is given in figure 1.3.

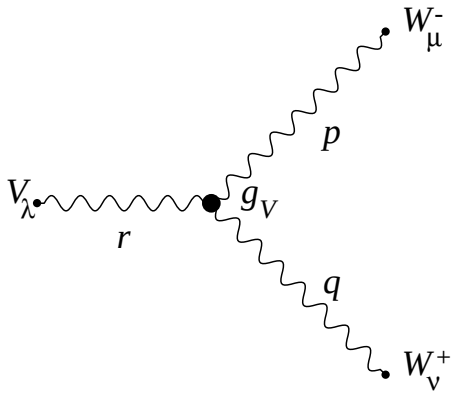

$$ig_V[(p-q)^\lambda g^{\mu\nu} + (q-r)^\mu g^{\nu\lambda} + (r-p)^\nu g^{\lambda\mu}]$$

for $(p+q+r) = 0$

$V = \gamma, Z$

$g_\gamma = e$

$g_Z = e\cot\theta_W$

r,p,q four–momenta of the fermions

$g^{\mu\nu}$ metric tensor

Figure 1.3: Feynman rule for the triple gauge boson vertex.

The triple gauge boson vertex part of the $\mathcal{SM}$ electroweak Lagrangian can be rewritten as

$$\begin{aligned}\mathcal{L}_{TGC} = &- ig_\gamma[g_1^\gamma A_\mu(W^{-\mu\nu}W_\nu^+ - W^{+\mu\nu}W_\nu^-) + \kappa_\gamma A^{\mu\nu}W_\mu^-W_\nu^+] \\ &- ig_Z[g_1^Z Z_\mu(W^{-\mu\nu}W_\nu^+ - W^{+\mu\nu}W_\nu^-) + \kappa_Z Z^{\mu\nu}W_\mu^-W_\nu^+],\end{aligned}$$

where four new parameters have been introduced, g_1^V and κ_V, to describe the coupling strength at the γW^+W^- and $Z^0W^+W^-$ vertices. In the $\mathcal{SM}$ these parameters have values $g_1^{\gamma,Z} = \kappa_{\gamma,Z} = 1$. In this form the connection between the charge Q_W, the magnetic dipole moment μ_W and the electric quadrupole moment q_W of the W and the coupling parameters

is evident:

$$
\begin{aligned}
Q_W &= e g_1^\gamma \\
\mu_W &= \frac{e}{2m_{\mathrm{W}}}(g_1^\gamma + \kappa_\gamma) \\
q_W &= -\frac{e}{m_{\mathrm{W}}^2}\kappa_\gamma .
\end{aligned}
$$

These expressions are similar to the ones used in nuclear physics to express the relation between the giromagnetic factors and the multipole moments of the charge distributions. This connection with the static properties of the W boson explains the origin of the term "anomalous couplings" for the g_1^V and κ_V parameters. While in nuclear physics values of the magnetic dipole moment different from those expected for pointlike particles are caused by the extended structure of the nuclei, in the cause of gauge bosons also extensions of the $\mathcal{SM}$ are considered. More generally the expression "anomalous couplings" is used referring to any possible deviations of the couplings from their $\mathcal{SM}$ values or also to indicate the parameters of additional terms present in the Lagrangian, as the ones introduced in the next sections.

1.4 Lorentz invariant description of the triple gauge boson vertex

There are several possibilities for describing possible deviations in the three gauge boson vertex from the $\mathcal{SM}$ prediction. The most general way of extending the Lagrangian consists in including all the terms which are permitted by Lorentz invariance. A total of seven operators is sufficient to describe the VWW vertex (where V is either the photon or the Z^0). Each boson can come in three different helicity states, which in principle would indicate that a total of nine operators is necessary. However two combinations can be excluded, since they correspond to a $J = 2$ spin. The most general Lagrangian then takes the form [23]:

$$
\begin{aligned}
-\mathcal{L}_{\mathrm{VWW}}/g_{\mathrm{VW^+W^-}} = {} & i g_1^V (W^+_{\mu\nu} W^{-\mu} V^\nu - W^+_\mu V_\nu W^{-\mu\nu}) + i\kappa_V W^+_\mu W^-_\nu V^{\mu\nu} \\
& + \frac{i\lambda_V}{m_{\mathrm{W}}^2} W^+_{\lambda\mu} W^{-\mu}_\nu V^{\nu\lambda} - g_4^V W^+_\mu W^-_\nu (\delta^\mu V^\nu + \delta^\nu V^\mu) \\
& + g_5^V \varepsilon^{\mu\nu\rho\sigma} \left(W^+_\mu (\delta_\rho W^-_\nu) - (\delta_\rho W^+_\mu) W^-_\nu \right) V_\sigma + \frac{i\tilde{\kappa}_V}{2} \varepsilon^{\mu\nu\rho\sigma} W^+_\mu W^-_\nu V_{\rho\sigma} \\
& + \frac{i\tilde{\lambda}_V}{2m_{\mathrm{W}}^2} \varepsilon^{\nu\lambda\rho\sigma} W^+_{\lambda\mu} W^{-\mu}_\nu V_{\rho\sigma} .
\end{aligned}
$$

The $\mathcal{SM}$ Lagrangian is recovered for $g_1^V = \kappa_V = 1$ and $\lambda_V = g_4^V = g_5^V = \tilde{\kappa}_V = \tilde{\lambda}_V = 0$. Often in the thesis the notations Δg_1^V and $\Delta\kappa_V$ are used to indicate deviations of the two non–zero coupling parameters from their $\mathcal{SM}$ value of 1. This general parametrisation of the VWW vertex contains in total 14 parameters, of which 2 (g_5^V) correspond to terms of the Lagrangian that violate separately $\mathcal{C}$ and $\mathcal{P}$, while 6 ($g_4^V, \tilde{\kappa}_V$ and $\tilde{\lambda}_V$) violate $\mathcal{CP}$. It should be noted that these couplings are, in general, form factors which depend on the momentum scale. This is of little importance for $\mathrm{e^+e^-}$ colliders, where the centre–of–mass energy is well defined, but it must be borne in mind at hadron colliders where the couplings are probed simultaneously over large energy ranges [24]. All terms which

involve anomalous couplings in this Lagrangian contain either one or two derivatives. Their contribution will therefore be proportional to the momentum (or the square of the momentum) of the interacting bosons. This will become relevant when studying the effects caused by eventual anomalous couplings. This general Lagrangian contains 5 operators of dimension 4 and 2 operators of dimension 6, corresponding to the λ_V and $\tilde{\lambda}_V$ parameters.

For the photon couplings, electromagnetic U(1) gauge invariance can be used to set $g_1^\gamma = 1$. In presence of the new terms in the Lagrangian, the relations giving the magnetic dipole μ_W and electric quadrupole q_W moments are:

$$\mu_W = \frac{e}{2m_{\mathrm{W}}}(1 + \kappa_\gamma + \lambda_\gamma)$$
$$q_W = -\frac{e}{m_{\mathrm{W}}^2}(\kappa_\gamma - \lambda_\gamma).$$

The parity violating terms in $\tilde{\kappa}_\gamma, \tilde{\lambda}_\gamma$ are instead related to the electric quadrupole d_W and magnetic quadrupole $\tilde{Q}_W$ moments of the W boson by the relations:

$$d_W = \frac{e}{2m_{\mathrm{W}}}(\tilde{\kappa}_\gamma + \tilde{\lambda}_\gamma)$$
$$\tilde{Q}_W = -\frac{e}{m_{\mathrm{W}}^2}(\tilde{\kappa}_\gamma - \tilde{\lambda}_\gamma).$$

This Lagrangian provides the most general framework for the description of experimental results, independently from theoretical assumptions on possible anomalous couplings and their causes. It is not used extensively from the experiments as the complete description of the data requires in principle measurements of all 14 form factors as a function of energy. Moreover it does not provide a framework for testing the effects caused by extensions of the $\mathcal{SM}$ in the sector of gauge couplings. For this purpose a different approach has to be followed. The framework generally used for calculating virtual effects from new physics at large mass scales is that of effective Lagrangians. All effects caused by heavy particles at low energy are parametrised using a set of unknown constants, the magnitude of which can be bound using experimental data and estimated for various classes of models. From these results informations can be extracted about new interactions, and if necessary dedicated experiments can be designed. This approach has been used in particle physics since the development of the Fermi theory of weak interactions [3].

The idea beyond the effective Lagrangian approach [25] is that the $\mathcal{SM}$ is only a lower energy approximation of another theory. The only two assumptions made in this kind of analysis are that the new physics cannot be observed directly, since its energy scale Λ is much larger than the available energy, and that the low energy particle spectrum is known and lies below the scale Λ. The new heavy particle are not observed directly, but affect the measurable quantities through virtual effects. The effects of this larger theory are computed using a Lagrangian which is an expansion in power of $1/\Lambda$, where Λ is the scale of the new physics:

$$\mathcal{L}_{eff} = \sum_n \frac{1}{\Lambda^n} \sum_i \alpha_i^{(n)} \mathcal{O}_i^{(n)}.$$

The operators $\mathcal{O}_i^{(n)}$ have dimensions $[\mathrm{mass}]^{n-4}$, are local functions of the light fields, and

obey the same gauge symmetry. The coefficients α_i are obtained from the parameters of the original high energy theory. In general all possible operators $\mathcal{O}$ allowed by local symmetries are included, and therefore the coefficients α of this expansion parametrise all possible effects at low energy. In practice the sum is truncated and only terms containing operators with the lowest dimensions will be included, as the remaining ones will be suppressed by powers of $1/\Lambda$.

1.5 Gauge couplings in models with a light Higgs boson

Initial attempts to build models of new physics which could cause anomalous couplings [26] were performed in a framework which introduces deviations from the $\mathcal{SM}$ that violate the SU(2) $\otimes$ U(1) gauge invariance. Very stringent bounds on anomalous couplings are obtained from low–energy measurements (like the ρ parameter or the evidence for loop corrections to the Z^0 propagator), since the 1–loop corrections from anomalous VWW interactions are quadratically or quartically divergent. These divergences can be avoided (or reduced to logarithmic ones) if gauge invariance under the SU(2) $\otimes$ U(1) group is imposed. This was first realised by De Rújula *et al.* [27], who studied the effect of operators $\mathcal{O}_i$ of dimension six, which are built using only the Higgs field Φ, its covariant derivative $D_\mu\Phi$ and the field strength tensors of the electroweak gauge fields $\mathcal{W}_{\mu\nu}$ and $\mathcal{B}_{\mu\nu}$. The complete list of these operators can be found for example in [28]. Higher order terms in ${m_W}^2/\Lambda^2$ or v^2/Λ^2, arising from higher dimensional operators are neglected. One important feature of this kind of analysis is that it emphasises the rôle played by the symmetry breaking mechanism in generating the anomalous couplings.

In this type of analysis [27, 29, 30], operators which involve fermions are neglected, as they would contribute terms which are proportional to m_f/Λ, and therefore are negligible (with the possible exception of terms involving the top quark). Neglecting also the operators that violate $\mathcal{CP}$ (which are considered in [30]), only 11 operators remain. In terms of these operators the Lagrangian can be written as

$$\mathcal{L} = \sum_{i=1}^{11} \frac{f_i}{\Lambda^2}\mathcal{O}_i$$

where the order of magnitude of the f_i parameters is expected to be 1. Four of these operators affect the gauge boson propagators already at the tree level and therefore are severely constrained from lower energy measurements. Among these four operators, two ($\mathcal{O}_{BW}$ and $\mathcal{O}_{DW}$) give also rise to anomalous couplings. Two of the remaining seven operators affect only the Higgs self–interactions. The remaining five operators are, in the notation of [30]:

$$\begin{aligned}
\mathcal{O}_{WW} &= \Phi^+ \mathcal{W}^-_{\mu\nu}\mathcal{W}^{-\mu\nu}\Phi \\
\mathcal{O}_{BB} &= \Phi^+ \mathcal{B}_{\mu\nu}\mathcal{B}^{\mu\nu}\Phi \\
\mathcal{O}_{W} &= \mathrm{Tr}[\mathcal{W}^+_{\mu\nu}\mathcal{W}^{-\nu\rho}\mathcal{W}^{-\mu}_{\rho}] \\
\mathcal{O}_{B\phi} &= (D_\mu\Phi)^+ \mathcal{B}^{\mu\nu}(D_\nu\Phi) \\
\mathcal{O}_{W\phi} &= (D_\mu\Phi)^+ \mathcal{W}^{-\mu\nu}(D_\nu\Phi).
\end{aligned}$$

Once symmetry breaking is performed, the first two operators $\mathcal{O}_{WW}$ and $\mathcal{O}_{BB}$ are in part reabsorbed in the renormalisation of the electroweak fields and enhance the branching ratio for the $H \to \gamma\gamma$ and $H \to Z^0\gamma$ processes. However they do not contribute to vertices with three gauge bosons and they affect the propagators only at the loop level, and therefore they are not severely constrained by low energy measurements. The remaining three operators give rise to anomalous gauge couplings. From a comparison of this effective Lagrangian with the most general Lorentz–invariant Lagrangian discussed in section 1.4 the following relations can be established between the parameters of the expansions in terms of $1/\Lambda^2$ and the anomalous couplings (see for example [29]):

$$\begin{aligned}
\kappa_\gamma &= 1 + (f_{B\phi} + f_{W\phi})]\frac{m_W^2}{2\Lambda^2}, \\
\kappa_Z &= 1 + [f_{W\phi} - \sin^2\theta_W(f_{B\phi} + f_{W\phi})]\frac{m_{Z^0}^2}{2\Lambda^2}, \\
g_1^Z &= 1 + f_{W\phi}\frac{m_{Z^0}^2}{2\Lambda^2} = \kappa_Z + \frac{\sin^2\theta_W}{\cos^2\theta_W}(\kappa_\gamma - 1), \\
\lambda = \lambda_\gamma = \lambda_Z &= \frac{3m_W^2 g_W^2}{2\Lambda^2} f_W.
\end{aligned}$$

Assuming that all the coefficients f_i are of the same order of magnitude, the λ_V couplings are expected to be suppressed by a factor g_W^2 in comparison to the three others.

The two important constraints resulting from this type of analysis,

$$\begin{aligned}
&g_1^Z = \kappa_Z + \tan^2\theta_W(\kappa_\gamma - 1) \qquad \text{and} \\
&\lambda_\gamma = \lambda_Z,
\end{aligned}$$

are a consequence of the fact that only operators of dimension six have been considered and that the chosen parametrisation respects the SU(2) $\otimes$ U(1) symmetry: these degeneracies are lifted when operators of dimension eight are taken into account. However the additional terms are proportional to v^2/Λ^2, and therefore they should be visible only for small scales Λ, which are already excluded by current measurements. The expression "SU(2) $\otimes$ U(1) constraints" will be used to refer to the constraints among TGC's obtained in this model.

The three operators $\mathcal{O}_i = \mathcal{O}_W, \mathcal{O}_{B\phi}, \mathcal{O}_{W\phi}$ can be rewritten (using the equation of motion of the $\mathcal{SM}$ Lagrangian) in terms of operators that affect the propagators of the weak bosons and which for this reason are severely constrained by the low energy measurements. However the particular combinations of operators corresponding to the three $\mathcal{O}_i$ happens to be much less constrained than the others. Therefore in the literature they are said to point into "blind directions" in the space of the operators of dimension 6 built using a model in which there is a physical Higgs boson. Since also the $\mathcal{O}_{BW}$ and $\mathcal{O}_{DW}$ operators might cause anomalous TGC's, these relations between anomalous couplings are valid only if these additional contributions can be neglected. At the level of precision achievable in current experiments, this is actually the case, since the two additional operators are severely constrained by low energy measurements.

This kind of analysis can be extended to the case of a very heavy Higgs boson or to models without a scalar resonance, which are usually dealt with using a chiral Lagrangian. The chiral Lagrangian is simply obtained with the replacements $\Phi \to$

$\exp(i\sigma^\alpha\chi^\alpha/v)(0,v/\sqrt{2})$ and $\Lambda \to 4\pi v$. The main effect of these changes is that operators of dimensions 6 and 8 formally appear at the same level, and therefore the relations among the couplings obtained in the case of a light Higgs boson no longer hold. However they can still be used as a guidance in the analysis, under the assumption that v^2/Λ^2 is small.

1.6 Gauge couplings in models without a physical Higgs boson

In the second common approach to effective Lagrangians, the masses of the W and Z bosons are not generated through the Higgs mechanism, but through the interaction with Goldstone bosons. Since there is no Higgs boson, the low–energy $\mathcal{SM}$ Lagrangian violates unitarity at a scale of $4\pi v \approx 3$ TeV, so that new physics should appear at a scale $\Lambda < 4\pi v$.

One particular realisation of this class of models [31, 32], which conserves the custodial $SU(2)_c$ symmetry of the $\mathcal{SM}$, is built using the field $\Sigma = \exp(i\vec{\omega}\cdot\vec{\sigma}/v)$, where the ω_i are the Goldstone bosons. The $SU(2)\otimes U(1)$ covariant derivative is then defined as

$$D_\mu\Sigma = \delta_\mu\Sigma + \frac{i}{2}g_W\mathcal{W}_\mu^a\sigma^a\Sigma - i2g'_W\mathcal{B}_\mu\Sigma\sigma^3.$$

The effective Lagrangian [33] is then built using the field strengths $\mathcal{W}_{\mu\nu}, \mathcal{B}_{\mu\nu}$ and covariant derivatives. Due to its similarity to low–energy QCD, this Lagrangian is generally known as chiral Lagrangian. The more general Lagrangian for triple gauge boson vertices can be expressed in terms of the two operators which appear in this chiral Lagrangian:

$$\mathcal{L} = -ig_W\frac{v^2}{\Lambda^2}L_{9L}[\mathcal{W}^{\mu\nu}D_\mu\Sigma D_\nu\Sigma^+] - ig'_W\frac{v^2}{\Lambda^2}L_{9R}[\mathcal{B}^{\mu\nu}D_\mu\Sigma D_\nu\Sigma^+],$$

where the $L_{9L,R}$ parameters are expected to be of $\mathcal{O}(1)$. As in the case of the model with a physical Higgs boson, one additional operator ($g_W g'_W L_{10}\mathrm{Tr}(\mathcal{B}^{\mu\nu}\Sigma^+\mathcal{W}^{\mu\nu}\Sigma)/16\pi^2$) is ignored since it is already constrained by LEP1 data.

Comparing this expression (after substituting the Goldstone bosons with the physical fields) with the Lagrangian of section 1.4 the following relations are obtained between the couplings and the parameters of the effective Lagrangian:

$$\begin{aligned}
\kappa_\gamma &= 1 + \frac{e^2}{2\sin^2\theta_W}\frac{v^2}{\Lambda^2}(L_{9L}+L_{9R}) \\
\kappa_Z &= 1 + \frac{e^2}{2\sin^2\theta_W\cos^2\theta_W}\frac{v^2}{\Lambda^2}(L_{9L}\cos^2\theta_W - L_{9R}\sin^2\theta_W) \\
g_1^Z &= 1 + \frac{e^2}{2\sin^2\theta_W\cos^2\theta_W}\frac{v^2}{\Lambda^2}L_{9L} \\
\lambda_\gamma = \lambda_Z &= 0.
\end{aligned}$$

The last equality can be easily understood by making a dimensional analysis of the operators in the Lorentz–invariant Lagrangian: the operators which enter in the λ_V terms contain three derivatives (two more than the terms in g_1^V, κ_V). Therefore they are of dimension 8 instead of dimension 6, and get no contribution from the operators considered in this effective Lagrangian, whereas in the light Higgs boson case these terms where foreseen but suppressed for a factor g_W^2.

The light Higgs boson scenario discussed in the previous section can be recovered

assuming $L_{9L} = 2f_{W\phi}$ and $L_{9R} = 2f_{B\phi}$, so that also in this case the relation $g_1^Z = \kappa_Z + \tan^2\theta_W(\kappa_\gamma - 1)$ is satisfied. The main difference between the two models is only in their Higgs content. In the second model without Higgs boson there is a more direct connection between anomalous couplings and the dynamics of the symmetry breaking.

1.7 Estimates of the size of anomalous TGC's

In the $\mathcal{SM}$ the triple gauge couplings receive contributions from loops, which will cause deviations from the tree level values indicated in section 1.4. The order of magnitude of these corrections is given by $g_W/16\pi^2 = 2.7\,10^{-3}$, which is well below the sensitivity of the experiments performed at LEP2, as explained in chapter 2. Precise predictions are known [34] and are in the range 3–6 10^{-3}, for $m_{\mathrm{H}} = 65$–1000 GeV/c^2 and $m_t = 175$ GeV/c^2. Predictions for the case of the minimal supersymmetric extension of the $\mathcal{SM}$ [35] are of the same order of magnitude.

Using the approach of effective Lagrangians and the two models described in sections 1.5 and 1.6 it is possible to make estimates of the order of magnitudes of contributions to TGC's not coming from $\mathcal{SM}$ particles [25, 36] without referring to a particular extension of the electroweak theory. The results of this type of analysis are that in general deviations in the TGC's from the $\mathcal{SM}$ values should not be in the range visible at LEP2 (in the best cases deviations of $\mathcal{O}(10^{-3})$ are predicted), unless the new particles and interactions causing these anomalous couplings are also directly observable. However the possibility of large cancellations, which would then reduce the effects of anomalous couplings on other observables, cannot be excluded. It is therefore necessary for experiments to search directly for evidence of anomalous TGC's, even though, in the light of the current theoretical understanding, such measurements will likely yield null results.

2 Measurements of triple gauge boson couplings

As shown in Chapter 1, the measurement of the self–coupling of the intermediate vector bosons provides a fundamental test of the non–Abelian structure of the electroweak theory. The evidence of the existence of these couplings, obtained from the study of radiative corrections to the Z^0 propagator, does not allow to constrain all the possible terms of the Lagrangian describing triple gauge boson vertices. Knowledge of this sector of the $\mathcal{SM}$ can only improve through new direct measurements of the coupling parameters. Currently, measurements of TGC's are performed both at Tevatron and at LEP2 and the ultimate precisions attainable are comparable. These measurements of TGC's are shortly reviewed in this chapter and compared with constraints obtained from the study of radiative corrections.

The processes sensitive to TGC's are either of the $1 \to 2$ type, annihilation of a fermion pair into a boson followed by emissions of two bosons, or of the $2 \to 1$ type, fusion of two bosons into a single one. At LEP2 the main channel is the doubly resonant W pair production, since it has for most parameters the highest sensitivity to TGC's, both through the total W^+W^- production cross section and through the production and decay angular distributions of the W bosons, as shown in section 2.1. The event selection and measurement techniques used by the LEP2 experiments are reviewed in section 2.2. Some sensitivity to the couplings is also retained in the $e^+e^- \to \nu\overline{\nu}\gamma$ final state, which receives contribution from the $W^+W^- \to \gamma$ fusion process. Measurements of this final state are described in section 2.3. Measurements of TGC's performed at hadron colliders in final states containing two electroweak bosons are reviewed in section 2.4. All the direct measurements of the coupling parameters are compared to constraints obtained from the study of radiative corrections to the Z^0 propagator and the study of rare decays in section 2.5. The chapter is closed in section 2.6 by a discussion of the precision reachable in TGC's measurements at the LHC and at future e^+e^- linear colliders.

2.1 Triple gauge couplings in the $e^+e^- \to W^+W^-$ process

The process best suited to the measurement of TGC's at LEP2 is $e^+e^- \to W^+W^-$, which proceeds through the 3 diagrams indicated in figure 2.1 (these three diagrams are called CC03 diagrams). In a second phase of the process the two W bosons decay into leptons and / or quarks. One basic assumption for the analysis of this process is that the production and decay phase of the W bosons can be treated independently, neglecting other diagrams which lead to the same four–fermion final state and other effects like interference between

initial and final state radiation, hadronisation, exchange of photons or gluons between final state particles, Bose–Einstein correlations, which may spoil this simplified picture.

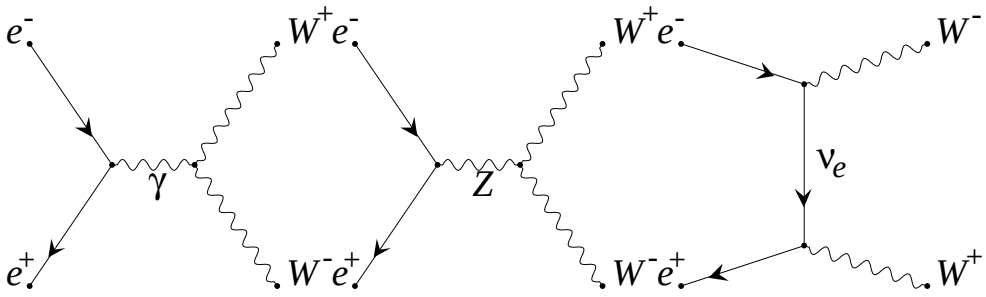

Figure 2.1: Feynman diagrams for the process $e^+e^- \to W^+W^-$.

Explicit expressions for the cross section of the $e^+e^- \to W^+W^- \to f_1\bar{f}_2f_3\bar{f}_4$ process have been derived in [23, 30] in terms of helicity amplitudes [37]. Integrating over all decay distributions of the W bosons, the differential production cross section for the $e^+e^- \to W^+W^-$ process is obtained:

$$\frac{d\sigma}{d\cos\theta_W} = \frac{\beta}{32\pi s}\sum_{\sigma\lambda\overline{\lambda}} |F^{\sigma}_{\lambda\overline{\lambda}}(s,\cos\theta_W)|^2,$$

where $\cos\theta_W$ is the polar angle of the W^- boson, measured with respect to the incoming electron direction, $\sqrt{s}$ is the centre–of–mass energy, σ is the electron helicity, λ and $\overline{\lambda}$ are the helicities of the two W bosons and β is the W boson velocity in units of c. All the dependence on the couplings, which are sensitive to different polarisation states of the two W's, is contained into the functions $F^{\sigma}_{\lambda\overline{\lambda}}(s,\cos\theta_W)$.

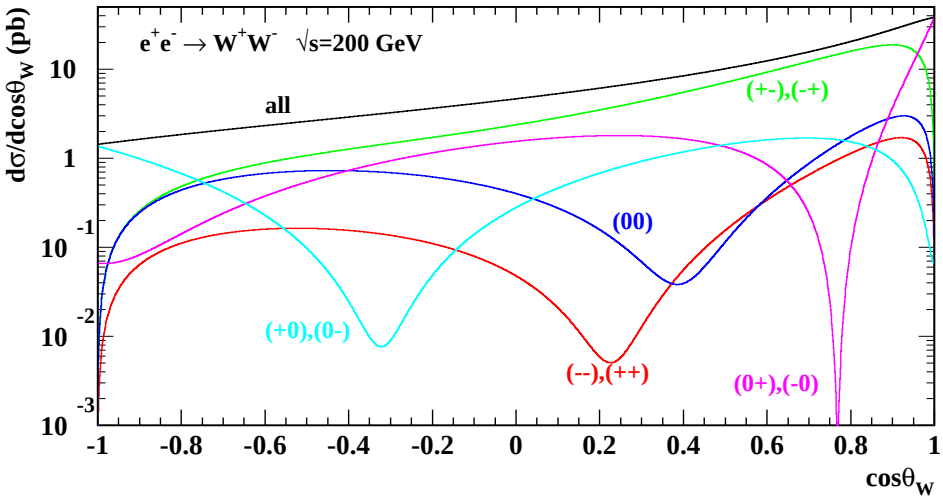

Figure 2.2: Angular distribution $d\sigma/d\cos\theta_W$ for $e^+e^- \to W^+W^-$. The $\mathcal{SM}$ contribution for different helicities (or combinations of helicities) of the W bosons $(\lambda,\overline{\lambda})$ are shown at $\sqrt{s} = 200$ GeV.

The contributions from different helicity combinations of the two W bosons are shown

in figure 2.2. Clearly the different helicity states have different angular distribution. When combined with the fact that different anomalous couplings give different contributions to the different helicity states it becomes attractive to do a polarisation analysis and separate the different helicity states, to reduce the effect of any possible cancellation among the contributions from the TGC's. Due to the $V-A$ structure of the weak interactions, the decay angular distributions of the W's can be used as polarisation analysers to separate the contributions from the different W helicities. Therefore to extract all the possible information from the events it is necessary to measure five angles, the W^- production angle, and two decays angles for each W, which give access to the W helicities. The decays angles are most easily given in the rest frame of the decaying W boson: for the W^- (W^+) the angles θ_1^* (θ_2^*) and ϕ_1^* (ϕ_2^*) refer to the direction of the outgoing particle (antiparticle). The definition of these angles is visualised in figure 2.3.

The expression of the differential cross section [23, 30] in terms of the helicity amplitudes shows how gauge invariance in the $\mathcal{SM}$ ensures that the unitarity limit of the cross section is not violated at high centre–of–mass energy. The $J=2$ partial wave receives contribution only from the t–channel ν_e exchange diagram and only through the transverse helicity combination $(\lambda,\overline{\lambda}) = (-,+)$, which at high energy gives a cross section which decreases like $1/s$. Violation of unitarity might occur only in the $J=1$ partial wave. The s–channel contribution from the γ and Z^0 annihilation, which is purely a $J=1$ partial wave, cancels exactly the t–channel ν_e exchange contribution, due to the equality of the coupling constants at the Weν_e and VWW vertices. This cancellation does not occur in presence of anomalous couplings. Since different anomalous couplings give different contributions to the helicity amplitudes this causes a distortion of the angular cross section and for most cases an increase in the total cross section. Anomalous couplings give contributions to the different helicity amplitudes which are proportional to $\sqrt{s}$ or s. Therefore the sensitivity to TGC's increases with the centre–of–mass energy, $\sqrt{s}$.

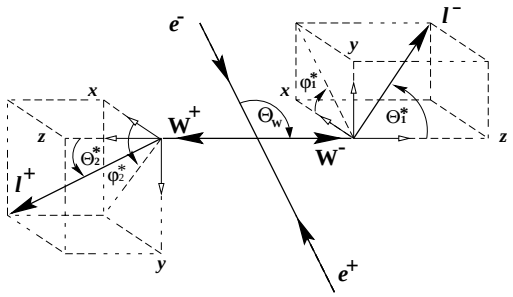

Figure 2.3: The definition of the 5 angles used in W^+W^- final states for the measurement of the W production and decay angles.

Another feature which appears from an analysis of the helicity dependence of the couplings is that different couplings cause similar effects on the total and differential cross sections. Correlations are expected between the $(\Delta\kappa_\gamma, \lambda_\gamma)$ and the $(\Delta g_1^z, \Delta\kappa_z, \lambda_z)$ sets of couplings, and their size is a function of energy. For example the correlations between $\Delta\kappa_\gamma$ and λ_γ ($\Delta\kappa_z$ and λ_z) tend to decrease with energy, whereas that between $\Delta\kappa_\gamma$ and Δg_1^z and that between $\Delta\kappa_\gamma$ and $\Delta\kappa_z$ become stronger. In addition, since $s \gg m^2_{Z^0}$, the couplings at the γW^+W^- and $Z^0W^+W^-$ vertices always enter in the helicity amplitudes through the same linear combination. This means that it is difficult to disentangle the two types of couplings. Together with the limited statistics available, this is a reason for using in the analysis the relations among couplings dictated by the model introduced in section 1.5: $\Delta g_1^z = \Delta\kappa_z + \tan^2\theta_W \Delta\kappa_\gamma$ and $\lambda_z = \lambda_\gamma$. The only way to distinguish between the $\Delta\kappa_\gamma$ and $\Delta\kappa_z$ (λ_γ and λ_z) couplings is to make use of other reactions or of polarised beams [23].

2.2 Measurement techniques and results from LEP experiments

As seen in the previous section both the total W pair production cross section and the production and decay angular distribution of the W bosons are sensitive to the TGC's. The measurement of the total cross section is based on high purity sample of $e^+e^- \to W^+W^-$ events, using different analyses depending on the decay modes of the W bosons:

- $W^+W^- \to q\overline{q}'\ell\overline{\nu}_\ell$ decays (total branching ratio of 43.9%) are characterised by the presence of a high energy lepton, two jets and missing energy. The selection of these events typically begins with the identification of the lepton as the highest momentum isolated track. The rest of the event is then forced into two jets. Vetoes are applied on events with isolated photons which may fake the signature of an electron, and on four fermion events with two charged leptons in the final states. The signal sample is selected by requiring high missing transverse momentum and placing cuts on the energy and isolation of the lepton. Purities in excess of 90% for efficiencies around 80% are obtained. The background is dominated by $e^+e^- \to q\overline{q}(\gamma)$ events and four–fermion final states not produced through the CC03 process.

- The $W^+W^- \to q\overline{q}'q\overline{q}'$ channel (branching ratio 45.5%) is characterised by final states which have four well separated hadronic jets. The missing energy is only due to radiation from the initial state and is therefore small. Events are selected by requiring large visible energy and invariant mass. Multijet production in $e^+e^- \to q\overline{q}(\gamma)$ collisions is characterised by smaller jet energies and jet–jet angles with respect to the $W^+W^- \to q\overline{q}'q\overline{q}'$ final states. This type of information is usually combined with global event properties (sphericity, the y_{34} jet parameter, ...) and in some cases also with mass related informations into neural networks or likelihoods, to yield selection efficiencies and purities of $\approx 80\%$.

- Fully leptonic WW events (total branching ratio 10.6%) are characterised by the presence of two energetic leptons or low multiplicity jets produced by the decay of τ's and large missing momentum due to the neutrinos. The event selections are based on the event topology and require two low multiplicity acoplanar jets (here a jet may also be a single leptonic track) and large missing transverse momentum. Events where a high energy lepton pair is produced trough e^+e^- annihilation are vetoed. High selection efficiencies are reached applying loose lepton identification criteria, although this leads to some cross–contamination from the τ decay channels, which must be then corrected for. The average efficiency is for all experiments around 70%, with purities in excess of 90%. Backgrounds are dominated by lepton pair production in the collisions of pairs of virtual photons emitted from the beams and by 4–fermion events of the ZZ type.

To interpret the measurement of the $e^+e^- \to W^+W^-$ cross section in terms of TGC's a maximum likelihood fit to the number of observed events is performed. The probability of observing the measured number of candidates is calculated using a Poisson distribution, whose expected value is a function of the couplings. This gives, for each experiment, a log–likelihood curve which is later added to the one obtained from the fit to the angular distribution to obtain the final measurement of the couplings. This procedure of separating the two measurements has the advantage of making use of the full sample of selected

$e^+e^- \to W^+W^-$ events for the rate measurement. Some of these events cannot be used for the analysis of the angular distributions, since the production and decay angles are not measured with sufficient accuracy. Each experiment has selected approximately 2500 W^+W^- events in their 1998 data, leading to cross section measurements with precisions of $\mathcal{O}(2\%)$. This allows measurements of the λ_γ and Δg_1^z couplings with an accuracy of ≈ 0.2. For the $\Delta\kappa_\gamma$ coupling the measurement of the $e^+e^- \to W^+W^-$ cross section gives instead an accuracy of ≈ 0.5.

Higher precision measurements of the couplings can be achieved studying the production and decay angular distribution of the W bosons. For this purpose it is necessary to reconstruct and identify all four primary fermions from the two W decays. This is not possible in any of the decay channels, for a wide variety of reasons:

- the impossibility of measuring the energies or momenta of neutrinos from W decay;
- the limited acceptance for initial-state radiated photons;
- the limited resolution on jet and lepton directions and energies;
- background from incorrectly identified events;
- the difficulty of deducing primary quark charges from measured hadronic jets;
- the reconstruction of neutrinos also from τ decays.

To improve the resolution on reconstructed angles, it is common to apply constraints to events, and then to refit the quantities required. Most common is the constraint of total energy and momentum conservation (corresponding to four equations) which assumes that any photon which may have been radiated along the beam direction can be neglected, so that the observed system should really have the full centre–of–mass energy, and zero total momentum in the laboratory frame. Constraints are also often imposed on the masses of the W's. In the $W^+W^- \to q\overline{q}'q\overline{q}'$ and $W^+W^- \to q\overline{q}'\ell\overline{\nu}_\ell$ channels the two decaying W's are constrained to have equal masses. For the measurement of TGC's the more stringent requirement that each W in every event has a mass equal to a fixed value of m_W is also applied. Although both constraints do not correspond to the true situation, they improve the performance, because the neglected effects, initial state radiation and the W width, are small compared to the relevant detector resolution. These considerations affect the different channels in different ways:

- In the $W^+W^- \to q\overline{q}'\ell\overline{\nu}_\ell$ decay channel, there are just one ($\ell =$ e or μ) or at least two ($\ell = \tau$) neutrinos. The total energy–momentum and equal mass constraints allow good reconstruction of the W decays, except that a two–fold ambiguity remains, regarding which of the two jets from the hadronic W decay should be identified as quark. Even in the $W \to \tau\overline{\nu}_\tau$ decay, the τ can be reconstructed, since the invariant mass of the observed and unobserved τ decay products is known to be the τ mass. The W charge assignment is generally correct, the only problem being in the $W^+W^- \to q\overline{q}'\tau\overline{\nu}_\tau$ channel for hadronic decays of the τ. Some additional cuts are needed to remove events in which the assignment of tracks to the τ is ambiguous, leading to a wrong measurement of the W charge. Since the $W^+W^- \to q\overline{q}'\ell\overline{\nu}_\ell$ channel has a large branching ratio and it can be selected with high efficiency with a correct determination of the W charge, it is the main channel for the measurement of

TGC's, despite the remaining two–fold ambiguity on the decay angles of one of the W's.

- In $W^+W^- \to q\overline{q}'q\overline{q}'$ decays the four jet directions can be identified with the directions of the four quarks. The connection between quarks and jets is difficult, since it must rely on jet charge [38] information. Furthermore the jets can be combined in three different ways to form the two W bosons, leading in some events to ambiguous solutions. If the jets are assigned to one W or the other using the invariant mass information, the combined charge of the two jet–pair systems can provide a useful separation between W^+ and W^- decays, where the average charge separation should be two units. Typically cuts are applied to improve the fraction of events in which the W charge assignment is correct. This increases the probability of a correct determination of the W charge to more than 80%, at the cost of a reduction in efficiency from more than 80% to 50–60%. The identification of the quark and antiquark coming from the same W is more difficult, since the charge separation is only unit, and not performed in the analysis. Therefore the W's helicities cannot be directly measured and in the fits the angular distributions of the W decay products are folded to take into account the quark–antiquark ambiguity.

- In the $W^+W^- \to \ell^-\overline{\nu}_\ell\ell'^+\nu_{\ell'}$ channel, there are at least two neutrinos. When the total energy–momentum and W–mass constraints are applied, the directions and energies of both charged leptons need to be known in order to reconstruct the production and decay angles of the W bosons, effectively restricting the analysis to the case where both leptons are electrons or muons. Even in this case, there remains a two–fold ambiguity on the reconstructed neutrino momenta. This ambiguity affects only the measurement of the decay angles $\phi^*_{1,2}$, while for the remaining three angles, $\cos\theta_W$ and $\theta^*_{1,2}$, there is a unique solution. This represents an advantage of this channel, as it allows to study correlations between the helicity of the two W's, compensating partially for the low branching fraction of this final state. Whilst some partial production and decay information might be extracted from doubly–leptonic W decays with τ's, the analysis of these decays is not performed due to the reduced sensitivity.

Several methods are used to measure the couplings starting from the measured angular distributions, unbinned and binned maximum likelihood methods, the optimal observables method [39] and the spin–density method [30] which in the end all give compatible results, allowing useful cross–checks:

- In the unbinned maximum likelihood method, the five fold angular distribution is parametrised as a function of the anomalous couplings by a simple analytic function which does not take into account the width of the W boson and initial state radiation (ISR). These have to be folded in the fitting function together with the detector resolution and acceptance. The advantage of this method is that it uses all the information present in the data, and does not require large Monte Carlo samples.

- In the binned maximum likelihood method all physical and detector effects are taken into account, at the cost of a loss of statistical precision, performing a fit of the data to distributions obtained from large Monte Carlo samples which have different values of the couplings.

- In the optimal observables method the angular distributions are not directly fitted, but used to form a function which is a series expansion of the differential cross section with respect to the anomalous couplings. The direction in the 5–dimensional space of the W production and decay angles which is most sensitive to the couplings is picked up by this optimal observable. The value of the couplings is then obtained from the mean of the distribution of the first derivative, from a likelihood fit to its 1–dimensional distribution, or using both the first and second derivative. For small values of the couplings this method retains the full power of an unbinned maximum likelihood fit, with the advantage of being much simpler. Therefore it is the most commonly used method, although the physical information is completely hidden in this optimal variable.

- The method which gives the most direct insight on the triple gauge couplings is the spin–density method, although it can only be applied to the $W^+W^- \to q\overline{q}'\ell\overline{\nu}_\ell$ channel. The polarisation properties of the produced W bosons are described by the 9×9 two–particle joint density matrix, which needs to be measured as a function of the W production angle $\cos\theta_W$. Due to the limited statistics available and the ambiguity in identifying the quark jet in hadronic decays, the single W spin density matrix is used instead. This hermitian 3×3 matrix has 6 independent elements, the diagonal elements representing the probability to produce a W boson in a given helicity state. The single W spin density matrix elements are extracted from the data using projection operators [40]. One feature of this method is that it allows to present the data without any assumption on the relations among couplings and to measure directly the differential cross section for producing longitudinal W bosons, the existence of which is the direct consequence of the Higgs mechanism. Such measurement has been pioneered with limited statistics by the OPAL Collaboration [41] and recently repeated by the L3 Collaboration [42]: $(24.4 \pm 4.8)\%$ of the W bosons produced at LEP2 have a longitudinal polarisation. The differential cross sections for producing W bosons with longitudinal and transverse polarisations are shown in figure 2.4.

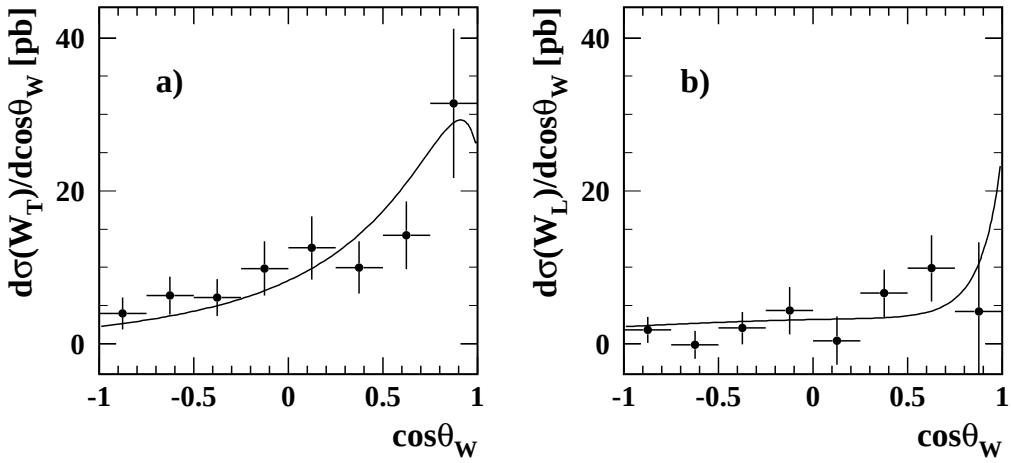

Figure 2.4: Cross section for longitudinally (*a*) and transverse (*b*) polarised W bosons.

For all these fitting methods Monte Carlo samples generated at different values of the couplings are used to check for biases in the event selection and in the fit procedure. Since

the available data samples are small and the detector resolution is not Gaussian, simulated events are used to check the correctness of the statistical error returned by the fit. The results are presented as likelihood curves for each W^+W^- final state and energy, which are then added together with those obtained from the event rate measurements to obtain the best possible constraint on the anomalous couplings. For the simplest fits only one of the Δg_1^z, $\Delta\kappa_\gamma$ and λ_γ couplings is varied, keeping the other two fixed at their $\mathcal{SM}$ value and assuming the relations introduced in section 1.5 between the γW^+W^- and $Z^0W^+W^-$ couplings. Multidimensional fits in which two or all three couplings are varied simultaneously are also performed. The sensitivity to TGC's in the $W^+W^- \to q\overline{q}'\ell\overline{\nu}_\ell$ channel is by a factor 2 higher than in the $W^+W^- \to q\overline{q}'q\overline{q}'$ and $W^+W^- \to \ell^-\overline{\nu}_\ell\ell'^+\nu_{\ell'}$ channels, which yield measurements of similar precision. An exception is the measurement of the λ_γ parameter where the sensitivity of the $W^+W^- \to \ell^-\overline{\nu}_\ell\ell'^+\nu_{\ell'}$ channel is similar to that of the $W^+W^- \to q\overline{q}'\ell\overline{\nu}_\ell$ channel.

Experiment	Measurement		
	Δg_1^z	$\Delta\kappa_\gamma$	λ_γ
ALEPH [43]	$-0.001^{+0.063}_{-0.050}$	$-0.013^{+0.144}_{-0.112}$	$-0.050^{+0.070}_{-0.059}$
DELPHI [44]	$-0.02^{+0.07}_{-0.06}$	$0.23^{+0.16}_{-0.16}$	$0.02^{+0.08}_{-0.08}$
L3 [45]	$-0.02^{+0.07}_{-0.07}$	$-0.12^{+0.16}_{-0.14}$	$0.00^{+0.07}_{-0.07}$
OPAL [41]	$-0.007^{+0.075}_{-0.071}$	$0.00^{+0.27}_{-0.19}$	$-0.113^{+0.076}_{-0.069}$
LEP Combined [46]	$-0.010^{+0.033}_{-0.033}$	$0.038^{+0.079}_{-0.075}$	$-0.037^{+0.036}_{-0.035}$
	95% CL limits		
	Δg_1^z	$\Delta\kappa_\gamma$	λ_γ
ALEPH	[−0.113,0.126]	[−0.217,0.223]	[−0.158,0.074]
DELPHI	[−0.14,0.11]	[−0.08,0.55]	[−0.14,0.19]
L3	[−0.15,0.12]	[−0.38,0.22]	[−0.13,0.15]
OPAL	[−0.14,0.14]	[−0.36,0.83]	[−0.25,0.04]
LEP Combined	[−0.073,0.055]	[−0.107,0.196]	[−0.104,0.034]

Table 2.1: One dimensional measurements of the Δg_1^z, $\Delta\kappa_\gamma$ and λ_γ parameters obtained by the LEP experiments and their combined results. Quoted errors include both statistical and systematic components. Also given are the 95% CL limits on the coupling, keeping the value of the other parameters at their $\mathcal{SM}$ value. All results shown are preliminary [47] and include data samples collected at $\sqrt{s} = 161$–189 GeV for different final states.

The precision on TGC's through the measurement of the production and decay angles of the W bosons is higher than that obtained from the total cross section measurement. Combining the two results, each experiment measures the λ_γ and Δg_1^z couplings with a precision of ≈ 0.06 and the $\Delta\kappa_\gamma$ coupling with a precision of ≈ 0.2, an improvement of a factor between 3 (for $\Delta\kappa_\gamma$) and 5 (for Δg_1^z and λ_γ) with respect to the measurement obtained from the total cross section alone. The most precise determination of the couplings is obtained combining the results of the four LEP experiment, taking into account correlations of systematic errors. The main systematic errors come from hadronisation uncertainties in the $W^+W^- \to q\overline{q}'\ell\overline{\nu}_\ell$ channel and from Bose–Einstein and colour reconnection effects in the $W^+W^- \to q\overline{q}'q\overline{q}'$ channel and are taken as fully correlated among the experiments. Also added in the combination are, for some experiments, results from the $\nu\overline{\nu}\gamma$ final state which are discussed in the next section and from single W production which are described in Chapter 3. The contribution of these other measurements is not relevant

for the Δg_1^z and λ_γ parameters, but it improves the precision on $\Delta\kappa_\gamma$ by a factor 2. This difference is visible in table 2.1 which gives the results obtained with 1–dimension fits by each experiment and the combination performed by the LEP Electroweak Working Group. Differently from the three other experiments the OPAL result does not include the measurement of TGC's obtained from the single W channel. Figure 2.5 shows the constraints on the couplings obtained from the combination of the two–dimensional fits. Also shown is the dependence of the W pair production cross section. From this measurement alone it is possible to exclude models in which the Z^0 does not couple to the W bosons.

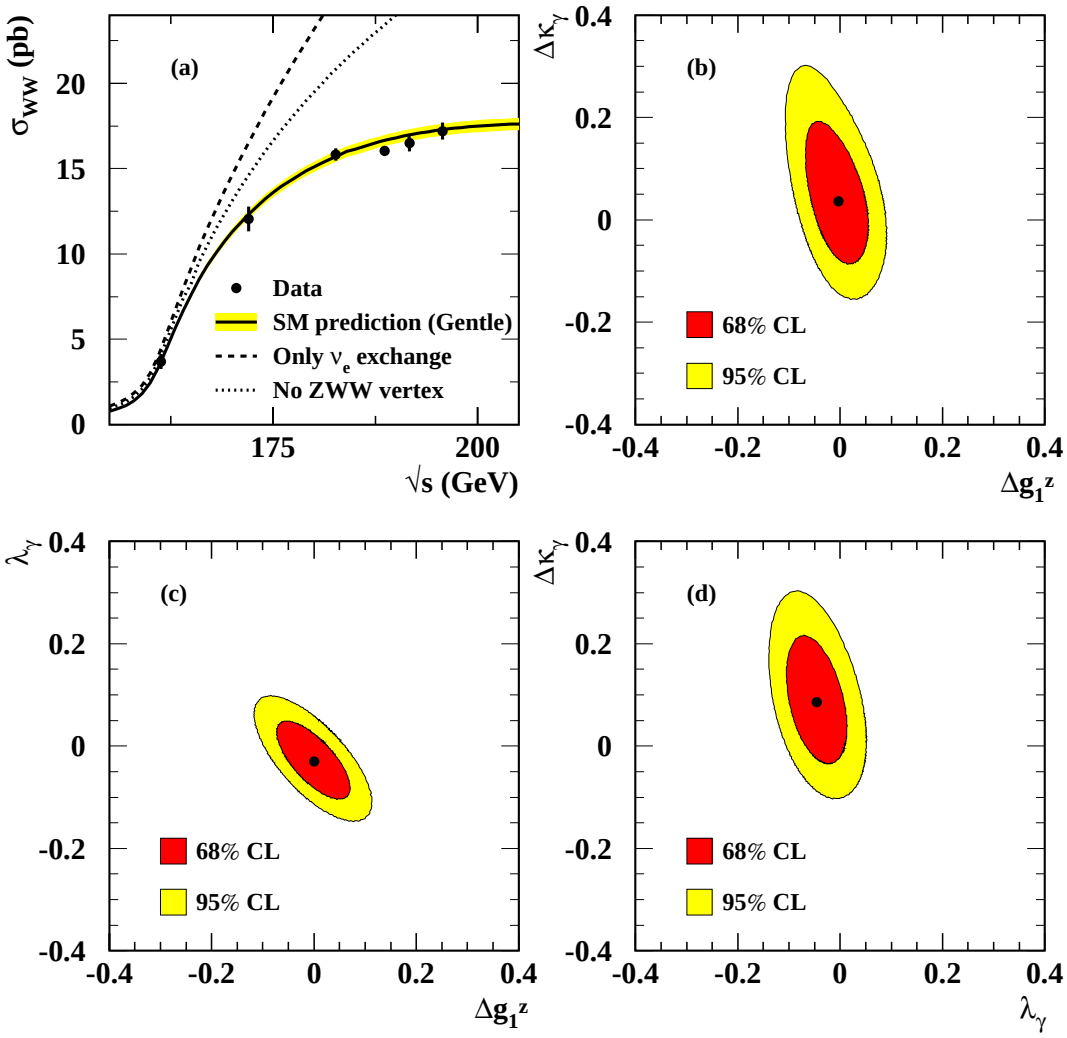

Figure 2.5: (*a*) The W^+W^- production cross section measured by the LEP experiments, compared with the $\mathcal{SM}$ prediction (indicated by the yellow band). The cross sections predicted if only the ν_e exchange diagram would contribute to this final state and if the $Z^0W^+W^-$ vertex does not exist are also shown. In (*b–d*) the 68% and 95% confidence level (CL) two–dimensional contours for different pairs of TGC parameters are shown, assuming for the third parameter the $\mathcal{SM}$ value. The points show the best parameter fit obtained combining results from all LEP experiments.

2.3 Gauge couplings measurements in boson fusion processes

Another interesting channel for the study of TGC's in e^+e^- collisions at LEP2 is the $\nu\overline{\nu}\gamma$ final state. The advantage of this channel is that it is sensitive only to the $\Delta\kappa_\gamma$ and λ_γ parameters. This reaction proceeds mainly through the *s*–channel annihilation process $e^+e^- \to Z^0 \to \nu\overline{\nu}$, in which the photon is emitted from the initial state. For $\nu = \nu_\mu, \nu_\tau$ this is the only contribution to this process and it is not sensitive to TGC's. For $\nu = \nu_e$ there are additional contributions from the *t*-channel exchange of a W boson and from the $W^+W^- \to \gamma$ fusion diagram shown in figure 2.6, which causes the dependency of the cross section on the couplings at the γW^+W^- vertex. Experimentally the signature of these events is a high energy isolated photon. The presence of the Z^0 resonance in the invariant mass of the two neutrinos causes a peak in the E_γ photon energy distribution at values $E_\gamma = (s - M_Z^2)/2\sqrt{s}$. These ISR photons are emitted preferably in the beam direction. Photons from the fusion process have instead a continuous spectrum and have an higher probability of being emitted at large angles. The sensitivity to anomalous couplings is therefore higher for photon energies different from those corresponding to the Z^0 resonance and for large angles with respect to the beam pipe. The sensitivity is maximal for energies larger than the radiative peak, since the couplings enter into terms which are proportional to the photon energy. This kinematic region presents the additional advantage of not being affected by higher order corrections [48]. This type of events, with one high transverse energy photon and missing energy can be identified with essentially no background. Less than 1% of the selected events are predicted to come from background sources.

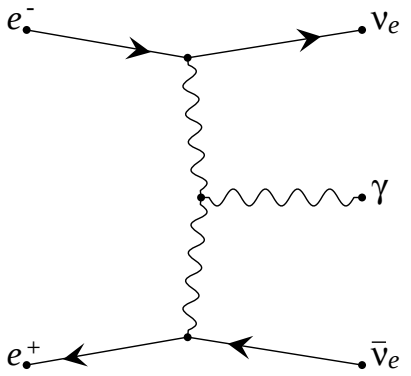

Figure 2.6: The $W^+W^- \to \gamma$ fusion diagram.

The $\nu\overline{\nu}\gamma$ final state has been used for the measurement of TGC's by three of the LEP collaborations [43, 44, 45]. In all cases the values of the couplings are obtained from a likelihood fit to the number of events and the two dimensional distribution of the photon energy and polar angle. Results based on the statistics collected up to 189 GeV are given in table 2.2. These results are of lower precision compared to the ones obtained from the study of the W^+W^- final states at LEP and of the $W\gamma$ final state at Tevatron, which is discussed in the next section. They do nevertheless provide a small improvement of the $\Delta\kappa_\gamma$ measurement and are therefore included by each experiment in their final results shown in section 2.2.

The equivalent boson fusion channel sensitive to the $Z^0W^+W^-$ couplings, $W^+W^- \to Z^0$, is not relevant at the current energy and integrated luminosity of the LEP experiments. This channel has a much smaller cross section (it is of higher order in g_W with respect to the $\nu\overline{\nu}\gamma$ final state) and suffers from a large background from pair production of Z bosons and from $q\overline{q}'\ell\overline{\nu}_\ell$ final states. There is currently no analysis which tries to select this channel to provide a measurement of the $Z^0W^+W^-$couplings independent from assumptions on

Experiment	Measurement	
	$\Delta\kappa_\gamma$	λ_γ
ALEPH [49]	$0.4 \pm 0.7 \pm 0.2$	$0.3 \pm 0.9 \pm 0.2$
DELPHI [44]	$0.7^{+0.77}_{-0.99} \pm 0.15$	$0.7^{+0.77}_{-0.99} \pm 0.15$
L3 [45]	$0.26 \pm 0.96 \pm 0.41$	$0.26^{+1.26}_{-1.25} \pm 0.99$

Table 2.2: Measurements of the $\Delta\kappa_\gamma$ and λ_γ parameters using the $\nu\overline{\nu}\gamma$ final state. The quoted errors are of respectively statistical and systematic origin.

the relations with the γW^+W^- couplings.

2.4 Measurements of TGC's at the Tevatron

In hadronic ($p\overline{p}$ and pp) collisions triple gauge couplings can be studied measuring the $W\gamma$, WZ and W^+W^- final states which are produced at leading order through the diagrams shown in figure 2.7. Calculations of the cross sections are available, including higher order QCD corrections [50]. Among these final states the $W\gamma$ process has the largest production cross section, ≈110 pb within the cuts used by the CDF and DØ experiments, whereas the cross sections for the production of two massive vector bosons varies between 5 and 10 pb.

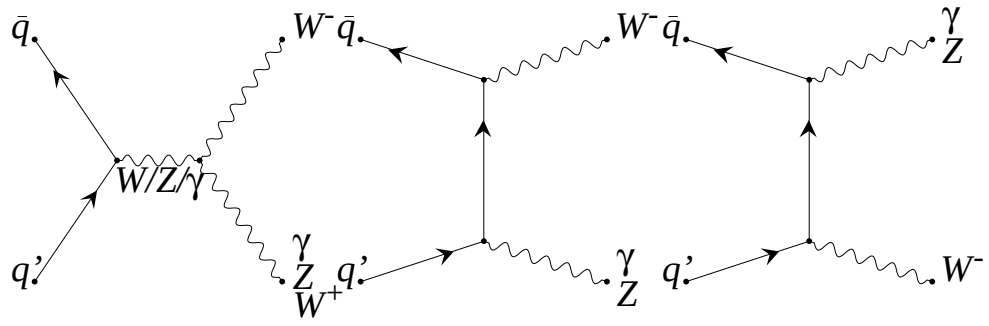

Figure 2.7: Diagrams leading to the $W\gamma$ and WZ final states in hadronic collisions.

The sensitivity to TGC's comes from the first diagram, which is a *s*–channel annihilation process. Therefore the signature of anomalous couplings is an enhanced event rate for high invariant masses of the two–boson system and for small rapidities [1], with a quadratic dependence on the TGC's. To reject background from multi–jet production, events are selected requiring that one of the weak bosons, the W in most analysis, decays into either electron or muon. For the second weak boson hadronic decays, which have a higher branching fraction, are also considered. Due the neutrino, the W momentum cannot be completely reconstructed and the invariant mass of the two bosons and their rapidity distributions cannot be used to extract the couplings. Instead the Tevatron experiments make use of the transverse energy distributions of the photon or the Z^0 in $W\gamma$ and WZ final states, and of the transverse momentum of the W decay leptons in $W^+W^- \rightarrow \ell^+\nu\ell^-\overline{\nu}$ events. These observables retain sensitivity to anomalous couplings through a combination of high mass event counting and angular distribution.

Rather pure samples of events are selected, due to the requirement of a lepton with large transverse momentum (above ≈ 20 GeV/*c*) and of significant missing transverse energy. In the $W\gamma$ final state, requiring an additional isolated and energetic photon gives

[1] In hadronic collisions the pseudorapidity, η, is used instead of the polar angle, the connection between the two being $\eta = -\log(\theta/2)$.

signal to background ratios of $\mathcal{O}(10)$, the main background being W+jet(s) production where one jet has a high energy π^0 misidentified as a photon. The bulk of the Wγ events comes however from W production followed by final state radiation of the lepton, which dominates the spectrum at small photon energies.

High signal to noise ratios can be obtained also in WW events with two leptonic decays: the main background in this case are $Z^0 \rightarrow \ell^+\ell^-$ events in which the missing energy is mismeasured, Wγ or W+jets events in which the photon or the jet is misidentified as electron and $t\bar{t}$ events.

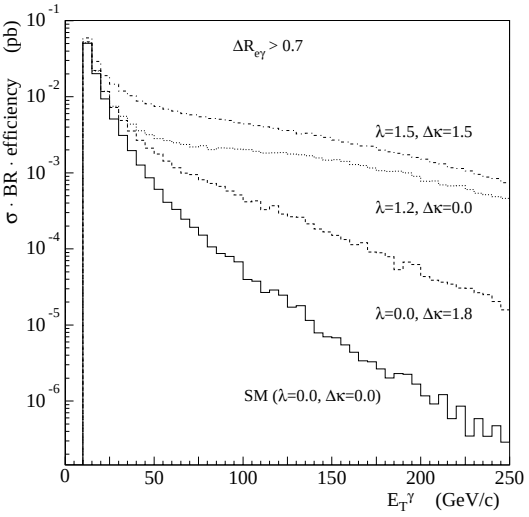

Figure 2.8: The predicted transverse energy, E_T^γ, spectrum of photons in the Wγ production for different γW^+W^- couplings.

The purity achievable in the case of WZ production followed by the decay into three charged leptons is also high, but this channel suffers from the small branching ratio and cross section. Hadronic decays of the W and the Z can be also used to select WZ and WW events, in final states with a lepton, missing energy and two jets. This final state suffers from a large QCD background from W production in association with multiple jets, and from multi–jet production. The same holds for the WZ final state in which the W decays hadronically into two jets and the Z into two charged leptons, given the smaller cross section and branching ratio into leptons.

Not all these channels have been investigated by CDF and DØ. The main channel is Wγ, which has been investigated by both experiments [51, 52]: in both cases the number of observed events is in agreement with the $\mathcal{SM}$ predictions. The only other final state where a cross section measurement has been performed is the $W^+W^- \rightarrow \ell^+\nu\ell^-\overline{\nu}$ channel [53]. For all other final states only upper limits on the cross sections are quoted [54, 55]. Nevertheless the absence of candidates in the WZ and WW final states can still be used to set stringent limits on anomalous couplings, due to the strong dependence of the cross section on TGC's at large transverse momenta. Since the coupling at the $Z^0W^+W^-$ vertex is larger than that at the γW^+W^- vertex by a factor $\cot\theta_W \approx 2$, limits on the $Z^0W^+W^-$ couplings are of the same quality of the γW^+W^- ones, the highest sensitivity being reached in the final state $WZ^0 \rightarrow \ell\nu$jj.

A remarkable difference in the measurement of couplings at hadron colliders is that a form factor dependence has to be introduced in the TGC's to avoid unitarity violation at high energies. This problem is not present at LEP, since experiments are carried out at a fixed centre–of–mass energy, whereas in hadronic collisions the effective $\sqrt{s}$ covers a large energy range. The Tevatron experiments use a dipole form factor, $\mathcal{F}$, with a scale, Λ, that multiplies each coupling parameter, $\mathcal{F} = 1/(1 + s/\Lambda^2)^2$, where $\sqrt{s}$ is the centre–of–mass energy of the hard scattering process. For large values of Λ the unitarity limit becomes more stringent than the experimental limit. For this reason Λ is chosen such that the constraint from unitarity is less stringent than the one obtained from measurements.

The maximum scale which can be probed with the current experimental data is of order 2 TeV.

The final states Wγ and $W^{\pm}Z^0 \to \ell^{\pm}\nu\ell^+\ell^-$ allow to measure separately the coupling parameters at the γW^+W^- and $Z^0W^+W^-$ vertices without theoretical assumptions. For all other channels involving W^+W^- final states or final states in which the resolution of the calorimeter does not allow to distinguish between the WZ and WW hypothesis (final states with one lepton, missing energy and two jets) the experiments have to make assumptions on the relation between the couplings at the γW^+W^- and $Z^0W^+W^-$ vertices. Originally both the CDF and DØ experiments have used the constraints $\Delta\kappa_\gamma = \Delta\kappa_z$ and $\lambda_\gamma = \lambda_z$, the first of which has no basis in any of the models proposed in Chapter 1. The DØ experiment has started since 1998 to quote results also using the relations derived in section 1.5 which are used by the LEP experiments. Using these relations among the couplings DØ has also obtained results [56] combining all the considered channels. These results, shown in table 2.3, may be directly compared with the ones obtained by the LEP experiments reported in section 2.2. With the currently accumulated statistics the measurements and limits of the single LEP experiments are better by a factor 2 than the ones quoted by DØ. The Tevatron results will improve with the data collected in Run 2, scheduled to start in autumn 2000. The limits should improve by a factor of 5 for a total integrated luminosity of 10 fb^{-1}, reaching a precision comparable to that of the final combined results of the LEP experiments [57].

Coupling	$\Lambda = 1.5$ TeV	$\Lambda = 2.0$ TeV
$\Delta\kappa_\gamma$	[-0.73,0.59]	[-0.67,0.56]
λ_γ	[-0.20,0.20]	[-0.18,0.19]
Δg_1^z	[-0.25,0.49]	[-0.23,0.47]

Table 2.3: One dimensional limits at 95% CL limits on the TGC parameters from a simultaneous fit to the DØ Wγ, WW $\to$dilepton, WW/WZ $\to \ell\nu$jj and WZ $\to$trilepton data samples for two different values of the cutoff parameter Λ.

2.5 Indirect limits on TGC's

Indirect limits on deviations of TGC's from their $\mathcal{SM}$ value can be obtained also for any process which has sensitivity to loops involving the electroweak bosons. The most stringent bounds on anomalous couplings are obtained from an analysis of the precision measurements of the Z^0 lineshape performed by the LEP experiments. In [58] the following 95% CL limits are obtained:

$$-0.055 < \Delta\kappa_\gamma < 0.065,$$
$$-0.067 < \Delta g_1^Z < 0.041.$$

These limits are comparable to bounds obtained from direct measurements performed using the data collected so far at LEP2, but they will not improve substantially in the future, even after the publication of the final analyses of the Z^0 lineshape. These indirect limits are in addition subject to to some theoretical uncertainties related to the model chosen to take into account source of TGC's beyond the $\mathcal{SM}$. Using a different theoretical approach,

a less stringent limit (4 times worse) is obtained in [59]. Constraints in the framework of the chiral Lagrangian are obtained in [60]. Constraints on possible anomalous TGC's can also be obtained from the study of rare decays of K and B mesons involving electroweak penguin diagrams [61] and from the $g-2$ measurement for the muon [62], but they are weaker.

2.6 Measurements at future accelerators

The measurement techniques developed for the Tevatron and LEP experiments will also be applied at the future colliders like the LHC, due to start in 2005, and at one of the proposed high energy linear e^+e^- colliders. With higher energies and integrated luminosities it should be possible to measure the anomalous couplings at least with a precision of $\mathcal{O}(10^{-3})$, which means accessing the region in which deviations from the tree level values are expected within the $\mathcal{SM}$ from higher order corrections, without requiring any new physics. The tests of the electroweak theory in the bosonic sector could then reach a precision similar to that obtained at LEP1 for the coupling between the Z^0 and fermions. In addition to TGC's it will also be possible to measure the quartic couplings. If no Higgs boson is found below 1 TeV, it is expected that interactions between the longitudinal components of electroweak bosons become strong.

The increase in sensitivity at higher energies is essentially due to the fact that the terms of the Lagrangian which are sensitive to anomalous couplings are proportional to the momenta of the particles involved in the triple gauge boson vertex. The increase in sensitivity with $\sqrt{s}$ is faster in e^+e^- collisions for the $e^+e^- \to W^+W^-$ process, since the two produced W bosons take the entire centre–of–mass energy. In contrast in other final states, $\nu\overline{\nu}\gamma/Z$ or single W production the particles involved in the triple gauge vertex have smaller momenta, reducing therefore the sensitivity to TGC's. For these other channels the precision achievable at future e^+e^- colliders improves with respect to that obtained at LEP2 mainly due to the expected higher integrated luminosity. The same holds also in the case of the LHC, since the bulk of the collisions occurs at low partonic centre–of–mass energies [63]. Scaling laws for the energy and luminosity dependence of TGC's can be found in [30].

The machine best suited for the measurement of triple (and quartic) gauge couplings is a high energy e^+e^- linear collider. One of the main advantages of this type of machine could be the availability of polarised beams which would allow to reconstruct completely the helicity structure of the $e^+e^- \to W^+W^-$ scattering. In this way it will be possible to measure separately the couplings at the γW^+W^- and $Z^0W^+W^-$ vertices in this channel, without recurring to other final states [64].

A precision of $\mathcal{O}(10^{-3})$ on the couplings could be reached already from a total cross measurement of similar accuracy either in the W^+W^- or single W final states. From an experimental point of view this requires an integrated luminosity of 100 fb^{-1}, corresponding approximately to one year of data taking for instantaneous luminosities of 10^{34} $cm^{-2}s^{-1}$, and a very careful control of systematic errors. A further improvement of one order of magnitude on the precision of the couplings measurements could be achieved studying the distribution of the W production and decay angles in the $e^+e^- \to W^+W^-$ reaction. For achieving this kind of accuracy it is crucial that radiative corrections in the four–fermion processes are known at the same level of precision. This requires a reduction of at least one order of magnitude in the uncertainties of current theoretical calculations.

3 Single W production at LEP

The previous chapter contained a discussion of the main channel for TGC's measurements at LEP2, $e^+e^- \to W^+W^-$. The description was based on the assumption that the production and decay of the W bosons can be handled separately, which is valid as long as the invariant masses of the two fermion pairs produced in the decay of both W's are close to m_W. If this is not the case additional diagrams contributing to the same final state should also be considered. The remaining Feynman diagrams give negligible corrections to the total cross section except for final states which contain one electron, $f\bar{f}'e^-\overline{\nu}_e$(with $f = e, \mu, \tau, q$), due to additional contribution from single W production and, in the case of the $e^+\nu_e e^-\overline{\nu}_e$ final state from neutral current diagrams (mainly Z^0Z^0, $Z^0\gamma^*$ and $e^+e^-Z^0$ production).

At tree level the total number of diagrams leading to the final states $q\overline{q}'e\overline{\nu}_e$, $\ell^+\nu_\ell e^-\overline{\nu}_e$ (for $\ell = \mu, \tau$) and $e^+\nu_e e^-\overline{\nu}_e$ is 20, 18 and 56 respectively, whereas only 10 diagrams describe the process $e^+e^- \to q\overline{q}'\mu\overline{\nu}_\mu$. The difference resides in diagrams which don't involve the annihilation of the initial e^+e^- pair, but rather the exchange of bosons in the *t*–channel. The contribution from these additional diagrams in the $f\bar{f}'e^-\overline{\nu}_e$ final state cannot be neglected, since it dominates at small electron scattering angles. The measurement of the $f\bar{f}'e^-\overline{\nu}_e$ cross section in this kinematic region is interesting for at least two reasons. First, it provides an independent way to study trilinear gauge couplings, with an enhanced sensitivity to the parameters of the γW^+W^- vertex. Second, it represents an important check of the calculations and Monte Carlo programs used to predict $\mathcal{SM}$ background to searches for new particles which decay through the emission of W bosons and invisible particles.

Theoretical aspects of single W production in e^+e^- collisions are discussed in this chapter, starting in section 3.1 with a description of the Feynman diagrams which lead to the $q\overline{q}'e\overline{\nu}_e$ final state and of how they dominate different regions of the phase space. Theoretical calculations of the cross section for the $e^+e^- \to q\overline{q}'e^-\overline{\nu}_e$ reaction are reviewed in section 3.2. Problems connected with the evaluation of the largest radiative corrections, initial state radiation and running of the coupling constants, are discussed in section 3.3. Section 3.4 contains a brief review of the results on single W production obtained by the other LEP experiments. The problem of a common definition of cross section is discussed in section 3.5 where a possible solution is proposed.

3.1 The CC20 set of diagrams and triple gauge couplings

At tree level the $q\overline{q}'e\overline{\nu}_e$ final state is produced in e^+e^- collisions through the 20 Feynman diagrams shown in figure 3.1, which form the CC20 set of diagrams. From a quantum mechanical point of view it is not possible to disentangle the contributions from all the diagrams and only the square of the sum of the amplitudes (the matrix element) is a phys-

ically measurable quantity, proportional to the differential cross section. However it is possible to distinguish different regions of the phase space in which one or more of the diagrams dominates the cross section:

- The first three diagrams (CC03 diagrams) represent the double resonant production of W bosons and give the largest contribution to the total cross section. The angular distribution of the W bosons produced in this process has already been shown in figure 2.2. Due to the presence of the *t*–channel neutrino exchange diagram, which gives the largest contribution to the cross section, the distribution of the polar angle of electrons is asymmetric and electrons are emitted preferably in the forward direction. The invariant masses of both fermion pairs coming from the decay of W bosons are peaked around m_{W}.

- In the next seven diagrams (number 4 to 10 in figure 3.1) only one of the two fermion pairs is resonating at $m_{\mathrm{f}\bar{\mathrm{f}}'} \approx m_{\mathrm{W}}$. These diagrams can be considered as a higher order correction to the fermion pair production process, final state radiation of a W boson. Therefore the electrons produced through these diagrams will have the same angular distribution of hadrons produced in the $\mathrm{e}^+\mathrm{e}^- \to \mathrm{f}\bar{\mathrm{f}}$ annihilation, with a strong forward–backward asymmetry. The momentum spectrum of the W boson constitutes a further difference between $\mathrm{q}\bar{\mathrm{q}}'\mathrm{e}\bar{\nu}_{\mathrm{e}}$ events produced through the CC03 diagrams and these other seven diagrams. The W boson produced in the CC03 process carries half of the centre–of–mass energy, whereas a continuous energy spectrum is expected in the case of W final state radiation. The order of magnitude of the contribution of the seven diagrams can be estimated starting from the $\mathrm{e}^+\mathrm{e}^- \to \mathrm{f}\bar{\mathrm{f}}$ non radiative cross section ($\mathcal{O}(20)$ pb at LEP2 energies), multiplying it by the weak coupling constant to take into account the additional vertices and a suppression factor for the kinematics. All together this leads to an estimate of the relative correction which is of order $g_W\Gamma_{\mathrm{W}}/m_{\mathrm{W}} \approx 10^{-4}$, giving a cross section of a few femtobarns.

- The first 10 diagrams form a gauge invariant subset [65] and they are the only one necessary to describe the production of the $\mathrm{q}\bar{\mathrm{q}}'\mu\bar{\nu}_\mu$ and $\mathrm{q}\bar{\mathrm{q}}'\tau\bar{\nu}_\tau$ final states. Apart from their single or double resonating behaviour these diagrams all represent *s*–channel processes, which contain the annihilation of two fermions into a boson. Even the *t*–channel neutrino exchange diagram (diagram number 3 in figure 3.1) can be seen as a $\nu_{\mathrm{e}}\mathrm{e}^- \to \mathrm{W}^-$ annihilation diagram, with initial state radiation of the other W boson. This common feature has important consequences for the treatment of initial state radiation, which will be discussed in section 3.3.

- On the contrary, the remaining ten diagrams (numbers 11 to 20) involve the exchange of a boson in the *t*–channel, and form a second gauge invariant subset. The second largest contribution to the $\mathrm{e}^+\mathrm{e}^- \to \mathrm{q}\bar{\mathrm{q}}'\mathrm{e}^-\bar{\nu}_{\mathrm{e}}$ cross section comes from the first four diagrams (11–14). From the point of view of the event kinematics these *t*–channel diagrams dominate a phase space region different from that of the CC03 diagrams. The exchanged photon has generally a low momentum transfer squared, $|t| = -(p-p')^2$, and therefore the electron has an angular distribution strongly peaked at small scattering angles, a region which is not normally instrumented due to the presence of the beam pipe. For this reason in the region of the phase space dominated by these diagrams only the hadronisation products of the two quarks can be detected and

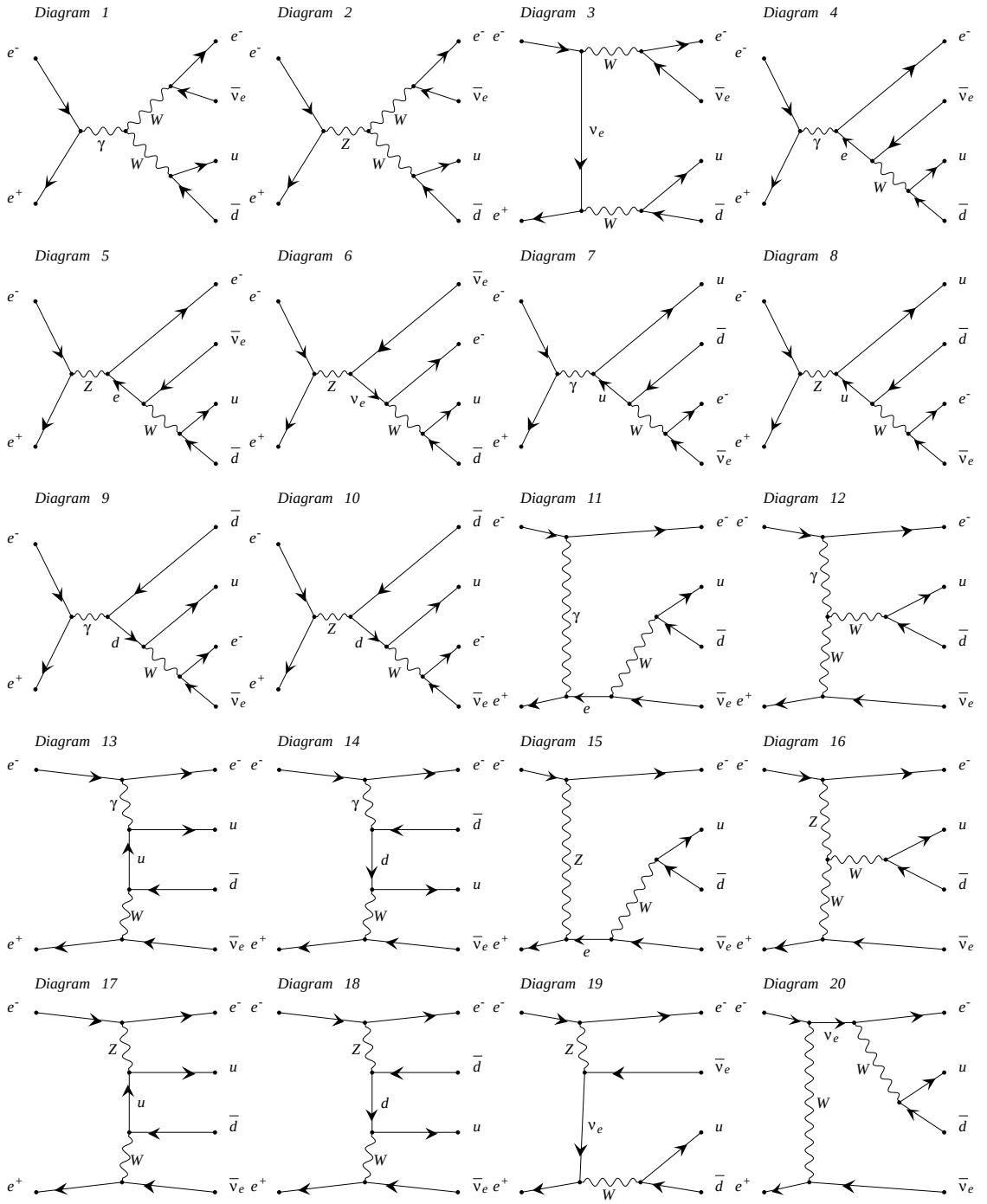

Figure 3.1: The CC20 diagrams for the $q\overline{q}'e\overline{\nu}_e$ final state.

measured. At the W emission vertex the momentum transfer is instead large, due to the presence of the propagator of a massive boson, and the neutrino is emitted generally at large angles with respect to the beam direction, giving on average large missing transverse momenta. Two of the diagrams give rise to final states in which the quark pair has an invariant mass close to m_{W} (diagrams 11 and 12). This kinematic region for the $\mathrm{e^+e^-} \to \mathrm{q\overline{q}'e^-\overline{\nu}_e}$ process corresponds therefore to the production of a single W boson. The signature of these events is a pair of jets recoiling in the transverse plane against the neutrino, accompanied by large missing momentum. The two other diagrams (13 and 14), commonly called multiperipheral diagrams, give preferably low invariant mass quark pairs. This enhancement at low values of $m_{\mathrm{q\overline{q}'}}$ is caused by the additional quark propagator present in these two diagrams. A further distinction between the CC03 diagrams and the *t*–channel diagrams is in the total momentum of the quark pair. Whereas the CC03 diagrams have a peak for W energies equal to the beam energy, the *t*–channel diagrams contribute mainly to the low momentum region.

- These four diagrams (11–14) can be interpreted as a $\gamma\mathrm{e} \to \mathrm{q\overline{q}'\overline{\nu}_e}$ scattering process, the flux of photons being provided by one of the two beams. The flux of photons and their energy increase logarithmically with the centre–of–mass energy of the $\mathrm{e^+e^-}$ collisions and therefore single W production dominates the $\mathrm{e^+e^-} \to \mathrm{q\overline{q}'e^-\overline{\nu}_e}$ at high energies, a region in which the cross section for the $\mathrm{e^+e^-} \to \mathrm{W^+W^-}$ process decreases like $1/s$. The contribution to the total cross from the two reactions is equal at $\sqrt{s} \approx 500$ GeV. Single W production dominates the $\mathrm{e^+e^-} \to \mathrm{q\overline{q}'e^-\overline{\nu}_e}$ process also below the W pair production threshold, since it is kinematically allowed. In the region above the W pair production threshold, the four *t*–channel diagrams contribute for approximately 15% of the total cross section. To understand that these diagrams do not represent a small radiative correction a simple comparison can be made between diagram 4 and diagram 11. Both diagrams correspond to final state radiation of a W boson in $\mathrm{e^+e^-} \to \mathrm{e^+e^-}$ scattering. The contribution of the *s*–channel diagram has been estimated above to be of the order of femtobarns with a simple argument. The same reasoning can be also applied to the *t*–channel diagram, but the $\mathcal{O}(10^{-4})$ multiplicative factor has to be applied to the Bhabha cross section which is several order of magnitude larger than the $\mathrm{e^+e^-} \to \mathrm{f\overline{f}}$ cross section.

- The contribution of the remaining 6 *t*–channel diagrams (15–20) is suppressed relative to that of the first 4, since they all involve the exchange of a massive boson instead of a photon. For this reason the momentum transfer squared, $|t|$, must be of the order of the boson mass at both vertices and the electron is emitted at large angles with respect to the beam direction, differently from the first four *t*–channel diagrams.

In summary the 20 diagrams giving the $\mathrm{q\overline{q}'e\overline{\nu}_e}$ final state can be separated in various categories, depending mostly on whether they contain *s*– or *t*–channel diagrams and on the invariant mass of the fermion pairs (double, single or non–resonant). The main contribution comes from the CC03 diagrams and from the *t*–channel photon exchange diagrams. The contribution from the two types of diagrams can be enhanced by selecting different kinematic regions, making use of the difference in the electron angular distributions. Since the two contributions dominate different phase space regions, the interference between the

different diagrams is expected to be small. This allows to approximate the $e^+e^- \to q\overline{q}'e^-\overline{\nu}_e$ process as the sum of two separate reactions: the double resonant pair production process corresponding to the CC03 diagrams and the single W production corresponding to the first four *t*–channel diagrams. This approximation implies neglecting the contribution from the remaining diagrams and the interference terms. It will be shown in chapter 5 that this approximation introduces an error in the cross section calculation much smaller than 1%, for centre–of–mass energies above the W pair production threshold.

Four of the 20 diagrams leading to the $q\overline{q}'e\overline{\nu}_e$ final state contain a triple gauge boson vertex. Two of these diagrams are part of the CC03 set, dominating the phase space region for the pair production of W bosons. The effect of TGC's in the $e^+e^- \to W^+W^-$ process has been already discussed in the previous chapter. The results presented there are valid even for a more sophisticated analysis including all the CC20 diagrams, since the additional diagrams give negligible contributions to the cross section in the phase space region of two resonant fermion pairs. The remaining two diagrams sensitive to the triple gauge boson are part of the *t*–channel set. They do correspond to the fusion processes $\gamma W^* \to W$ (diagram 12) and $Z^0W^* \to W$ (diagram 16). As explained above the contribution of the second of these diagrams is mainly at large electron scattering angles, but it is suppressed due to the presence of the mass term in the Z^0 propagator. The other diagram instead is part of the *t*–channel diagrams that dominate the cross section for small electron scattering angles. For this reason in this kinematic region the $e^+e^- \to q\overline{q}'e^-\overline{\nu}_e$ reaction will have an enhanced sensitivity to the couplings at the γW^+W^- vertex with respect to those at the $Z^0W^+W^-$ one, contrary to the $e^+e^- \to W^+W^-$ process, which has equal sensitivity to the two types of couplings [66, 67]. These differences will be discussed in detail in chapter 5 on the basis of Monte Carlo studies.

This description of the different CC20 diagrams, of how they dominate different phase space regions and have different sensitivities to TGC's applies also to the $e^+e^- \to \ell^+\nu_\ell e^-\overline{\nu}_e$ reactions for $\ell = \mu, \tau$. Only 18 diagrams are necessary for these two final states: since the weak isospin 1/2 particle in the leptonic doublet is the neutrino, diagrams 7 and 13 are absent. In the case of the $e^+\nu_e e^-\overline{\nu}_e$ final state there are additional contributions. In the *s*–channel, the final state can be reached through Z^0Z^0 and $Z^0\gamma^*$ production and both processes have a cross section similar to that of W pair production. The *t*–channel receives a large contribution from the single Z production process, which is the neutral current equivalent of the single W reaction. The presence of all these additional contributions has the effect of reducing the sensitivity to triple gauge couplings. As for the $q\overline{q}'e\overline{\nu}_e$ final state it is possible in the leptonic final states to make a distinction between W pair and single W production. The topology of the single W events with a leptonic decay is even more striking than in the hadronic case: the only visible particle is a high energy lepton (the average energy is of order $m_W/2$ for resonant production of a W boson), or a narrow low multiplicity jet coming from the τ decay.

3.2 Calculations of the single W cross section

Calculations of the cross section for the $e^+e^- \to f\overline{f}'e^-\overline{\nu}_e$ process which include all the tree level four–fermion diagrams have become available only in the last few years. Differently from the calculations of the $e^+e^- \to W^+W^-$ process which are available in analytical form, only numerical results are available, usually in the form of Monte Carlo programs. This is

due to the complexity of the matrix element (containing 20 diagrams instead of 3), which has peaks in different regions of the four–body phase space, as discussed in the previous section. One possible approximation is to consider separately the CC03 diagrams and add to them the contribution of diagrams 11–14 of figure 3.1. This results in a simpler calculation of the cross section, with the drawback that all other additional contributions are neglected.

Another possible approximation is the use of massless matrix elements, although this prevents from integrating the cross section in the region of small scattering angles of the electron, as discussed in [68]. In this region the cross section diverges like $\log m_e^2$, where m_e is the electron mass, due to the $1/|t|^2$ propagator term. Another divergence is due to the multiperipheral diagrams 13 and 14, which give a $\log m_q^2$ behaviour for low quark masses, m_q. Programs based on massless matrix elements usually implement phase space cuts which ensure convergence of the cross section calculation [69]. For this reason it is preferable to use Monte Carlo programs which make use of fully massive matrix elements

To ensure that the calculation of the total cross section gives finite results, gauge invariance must be respected, even when massive matrix elements are used. This is due to the large cancellation between the *t*–channel diagrams 11 to 14, similarly as for the CC03 diagrams. Even in the absence of anomalous TGC's, gauge invariance is violated once the finite width of the W boson is taken into account. Several methods exist in the literature [70, 71] to take into account the width of the W boson preserving the gauge invariance, but they are not implemented in all the Monte Carlo programs.

The list of available programs for calculating the $e^+e^- \to q\overline{q}'e^-\overline{\nu}_e$ cross section in the small electron scattering angle region is given in table 3.1. The table indicates also the main features of the different programs, as the type of matrix element calculator used, whether it is based on the full set of four–fermion diagrams and the possibility of anomalous TGC's. Only the first four programs have been used for the studies presented in this thesis. Other programs were excluded either because the code was unavailable, or because they were not different from the other ones, apart from the numerical implementation of the calculation. It is unfortunate that one of the codes, WTO [68], was not available, since it uses a completely different approach, based on the equivalent photon approximation. Newer codes are becoming available in the framework of the currently ongoing LEP2 Monte Carlo Workshop [72], but these are more relevant for the issues of radiative corrections which are discussed in the next section.

Monte Carlo program	matrix element	diagrams included	TGC's	ISR
grc4f [73]	massive	all	yes	collinear,p_T^γ
KORALW [74]	massive	all	no	p_T^γ
EXCALIBUR [75]	massless	all	yes	collinear
ERATO [76]	massless	all	yes	collinear
PYTHIA [77]	massive	11 and 12	no	collinear
WTO [68]	massive	all	no	collinear
WPHACT [78]	massive	all	no	collinear
COMPHEP [79]	massive	all	no	collinear

Table 3.1: Monte Carlo programs for the calculation of the $e^+e^- \to q\overline{q}'e^-\overline{\nu}_e$ cross section.

3.3 Radiative corrections

All calculations of the CC20 cross section described in the previous section are based on the set of tree level diagrams and do not take into account radiative corrections. Currently no calculation is available of first order electromagnetic radiative corrections in the phase space region dominated by single W production. The largest corrections are initial and final state photon radiation and loop effects in the propagators. All other electroweak corrections are neglected. QCD corrections to the hadronic final state are also considered.

The largest radiative correction in the calculation of the single W cross section is initial state radiation. To take into account the emission of photons from the beam electrons the cross section for the $e^+e^- \to q\overline{q}'e^-\overline{\nu}_e$ process, calculated in the rest frame after ISR, is convoluted with a radiator function which accounts for ISR probability. This decreases the effective centre–of–mass energy of the four–fermion system, leading to a reduction of the cross section larger than the precision reachable by a single experiment at the end of the LEP2 program. It is therefore necessary to evaluate correctly the size of this effect.

In all currently available Monte Carlo programs the effect of ISR is computed assuming that the four–fermion production happens through an annihilation (*s*–channel) process. Radiative corrections are then proportional to $\log(s/m_e^2)$. The *s* dependence of this correction term originates from the cancellation between the infrared ISR corrections on the e^+ and e^- lines and the correction of the $e^+e^-\gamma/Z^0$ vertex. Using this approach the cross section at LEP2 energies is reduced by $\approx 12\%$ in the phase space region dominated by single W production. However in this kinematic region the basic assumption of this calculation is wrong, since the $e^+e^- \to q\overline{q}'e^-\overline{\nu}_e$ reaction is dominated by *t*–channel diagrams and the ISR corrections are proportional to $\log(|t|/m_e^2)$. This happens because in the *t*–channel diagrams the cancellation of infrared corrections does not occur between the e^+ and e^- lines, but between the incoming and outgoing e^- line. The reduction of the cross section due to ISR is therefore smaller than the one predicted. None of the Monte Carlo programs used for this thesis implements correctly the emission of ISR photons in *t*–channel diagrams. Preliminary results obtained using Monte Carlo generators which are still not publicly available indicate that the cross section is reduced by approximately 6–8% [80, 81]. This is roughly half of the effect predicted when ISR is treated assuming that the reaction proceeds through *s*–channel diagrams, compatible with having very small corrections at the $e^- \to e^-\gamma$ vertex, and using the standard *s*–channel treatment for the $e^+ \to W^+\overline{\nu}_e$ vertex.

Another difference between the two ISR treatments is in the distribution of the transverse momentum p_T^γ of ISR photons. A correct modelling of the p_T^γ spectrum is important for the study of the single W production process, as it affects the angular distribution of the final state electron, and therefore the selection efficiency. For *t*–channel processes it is expected that p_T^γ is small, due to the cancellation which occurs between initial and final state radiation. The p_T^γ spectrum can instead extend to higher values in processes dominated by *s*–channel diagrams. Most of the Monte Carlo programs currently available implement initial state radiation assuming that photons are emitted collinear to the beam direction, and only two programs, grc4f and KORALW, can simulate the p_T^γ distribution, using respectively a QED parton shower [82] and the YFS exponentiation [83], but only for *s*–channel processes. In the kinematic region dominated by single W production it is preferable to use the collinear approach in the simulation of ISR. An upper limit on the effect of the transverse momentum distribution can be obtained comparing the selection

efficiencies obtained on different event generators which include a transverse momentum for ISR photons in the *s*–channel approximation. From an experimental point of view this systematic error can be kept small avoiding stringent cuts in the energy deposits of the detector placed at small angle with respect to the direction of the beam pipe.

Electromagnetic radiation can also be emitted from charged particles in the final state. This does not affect the total cross section, but might distort the distributions of the quantities used in the event selection and therefore lead to a wrong estimate of the detection efficiency. Final state radiation can be emitted from the quark pair and from the electron. As discussed above, the emission from the final state electron is partially cancelled by ISR on the kinematic region dominated by single W production. Therefore in a simplified description of this process it is preferable to consider only final state radiation from the two quarks. This approach avoids also the problems arising from the use of the PHOTOS [84] program commonly used to simulate final state radiation. In this program the assumption is made that final state radiation is emitted from a fermion produced in the decay of a resonance. This is valid for the fermion pair coming from the decay of a W boson in the CC03 process, but not for the electron of the single W process.

Another large correction to the total cross section for the CC20 process comes from loop corrections in the photon propagator. This type of corrections is generally taken into account in LEP2 analyses using for the QED coupling constant the value at the W pair production threshold $\alpha_{em}(4m_W^2) = 1/128.07$. However this approximation is valid only for the *s*–channel diagrams. In the phase space region dominated by single W production the photon has a much smaller momentum transfer squared $|t| \approx 0$ GeV^2 and the electromagnetic coupling constant should be evaluated at this scale [85, 67]. For the analysis a value of $\alpha_{em} = 1/135.0$ is used. It is derived in a simple way considering the average of α_{em} obtained from a set of Monte Carlo events generated in the phase space region dominated by single W production. The cross section in this kinematic region is proportional to $\alpha_{em}^2(|t|)$ and therefore this corresponds to a 3% correction with respect to the $\alpha_{em}(0)$ value of the cross section. The value of of this correction has been recently confirmed with a more refined calculation [80]. At this level of precision it can be assumed that the coupling constant α_{em} appears as a multiplicative factor, neglecting eventual dependencies of the differential cross section on α_{em}.

QCD represents another possible source of large corrections to the cross sections. For most of the diagrams leading to the $q\overline{q}'e\overline{\nu}_e$ final state, the QCD corrections can be reabsorbed into the definition of the width of the W boson. This is not possible for the multiperipheral diagrams (diagrams 13, 14, 17 and 18 in figure 3.1). For these diagrams QCD corrections can be calculated assuming a pointlike coupling of the photon to quarks, but this assumption is valid only for sufficiently high values of $m_{q\overline{q}'}$ or $|t|$. In the small angle region ($|t| \approx 0$ GeV^2) the photon is quasi real and the contribution from the hadronic fluctuations of the photon, usually called resolved photon component, must also be considered. This is done for $\gamma\gamma$, $e\gamma$ and γp collisions using a structure function for the photon, but there is currently no theoretical calculation of the CC20 process which includes this additional contribution. Therefore in the region of low $m_{q\overline{q}'}$ and small scattering angles, which is part of the single W phase space, the cross section for the $e^+e^- \to q\overline{q}'e^-\overline{\nu}_e$ has large theoretical uncertainties. It is therefore preferable to restrict the analysis to high values of $m_{q\overline{q}'}$. This has no consequence for the measurement of TGC's, since sensitivity to the couplings is obtained only for $m_{q\overline{q}'} \approx m_W$. This theoretical uncertainty represents however

a big drawback in the search for new particles which lead to final states with low visible energy and large missing momenta.

3.4 Measurements of single W production at LEP

Results on single W production have been presented so far by all LEP collaborations but it is difficult to make direct comparisons because in each analysis a different cross section definition is used. This limits the precision with which theoretical calculations can be tested and for this reason the four LEP collaborations have recently agreed upon a common signal definition, which will be discussed in the next section and used for the analysis presented in this thesis. Comparisons of results on TGC's are even more difficult, since each collaboration adopts different assumptions for the treatment of backgrounds which are also sensitive to the coupling parameters.

The different signal definitions used for the single W cross section measurement are given in table 3.2. Two of the collaborations adopt a definition which uses all the CC20 diagrams and restricts the phase space with kinematic cuts, whereas the DELPHI collaboration uses a subset of diagrams, complemented by kinematic cuts. This latter definition allows to use the knowledge of the W decay branching fraction in the cross section fit for relating the measured number of events in the various final states, although it also requires correction factors (up to 50% in the $e^+\nu_e e^-\overline{\nu}_e$ channel) to take into account contributions from other diagrams.

Experiment	Diagrams	Kinematic cuts
$e^+e^- \to q\overline{q}'e^-\overline{\nu}_e$ channel		
ALEPH [86]	all	$\theta_{e^-} < 34$ mrad, $m_{q\overline{q}'} > 60$ GeV/c^2
DELPHI [87]	11,12	$\theta_{e^-} < 37$ mrad
L3 [88]	all	$\theta_{e^-} < 77$ mrad, $\min(E_q, E_{q'}) > 15$ GeV
$e^+e^- \to \ell^+\nu_\ell e^-\overline{\nu}_e$ channel (for $\ell = \mu, \tau$)		
ALEPH	all	$\theta_{e^-} < 34$ mrad, $E_{\ell^+} > 20$ GeV, $\lvert\cos\theta_{\ell^+}\rvert < 0.95$
DELPHI	11,12	$\theta_{e^-} < 37$ mrad
L3	all	$\theta_{e^-} < 77$ mrad, $E_{\ell^+} > 15$ GeV
$e^+e^- \to e^+\nu_e e^-\overline{\nu}_e$ channel		
ALEPH	all	$\theta_{e^-} < 34$ mrad, $E_{e^+} > 20$ GeV, $\lvert\cos\theta_{e^+}\rvert < 0.95$
DELPHI	11,12	$\theta_{e^-} < 37$ mrad, $E_{e^+} > 30$ GeV, $\lvert\cos\theta_{e^+}\rvert < 0.72$
L3	all	$\theta_{e^-} < 77$ mrad, $E_{e^+} > 15$ GeV, $\lvert\cos\theta_{e^+}\rvert < 0.75$

Table 3.2: Definitions of the single W signal used so far by the LEP collaborations. For each signal definition the list of included diagrams and of kinematic cuts are given. The numbering scheme used for the list of Feynman diagrams included in the cross section calculation refers to figure 3.1.

The procedures used to select single W events in the various experiments are rather similar. For the hadronic channel they all require two acoplanar jets, large transverse missing momentum and invariant masses in the m_W region, where the acoplanarity is defined as the complement to 180° of the angle between the two jets in the plane transverse to the beam axis. Vetoes are applied to reject leptons from $W^+W^- \to q\overline{q}'\ell\overline{\nu}_\ell$ decays. Selection efficiencies vary between 26% (DELPHI) and 51% (L3), for purities between 28% (DELPHI) and 37% (ALEPH). The higher efficiency of the L3 analysis is due to the fact that the single

W cross section is not determined from a event counting (as in the other two experiments), but from the fit to the distribution of a discriminating variable, the output of a neural network. The overall purity in this case is as low at 17%, but for high values of the neural network output it reaches 60%. The second difference between the L3 event selection and the other two is that very loose cuts are applied on energy deposits in the forward directions. As a result of these differences the statistical error of the L3 analysis is almost a factor 2 better than that of the DELPHI one, the ALEPH one lying in between the two. Selection efficiencies and purities are generally higher for the selection of events in the leptonic channel. Efficiencies and purities for the electronic and muonic final states are in the 70% range (background in the electron channel is slightly higher due to the irreducible $e^+e^-Z^0$ background, with $Z^0 \to \nu_{\mu,\tau}\overline{\nu}_{\mu,\tau}$), while for the τ channel the efficiency is generally lower. In the leptonic channel differences in efficiency and purity between the various experiments are smaller than in the hadronic final state.

The second difference between experiments is the strategy adopted for measuring the $\Delta\kappa_\gamma$ and λ_γ couplings. The quantity which has the largest sensitivity to the couplings in the single W channel is the total cross section. The TGC's can be obtained from a likelihood fit to the observed number of events. This however requires that the expected background has a small dependence on the TGC's, particularly on the parameters describing the $Z^0W^+W^-$ vertex. This assumption is not valid for the hadronic final state which in all analyses suffers from a large background of $W^+W^- \to q\overline{q}'\ell\overline{\nu}_\ell$. When the constraints on TGC's obtained from the analysis of the single W sample are combined with those from the analysis of the $e^+e^- \to W^+W^-$ process, the presence of this $W^+W^- \to q\overline{q}'\ell\overline{\nu}_\ell$ background in the selected single W sample (and vice versa) can lead to double counting of events.

In the analysis of the ALEPH collaboration the extraction of TGC's is performed assuming for the $W^+W^- \to q\overline{q}'\ell\overline{\nu}_\ell$ background the $\mathcal{SM}$ values of the coupling parameters. In the intention of the authors this would correspond to assigning all the dependence of the cross section on TGC's to the single W component of the selected sample and would lead therefore to conservative limits on the parameters. This assumption is however not correct, since the cross section of the W^+W^- and single W events have a different dependence on the $\Delta\kappa_\gamma$ parameter. In the first case the cross section is minimal at $\Delta\kappa_\gamma \approx 0.5$, whereas for the single W events the cross section is minimal at $\Delta\kappa_\gamma = -1$, as shown in section 5.4. The problem of double counting of events is not considered when single W results on TGC's are combined with results of the $e^+e^- \to W^+W^-$ analysis.

All these problems are avoided by the DELPHI collaboration. In their analysis they do not derive the coupling parameters from the measured single W cross section, but rather use all events selected in the channel with two jets and missing energy, independently from their origin. For the couplings at the γW^+W^- and $Z^0W^+W^-$ vertices the SU(2) $\otimes$ U(1) relations introduced in section 1.5 are used for all events. This approach makes a consistent use of the events and avoids any double counting problem. It has the disadvantage that the peculiarity of the single W channel is partially lost, due to the presence of a large $e^+e^- \to W^+W^-$ component in the selected sample.

The L3 collaboration derives two types of constraints on the anomalous couplings. The first case is aimed at obtaining the best possible results from the selected sample of single W events. The SU(2) $\otimes$ U(1) constraints among the parameters of the γW^+W^- and $Z^0W^+W^-$ vertices are used for the $W^+W^- \to q\overline{q}'\ell\overline{\nu}_\ell$ background assuming that $\Delta g_1^z = 0$, whereas the selected single W events are sensitive only to $\Delta\kappa_\gamma$ and λ_γ. These two pa-

rameters are then obtained from a fit to the distribution of the output variable of a neural network which discriminates between the two types of events. For certain values of the parameters this procedure gives a large weight to the $e^+e^- \to W^+W^-$ component of the sample, enhancing the sensitivity to the parameters of the $Z^0W^+W^-$ vertex. It is therefore not clear how much the quoted limits can be interpreted as limit on the γW^+W^- couplings only. Since the sample selected in this analysis overlaps partially with that used in the analysis of W^+W^- production, it is not suited for a combination of results. For this reason the L3 collaboration performs also a second fit for the anomalous couplings. In this second fit double counting of events is avoided by explicitly removing events used also for the W^+W^- channel. The SU(2) $\otimes$ U(1) relations among couplings are used for all events.

The results of the three other LEP experiments obtained from the single W channel are reported in table 3.3 (for the L3 analysis only the results obtained with the second fit are shown). This will allow in chapter 9 a comparison with the results of the analysis presented in this thesis. These results on TGC's are already included in the global combination of TGC measurements reported in table 2.1. A direct comparison is not easy for the reasons given above. Given the smallness of the data samples, statistical fluctuations can give large biases in the results. Only the availability of the expected statistical errors of each analysis would allow a thorough comparison of results.

Experiment	Measurement	
	$\Delta\kappa_\gamma$	λ_γ
ALEPH [86] (161–189 GeV)	$-0.24^{+0.17}_{-0.23} \pm 0.06$	$0.01^{+0.35}_{-0.37} \pm 0.09$
DELPHI [44] (161–189 GeV)	$0.25^{+0.28}_{-0.38} \pm 0.08$	$0.53^{+0.31}_{-1.14} \pm 0.09$
L3 [45] (161–183 GeV)	$0.12^{+0.27}_{-0.31} \pm 0.26$	$-0.52^{+1.16}_{-0.36} \pm 0.32$

Table 3.3: Measurements of the $\Delta\kappa_\gamma$ and λ_γ parameters using the sample of events selected in the single W analyses. The quoted errors are of respectively statistical and systematic origin. Also indicated is the data set used for the measurement.

3.5 Common definition of the single W cross section

All the differences in the definition of the single W cross section come from the fact that the applied cuts depend on the angular acceptance of the luminosity monitors which are used to veto events with large electromagnetic energy deposits close to the beam direction. As argued in section 3.3 a tight cut on this quantity is not desirable, since the current event generators do not handle correctly ISR in four–fermion processes which are dominated by t–channel diagrams. To avoid these problems and allow a comparison and a combination of results from different experiments, a common cross section definition should be applied, based either on cuts on kinematic invariant quantities or on a subset of diagrams, like it is done for the W^+W^- or Z^0Z^0 cross sections, or on a combination of both.

In the first approach the single W cross section could be defined as the CC20 cross section with cuts on two kinematic invariant quantities: the four–momentum transfer from the initial to the final state electron, $t = (p - p')^2$, where p and p' are the four–momenta of the initial and final state electrons, and the invariant mass $m_{\bar{f}f'}$ of the fermion pair coming from the decay of the W. This definition, however, has two shortcomings. First, the t variable cannot be directly measured in the experiment, since the final state electron is not

observed and its momentum cannot be determined from energy–momentum conservation due to the presence of a neutrino in the final state. Second, $m_{\bar{f}f'}$ cannot be measured in $\ell^+\nu_\ell e^-\overline{\nu}_e$ final states, due to the non observability of the neutrino.

A cross section definition based on diagrams does not have these problems, but it has some ambiguities as to which diagrams should be included in the calculation of the cross section. These ambiguities can be avoided by choosing a gauge invariant subset of diagrams. For the analysis presented in this thesis the single W cross section definition uses all the *t*–channel diagrams of the $e^+e^- \to q\overline{q}'e^-\overline{\nu}_e$ process. This corresponds to the diagrams number 11–20 in figure 3.1 for the $q\overline{q}'e\overline{\nu}_e$ final state, and not only to the four diagrams 11–14 which dominate this process. The remaining six diagrams are included in order to obtain a gauge invariant set [65] and ensure a correct behaviour of the cross section at high energies. For the $e^+e^- \to \ell^+\nu_\ell e^-\overline{\nu}_e$ (for $\ell = \mu, \tau$) process there are 9 *t*–channel diagrams, whereas in the case of the $e^+\nu_e e^-\overline{\nu}_e$ final state there are in total 37 *t*–channel diagrams. The large increase in the number of diagrams for the latter process is due mainly to one additional process contributing to the *t*–channel cross section: $e^+e^- \to e^+e^-Z^0$, which is essentially Bhabha scattering with initial or final state radiation of $Z^0 \to \nu_e\overline{\nu}_e$.

The definition of single W cross section in terms of diagrams assumes that contributions from higher order electroweak and, for hadronic final states, QCD corrections are small. The electroweak corrections (coming mostly from initial state radiation) have been discussed already in section 3.3 and are believed to be known with a precision of few percent of the total *t*–channel cross section. The same is not true for the QCD corrections in the low $m_{q\overline{q}'}$ region. Therefore the signal region for the *t*–channel cross section has been restricted to values of the hadronic invariant mass $m_{q\overline{q}'}$ larger than 40 GeV/c^2. Events which have $m_{q\overline{q}'} < 40$ GeV/$c^2$are considered as background, also if they are produced through *t*–channel diagrams. The precise value of the cut, $m_{q\overline{q}'} > 40$ GeV/c^2, has been chosen in the framework of the LEP2 Monte Carlo Workshop. It is based on the assumption that for higher invariant masses the QCD corrections are negligible, rather than on a calculation of the correction themselves.

As a result of the separation of the $f\overline{f}'e^-\overline{\nu}_e$ diagrams into two gauge–invariant classes, the *s*–channel cross section should be considered in the analysis as a background to be subtracted from the sample of selected events in order to obtain the *t*–channel cross section. The same applies also for the interference between *s*– and *t*–channel diagrams. Since this interference is destructive, this procedure requires subtracting negative contributions from the cross section, which however for the hadronic, μ and τ channels are negligible above the W pair production threshold, as shown in section 5.3. In the electron channel the interference is large, and this is mostly due to the additional diagrams contributing to the same final state.

In summary, for the measurement of the cross section the single W signal is given by the *t*–channel diagrams contributing to the $e^+e^- \to f\overline{f}'e^-\overline{\nu}_e$ final states. In the hadronic channel the additional cut $m_{q\overline{q}'} > 40$ GeV/c^2 is applied to avoid the kinematic region in which QCD corrections may be large. This definition has been recently proposed and will be used in future by all the LEP collaborations, so that it will be possible to combine the different results and test the theoretical predictions with a precision better than 5% using all the data accumulated at the end of the LEP2 program.

4 The OPAL detector

OPAL[89] is one of the four large detectors built for the e^+e^- storage ring at LEP. It is a multipurpose hermetic apparatus designed to detect all types of interactions occurring in e^+e^- collisions with efficient and accurate reconstruction and unambiguous classification of the events. The main features of the detector are:

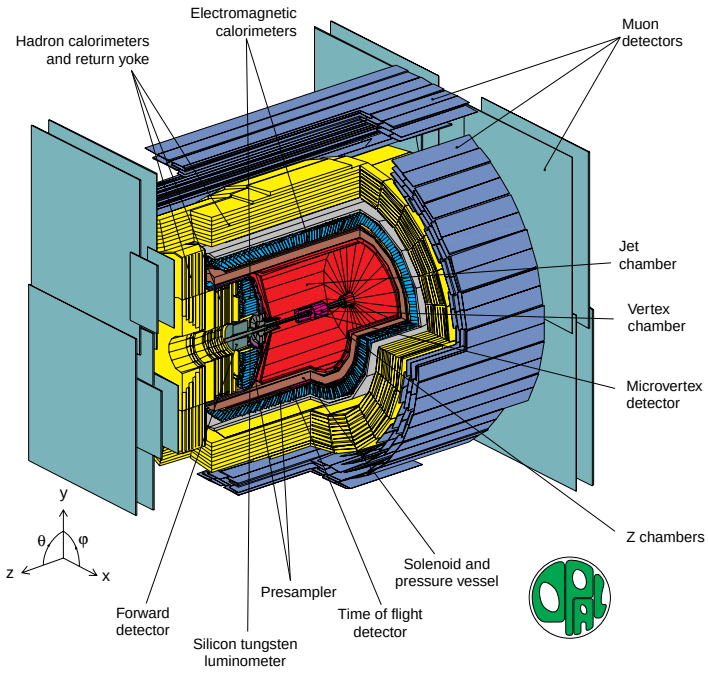

Figure 4.1: General layout of the OPAL detector.

- tracking of charged particles in the central region of a solenoidal coil with measurements of their direction and momentum, particle identification by dE/dx and reconstruction of primary and secondary vertices at and near the interaction region;
- identification of photons and electrons and measurement of their energy;
- measurement of hadronic energy by total absorption using the magnet yoke instrumented as a calorimeter;
- identification of muons by measurement of their position and direction within and behind the hadron absorber;
- measurement of absolute machine luminosity using Bhabha scattering events in the very forward direction with respect to the beam line.

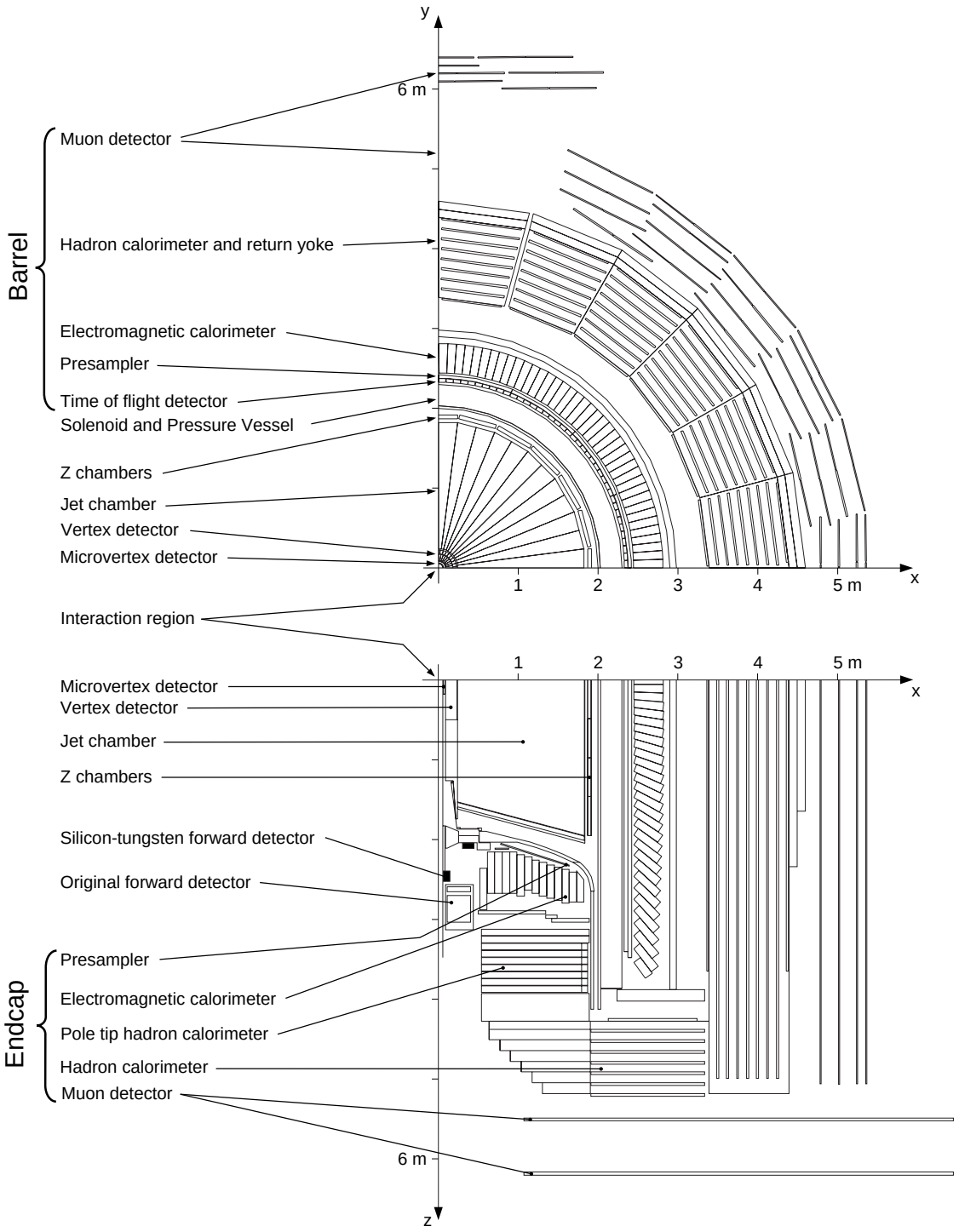

Figure 4.2: Cross section of a quadrant of the OPAL detector (*top*) perpendicular to the LEP beam axis, and (*bottom*) parallel to the beam axis.

The general layout of the detector is shown in figure 4.1, indicating the location and relative size of the various components. Figure 4.2 shows cross sections of the detector parallel and perpendicular to the beam axis. The coordinate system used in OPAL is shown in figure 4.1: the x axis is horizontal and points approximately towards the centre of LEP, the y axis is vertical and the z axis is in the e^- beam direction. The polar angle θ is measured from the z axis and the azimuthal angle ϕ describes rotations around the z axis starting from the x axis.

The different parts of the OPAL detector are described briefly in sections 4.1–4.5 (a complete description can be found in [90]). When appropriate upgrades made in view of the LEP2 running phase are discussed. A description of the use of the different detector components for lepton identification and measurement of the kinematic quantities used in the analysis follows in sections 4.6 and 4.7. Issues related to detector calibration for the high energy running periods are the subject of section 4.8. Finally the chapter is closed by a description of the accelerator operation, machine related backgrounds and luminosity measurement in sections 4.9–4.11.

4.1 The tracking system

The central tracking system consists of four detectors arranged in cylindrical shells around a 56.5 mm radius beam pipe and immersed in the 0.435 T magnetic field provided by a solenoid. Starting from the interaction point particles emitted at large angles with respect to the beam direction cross first a silicon strip microvertex detector with two dimensional readout, then a high resolution drift detector, a large volume jet–chamber and the z–chambers.

The silicon strip microvertex detector [91] consists of two concentric layers of 12 (inner layer) and 15 (outer layer) ladders of 5 back–to–back ϕ and z wafers, giving almost full angular coverage for $\cos\theta < 0.89$ for two layers (0.93 for the inner layer only). The single hit resolution including the alignment uncertainty is 10 μm and 15 μm for the ϕ and z direction respectively. In the analysis described in this thesis the silicon microvertex detector is used only for pattern recognition purposes. The requirement that tracks have at least one associated hit in either layer of the silicon detector usually results in a better measurement of the polar angle of the tracks, and allows to recover part of the data where the vertex chamber was not functional due to trips of the high voltage system.

The vertex detector is a 1 meter long, 470 mm diameter, cylindrical drift chamber based on a scaled down jet chamber design. The chamber consists of an inner layer of 36 cells with 12 axial wires each and an outer layer of 36 small angle (4°) stereo cells with 6 wires each. The combination of stereo and axial cell information provides an accurate z measurement for charged particles close to the interaction region. The axial cells of the vertex chamber provide a precise ($\sigma \sim 50$ μm) measurement of position in the $r\phi$ plane to aid the measurement of secondary vertex topologies in e^+e^- annihilation events, while maintaining a good multi–hit detection capability to resolve individual particles within jets.

The jet chamber (CJ) is designed to combine good space and double track resolution, essential for the efficient recording of jet–like events, with the possibility of particle identification. The sensitive volume of the jet chamber is a cylinder with a length of about 4 m, surrounding the vertex detector. The outer diameter is 3.7 m, the inner 0.5 m. The chamber is subdivided into 24 identical sectors, each containing a plane with 159 sense wires.

At least 8 points on a track are obtained over a solid angle of 98% of 4π. For each point true three–dimensional coordinates (r,ϕ, z) are determined from the wire position, the drift time and from a charge division measurement. The charge division method requires the measurement of the integrated charges for each hit at both ends of the signal wire. The ratio of these charges determines z, and their sum is used to calculate the energy loss $\mathrm{d}E/\mathrm{d}x$ of the particle in the chamber gas. The single hit resolution of the jet chamber, averaged over all drift distances, was measured to be $\sigma_{r\phi} \sim 135$ μm in $r\phi$ and $\sigma_z \sim 4.5$–6.0 cm in the z-direction. The $r\phi$ double hit resolution is 2.5 mm. The single hit efficiency is 99.2% including the efficiency for the pattern recognition to associate a certain hit to a track. The track reconstruction efficiency inside jets for tracks with a momentum $p > 0.1$ GeV/c and $|\cos\theta| < 0.95$ is 97.9%.

The z–chambers are arranged to form a barrel layer around the jet chamber covering the polar angle from 44° to 136° and 94% of the azimuthal angle. They are designed to make precise measurements of the z coordinates of charged particles as these leave the jet chamber and thus to improve both the polar angle and invariant mass resolutions. The resolution is determined by the precision of the survey, and is around 300 μm, while the $r\phi$ resolution is of the order of 1.5 cm.

The single track resolution of the combined tracking system is determined using events of the type $\mathrm{e^+e^-} \to \mu^+\mu^-$ at the $\mathrm{Z^0}$ pole with a centre–of–mass energy of 2×45.6 GeV. The momentum resolution is obtained from a gaussian fit to the inverse momentum distributions of positively and negatively charged muons. The contribution of multiple scattering and both initial and final state radiation can be neglected for high momentum muon pairs. For lower momenta multiple scattering becomes the dominating contribution to the momentum resolution. The momentum resolution in the barrel region ($|\cos\theta| < 0.7$) can be written as:

$$\frac{\sigma_p}{p} = \frac{\sigma_{p_T}}{p_T} = \sqrt{(0.02)^2 + (0.0015 \cdot p_T)^2}$$

where p_T is the transverse momentum in GeV/c. The error from the measurement of the polar angle can be neglected for $|\cos\theta| < 0.7$ and does not contribute to the momentum error. Below a transverse momentum of 13 GeV/c the resolution is limited by multiple scattering originating mainly from the high gas pressure of the central detectors.

The performance of the tracking system for the high energy runs at LEP2 is shown in figure 4.3: the resolutions achieved are only marginally worse than those obtained during the $\mathrm{Z^0}$ running, despite the fact that much smaller data samples are available for calibration purposes.

Only the tracks which satisfy the following quality criteria are considered in the analysis:

- $p_T > 0.15$ GeV/c, $|p| < 100$ GeV/c, where $|p|$ and p_T are respectively the reconstructed momentum and transverse momentum of the tracks;
- associated hit multiplicity in CJ larger than 50% of the one expected from the geometrical acceptance of the jet chamber, with a minimum of at least 40 hits;
- $|d_0|$ <2.0 cm and $|z_0|$ <25.0 cm, where $|d_0|$ and $|z_0|$ are respectively the impact parameters of the tracks at the interaction point in the $r\phi$ and rz planes;

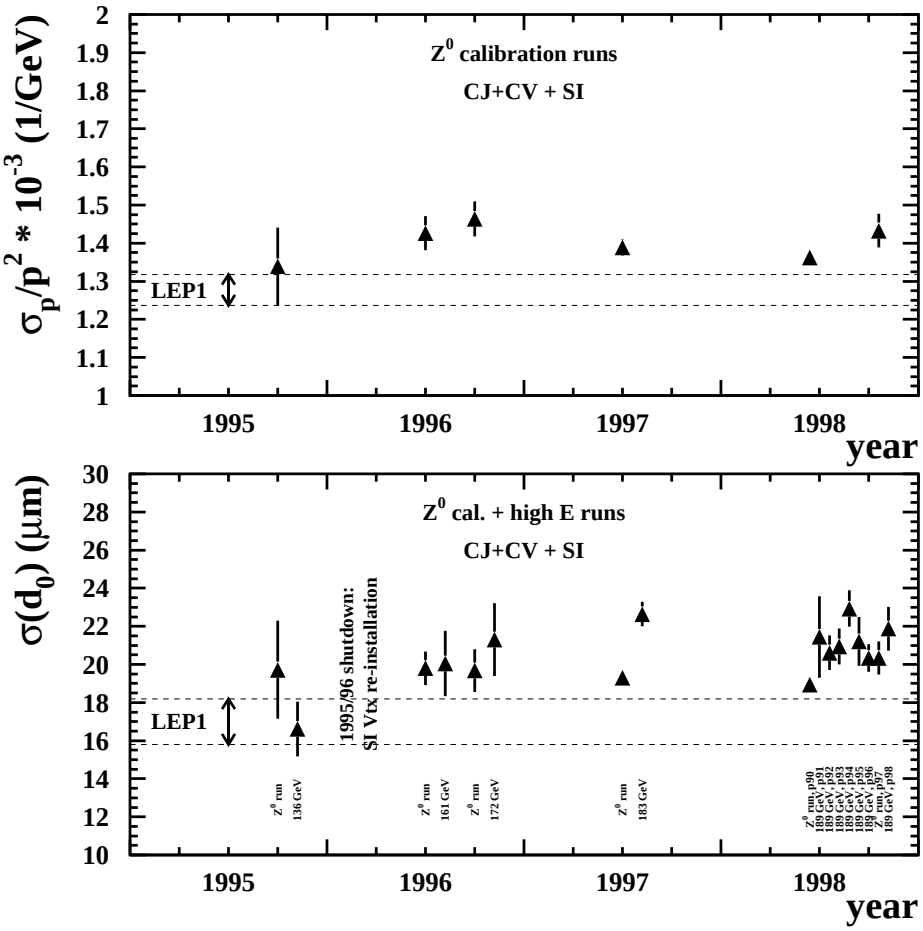

Figure 4.3: Momentum resolution (*top*) measured during the Z^0 calibration runs with $\mu^+\mu^-$ events, and impact parameter resolution (*bottom*) measured during Z^0 calibration runs and LEP2 running periods with $\mu^+\mu^-$ and Bhabha events. The horizontal bands show the resolutions obtained during the Z^0 LEP running period.

- $\chi^2_{2d} < 100$ and $\chi^2_{rz} < 100$, where χ^2_{2d} and χ^2_{rz} are the χ^2 of the track fit in the $r\phi$ and rz projections;

- the relative error of the track momentum measurement should be smaller than 50% in a region of 2.5° around the anode planes, where high momentum tracks are poorly measured.

Tracks not satisfying these criteria are not considered in the jet reconstruction and in the energy flow measurement. Events with a large number of tracks not satisfying the selection criteria usually arise from beam–gas or beam–wall interactions, or from off–momentum beam particles entering the tracking volume.

4.2 Electromagnetic calorimeter

The electromagnetic calorimeter detects and measures the energies and positions of electrons, positrons and photons ranging from tens of MeV to 100 GeV. It provides π^0–photon

discrimination, and in conjunction with the central tracking system, electron–hadron discrimination. It is a total absorption calorimeter mounted between the coil and iron yoke of the magnet. The OPAL electromagnetic calorimeter consists of, from large angle to small angle, the barrel (EB) and the endcap (EE) lead glass calorimeters, the forward detector (FD) and the silicon-tungsten calorimeter (SW). The gap between the forward detector and endcap calorimeter is filled with the gamma catcher (GC), a lead-scintillator sandwich calorimeter. The barrel and endcap calorimeters together cover 98 % of full solid angle with no geometrical holes. The hermeticity is completed by the forward detectors and the entire OPAL electromagnetic calorimeter covers 99.97 % of the full solid angle with active components. In front of the barrel and endcap lead glass calorimeters are the presampler devices. They measure the position and size of the shower developed in the material in front of the calorimeter (mainly the coil and the pressure vessel of the central tracking chambers) to improve the overall spatial and energy resolution and provide information for better spatial separation of photons and electron / hadron discrimination. There are two regions where the energy resolution is poor: the first, around $|\cos\theta| = 0.8$, corresponds to the the transition between EB and EE which are separated by the 1.5 radiation lengths (X_0) thick coil. In the second region, near to $|\cos\theta| = 0.98$ at the edge of the EE, showers are not fully contained in the lead glass.

The forward detector and the silicon–tungsten calorimeter are mainly used to measure the luminosity of LEP by detecting small–angle Bhabha scattering, and they contribute to the electromagnetic coverage of OPAL. figure 4.4 shows a cross section through the forward detector between 2 and 3 m from the interaction point, showing the gamma catcher, the two calorimeters (SW and FD), and the MIP–plug scintillator installed in 1997 (whose possible use is described below in section 4.3).

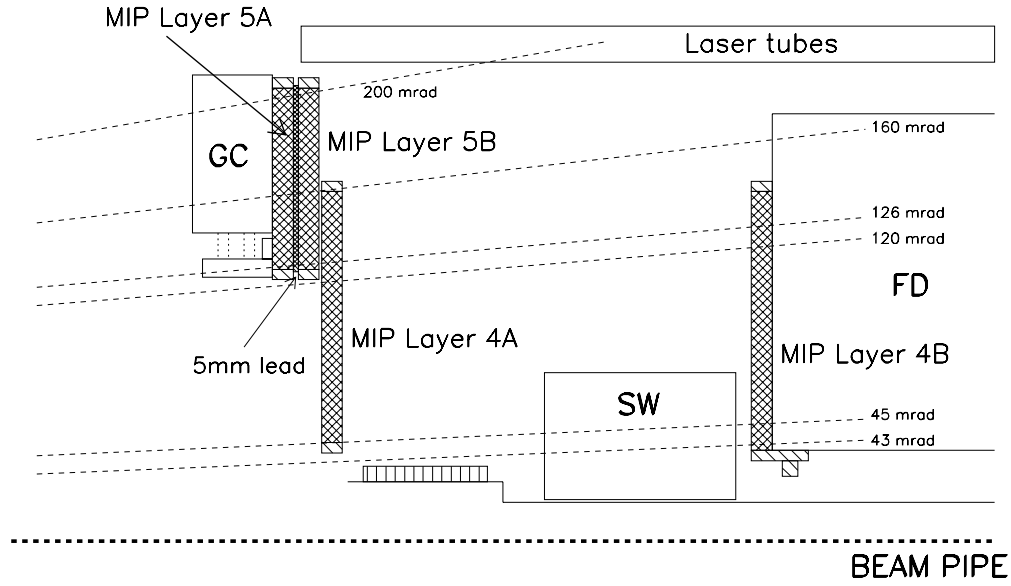

Figure 4.4: Schematic diagram illustrating the position of the calorimeters and the scintillators in the forward detector region (not to scale).

The forward calorimeter (FD) is a sampling lead–scintillator calorimeter with a depth of 20 X_0, complemented by three planes of proportional tubes located after the first lon-

gitudinal sampling (4 X_0) allowing the measurement of individual shower positions. The gamma catcher is a ring of eight individual lead-scintillator calorimeter modules at each end of OPAL with a thickness of 7 X_0. The gamma catcher fills in the gap in coverage between the upper edge of the forward calorimeter and the inner blocks of the EE. Although non-containing this calorimeter it plays an important role in ensuring the hermeticity of OPAL.

The SW luminometer [92] consists of two cylindrical calorimeters installed around the LEP beam pipe at $\pm$2389 mm from the interaction point. The detector was designed to measure the position and energy of electrons produced in small–angle Bhabha scattering in order to determine the luminosity of the LEP beams with a precision exceeding 10^{-3} [93]. Each calorimeters consists of 19 layers of silicon wafers sandwiched between tungsten absorber plates. The calorimeters cover the angular region between 62 and 142 mm from the beam axis (between 26 and 60 mrad). In preparation for the high energy running at LEP2 tungsten shields designed to protect the tracking detectors from synchrotron radiation were installed around the beam pipe. The shields, 5 mm thick and 334 mm long, present roughly 50 radiation lengths to particles originating from the interaction region, almost completely absorbing electromagnetically showering particles between 26 and 33 mrad from the beam axis.

For the reconstruction of the energy flow in the events only showers having a minimum energy of 100 MeV in the barrel and 250 MeV in the endcaps are considered . Higher thresholds of 5 GeV (GC) and 2 GeV (FD and SW) are used in the forward detectors.

4.3 The time of flight systems

Two sets of scintillation counters provide time–of–flight information in the barrel and in the endcaps. In the barrel the time-of-flight system covers the region $|\cos\theta| < 0.82$. It consists of 160 scintillation counters located just outside the solenoid coil. For the LEP2 running phase a time–of–flight system has been installed also in the endcaps [94], covering angles down to 43 mrad from the beam direction. A different technique is adopted to avoid dead spaces: thin scintillating tiles are readout through embedded wavelength shifting fibers. In the polar angle region between the 200 mrad limit of the pole tip hadron calorimeter (described later in section 4.4) and 43 mrad, the scintillating tiles (which later are briefly called MIP–plug detector) can be used to extend the angular range for detecting minimum ionising particles. In this angular range the existing system of small angle calorimeters (described in section 4.2) is sensitive only to electrons and photons.

The time of flight systems are not directly used in the analysis presented in this thesis, since cosmic rays do not represent a dangerous background due to the high multiplicity requirement. However the time of flight systems play an important role at the trigger level, providing redundant information in addition to the track and energy triggers.

4.4 Hadronic calorimeters and muon detectors.

The hadron calorimeter measures the energy of hadrons emerging from the electromagnetic calorimeter and assists in the identification of muons. It is formed by instrumenting the iron of the magnet return yoke with layers of limited streamer chambers or thin gap chambers. The return yoke provides 4 or more interaction lengths of absorber over a solid

angle of 97% of 4π. The dual role played by the iron constrains the design of the hadron calorimeter. Further constraints are imposed by the choice of a lead glass electromagnetic calorimeter. The lead glass and the magnet coil constitute 2.2 interaction lengths of material, yielding a large probability of hadronic interactions being initiated in the lead glass. The hadron calorimeter therefore works as an energy "tail catcher" so that the best measurement of hadron energy is obtained by combining its signals with those from the lead glass and with the momentum information for charged tracks as explained in section 4.7. The hadron calorimeter is constructed as a cylindrical barrel surrounding the inner OPAL detectors, two outer end caps and two pole tips (inner end caps). The pole tip hadron calorimeter complements the barrel and endcap ones by extending the solid angle coverage from $|\cos\theta| = 0.91$ to 0.99. For the reconstruction of the energy flow of the event only the hadron calorimeter clusters which have an energy deposit larger than 600 MeV, and the pole tip clusters with energies above 2 GeV are considered.

The entire hadron calorimeter is surrounded by the muon detector. Of the full solid angle, 93% is covered by at least one layer of detectors. Over most of this solid angle the amount of material that a particle has to traverse exceeds 1.3 m of iron equivalent (7 interaction lengths for pions). This is required to reduce the probability of a pion not interacting to less than 10^{-4}. Muon identification relies on extrapolating the track seen in the central detector through the absorber, allowing for energy loss and multiple Coulomb scattering, and looking in the muon detector for a track matching both in position and angles. The positional and angular accuracies of the muon detector are designed to be less than the uncertainties due to multiple Coulomb scattering at the highest possible LEP2 energy and are about 2 mm and 3 mrad respectively. Muons with less than 2 GeV/c momentum nearly always range out in the absorber, while those with more than 3 GeV/c momentum usually penetrate to the muon detector. Some of the stopping muons may be identified in the hadron calorimeters. Hadrons can fake the signature of a muon either through decays in flight or punch–through. The two processes constitute the main background to prompt muons at low and high momenta respectively.

4.5 Trigger, data acquisition and offline processing

The function of the data acquisition (DAQ) system [95] in OPAL is to read out the data of each subdetector, to merge all the informations corresponding to a single interaction and to record the event. Bunch crossings in LEP occur every 22.2 μs but the DAQ electronics are not fast enough to read out at such a frequency. Thus an event trigger is required, in order to reduce the data flow. In addition, the DAQ system performs monitoring tasks to verify the performance of the detector and the quality of the data and computes the calibration constants later used in the event reconstruction. It also monitors the operation parameters of the detector and provides automatic exchange of monitoring information between OPAL and LEP.

The DAQ system is implemented as a hierarchical system. At the lowest level is the readout electronics, which is located in crates implementing different protocols, but all read out through VME systems, which also perform data reduction as pedestal subtraction, zero–suppression and pulse shape analysis. The data from different subdetectors (or different part of the same subdetector) are then collected, synchronised and merged in an event builder. This readout procedure is started from a trigger using fast signals from

some of the subdetectors. The event builder then forwards events to the filter [96], which performs the tasks of thorough monitoring and of classification of events based on a partial event reconstruction. The filter is also normally used as a second–level software trigger to reject obvious backgrounds which are accepted by the first–level hardware trigger, like interactions of off–momentum electrons with the beam pipe, cosmic rays and detector noise.

The trigger decision is based on informations from the track–trigger processor, which combines the signals of the vertex chamber and the jet chamber, time–of–flight detectors, electromagnetic calorimeter, muon detector and forward detectors. A complete description of the OPAL trigger system can be found in [97]. The different subdetectors provide independent trigger signals which are put together by a central trigger logic. The subdetector signals are of two types: direct trigger signals based on a single detector component such as total energy or track multiplicity with relatively high thresholds, and coincidence trigger signals based on the presence of lower threshold signals in spatial coincidence from two or more subdetector components. For this purpose each subdetector contributing to the trigger decision is divided into a 6×24 $\theta\phi$ matrix of overlapping bins in polar and azimuthal angles. The matrix provides spatial correlations of hits within and between subdetectors.

A positive trigger decision requires the presence of a predefined combination of direct and coincidence signals. These combinations are programmed into the central trigger logic. The high redundancy of trigger signals in all physics channels enables OPAL to trigger with high efficiency while keeping the rate from backgrounds and detector noise at a manageable level. The efficiency for selecting hadronic Z^0 decays has been studied using independent subsets of the signals used in the final trigger decision and found to be greater than 99.9%. Given the high mass of the W boson and the fact that decay multiplicities depend only logarithmically on the invariant mass of the hadronic system it is assumed that the trigger is fully efficient also for the single W production process studied in this thesis. This assumption relies on the requirements of a high track multiplicity and of a large energy deposit in the electromagnetic calorimeter in the event selection presented in chapter 6, and is supported from trigger studies on simulated events. Further support comes from the study of the trigger efficiency for jet events produced in $\gamma\gamma$ collisions [98]: apart from the high missing transverse momentum these events have the same multiplicity and kinematics of the $q\overline{q}'e\overline{\nu}_e$ events in the low hadronic mass region, where the W boson is produced off–shell.

The events selected by the filter are passed to a farm of workstations which performs after a short time delay the reconstruction of physical quantities, such as track trajectories and energy deposits, starting from the digitised data. The time delay is necessary for computing calibration constants used in the event reconstruction. The reconstruction is performed by a set of FORTRAN routines known collectively as ROPE [99]: most of the routines handle individual subdetectors, while others have a more general scope, such as merging tracks from different detector components or performing particle identification.

Monte Carlo programs for detector simulation are an essential tool in understanding and analysing data from large experiments in high energy physics. The OPAL experiment uses a Monte Carlo program called GOPAL [100] based on the GEANT [101] simulation package, which provides a framework for the definition of the detector geometry, and controls the tracking of particles through this geometry using well–tested routines to simulate interactions. Simulated events are then subjected to the same reconstruction and analysis

procedure applied to the real data, the only difference being that for Monte Carlo events information concerning the original particle content and the association between hits and particles is also available.

4.6 Lepton identification

Efficient lepton rejection is one of the important tools for the selection of the single W signal described in chapter 6. Leptons from the $W^+W^- \to q\overline{q}'\ell\overline{\nu}_\ell$ process are generally isolated and can be identified with criteria already used at LEP1 for the selection of leptonic decays of the Z^0. More difficult is the identification of those leptons which are close in angle with one of the hadronic jets from the W decay. Here the criteria developed for identifying leptons from the decay of heavy quarks are used.

Isolated electrons and muons from the leptonic decay of W bosons are identified as in [102]. A track is considered as an electron candidate requiring a tight match (within $\pm 1°$) between the ϕ coordinate measured by the tracking system and the calorimeter, removing tracks consistent with photon conversions and requiring the ionisation energy loss dE/dx and the ratio between the energy deposited in the electromagnetic calorimeter and the track momentum to be compatible with the expectation for an electron. Rejecting candidates with significant associated hadronic activity beyond the electromagnetic calorimeter further enhances the purity of the electron signal (hits are allowed only in the first two layers of the hadron calorimeter). A muon candidate is a track which has either two associated hits in the muon chambers or associated hits in at least four layers of the hadron calorimeter (with a maximum average of two associated hits per layer, and at least one hit in one of the last three layers of the calorimeter): a hit is considered associated to the track if the difference in the ϕ coordinate is smaller than $4°$. The energy deposit in the electromagnetic calorimeter associated to the track is required to be smaller than 3 GeV in the barrel and in the endcaps, and smaller than 5 GeV in the transition region.

Electrons contained within jets are identified using an artificial neural network originally developed for b physics studies at the Z^0 peak [103]. Six variables are used as input to the network: the momentum and polar angle of the track, the energy-momentum ratio, $E/|p|$, the number of electromagnetic calorimeter blocks contributing to the energy measurement, the ionisation energy dE/dx and its error. Two additional input variables are used in the endcaps: the differences $\Delta\theta$ and $\Delta\phi$ between the angles measured by the tracking system and the electromagnetic calorimeter. Photon conversion candidates are rejected by another neural network algorithm, using spatial matching, invariant mass and momentum information of the electron candidate and an oppositely charged partner track. Background to prompt electrons identified by this algorithm consists of misidentified hadrons, untagged photon conversions and a small number of electrons from Dalitz decays of light mesons. They can be studied using tagged samples of $\pi^\pm$ from K^0_s and 3–prong $\tau^\pm$ decays. Efficiencies can be measured using $e^\pm$ from photon conversions identified in the tracking detectors.

Criteria for the identification of muons within hadronic jets are discussed in [104]. Track segments are reconstructed in the four–layer external muon chambers independently of tracks found in the central detectors. The central tracks are extrapolated through the material and magnetic field of the detector to the muon chambers. The presence of a matching segment and the quality of the positional match between the extrapolated track

and the muon segment are used to identify muons. The angular separation at the point of closest approach of the extrapolation to the segment is evaluated in ϕ and θ. A matching parameter, χ_{pos}, is constructed by adding these differences in quadrature, first normalising each by its expected error. This error includes both reconstruction and multiple scattering uncertainties. Muon candidates are selected by requiring $\chi_{pos} < 3$, considering only the best matched muon segment for each central track, and only the best matched central track for each muon segment. Finally, the measured dE/dx is required to be consistent with a muon. This latter requirement rejects 60% of charged kaon tracks otherwise misidentified as muons, and removes only 4% of prompt muons. Muon pair events from decay of the Z^0 and from two–photon collisions can be used to study the accuracy of the modelling of the efficiency in the Monte Carlo. As for the case of electrons, backgrounds can be studied with tagged $\pi^{\pm}$ samples.

Identification of the τ leptons is a difficult task in a hadronic environment. Several packages for τ identification [105] have been developed, but they are either suited to low multiplicity events or to isolated τ's. Some of the τ's may be identified as electrons or muons if they undergo a leptonic decay and the resulting energy of the lepton is high enough: the lepton identification criteria described above become inefficient below 2 GeV. Final states containing hadronically decaying τ's are better identified using the global event properties, as done for the $W^+W^- \to q\overline{q}'\tau\overline{\nu}_\tau$ channel [106], rather than by tagging the τ's themselves. For these reasons in the analysis described in chapter 6 none of the available τ identification packages is used and only a veto on the events identified as $W^+W^- \to q\overline{q}'\tau\overline{\nu}_\tau$is applied.

Direct measurements of efficiencies and purities of the lepton identification criteria cannot be repeated at LEP2 given the smallness of the data samples. The inefficiency introduced by the lepton veto on the single W signal can be measured directly on the data using the tagged samples of hadronic W decays. A systematic error is assigned to take into account the statistical precision of the test and eventual discrepancies between data and simulation. The systematic uncertainties assigned in the quoted literature for the efficiency and the purity of the lepton identification criteria in the LEP1 analyses introduce negligible systematic errors.

4.7 Energy flow measurement

In hadronic final states charged particles carry about two thirds of the total energy. In the OPAL detector they are measured with better momentum and angular resolutions by the central tracking devices than by the calorimeters, with the exception of high energy electrons. To obtain the total visible energy in the events or the energy of a jet the energy from charged particles must be added to that of the neutral ones measured in the calorimeters, avoiding double counting. Naively double counting can be avoided just by using calorimeter clusters not associated to tracks. Due to overlapping showers in the core of jets this is not an optimal method to estimate the energy of a jet. To estimate the total visible energy of the events as well as the momentum of jets an algorithm [107] is employed which uses the average response of the calorimeters to hadronic tracks. The energy deposited in clusters not associated to any tracks is added to the energy of charged particles, all assumed to have the pion mass. For clusters associated to tracks only the fraction of energy which exceeds the expected energy deposit of a pion with a corresponding

momentum is used to calculate the energy flow. Correction factors are applied to the energy deposits in the electromagnetic and hadronic calorimeters to take into account their different energy response to hadrons, as explained in [108]. This algorithm is not applied to tracks identified as electrons or muons, which have energy deposits in the calorimeters different from those of pions. If a track is identified as an electron the energy in the electromagnetic calorimeter is not corrected, whereas for muons the energy deposit in the calorimeters is assumed to be that of a minimum ionising particle. The energy deposited in the forward detectors is added to the total visible energy of the events without applying any correction. The resolution of this algorithm for the measurement of the visible energy in the events can be extracted from a fit to the invariant mass spectrum of jet pairs in events collected at the Z^0 peak shown in figure 4.5f: the width of the peak is dominated by the energy resolution of the detector and is of $\sim$ 9 GeV corresponding to a resolution of 10%, better than what expected from the intrinsic response of the OPAL calorimeters to hadrons.

4.8 Detector calibration with Z^0 data

At the beginning of each year of LEP2 data taking the detector is calibrated with a short run on the Z^0 peak. Approximately 1.0 pb^{-1} 2.1 pb^{-1} and 3.1 pb^{-1} were collected in the 1996, 1997 and 1998 LEP2 running periods. These high statistics samples (containing approximately $9\,10^3$ muonic and $2\,10^5$ hadronic decays of the Z^0) are used to control the alignment and to calculate the calibration constants of the various subdetectors. These detector parameters are then checked during the high energy running. The validity of the simulation program used in the various LEP2 analyses can be cross checked on these samples, since the event generator simulating Z^0 decays is tuned on the much larger LEP1 data set. Any discrepancy between the simulation and the data observed on these Z^0 samples is therefore assumed to be due to inaccuracies in the detector simulation program and treated as a possible source of systematic error for the LEP2 analyses.

For the analysis described in this thesis it is interesting to check that measured jet energies and angles and missing transverse momentum are correctly reproduced in the Monte Carlo samples. Two jets events are identified in a sample of hadronic Z^0 decays selected as in [109] requiring a value of the thrust [110] parameter larger than 0.8 and the y_{23} parameter in the Durham [111] recombination scheme smaller than 0.02, y_{23} being the value of the jet resolution parameter at which the event classification changes from 3 to 2 jets.

The distributions of the following quantities in the Z^0 data and in the corresponding Monte Carlo simulation are then compared:

- the acoplanarity of the two jets, defined as the complement to 180° of the angle between the two jets in the plane transverse to the beam axis. This quantity is expected to have a distribution sharply peaked at zero, with a width dominated by detector resolution effects.
- the estimated uncertainty on the acoplanarity, computed through error propagation from an estimate of the error on the jets momenta.
- the sum of the cosine of the polar angles of the two jets. Also this quantity should peak at zero, with a width dominated by the detector resolution.
- the missing transverse momentum.

- the sum of the energies of the two jets and their invariant mass. These two quantities should give a distribution peaked at the centre–of–mass energy. Their width is a measurement of the energy resolution of the detector.

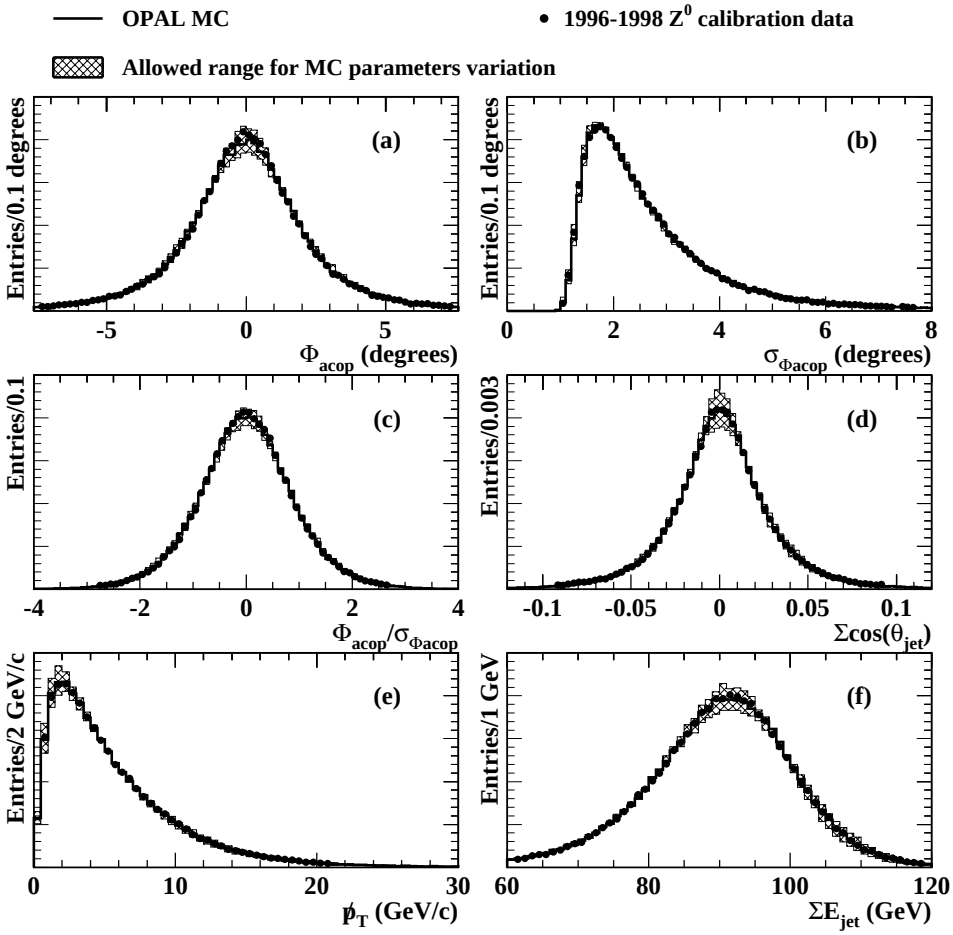

Figure 4.5: Distribution of acoplanarity angle (*a*), of its error (*b*), of their ratio(*c*), of sum of the polar angles of the jets (*d*), of the missing transverse momentum (*e*) and of the sum of the energies of the jets (*f*) for the 1997 Z^0 data. The points shown the data and the thick line the Monte Carlo sample after applying the smearing procedure described in the text. The hatched region indicates the allowed range of variation of the smearing parameters.

The Monte Carlo gives a good description of the data, though closer investigation indicates that all distributions are slightly wider in the data than in the Monte Carlo. This discrepancy is attributed to inaccuracies of the detector simulation program. The kinematic quantities used in the event selection are therefore smeared in the Monte Carlo in order to obtain a better description of the data. The smearing procedure consists in adding small corrections to the kinematic quantities used in the event selection. The smeared distribution of the kinematic quantities used in the analysis are shown in figure 4.5. Eventual systematic errors associated with this procedure can be assessed by varying the size of the applied corrections within the range allowed by the Z^0 data: the systematic error is evaluated by multiplying the smearing parameters by a factor which is varied between 0 (no smearing) and 1.5 or 2 depending on the measured quantity. The corresponding variation is indicated by the grey band in figure 4.5.

For some of the measured quantities (the θ_{jet} and ϕ_{jet} angles of the jets, the invariant mass of the jet pair M_{jj}) the corrections applied in the smearing procedure consist in a shift, μ, of the distribution and an additional correction extracted randomly from a gaussian distribution. The variance, σ^2, of this distribution is obtained as the difference between the variances of the data and Monte Carlo distributions (estimated either from the RMS of the distributions or from a gaussian fit).

A simple multiplicative scaling factor f is instead applied to the remaining measured quantities (the error on the ϕ angles of jets σ_ϕ, used to estimate the error on the acoplanarity, and the missing transverse momentum). This scaling factor is the ratio of the mean values of the distribution of the measured quantities in the Z^0 data and in the Monte Carlo.

Measured quantity	Shift (μ)	Width (σ)	Scale (f)	Range for systematic errors
Data taken at $\sqrt{s} = 161$ and 172 GeV				
ϕ_{jet}	$-0.015°$	$0.39°$		0–1.5
θ_{jet}	$0.09°$	$0.35°$		0–1.5
M_{jj}	700 MeV	3.8 GeV		0–1.5
σ_ϕ			1.006	0–2
$\not{p}_T$			1.097	0–2
Data taken at $\sqrt{s} = 183$ GeV				
ϕ_{jet}	$-0.015°$	$0.33°$		0–1.5
θ_{jet}	$-0.006°$	$0.43°$		0–1.5
M_{jj}	140 MeV	2.6 GeV		0–1.5
σ_ϕ			1.005	0–2
$\not{p}_T$			1.069	0–2
Data taken at $\sqrt{s} = 189$ GeV				
ϕ_{jet}	$-0.008°$	$0.38°$		0–1.5
θ_{jet}	$-0.005°$	$0.36°$		0–1.5
M_{jj}	620 MeV	2.8 GeV		0–1.5
σ_ϕ			1.005	0–2
$\not{p}_T$			1.067	0–2

Table 4.1: Parameters used in the smearing procedure for the Monte Carlo events corresponding to the different LEP2 data sets. Only the average values of the parameters is shown, the actual smearing procedure using different values depending on the polar angle of the jets.

The angular dependence of the smearing parameters is studied dividing the Z^0 sample in 5 angular bins: two for the barrel, one for the transition region between barrel and endcaps, and two for the endcaps. The energy dependence of the required correction factors has been studied in [112] and found to be negligible. The average smearing parameters for the different observables used in the event selection are given in table 4.1. The width of the smearing gaussians should be compared with the measured jet angular resolutions ($1.65°$ in ϕ and $1.25°$ in θ) and the width of the invariant mass distribution of jet pairs (~ 10 GeV). The applied corrections imply that the angular resolutions are underestimated in the Monte Carlo by at most 1.5% in ϕ and 6.5% in θ and the jet pair invariant mass resolution by 3.4%.

The largest discrepancies between the Monte Carlo and Z^0 data are seen for the 1996 sample in the distribution of the cosine of the polar angle of the jets and for the missing transverse momentum. Both are due to a problem in the simulation of the response of the hadronic calorimeter, which was fixed for the 1997 simulation. Therefore the required correction for 1997 and 1998 are smaller.

4.9 LEP operation

Since 1996 the LEP accumulation ring is operated above the threshold for pair production of W bosons. To compensate the energy lost through synchrotron radiation (which grows like the fourth power of the beam energy) superconducting cavities have been installed during various shutdown periods of the machine, allowing a gradual increase of the centre–of–mass energy. In July 1996 LEP was operated for 5 weeks with nominal beam energies of 80.65 GeV, and luminosities between 10 and 12 pb^{-1} were delivered to the four LEP experiments. Following the installation of additional superconducting cavities beam energies of 86 GeV were reached in October 1996, and 11 pb^{-1} delivered to the experiments. The maximum instantaneous luminosity achieved in 1996 was $3.4\,10^{31}$ $cm^{-2}s^{-1}$ for beam currents of 4–6 mA, running most of the time with 4×4 bunches in the machine. The main limitation during this running period was the stability of the RF system.

After the addition of other superconducting cavities LEP run in 1997 mostly with beam energies of 91.5 GeV. Depending on the state of the RF system some fills were taken at slightly lower beam energies. The luminosity was typically a factor 2 higher than in 1996, and given the longer running period more than 60 pb^{-1} were delivered to the LEP experiments. The increase in luminosity was obtained through higher beam currents and reduced beam size at the interaction points. In 1998 the beam energy was raised to 94.5 GeV and a new optics was used. This allowed to store higher currents in the machine, which together with reduced betatron functions at the interaction points gave higher luminosities (peak values of the luminosities reached 10^{32} $cm^{-2}s^{-1}$). The average total delivered luminosity to the four LEP experiments reached almost 200 pb^{-1} at the end of the data taking period.

The energy of the beams is measured during the fills using NMR probes installed in some of the accelerator magnets. Outside of physics fills the total bending field of the dipoles is measured with a flux loop method. These two methods provides mostly a check of the stability of the magnetic field of the machine. To set the absolute energy scale the method of resonant depolarisation [113] was used in 1997 to measure the beam energy at four different points between 40 and 55 GeV, and one additional point at 60 GeV was measured in 1998. An error of 20–30 MeV is assigned to the beam energy, to allow for uncertainties in the extrapolation from 60 to 94.5 GeV. This represents a negligible source of systematic error for the analysis described in this thesis. In addition to the absolute energy of the beams also the energy spread at the interaction points has been measured. It rises from 105 MeV for $\sqrt{s} = 161$ GeV to 170 MeV at $\sqrt{s} = 189$ GeV.

4.10 Machine backgrounds

The detector simulation program reproduces correctly the response of the OPAL detector, as discussed in section 4.5 and 4.8. However it does not contain a simulation of back-

grounds generated by the presence of the circulating beams in the machine. These backgrounds have two different origins: there is a component of synchrotron radiation emitted by the beams when passing through the quadrupoles of the focusing system and a component of off–momentum beam particles. These backgrounds can be estimated using random beam crossing triggers which are normally collected during data taking at a rate of approximately 0.25 Hz.

The synchrotron radiation component of the background is greatly reduced by the presence of collimators and shielding masks. The detectors mostly affected by this type of background are the vertex detector and the central jet chamber. Whenever there is a strong component of synchrotron radiation background originating mostly from problems in the steering of the beams, the chambers are flooded with hits at small radii, spread all along the length of the detector. This can cause a problem to the pattern recognition programs and therefore such events are usually rejected at the filter level, unless there is substantial activity in the detector at large polar angles. Usually such bad beam conditions are recognised by the shift and / or the LEP operation crew and corrected, without causing data losses.

The off–momentum background was instead a major problem during OPAL operation in 1997. The configuration of the focusing system is such that off–momentum electrons of around 20 GeV are focused and hit the detector in the forward calorimeters. The off–momentum electrons originated mostly in beam–gas collisions in one of the copper RF cavities due to poor vacuum conditions. The additional energy deposited in the forward calorimeters causes a data loss if it exceeds a threshold which is in use in the analysis. Losses of up to 5% of the data have been observed in analyses which make use of tight energy cuts in FD and / or SW.

centre–of–mass energy (GeV)			
161	172	183	189
$(5.24 \pm 0.21)\,10^{-3}$	$(2.55 \pm 0.17)\,10^{-3}$	$(3.10 \pm 0.11)\,10^{-3}$	$(1.36 \pm 0.05)\,10^{-3}$

Table 4.2: Efficiency losses for the vetoes on the energy deposits in the forward detectors caused by beam related backgrounds as measured with random beam crossings.

In the analysis loose cuts are applied on the energy deposits in FD and SW, to avoid possible dependencies on the correct modelling of the transverse momentum of the ISR photons in the $e^+e^- \to q\overline{q}'e^-\overline{\nu}_e$ process. Events with energy deposits in FD or SW compatible with those expected from radiative Z^0 production are rejected. The cut on the largest energy deposit is placed 6 GeV below the photon energy calculated assuming two body kinematics. The resulting loss of efficiency estimated using random beam crossing triggers is given in table 4.2. For the four data sets considered the efficiency loss is smaller than 0.5%, and the uncertainty on this number causes a negligible systematic error.

For some of the quantities used in the event selection a correction is applied to take into account the presence of beam related backgrounds. These corrections, listed in table 4.3, affect only a tiny fraction of the events. They are obtained from the distribution of the quantities measured in random beam crossing events. A systematic error is assigned to this procedure by removing and doubling the correction.

Measured quantity	Fraction of events affected	Correction to to applied
Data taken at $\sqrt{s} = 161$ GeV		
Number of tracks	$(0.062 \pm 0.007)\%$	$+1.4$
Fraction of good tracks	$(1.31 \pm 0.04)\%$	$+0.022$
$E_{ECal}/\sqrt{s}$	$(1.05 \pm 0.03)\%$	$+0.007$
Maximum energy deposit in FD	$(4.95 \pm 0.06)\%$	$+16.6$ GeV
Maximum energy deposit in SW	$(5.04 \pm 0.06)\%$	$+18.9$ GeV
Data taken at $\sqrt{s} = 172$ GeV		
Number of tracks	$(0.048 \pm 0.008)\%$	$+2.4$
Fraction of good tracks	$(0.51 \pm 0.02)\%$	$+0.054$
$E_{ECal}/\sqrt{s}$	$(1.07 \pm 0.03)\%$	$+0.006$
Maximum energy deposit in FD	$(2.02 \pm 0.05)\%$	$+$ 7.2 GeV
Maximum energy deposit in SW	$(1.60 \pm 0.04)\%$	$+24.3$ GeV
Data taken at $\sqrt{s} = 183$ GeV		
Number of tracks	$(0.122 \pm 0.007)\%$	$+2.0$
Fraction of good tracks	$(1.05 \pm 0.02)\%$	$+0.061$
$E_{ECal}/\sqrt{s}$	$(1.42 \pm 0.02)\%$	$+0.007$
Maximum energy deposit in FD	$(1.55 \pm 0.02)\%$	$+$ 6.7 GeV
Maximum energy deposit in SW	$(3.75 \pm 0.04)\%$	$+24.3$ GeV
Data taken at $\sqrt{s} = 189$ GeV		
Number of tracks	$(0.130 \pm 0.005)\%$	$+2.2$
Fraction of good tracks	$(1.13 \pm 0.02)\%$	$+0.071$
$E_{ECal}/\sqrt{s}$	$(1.00 \pm 0.01)\%$	$+0.010$
Maximum energy deposit in FD	$(0.82 \pm 0.01)\%$	$+$ 5.8 GeV
Maximum energy deposit in SW	$(0.66 \pm 0.01)\%$	$+35.2$ GeV

Table 4.3: Corrections applied to the Monte Carlo events corresponding to the different LEP2 data sets to take into account beam related backgrounds.

4.11 Luminosity measurement

The integrated luminosity is measured using small-angle Bhabha scattering events recorded in the forward calorimetry. The primary detector is the silicon–tungsten luminometer. Bhabha scattering events are selected by requiring a high energy cluster in each end of the detector, using asymmetric acceptance cuts. The energy in each calorimeter has to be at least half the beam energy, and the average energy has to be at least three quarters of the beam energy. The two highest energy clusters are required to be back-to-back in ϕ, $(|\phi_R - \phi_L| - \pi) < 200$ mrad, where ϕ_R and ϕ_L are the azimuthal angles of the cluster in the right– and left–hand calorimeter respectively. They are also required to be collinear, by placing a cut on the difference between the radial positions, $\Delta\mathrm{R} = |\mathrm{R}_R - \mathrm{R}_L| < 25$ mm, where R_R and R_L are the radial coordinates of the clusters on a plane approximately 7 radiation lengths into the calorimeter. This cut, corresponding to an acollinearity angle of about 10.4 mrad, effectively defines the acceptance for single–photon radiative events, thus reducing the sensitivity of the measurement to the detailed energy response of the calorimeter.

The error on the luminosity measurement is dominated by data statistics for $\sqrt{s} = 161$–

172 GeV, and by systematics for the high statistics samples collected at $\sqrt{s} = 183$ and 189 GeV. The largest systematic uncertainty arises from theoretical knowledge of the cross-section (0.25%), with detector effects amounting to a further 0.20%–0.25% at the different energies. The integrated luminosities of the data samples used in the analysis presented in this thesis are given in table 4.4. The quoted values include the correction for the inefficiency caused by the veto on the energy deposits in the forward detectors, as discussed in section 4.10, and by status cuts used to ensure that all the detector components used in the analysis are fully functional. Also given are the luminosity–weighted centre–of–mass energies for the three data sets.

Nominal energy	Integrated luminosity	Average centre–of–mass energy
161	(9.95±0.05) pb^{-1}	(161.34±0.06) GeV
172	(10.31±0.06) pb^{-1}	(172.02±0.06) GeV
181–184	(56.79±0.25) pb^{-1}	(182.68±0.05) GeV
189	(173.96±0.39) pb^{-1}	(188.64±0.04) GeV

Table 4.4: Integrated luminosities and luminosities–weighted centre–of–mass energies for the data sets used for the analysis.

5 Monte Carlo studies

Differences between W pair and single W production, which both contribute to the $q\overline{q}'e\overline{\nu}_e$ final state in e^+e^- collisions, have been discussed qualitatively in chapter 3. It was shown that the single W contribution to the cross section can be enhanced by requiring that the electron is scattered at small angles with respect to the direction of the incoming beams. This selects events with a high probability of being produced through the *t*–channel diagrams, which have a higher sensitivity to the $\Delta\kappa_\gamma$ coupling with respect to the *s*–channel diagrams.

The discussion of chapter 3 is continued using Monte Carlo studies performed with different programs. These studies are performed at the generator level, using the four–momenta of the fermions as given by the Monte Carlo programs and ignoring detector resolution, selection efficiency and background effects. The settings used in different Monte Carlo programs are briefly summarised in section 5.1. Differences between W pair and single W production are discussed in section 5.2, where simple kinematic cuts to separate the two processes are derived. Interference effects between *s*– and *t*–channel diagrams are described in section 5.3. The dependence of the total cross section for $q\overline{q}'e\overline{\nu}_e$ production from anomalous couplings is investigated in section 5.4, where possible differences among different event generators are also considered. Finally, the use of kinematic information of the events compatible with single W production in the extraction of TGC's is studied in section 5.5.

5.1 Parameters settings in different Monte Carlo programs

The $q\overline{q}'e\overline{\nu}_e$ final state is simulated using three of the Monte Carlo programs listed in table 3.1: grc4f [73], KORALW [74] and EXCALIBUR [75]. A fourth program, ERATO [76], is used only in this chapter to calculate total cross sections and their dependence on TGC's.

The following set of input parameters is used in grc4f and KORALW for the calculation of the $e^+e^- \to q\overline{q}'e^-\overline{\nu}_e$ cross section in the phase space region dominated by single W production: $m_W = 80.33$ GeV/c^2, $\Gamma_W = 2.093$ GeV/c^2, $m_{Z^0} = 91.1887$ GeV/c^2, $\alpha_{em} = 1/135.0$. The G_μ scheme is used for setting the remaining initial parameters. In this scheme the weak mixing angle is a derived quantity,

$$\sin^2\theta_W = 1 - m_W^2/m_{Z^0}^2 = 0.22398,$$

and the weak couplings of the W and Z bosons are obtained from the Fermi constant G_F. For EXCALIBUR and ERATO a different approach is used, as these two programs do not implement the G_μ scheme. To ensure that all couplings of fermions to the weak bosons assume the same values as in grc4f and KORALW, the weak mixing angle is fixed at

$\sin^2\theta_W = 0.21862$ for $\alpha_{em} = 1/135.0$. Naive QCD corrections are included in all programs and the strong coupling constant is set to $\alpha_S(m_{Z^0}) = 0.12$. The width of the W boson in propagators is assumed to depend on the centre–of–mass energy like $\Gamma_W\sqrt{s}/m_W c^2$ in grc4f and KORALW, while it is fixed at Γ_W in EXCALIBUR and ERATO. In grc4f and KORALW quark masses and mixing angles are taken into account, while EXCALIBUR and ERATO implement only massless matrix elements.

The value $\alpha_{em}(4m_W^2) = 1/128.07$ is used in all programs when the total cross section for the $e^+e^- \to q\overline{q}'e^-\overline{\nu}_e$ process is calculated without kinematic cuts. This value is better suited for the description of the *s*–channel diagrams which dominate this cross section. In EXCALIBUR and ERATO this requires that for the weak mixing angle the value $\sin^2\theta_W = 0.230456$ is used.

5.2 Cuts for isolating the single W signal

The different contributions to the CC20 cross section have already been discussed in section 3.1. The differences between the contributions from *s*– and *t*–channel diagrams are shown for the most relevant distributions in figures 5.1a–5.1c, using a set of $q\overline{q}'e\overline{\nu}_e$ events generated at $\sqrt{s} = 184$ GeV with the grc4f Monte Carlo.

The first of this figures shows the distribution of the cosine of the polar angle of the final state electron, $\cos\theta_{e^-}$. The contribution from the *t*–channel diagrams is concentrated essentially in the last bin of the histogram, at $\cos\theta_{e^-} > 0.98$. Below this value the cross section is completely dominated by W pair production. The resonant behaviour of single W production is evident from figures 5.1b and 5.1c. While the *s*–channel diagrams have a peak in both combinations of invariant masses from final state fermions corresponding to the decays of the two W bosons, $m_{e\nu}$ and $m_{q\overline{q}'}$, the *t*–channel diagrams do not show any enhancement in the $m_{e\nu}$ spectrum. As a function of $m_{q\overline{q}'}$ the cross section shows a large enhancement at small invariant masses in addition to the peak at $m_{q\overline{q}'} \approx m_W$, due to the contribution from the multiperipheral diagrams (numbers 13 and 14 in figure 3.1).

In the region $\cos\theta_{e^-} > 0.98$ the *t*–channel diagrams contribute more than 90% to the cross section (figure 5.1c). The residual contamination from W pair production is clearly visible as a small peak around 60 GeV/*c* in the distribution of the total momentum of the quark pair in figure 5.4b. This contamination could be in principle reduced by applying a tight cut on the angle of the outgoing electron. This strategy is adopted in the ALEPH and L3 analyses, where the angular cut on the electron is used for the signal definition. The event selection described in chapter 6 does not apply any cut on the scattering angle of the electron. The requirement $\cos\theta_{e^-} > 0.98$ is used in here and in chapter 6 only for illustrative purposes. In section 5.4 this cut is used to compare different Monte Carlo programs and to show the different sensitivity of the single W process to anomalous couplings compared to that of the $e^+e^- \to W^+W^-$ process.

The cross sections computed by different event generators are compared in table 5.1 for the four different centre–of–mass energies considered in the analysis, using the simple requirement on the cosine of the polar angle of the electron, $\cos\theta_{e^-} > 0.98$, to select the phase space region dominated by single W production. An additional requirement on the cosine of the polar angle of both quarks, $|\cos\theta_q| < 0.98$, is applied to avoid problems in massless Monte Carlo programs due to the divergence in the multiperipheral diagrams. Differences between the various event generators are largest at the W pair production

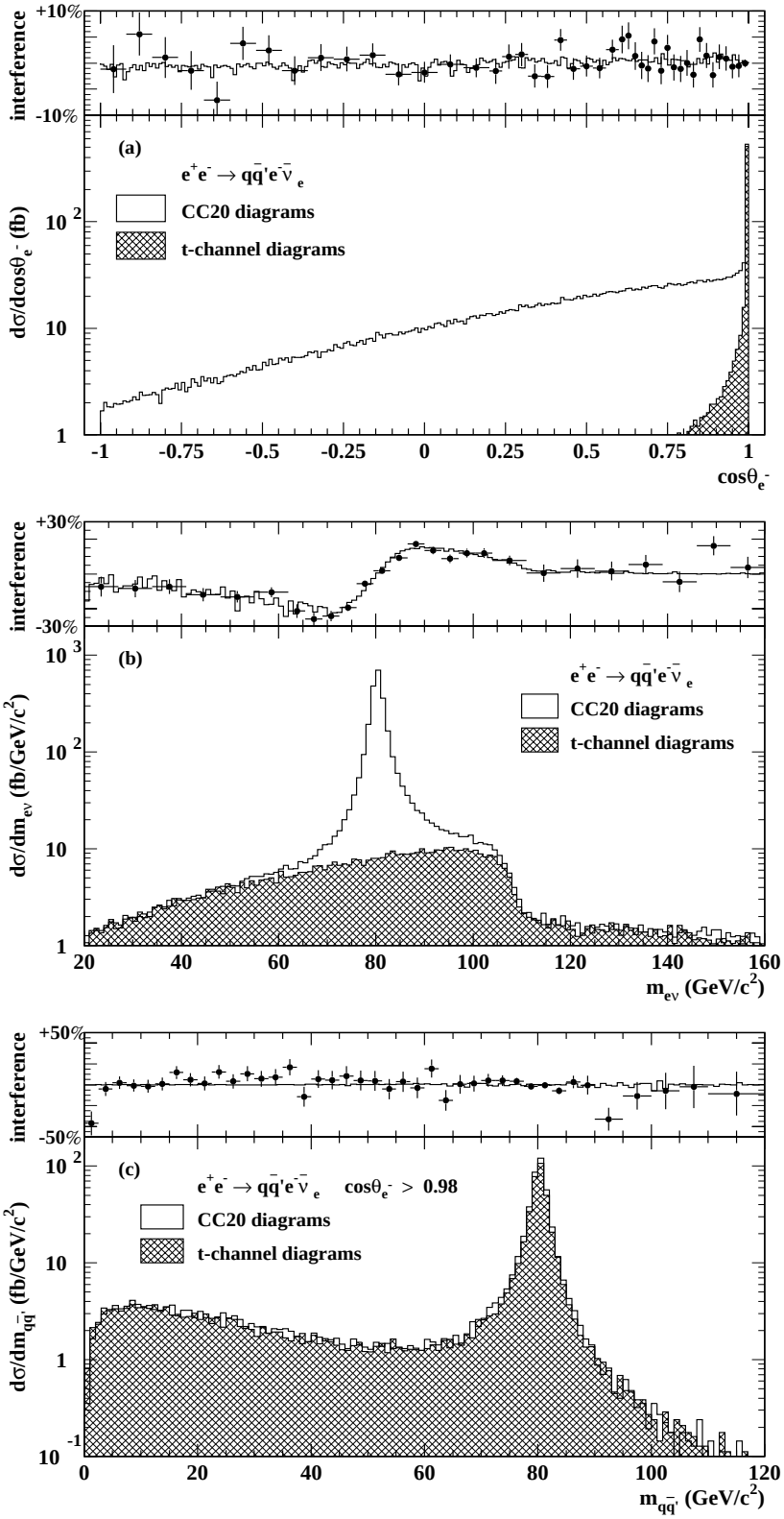

Figure 5.1: Differential cross section with respect to $\cos\theta_{e^-}$ (*a*), $m_{e\nu}$ (*b*) and $m_{q\overline{q}'}$ (*c*, restricted to the range $\cos\theta_{e^-} > 0.98$). The hatched histograms indicate the contribution from the *t*–channel diagrams. The upper part of each plot contains the distribution of the interference term normalised to the differential cross section calculated using the full set of four–fermion histograms. This interference term is either calculated as a weight on a event by event basis (line) or subtracting differential distributions of the *s*– and *t*–channel diagrams from the full four–fermion differential distribution (dots).

threshold, $\sqrt{s} \approx 161$ GeV, and tend to decrease with increasing centre–of–mass energy.

Program	$\sqrt{s} = 161$ GeV	$\sqrt{s} = 172$ GeV	$\sqrt{s} = 183$ GeV	$\sqrt{s} = 189$ GeV
grc4f	(202.61±0.14) fb	(283.59±0.19) fb	(361.79±0.24) fb	(417.42±1.42) fb
KORALW	(212.22±0.26) fb	(294.98±0.28) fb	(371.98±0.43) fb	(423.07±1.48) fb
EXCALIBUR	(217.14±0.18) fb	(300.24±0.22) fb	(381.51±0.29) fb	(427.17±1.50) fb
ERATO	(215.64±1.52) fb	(297.20±1.24) fb	(377.50±1.60) fb	(422.71±5.16) fb

Table 5.1: Comparison of the $e^+e^- \to q\overline{q}'e^-\overline{\nu}_e$ cross section for $\cos\theta_{e^-} > 0.98$ at different centre–of–mass energies, $\sqrt{s}$, for four different Monte Carlo programs.

5.3 Interference effects in the $e^+e^- \to q\overline{q}'e^-\overline{\nu}_e$ channel

The contribution of the *s*–channel diagrams and that of the *s*–*t*–channel interference should be considered as backgrounds in the measurement of the *t*–channel cross section of the $e^+e^- \to q\overline{q}'e^-\overline{\nu}_e$ reaction. The interference term is calculated using the Monte Carlo in two different ways:

- The first consists in generating three sets of events: using the full CC20 matrix element, only the *s*–channel or only the *t*–channel diagrams. At the level of the total cross section the interference term is calculated as the difference between the CC20 cross section and the *s*– and *t*–channel cross sections. The same procedure can be applied to differential cross sections, but leads to large uncertainties in regions of the phase space in which the cross section is small.

- For this reason a second technique, based on event weights and described in appendix A, is also used. The difference between CC20, *s*– and *t*–channel diagrams is not calculated at the level of cross sections, but on a event by event basis. This last method avoids large statistical uncertainties which may result from the subtraction of large numbers, and is better suited to the study of interference effects in differential distributions.

The interference between *s*– and *t*–channel diagrams in the $e^+e^- \to q\overline{q}'e^-\overline{\nu}_e$ process gives a negative contribution to the cross section. This contribution is smaller than 1% relative to the total cross section above the W pair production threshold. Only close to the W pair production threshold the interference term is not negligible, since it amounts to a negative contribution of 8% to the total cross section.

For the measurement of the *t*–channel cross section it is anyhow necessary to study the effect of the interference term on the accepted cross section. This effect may be larger or smaller than the values quoted above for the total cross section, which may result from cancellations between different regions of the phase space. To investigate the effects of interference in the phase space region accepted by the event selection described in chapter 6 two different methods are applied:

- The size of the interference term can be calculated using fully simulated samples of events generated using all the CC20 diagrams, or only *s*– and *t*–subsets of diagrams. This approach is followed in chapter 8, and gives for the interference term results

which are compatible with zero within the available Monte Carlo statistics. This translates into a systematic uncertainty of 0.5% on the cross section measurement.

- To increase the statistical precision of the test, larger Monte Carlo samples are used and a simplified parametrisation of the detector response and of the selection efficiency are applied, without processing the events through the detector simulation and reconstruction programs. In this case it is found that the interference term contributes for less than 0.3% to the accepted cross section at the W pair production threshold and less than 0.1% for $\sqrt{s} \geq 170$ GeV.

Both methods indicate that the effect of the interference between the *s*– and *t*-channel diagrams is negligible for the *t*–channel cross section measurement presented in chapter 8. Using similar methods this conclusion is obtained also for the measurement of the $q\overline{q}'e\overline{\nu}_e$ contribution to the $e^+e^- \to W^+W^-$ cross section well above the W pair production threshold.

The situation is different when differential cross sections are considered. The most striking effect of the interference between the *s*– and *t*–channel diagrams in the $e^+e^- \to q\overline{q}'e^-\overline{\nu}_e$ process is a 70 MeV mass shift in the position of the peak of the invariant mass of the electron and the neutrino, $m_{e\nu}$. For $m_{e\nu} < m_W$ the interference between *s*– and *t*–channel diagrams is negative, while the opposite happens for $m_{e\nu} > m_W$, as shown in figure 5.1b. The size of this interference term can be as large as 20% of the cross section for $|m_{e\nu} - m_W| \approx 10$ GeV/c^2. Integrated over all invariant masses, the positive and negative interference terms on the two sides on the W peak cancel, giving a total close to zero, as visible for example in the angular distribution of the electron and the invariant mass of the quark pair $m_{q\overline{q}'}$(figures 5.1a and 5.1c). The presence of this interference term and the consequent mass shift in the $q\overline{q}'e\overline{\nu}_e$ channel have been often neglected in W mass measurements performed at LEP [114], introducing a large systematic error, since the mass shift is of the same order of magnitude as the desired experimental accuracy of the measurement.

5.4 Dependence of the cross section on TGC's

The dependence of the $e^+e^- \to q\overline{q}'e^-\overline{\nu}_e$ cross section on the anomalous couplings defined in section 1.4 has been studied using different Monte Carlo programs. The total cross section predicted by the EXCALIBUR Monte Carlo for this process at $\sqrt{s} = 184$ GeV as a function of the $\Delta\kappa_\gamma$ and λ_γ couplings is shown in figures 5.2a and 5.2b, assuming the SU(2) $\otimes$ U(1) relations among the couplings and $\Delta g_1^z = 0$. Also shown is the dependence of the cross section for the process $e^+e^- \to q\overline{q}'\mu\overline{\nu}_\mu$, which can only proceed through the *s*–channel diagrams. The curves have been obtained fitting the cross sections obtained for various values of the couplings with the function

$$\sigma(x) = \sigma_{SM}(1 + \alpha x + \beta x^2),$$

where σ_{SM} is the cross section when the couplings assume their $\mathcal{SM}$ values, x is one of the couplings and α and β are the fit parameters. Only linear and quadratic terms are necessary to describe the dependence of the cross section on TGC's, since the coupling parameters enter linearly in the interaction Lagrangian.

If the couplings assume their $\mathcal{SM}$ values $\Delta\kappa_\gamma = \lambda_\gamma = 0$, the additional contribution from the *t*–channel diagrams increases the cross section of the $e^+e^- \to q\overline{q}'e^-\overline{\nu}_e$ process by

$\approx$ 20% for centre–of–mass energies between 180 and 200 GeV with respect to the $\mathcal{SM}$ cross section of the $e^+e^- \to q\overline{q}'\mu\overline{\nu}_\mu$ process. The dependence of the total cross section on the $\Delta\kappa_\gamma$ parameter is stronger for the $q\overline{q}'e\overline{\nu}_e$ final state than for $q\overline{q}'\mu\overline{\nu}_\mu$, and this is entirely due to the contribution from the *t*–channel diagrams. This is made evident by two additional curves in figures 5.2a and 5.2b which show the contribution to the $e^+e^- \to q\overline{q}'e^-\overline{\nu}_e$ cross

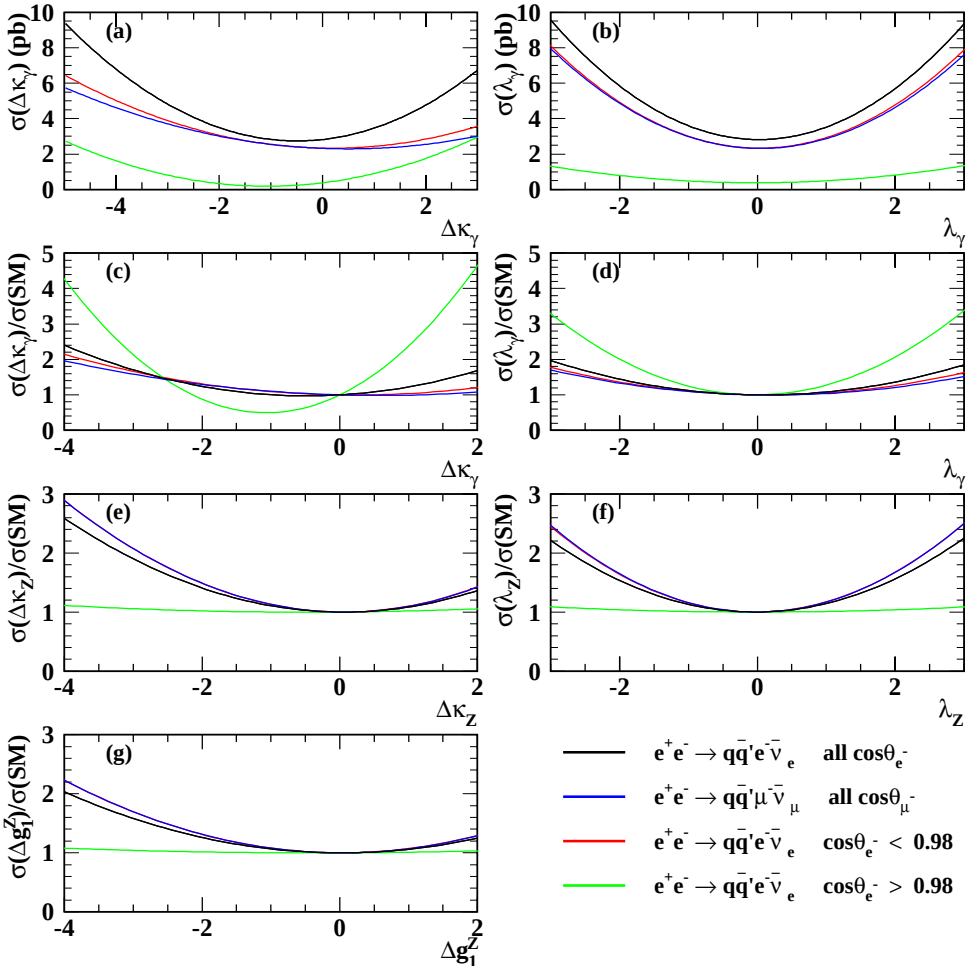

Figure 5.2: The total cross section for the $q\overline{q}'e\overline{\nu}_e$ and $q\overline{q}'\mu\overline{\nu}_\mu$ final states is shown in (*a*) and (*b*) as a function of the $\Delta\kappa_\gamma$ and λ_γ parameters, assuming the SU(2) $\otimes$ U(1) relations among TGC's and $\Delta g_1^z = 0$. Also shown are the contributions to the $q\overline{q}'e\overline{\nu}_e$ cross section from events with $\cos\theta_{e^-}$ smaller and larger than 0.98. In (*c*–*g*) the ratio of the total cross section to the $\mathcal{SM}$ cross section is shown as a function of the 5 different coupling parameters: $\Delta\kappa_\gamma$, λ_γ, $\Delta\kappa_z$, λ_z and Δg_1^z. In (*c*–*g*) the curve for the $q\overline{q}'e\overline{\nu}_e$ final state in the region $\cos\theta_{e^-} < 0.98$ overlaps with the curve for the $q\overline{q}'\mu\overline{\nu}_\mu$ final state.

section coming from the phase space regions $\cos\theta_{e^-} < 0.98$ and $\cos\theta_{e^-} > 0.98$. The first of these two phase space regions is dominated by *s*–channel diagrams. The magnitude and dependence of the $e^+e^- \to q\overline{q}'e^-\overline{\nu}_e$ cross section on TGC's in this phase region are similar to that of the $e^+e^- \to q\overline{q}'\mu\overline{\nu}_\mu$ process. The additional contribution to the total cross section of the $e^+e^- \to q\overline{q}'e^-\overline{\nu}_e$ process comes entirely from the second phase space region ($\cos\theta_{e^-} > 0.98$) and is responsible for the different dependence on TGC's.

These differences are even more clear when the enhancement factor of the cross section

is studied as a function of the 5 different couplings. The enhancement factor is defined as the ratio $\sigma(x)/\sigma_{\rm SM}$ and is shown in figures 5.2c–5.2g for the total $e^+e^- \to q\overline{q}'e^-\overline{\nu}_e$ and $e^+e^- \to q\overline{q}'\mu\overline{\nu}_\mu$ cross sections, as well as for the contributions to the $e^+e^- \to q\overline{q}'e^-\overline{\nu}_e$ cross section from the two angular regions $\cos\theta_{e^-} < 0.98$ and $\cos\theta_{e^-} > 0.98$.

As a function of $\Delta\kappa_\gamma$ the $e^+e^- \to q\overline{q}'e^-\overline{\nu}_e$ cross section in the phase space region $\cos\theta_{e^-} > 0.98$ has a behaviour completely different from all others cross sections. Whereas all other cross sections have a minimum for $\Delta\kappa_\gamma \approx 0.5$, the $e^+e^- \to q\overline{q}'e^-\overline{\nu}_e$ cross section for $\cos\theta_{e^-} > 0.98$ is minimal at $\Delta\kappa_\gamma = -1$, in correspondence of a zero of the amplitude of the *t*–channel $\gamma W^* \to W$ fusion diagram (diagram 12 in figure 3.1). In addition, the rate of variation of the $e^+e^- \to q\overline{q}'e^-\overline{\nu}_e$ cross section for $\cos\theta_{e^-} > 0.98$ for values of $\Delta\kappa_\gamma$ close to the $\mathcal{SM}$ is at least 15 times larger than for all other cross sections.

Similar conclusions can be drawn also for the dependence of the cross section on the λ_γ coupling, although in this case the minimum of all cross sections occurs always for $\lambda_\gamma = 0$. On the contrary when the dependence of the cross section on $\Delta\kappa_z$, λ_z and Δg_1^z is considered, it is found that the $e^+e^- \to q\overline{q}'e^-\overline{\nu}_e$ cross section in the $\cos\theta_{e^-} > 0.98$ phase space region has a small sensitivity, and that the dependence of the total cross section without phase space cuts is similar to that of the $e^+e^- \to q\overline{q}'\mu\overline{\nu}_\mu$ process. This is an expected result, since the contribution from the *t*-channel diagram sensitive to the $Z^0W^+W^-$ coupling (diagram 16 in figure 3.1) is negligible, as discussed in section 3.1. For the measurement of TGC's this reduced sensitivity to the $Z^0W^+W^-$ couplings is the largest advantage of the single W channel, as it allows to avoid the use of the $SU(2) \otimes U(1)$ relations in the analysis.

These cross section ratio curves allow to extract the sensitivity of the different processes to the anomalous couplings. For small values of the coupling parameters the quadratic term in the formula which gives the dependence of the cross section on TGC's can be neglected, obtaining $\sigma(x) = \sigma_{\rm SM}(1+\alpha x)$. Taking the derivative of this formula with respect to x and inverting it, the error on the coupling which can be achieved from a measurement of the cross section alone is found to be

$$\Delta x = 1/|\alpha|\sqrt{N},$$

where N is the number of events in the selected sample.

When this formula is applied to the cross section of the $e^+e^- \to q\overline{q}'e^-\overline{\nu}_e$ process in the phase space region $\cos\theta_{e^-} > 0.98$, it predicts that the error on $\Delta\kappa_\gamma$ scales approximately as $0.06\sqrt{500/\mathcal{L}}$, where $\mathcal{L}$ is the luminosity of the sample in pb^{-1}. For the total W pair production cross section this error scales instead as $0.14\sqrt{500/\mathcal{L}}$, but it improves by a factor 3 when informations from differential distributions are included in the fit for the anomalous couplings. As a result the two final states, W pair and single W, have a similar sensitivity to the $\Delta\kappa_\gamma$ coupling, and this constitutes the main reason for the measurement of the $e^+e^- \to q\overline{q}'e^-\overline{\nu}_e$ cross section in the phase space region dominated by single W production, despite the smallness of the cross section.

For λ_γ the quadratic term in the expression of the cross section cannot be neglected and is instead more important than the linear one. In this case the error on the coupling is found to scale as

$$\Delta x = 1/(\beta\sqrt{N})^{1/2}.$$

The expected error from the cross section measurement alone scales as $0.43(500/\mathcal{L})^{1/4}$ for

the $e^+e^- \to q\overline{q}'e^-\overline{\nu}_e$ process in the $\cos\theta_{e^-} > 0.98$ region. For the W pair production cross section the error scales instead as $0.14(500/\mathcal{L})^{1/4}$ and an additional reduction factor of 5 must be considered, to take into account the information from differential distributions. The analysis of single W production is therefore not competitive for the measurement of the λ_γ parameter.

The shape of the cross section as a function of the TGC's affects also the measurement error. If the measured cross section is smaller than the $\mathcal{SM}$ expectation the statistical errors will be in general smaller than the values predicted with these simple scaling laws, and the result will be slightly biased in the $\Delta\kappa_\gamma < 0$ direction. The opposite happens if the measured cross section is larger than the $\mathcal{SM}$ expectation.

The different shape of the cross section curves for $\Delta\kappa_\gamma$ and λ_γ has some consequences also for the limits on the anomalous couplings which can be obtained from the analysis of the $e^+e^- \to q\overline{q}'e^-\overline{\nu}_e$ process in the region dominated by single W production. As a function of $\Delta\kappa_\gamma$ the cross section is symmetric around $\Delta\kappa_\gamma = -1$, and it is smaller than the $\mathcal{SM}$ prediction in the range $-2 < \Delta\kappa_\gamma < 0$. As a function of λ_γ the cross section is instead at its minimum if the coupling assumes its $\mathcal{SM}$ value $\lambda_\gamma = 0$ and the cross section is symmetric around this value.

The consequence of the symmetry of the cross section curve is that there are always two possible solutions for the couplings, one at $\Delta\kappa_\gamma$ and a second one at $-(2+\Delta\kappa_\gamma)$. As a function of λ_γ there will be only one solution, $\lambda_\gamma = 0$ if, due to a statistical fluctuation, the measured cross section is smaller than the $\mathcal{SM}$ one, and two symmetric solutions $\pm|\lambda_\gamma|$ in the opposite case. In the next section it will be shown that these ambiguities can be resolved using the kinematic distributions of the final state products. Another possibility is to use the $e^+e^- \to W^+W^-$ reaction, which has a different functional dependence of the cross section on the TGC's.

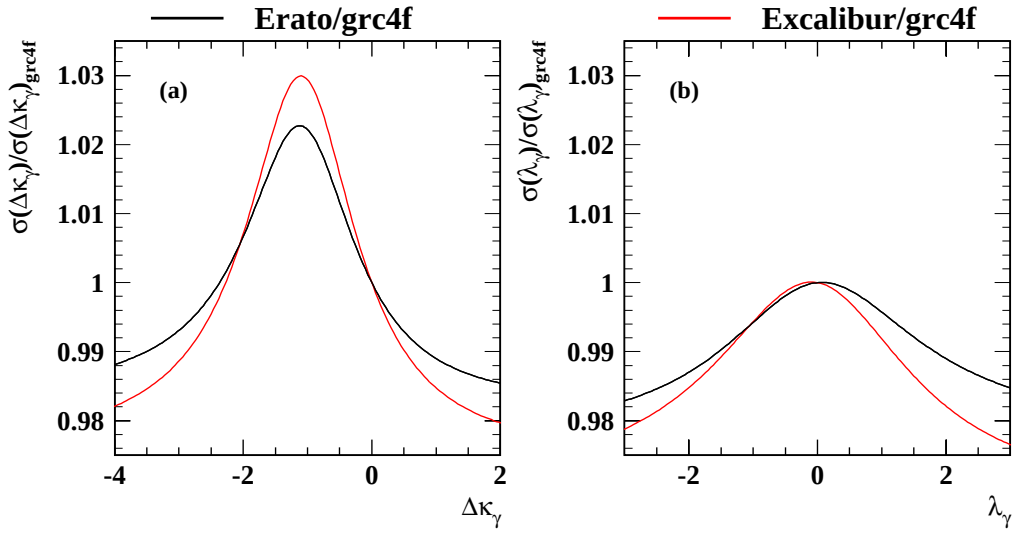

Figure 5.3: Ratio of the $q\overline{q}'e\overline{\nu}_e$ cross section dependence on the $\Delta\kappa_\gamma$ (*a*) and λ_γ (*b*) couplings in different Monte Carlo programs.

Eventual differences between different event generators in the TGC's dependence of the $e^+e^- \to q\overline{q}'e\overline{\nu}_e$ cross section have also been considered. Differences between generators can be as large as 6% in the absolute cross section (table 5.1), due to the different

treatment of W width and initial state radiation, and to the use of massive or massless matrix elements. Once the dependence on the anomalous couplings is taken into account, by dividing each cross section by the $\mathcal{SM}$ one, the agreement is better than 3% for all values of the couplings. As an example ratios of the dependence of the cross section for the $e^+e^- \to q\overline{q}'e^-\overline{\nu}_e$ process in the $\cos\theta_{e^-} > 0.98$ phase space region between different Monte Carlo programs are shown in figure 5.3 as a function of $\Delta\kappa_\gamma$ and λ_γ. Differences in the dependence of the cross section from the couplings are largest in the region $\Delta\kappa_\gamma \approx -1$, as in this case single W production is suppressed and the cross section becomes more sensitive to the detailed description of the multiperipheral process. These differences will be considered in chapter 9 as a possible source of systematic errors.

5.5 Use of differential distributions in the fit

As discussed in section 2.1, TGC's are best constrained in the $e^+e^- \to W^+W^-$ reaction by measuring the differential cross section and distinguishing different helicities of the produced W bosons. In practice this requires measuring the differential cross section with respect to the W production and decay angles. With the statistics collected by the LEP experiments the use of angular distributions improves by a factor larger than 3 the precision with which the coupling parameters are measured. This suggests to check whether also in the single W final state differential distributions can be used to improve the constraints on TGC's.

In the case of single W production there are no theoretical predictions for the cross section of different helicity states as a function of the W production angle which could be used to study the dependence of the kinematic of the $q\overline{q}'e\overline{\nu}_e$ final state from the anomalous couplings. In analogy with the $e^+e^- \to W^+W^-$ process it can be assumed that a measurement of the W helicity as a function of the W production angle yields improvements in the TGC's fit. One additional variable whose distribution may be affected by TGC's is the neutrino momentum, $\overrightarrow{p_\nu}$, which is a related to the helicity of the intermediate W boson in the $\gamma W^* \to W$ fusion process (diagram 12 in figure 3.1). Since the final state electron is not detected only the transverse component of $\overrightarrow{p_\nu}$ can be measured, assuming it coincides with the missing transverse momentum, $\not{p}_T$. It is not clear that these variables, the W production angle, the helicity of the final state W and the missing transverse momentum, retain the highest sensitivity to anomalous couplings.

It is therefore interesting to investigate the sensitivity of other variables, which experimentally might be measured more precisely. In the $q\overline{q}'e\overline{\nu}_e$ events with a kinematic compatible with that of single W production, there are at most three independent quantities which can be measured, assuming that the electron is not detected:

- the cosine of the polar angle of the sum of the two quarks momenta, $\cos\theta_{jj}$;
- the total momentum of the two quarks, $|p_{jj}|$;
- the angle between the up–type quark and the total momentum of the quark pair, calculated in the rest frame of the two quarks, $\cos\theta^*$.

The third of these variables is introduced to measure the W helicity, as in the case of W pair production. The second possible decay angle, ϕ^*, cannot be used in the single W production case, since for unpolarised beams the final state has a rotational symmetry in

the azimuthal angle. Since the TGC's introduce terms in the Lagrangian which are proportional to the momentum of the W boson, it is expected that in presence of anomalous couplings the differential cross section $d\sigma/d|p_{jj}|$ is enhanced for large values of $|p_{jj}|$. An enhancement of similar origin is predicted at large polar angles (small values of $|\cos\theta_{jj}|$) for the distribution of the direction of the W boson. These two variables can be combined into a single one, the transverse momentum of the jet pair, p_{jj}^{T}. An enhancement of the distribution of this quantity at large values of p_{jj}^{T} is expected in presence of anomalous couplings.

One problem with this set of three variables is that it assumes that up–type quarks can be distinguished form the down–type quark in the W decay, which in turns requires the measurement of jet charges in the final state. For quarks other than the *b* quark, the jet charge technique is almost totally insensitive to the sign of the quark charge, and therefore it should be assumed in the analysis that only the absolute values of $\cos\theta_{jj}$ and $\cos\theta^*$ are measurable in the $\mathrm{q\overline{q}'e\overline{\nu}_e}$ final state, for kinematic configurations compatible with single W production. In addition the reconstruction of $\cos\theta^*$ requires a Lorentz transformation, leading to a poor experimental resolution on this quantity. This suggests to replace $|\cos\theta^*|$ with other related quantities which are directly measured, like the polar angles of the two quarks, $\cos\theta_j$, provided the sensitivity to TGC's is not reduced. Also in the case of the polar angles of the jets only the absolute value of $\cos\theta_j$ can be used in the fit, since different quark charges cannot be measured experimentally. The use of $\cos\theta_j$ for the fit used to extract TGC's introduces a further complication, since each event contributes two values. For this reason also simple linear combinations of the angles of the two jets are considered.

From an experimental point of view the simplest method to include the differential distributions in the procedure to extract the anomalous couplings is that of a binned maximum likelihood fit. This allows to take into account all detector resolution and selection efficiency effects. In the case of two– and three–fold differential cross sections this method requires large Monte Carlo samples to parametrise the dependence of the accepted cross section on the anomalous couplings. This may prevent the use of multidimensional distributions in the TGC's fit and is the reason for searching the minimal set of variables which has the largest sensitivity to anomalous couplings. This would allow in turn to use one–dimensional fits or at most two–dimensional fits, without considerable losses of sensitivity.

This method of including the information from differential distributions in the fit for the anomalous couplings is the only feasible one for the single W kinematic region. The optimal observable method used for the measurement of TGC's in the $\mathrm{e^+e^-} \to \mathrm{W^+W^-}$ channel (section 2.2) cannot be applied to the single W case as it requires the availability of an analytical or numerical expression of the differential cross section with respect to the measured variables. The differential cross section for the $\mathrm{e^+e^-} \to \mathrm{q\overline{q}'e^-\overline{\nu}_e}$ reaction is available only in the form of FORTRAN codes (section 3.2), and only differentiated with respect to the momenta of all the final state fermions. To calculate for each event the optimal observable it would be necessary to perform an integration over the unmeasured variables, the electron and neutrino momenta. This procedure is unfeasible as it requires long computation times, even not considering detector resolution effects, which would necessitate an additional convolution of the differential cross section with a detector response function.

The distributions of the various kinematic quantities considered above for the inclusion in the TGC's fit are shown, for events in the single W kinematic region generated at $\sqrt{s} =$

200 GeV using the grc4f program, in figures 5.4 and 5.5 as a function of the $\Delta\kappa_\gamma$ and λ_γ parameters respectively, fixing the second coupling at its $\mathcal{SM}$ value, $\Delta g_1^z = 0$ and using for $\Delta\kappa_z$ and λ_z the SU(2) $\otimes$ U(1) relations of section 1.5. All distributions are normalised to the total cross section as a function of the coupling parameters, in order to be sensitive only to the shape of the differential cross sections.

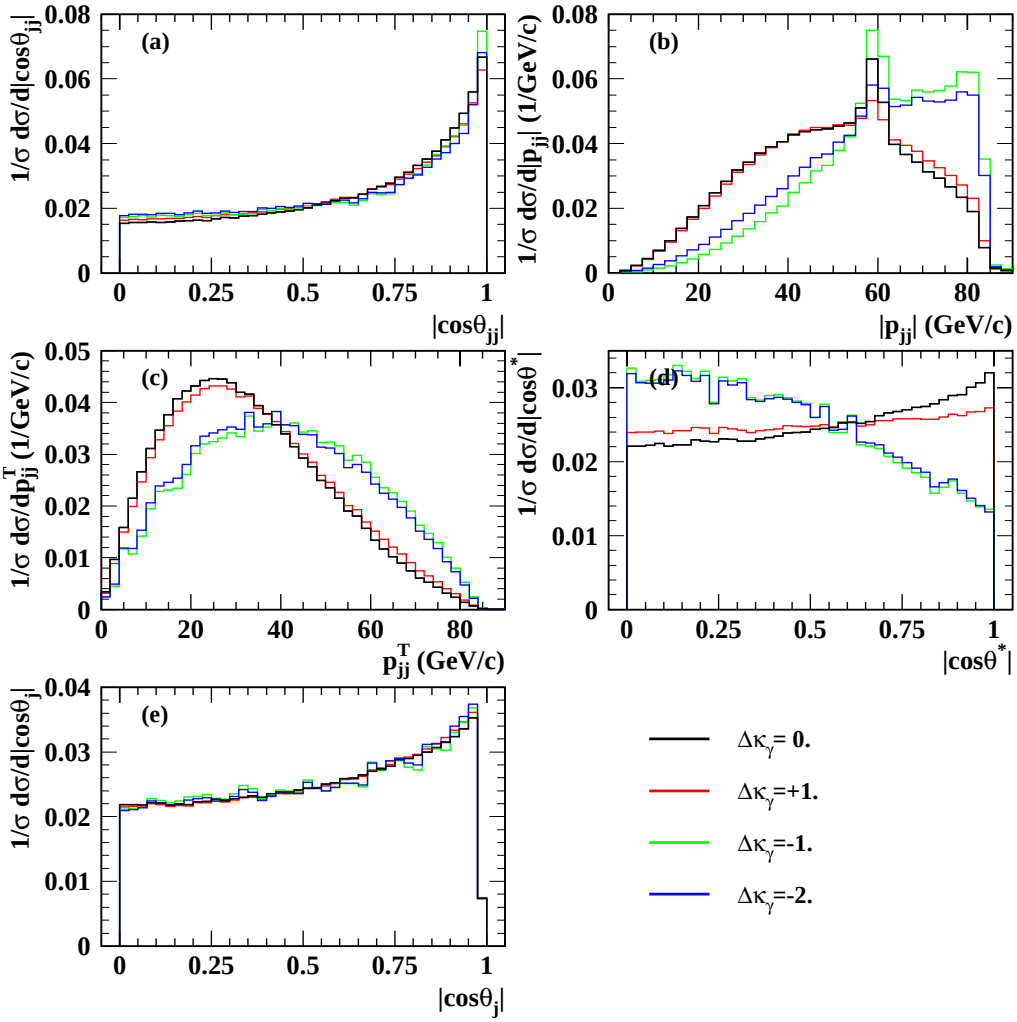

Figure 5.4: Dependence of the differential cross sections on the $\Delta\kappa_\gamma$ coupling: (*a*) shows the dependence from the angle of the jet pair, $|\cos\theta_{jj}|$, (*b*) and (*c*) from its total, $|p_{jj}|$, and transverse, p_{jj}^{T}, momentum. In (*d*) the decay angular distribution of quarks in the W rest frame, $|\cos\theta^*|$, is considered. The angular distribution of quarks, $|\cos\theta_j|$ (2 entries per event), is shown in (*e*).

These distributions show clearly that $|\cos\theta_{jj}|$ has a very small sensitivity to the $\Delta\kappa_\gamma$ and λ_γ couplings. The distribution of $|\cos\theta^*|$ is instead sensitive to the $\Delta\kappa_\gamma$ parameter, while that of $|\cos\theta_j|$ shows some discriminating power for positive values of the λ_γ coupling. The reduced sensitivity of these angular distributions to some or all the couplings is mostly due to the fact that quark charges cannot be accessed experimentally. This problem does not affect the measurement of $|p_{jj}|$ and of p_{jj}^{T} which show a much larger sensitivity to TGC's. This should allow a reduction of the measurement errors on $\Delta\kappa_\gamma$ (mostly for $\Delta\kappa_\gamma < 0$))

and on λ_γ.

To quantify these statements a study has been performed using a large set of Monte Carlo samples of $q\overline{q}'e\overline{\nu}_e$ events each corresponding to a total luminosity of 500 pb^{-1}. All samples have been generated at $\sqrt{s} = 200$ GeV using the grc4f program. Simple kinematic cuts are applied to emulate the acceptance of the analysis described in chapter 6, but a 100% selection efficiency, perfect detector resolution and absence of background are assumed. This study will be only indicative of the absolute precision which can be achieved for the measurement of the couplings using data. It is however more reliable for what concerns relative differences among different types of fits.

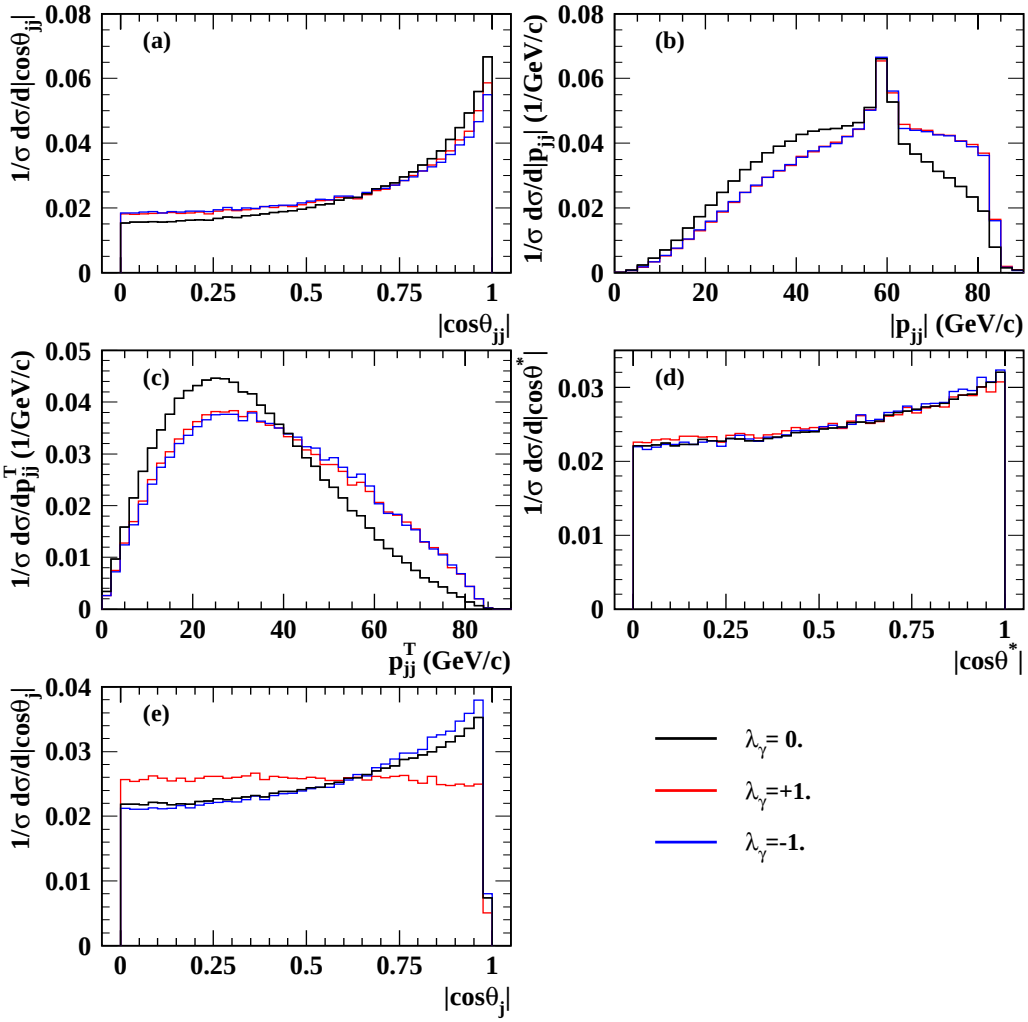

Figure 5.5: Dependence of the differential cross sections on the λ_γ coupling: (*a*) shows the dependence on the angle of the jet pair, $|\cos\theta_{jj}|$, (*b*) and (*c*) from its total, $|p_{jj}|$, and transverse, p_{jj}^{T}, momentum. In (*d*) the decay angular distribution of quarks in the W rest frame, $|\cos\theta^*|$, is considered. The angular distribution of quarks, $|\cos\theta_j|$ (2 entries per event), is shown in (*e*).

For each Monte Carlo sample several extended maximum likelihood fits are performed, using one–, two– and three–fold differential distributions, comparing the number of events observed in the various bins with predictions which are functions of $\Delta\kappa_\gamma$ and λ_γ. The like-

lihood curves obtained in each fit are then used to check that no biases are present in the procedures and that the error returned by the fit is correctly estimated. Eventual biases appear as deviations of the average fit results from the $\mathcal{SM}$ value, while the errors can be checked using pull distributions. The pull is the difference between the direct measurement and the expected value, normalised dividing by the estimated error of this difference. Under the usual assumption of Gaussian errors, pulls should exhibit a normal distribution. This method allows to compare the resolutions on $\Delta\kappa_\gamma$ and λ_γ expected for fits which use different kinematic informations. It also allows to assess how often the fit is affected by the presence of a second minimum.

Examples of the two–dimensional confidence level contours in the ($\Delta\kappa_\gamma$,λ_γ) plane obtained in one of these simulated experiments are shown in figure 5.6 (*a–i*) for 9 different fits. The fit which uses only the total cross section information (figure 5.6a) cannot distinguish among the solutions which lie approximately on the ellipse $(\Delta\kappa_\gamma + 1)^2 + {\lambda_\gamma}^2 \approx 1$. Therefore the allowed region at the 95% confidence level appears as a ring in the ($\Delta\kappa_\gamma$,λ_γ) plane. Projected on the $\Delta\kappa_\gamma$ axis it leads to two possible solution which occur with similar probability. This ambiguity is partially resolved when the kinematic information on the events is added to the fits. The effect of the inclusion of one of the various kinematic quantities in a one–dimensional binned likelihood fit is shown in figures 5.6b–f, for the same simulated experiment. The inclusion of either $|p_{jj}|$ or p_{jj}^{T} removes almost completely the above mentioned ambiguity on $\Delta\kappa_\gamma$, whereas the inclusion of angular informations yields smaller improvements. A similar improvement is also visible for the λ_γ parameter. The couplings can be further constrained using fits to two– and three–fold differential distributions, as shown in figures 5.6g–h.

The averages obtained from repeating this procedure for an ensemble of 2343 experiments are shown in table 5.2. If only the total cross section is used in the fit, there are always two $\Delta\kappa_\gamma$ regions which are allowed at the 95% confidence level. The inclusion of either $|p_{jj}|$ or p_{jj}^{T} resolves always the ambiguity between the two possible solutions $\Delta\kappa_\gamma = 0$ and $\Delta\kappa_\gamma \approx$ -2 and ensures that the correct $\mathcal{SM}$ minimum at $\Delta\kappa_\gamma = 0$ is chosen. The shape of the likelihood curve is such that there is always only one region allowed at the 95% confidence level. Of all the possible angular variables only $|\cos\theta^*|$ can be used to resolve the ambiguity in $\Delta\kappa_\gamma$, although less efficiently than the two momentum variables. If the λ_γ parameter is considered instead of $\Delta\kappa_\gamma$, it is found that the distribution of the difference between the polar angles of the two quarks, $|\cos\theta_{j_1} - \cos\theta_{j_2}|$, induces the largest reduction in the expected measurement error.

Assuming that the statistics of the Monte Carlo sample, which is used for the parametrisation of the differential cross section as a function of the couplings, allows only the use of a single differential cross section, the best suited variable is the transverse momentum of the jet pair, p_{jj}^{T}. For the λ_γ coupling this corresponds to a reduction of 28% in the expected error and of 18% in the allowed region at the 95% confidence level. Larger improvements can be achieved with fits which use two– and three–fold differential distributions. The largest improvement is found when a two dimensional binning in p_{jj}^{T} and $|\cos\theta_{j_1} - \cos\theta_{j_2}|$ is used, while adding a third variable, like $|\cos\theta^*|$, gives only another modest improvement.

Comparing the expected errors from the fit to the two–dimensional differential distribution with those expected from a fit to the total cross section only it is found that the expected error on λ_γ is reduced by a factor 1.8, while the region allowed at the 95% confidence level is reduced by a factor 1.5. For $\Delta\kappa_\gamma$ there is no improvement in the expected

error nor in the allowed region at the 95% confidence level. The only effect of the inclusion of the kinematic information in the TGC's fit is the removal of the ambiguity in $\Delta\kappa_\gamma$.

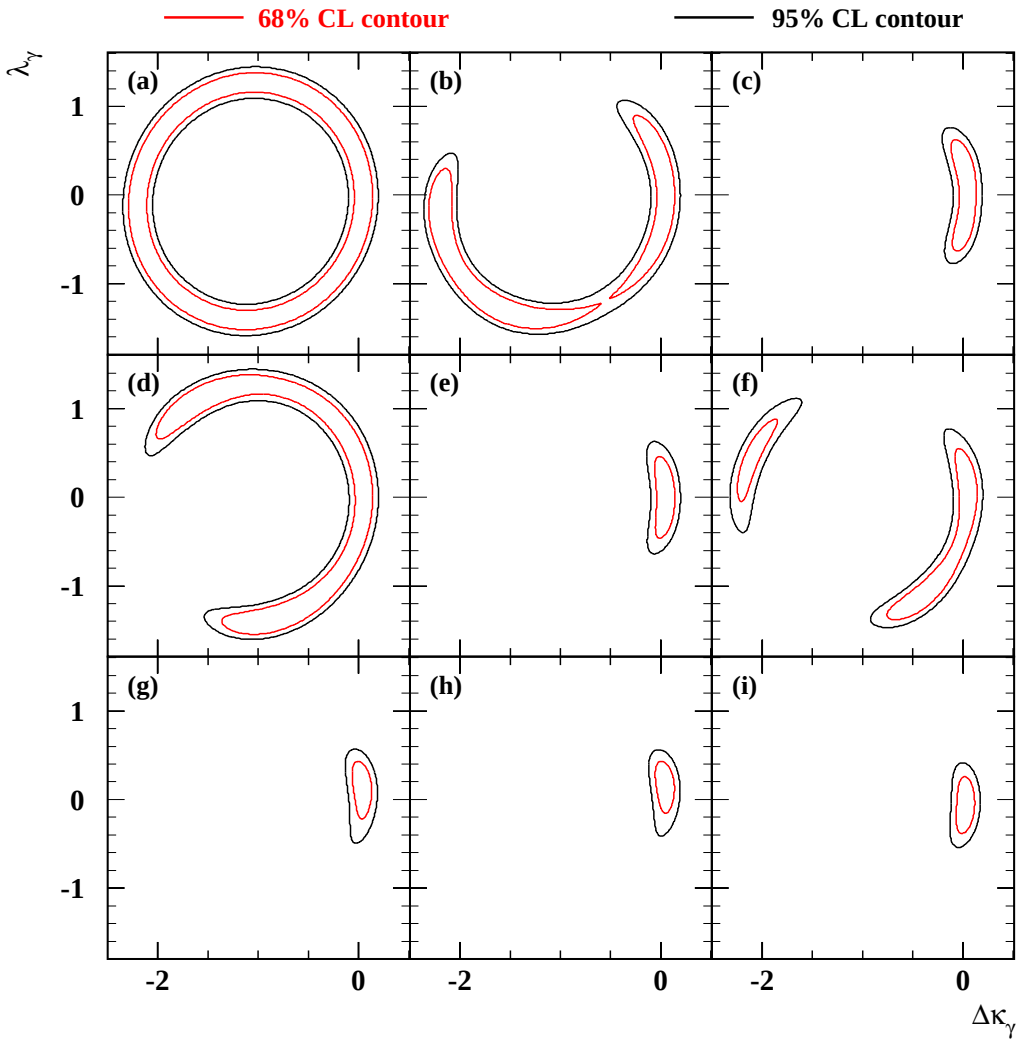

Figure 5.6: 68% (red curves) and 95% (black curves) confidence level contours on the $\Delta\kappa_\gamma$ and λ_γ parameters obtained from one simulated experiment using different fits for the TGC's. In (*a*) only the total cross section informations is used. In (*b–h*) different one, two and three dimensional differential distributions are used, as explained in table 5.2. In (*i*) a three dimensional distribution is used in the fit for the anomalous couplings assuming that different quark charges can be identified perfectly.

This lack of improvement in the $\Delta\kappa_\gamma$ measurement when differential distributions are used in the TGC's fit is investigated performing additional fits, under the assumption that quarks can be distinguished from antiquarks with 100% efficiency (figure 5.6i). This allows to use unfolded angular distributions, extracting all the information which is available in the events. Using a fit to the three–fold differential cross section only a tiny improvement, 2%, in the expected $\Delta\kappa_\gamma$ error is found, whereas for λ_γ the improvement is 15%. The reason for this different dependence on the couplings can be traced back to the form of the Lagrangian describing the triple gauge boson vertex, discussed in section 1.4. The term in κ_γ involves the fields of the W bosons and the derivative of the photon field. Therefore the

Differential distribution used in the fit	Fraction (%) of simulated experiments with					$\sigma_{\Delta\kappa_\gamma}$	σ_{λ_γ}	Allowed region at 95% confidence level (CL) in	
	$2\,\Delta\kappa_\gamma$ minima	$2\,\lambda_\gamma$ minima	$2\,\Delta\kappa_\gamma$ regions	$2\,\lambda_\gamma$ regions	wrong $\Delta\kappa_\gamma$ minimum			$\Delta\kappa_\gamma$	λ_γ
Cross section only (*a*)	100.0	51.9	100.0	2.5	48.6	0.063	0.470	$[-0.117, 0.119]$	$[-0.632, 0.606]$
Fits to one–dimensional differential cross sections									
$\lvert\cos\theta_{jj}\rvert$ (*b*)	87.5	40.8	87.5	3.0	28.8	0.061	0.420	$[-0.117, 0.119]$	$[-0.605, 0.583]$
$\lvert p_{jj}\rvert$ (*c*)	0.0	46.1	0.0	2.3	0.0	0.061	0.369	$[-0.117, 0.119]$	$[-0.552, 0.523]$
$\lvert\cos\theta^*\rvert$ (*d*)	0.8	41.7	0.8	2.3	0.3	0.061	0.425	$[-0.117, 0.119]$	$[-0.634, 0.598]$
p_{jj}^{T} (*e*)	0.1	41.9	0.1	2.7	0.0	0.061	0.341	$[-0.117, 0.119]$	$[-0.509, 0.510]$
$\lvert\cos\theta_{j_1} - \cos\theta_{j_2}\rvert$ (*f*)	29.5	7.4	29.5	1.0	10.6	0.061	0.352	$[-0.117, 0.119]$	$[-0.561, 0.449]$
$\lvert\cos\theta_{j_1} + \cos\theta_{j_2}\rvert$	2.9	30.5	2.9	3.7	0.8	0.061	0.425	$[-0.117, 0.119]$	$[-0.632, 0.576]$
$\lvert\cos\theta_{j_{1,2}}$	100.0	19.2	100.0	2.0	40.8	0.061	0.377	$[-0.117, 0.119]$	$[-0.618, 0.520]$
Fits to two–dimensional differential cross sections									
p_{jj}^{T}, $\lvert\cos\theta_{j_1} - \cos\theta_{j_2}\rvert$ (*g*)	0.0	3.4	0.0	0.5	0.0	0.061	0.261	$[-0.117, 0.119]$	$[-0.417, 0.371]$
$\lvert\cos\theta_{jj}\rvert$, $\lvert p_{jj}\rvert$	0.0	37.4	0.0	2.9	0.0	0.061	0.331	$[-0.117, 0.119]$	$[-0.491, 0.498]$
$\lvert\cos\theta_{jj}\rvert$, $\lvert\cos\theta^*\rvert$	0.4	33.9	0.4	3.7	0.1	0.061	0.411	$[-0.117, 0.119]$	$[-0.604, 0.564]$
$\lvert p_{jj}\rvert$, $\lvert\cos\theta^*\rvert$	0.0	40.8	0.0	2.8	0.0	0.061	0.355	$[-0.117, 0.119]$	$[-0.547, 0.516]$
p_{jj}^{T}, $\lvert\cos\theta_{j_{1,2}}$	0.0	12.1	0.0	1.3	0.0	0.061	0.377	$[-0.117, 0.119]$	$[-0.474, 0.437]$
p_{jj}^{T}, $\lvert\cos\theta_{j_1} + \cos\theta_{j_2}\rvert$	0.0	31.9	0.0	3.5	0.0	0.061	0.332	$[-0.117, 0.119]$	$[-0.505, 0.478]$
Fits to three–dimensional differential cross sections									
p_{jj}^{T}, $\lvert\cos\theta_{j_1} - \cos\theta_{j_2}\rvert$, $\lvert\cos\theta^*\rvert$ (*h*)	0.0	2.3	0.0	0.1	0.0	0.061	0.245	$[-0.117, 0.119]$	$[-0.406, 0.355]$
p_{jj}^{T}, $\lvert\cos\theta_{j_1}\rvert$, $\lvert\cos\theta_{j_2}\rvert$	0.0	3.5	0.0	0.4	0.0	0.061	0.259	$[-0.117, 0.119]$	$[-0.421, 0.377]$
$\lvert\cos\theta_{jj}\rvert$, $\lvert p_{jj}\rvert$, $\lvert\cos\theta^*\rvert$	0.0	32.0	0.0	3.6	0.0	0.061	0.326	$[-0.117, 0.119]$	$[-0.492, 0.478]$
p_{jj}^{T}, $\lvert\cos\theta_{j_{1,2}}$, $\lvert\cos\theta^*\rvert$	0.0	9.8	0.0	1.0	0.0	0.061	0.270	$[-0.117, 0.119]$	$[-0.462, 0.424]$
Fits to two–dimensional differential cross sections including quark charge information									
p_{jj}^{T}, $\cos\theta_{j_1} - \cos\theta_{j_2}$, $\cos\theta^*$ (*i*)	0.0	1.3	0.0	0.1	0.0	0.059	0.210	$[-0.114, 0.115]$	$[-0.349, 0.326]$
$\cos\theta_{jj}$, $\lvert p_{jj}\rvert$, $\cos\theta^*$	0.0	18.9	0.0	2.7	0.0	0.060	0.223	$[-0.116, 0.117]$	$[-0.388, 0.366]$

Table 5.2: Results obtained with different fitting procedures on an ensemble of Monte Carlo experiments. In some cases the correspondence with figure 5.6 is indicated. For each fit the fraction of experiments in which two minima or two allowed regions at the 95% CL are found in the likelihood curves for $\Delta\kappa_\gamma$ and λ_γ are given. For $\Delta\kappa_\gamma$ the probability of choosing the minimum at $\Delta\kappa_\gamma \approx -2$ is also shown. Also included are the average expected error on $\Delta\kappa_\gamma$ and λ_γ and the average boundaries of the regions allowed at the 95% CL.

anomalous term is proportional to the momentum of the virtual photon, which is usually small in the single W kinematic region. The term of the Lagrangian which is sensitive to λ_γ contains also the derivative of the W boson field, and therefore is proportional to the W momentum, which is usually larger than the photon momentum. This explains the different behaviour of the two couplings in the TGC's fit when also kinematic informations are used.

In summary, differential distributions can be used in the fit for the anomalous couplings, mainly for removing ambiguities in the $\Delta\kappa_\gamma$ parameter. For this purpose the best suited variable to be used in the fit is the total transverse momentum of the jet pair. If the available Monte Carlo statistics is sufficient further improvements can be obtained in the expected λ_γ error by fitting the two–fold differential distribution in p_{jj}^{T} and $|\cos\theta_{j_1} - \cos\theta_{j_2}|$. It is also found that only limited improvements can be obtained even assuming that quark can be distinguished from antiquarks with 100% efficiency. Considering that experimentally the purity obtained using the jet charge method is only slightly larger than 50%, this small possible improvement disfavours any complex fit procedure requiring jet charge tagging of the jets.

6 Event selection

This chapter contains the description of the procedure adopted to isolate a sample of $q\overline{q}'e\overline{\nu}_e$ events in the kinematic region dominated by single W production, which is then used in chapter 8 for the measurement of the *t*-channel cross section and in chapter 9 for the extraction of the triple gauge couplings. The data and Monte Carlo samples used in the analysis are briefly summarised in section 6.1. The strategy used for optimising the event selection for the two goals of the analysis is described in section 6.2. To improve the purity of the selected sample a two stage procedure is adopted. Events clearly inconsistent with an hadronic final state with missing energy are first removed with the preselection described in section 6.3. The remaining events are then classified as signal or background using a relative likelihood selection based on kinematical variables and discussed in section 6.4. Section 6.5 contains a description of the changes in the selection procedure which were necessary for the analysis of the 1998 data. In this chapter only statistical uncertainties on the Monte Carlo predictions are considered. Systematic uncertainties are estimated in chapter 7.

6.1 Data and Monte Carlo samples.

The analysis uses a sample of (251.01 ± 0.65) pb^{-1} total integrated luminosity collected at e^+e^- centre–of–mass energies between 161 and 189 GeV. The integrated luminosities recorded at each energy point are given in table 4.4.

Details concerning the simulation of the $e^+e^- \to q\overline{q}'e^-\overline{\nu}_e$ signal in the kinematic region dominated by the single W process have been discussed in section 5.1. Hadronisation of the final state is performed using the JETSET program [77], with parameters tuned using data collected at the Z^0 peak [115]. To assess uncertainties related to the hadronisation process, the same four–fermion events are also hadronised using the HERWIG program [116].

Backgrounds from processes with four fermions in the final state are evaluated using KORALW [74], except for the $e^+e^-f\overline{f}$ final states which are simulated using grc4f [73]. KORALW cannot be used for the $e^+e^-f\overline{f}$ final states, since it cannot simulate correctly the portion of the phase space dominated by Z^0e^+e- production. grc4f and EXCALIBUR [75] are used to check the predictions of the KORALW MC. Although internally KORALW uses the same matrix element calculator of grc4f, it is used as a reference sample for backgrounds since it provides a better treatment of initial state radiation and it includes polarisation effects in τ decays. Hadronic events produced through the $e^+e^- \to q\overline{q}(\gamma)$ process are simulated using the $\mathcal{KK}$ program [117], PYTHIA [77] and HERWIG. The $\mathcal{KK}$ program uses internally the same hadronisation routines of PYTHIA, and is preferred to the latter program since it provides a better treatment of initial and final state radiation. Back-

grounds from two–photon processes are evaluated using HERWIG for events in which one of the photons has a large momentum transfer Q^2 and using PHOJET [118] for events in which both photons have a small Q^2. The separation of the two categories is given by $Q^2 = 5\,\mathrm{GeV}^2/c^2$. In the first of these kinematic regions PYTHIA and TWOGEN [119] are used to generate additional Monte Carlo samples using different theoretical models and photon structure functions. PYTHIA is also used for generating control samples in the small Q^2 region. Double counting of the $e^+e^-f\bar{f}$ final state between four–fermion and two–photon samples is avoided by separating contributions from different classes of diagrams.

At least two independent Monte Carlo estimates are available for each category of background, with the exception of $e^+e^-f\bar{f}$ final states produced through four–fermion processes. Most Monte Carlo samples used to estimate the composition of the selected samples correspond to integrated luminosities larger than those of the data by at least a factor 50. The statistical error on the background estimates thus obtained is therefore much smaller than the statistical error of the data. An exception is represented by the Monte Carlo samples used to simulate two–photon processes, which due to the large cross section ($\mathcal{O}(\mathrm{nb})$ for the kinematical cuts applied) have a statistics corresponding to an integrated luminosity similar to that of the data collected in 1998.

6.2 Analysis strategy

As discussed in Chapter 5 the $q\bar{q}'e\bar{\nu}_e$ final state in the kinematic region dominated by the single W diagrams is characterised by two non–collinear jets coming from the hadronic decay of the W boson recoiling against the neutrino in the transverse plane. Only about half of the centre–of–mass energy is visible in these events since in addition to the neutrino also the electron leaves the detector undetected along the beam pipe. The largest reducible background to this type of signature is constituted by $W^+W^- \to q\bar{q}'\ell\bar{\nu}_\ell$ decays where the lepton is not identified or poorly measured. This background introduces an additional dependence of the accepted events on the anomalous couplings. The $q\bar{q}\nu\bar{\nu}$ final state gives an almost irreducible background, due to the limited mass resolution of the detector. This background is however smaller than the $W^+W^- \to q\bar{q}'\ell\bar{\nu}_\ell$ decays and independent from the anomalous couplings considered in the analysis. The background from hadronic events produced in the $e^+e^- \to q\bar{q}(\gamma)$ and $\gamma\gamma \to q\bar{q}$ reactions is easily reduced with cuts on the missing transverse momentum, on the collinearity of the jet pair and on the visible mass. Four quarks final states from the decay of pairs of weak bosons in the $e^+e^- \to W^+W^-$ and $e^+e^- \to Z^0Z^0$ reactions are suppressed from cuts on the total visible energy of the event. Purely leptonic final states are rejected with high efficiency by cuts on the multiplicity of charged tracks and clusters in the calorimeter.

The event selection procedure presented in the next sections is aimed at the measurement of the *t*–channel production cross section of the $q\bar{q}'e\bar{\nu}_e$ final state and at the measurement of the coupling parameters $\Delta\kappa_\gamma$ and λ_γ using a sample of four–fermion events enriched in the single W kinematic region. These two goals are achieved using a common preselection, aimed at rejecting the events which are clearly inconsistent with an hadronic final state with missing energy, followed by two similar likelihood selections based on kinematic variables and used to classify the events as signal or background.

Both selections are optimised with the aim of reducing the statistical error of the measurement to be performed. This assumes that any systematic contribution to the errors can

be controlled to be much smaller than the statistical component. This hypothesis is well verified (chapter 7), also for the smallness of the cross–section of the process under study and the limited luminosity available at LEP2.

To minimise the statistical error of the cross section measurement, the event selection is tuned to maximise a quality factor defined as the product of the signal efficiency ε and purity $\mathcal{P}$. This maximisation is performed studying the quality factor as a function of the values of the cuts used in the preselection and of the cut on the event likelihood used to classify the events as signal and background.

If the background from $W^+W^- \to q\overline{q}'\ell\overline{\nu}_\ell$ decays could be reduced to a negligible level, the same principle of maximising the product of signal efficiency and purity could be applied also to the event selection used for the TGC's measurement. The fact that the $W^+W^- \to q\overline{q}'\ell\overline{\nu}_\ell$ background has a different functional dependence on the anomalous couplings (section 5.4) and cannot be completely eliminated prevents the use of this criterion for the optimisation of the event selection. The optimisation is instead carried out minimising the expected measurement error of the $\Delta\kappa_\gamma$ coupling, taking into account the dependence of all the selected events on the TGC's, independently from the production process (single W or W pair). This strategy has the advantage that there is no need to separate the $q\overline{q}'e\overline{\nu}_e$ final state into a single W signal component and a $W^+W^- \to q\overline{q}'e\overline{\nu}_e$ background component.

During the optimisation of the event selection aimed at the measurement of the couplings, only the total cross section information is used in the TGC's fit, although also kinematical informations from the selected events are used to obtain the final result presented in chapter 9. This simplification does not represent a limitation of the optimisation procedure since the error on $\Delta\kappa_\gamma$ does not improve when differential distributions of kinematical observables of the $q\overline{q}'e\overline{\nu}_e$ final state are included in the fit for the anomalous couplings, as shown in section 5.5. The additional informations given by differential distributions remove only the twofold ambiguity present in the dependence of the total cross section on the TGC's.

The effect of all quantities used in the event selection procedure on the expected error on the $\Delta\kappa_\gamma$ parameter has been calculated in the following way:

- Any cut making use of the quantity under study is varied if the quantity is used in one of the preselection cuts. If the quantity is one of the variables which enters in the calculation of the final event likelihood, a different likelihood is calculated, which does not involve this variable. If the quantity studied is the final event likelihood, the final selection cut is varied.

- These changes give a new event selection, to which corresponds a different functional dependence of the total expected number of events on the anomalous couplings. This function is calculated using fully simulated Monte Carlo samples generated with different values of the couplings and applying the reweighting techniques of appendix A.

- The expected statistical uncertainty of the analysis for the new set of selection cuts is computed by performing many times the maximum likelihood fit to the number of observed events using samples of signal and background Monte Carlo events with an integrated luminosity corresponding to that of the OPAL data. For all components of each selected subsample, the number of events are randomly selected from

Poisson distributions with a mean equal to the expected number of events.

- For each simulated experiment the fitted values of $\Delta\kappa_\gamma$ and λ_γ, their errors and the 95% CL limits on the couplings are obtained from the log–likelihood curve, as it is done for the data. The distribution of these quantities, obtained repeating this procedure many times, are used to predict the expected statistical errors and 95% CL limits on $\Delta\kappa_\gamma$ and λ_γ. For each new event selection 3000 experiments are simulated with this procedure, implying that the relative uncertainty on the predicted errors and 95% CL limits is of 2%.

It is found that the optimisation procedures for the cross section and the couplings measurements give similar result for what concerns the preselection part of the analysis, which for simplicity is kept unique. Only the final cuts on the two event likelihoods are optimised separately for the two measurements.

For the measurement of the anomalous couplings the expected error on the $\Delta\kappa_\gamma$ parameter remains constant over a large range of cuts on the final event likelihood. This is the result of the different sensitivity of the $q\overline{q}'e\overline{\nu}_e$ final state to the $\Delta\kappa_\gamma$ coupling, with respect to the $q\overline{q}'\mu\overline{\nu}_\mu$ and $q\overline{q}'\tau\overline{\nu}_\tau$ final states, which has already been discussed in section 5.4. When the selected events are dominated by the two latter processes the coefficients of the functional dependence of the accepted cross section on the $\Delta\kappa_\gamma$ coupling are reduced in absolute value and the minimum of the accepted cross section moves towards positive values of $\Delta\kappa_\gamma$. As a consequence the expected error on $\Delta\kappa_\gamma$ increases. Conversely if the contribution of the $q\overline{q}'e\overline{\nu}_e$ final state dominates, the coefficient of the quadratic term increases in magnitude and the minimum of the accepted cross section moves towards the value of $\Delta\kappa_\gamma = -1$.

The relative contribution of the WW and single W processes to the selected sample can be varied with the cut on the final likelihood used for the measurement of TGC's. A purer $q\overline{q}'e\overline{\nu}_e$ sample in which the electron is scattered predominantly in the forward direction can be selected tightening the cut on the likelihood, at the cost of an efficiency reduction. The higher signal purity does not however directly correspond to an improvement of the expected error on the $\Delta\kappa_\gamma$ parameter, since the increase in the statistical error may compensate the enhanced sensitivity to the anomalous couplings. On the other side, an increased efficiency can only be obtained decreasing the purity of the selected sample. In this case the reduction of the statistical error of the coupling measurement is compensated by a smaller sensitivity to the TGC's. As a result of these two competing effects the expected error on the $\Delta\kappa_\gamma$ parameter does not vary as the cut on the final event likelihood is varied over a large range, even for relative variations of 20% of the selection efficiency, corresponding to an absolute change of 5% in the signal purity.

The following sections contain a description of the preselection procedure common to the *t*–channel cross section measurement and to the measurement of TGC's, followed by a description of the final likelihood selection used for the extraction of the couplings. The event likelihood used for the cross section measurement is instead described in chapter 8. The contribution to the selected sample from four–fermion events is divided in two classes for illustrative purposes only:

- The $q\overline{q}'e\overline{\nu}_e$ events in which the electron is scattered in the forward direction at $\cos\theta_e > 0.98$ are representative of the phase space region dominated by single W production and considered as signal. For these events the distribution of all quantities

considered in the analysis is represented by hatched histograms in figures 6.1–6.13. The expected number of events from this process are given in the "We$\overline{\nu}_e$" column in the summary tables 6.1 and 6.2.

- The remaining $q\overline{q}'e\overline{\nu}_e$ events and all other four–fermion final states are considered as background. In all distributions their contribution is added to that of other processes, $e^+e^- \to f\overline{f}$ and $\gamma\gamma \to q\overline{q}$, and represented by white histograms. In the summary tables the total contribution from these processes to the number of selected events is given in the "Σ_{BG}" column.

In all plots the solid line indicates the total Monte Carlo expectation, while data are shown with error bars.

6.3 Preselection

Multihadronic events are selected requiring at least 6 good reconstructed tracks, adopting the quality criteria described in section 4.1. This cut has a twofold purpose: it removes almost completely fully leptonic final states and reduces beam related backgrounds. As discussed in section 4.10 these events are characterised by a large number of tracks which are reconstructed with large impact parameters to the nominal interaction point and small number of measured points, failing therefore the track quality criteria. Further rejection of beam induced backgrounds is achieved by requiring that the ratio between the number of tracks satisfying the quality criteria and the total number of tracks is larger than 0.2. In addition the reconstructed vertex of the event is required to be within ± 1 mm in the transverse plane from the measured position of the interaction point. These loose criteria remove only $\sim$ 3% of the $q\overline{q}'e\overline{\nu}_e$ final states with an electron emitted in the forward direction at $\cos\theta_e > 0.98$. These are mainly events where at least one of the two jets is emitted at small polar angles and therefore not properly detected. These events would be anyhow removed at a later stage of the selection since the kinematic quantities used in the likelihood selection are poorly measured. Hadronic events produced in $\gamma\gamma$ collisions are largely rejected by these quality cuts as their hadronic activity prefers low multiplicities and small polar angles.

Tracks and calorimeter clusters are assigned to two jets using the Durham [111] recombination scheme. Only events which satisfy the cut $y_{23} < 0.2$ are further considered in the analysis, y_{23} being the value of the jet resolution parameter at which the event classification changes from 3 to 2 jets. As discussed in section 4.7 measured jet energies are corrected for double counting using the algorithm described in [107]. The corrected jet energies are then used to compute the missing momentum vector. Each jet is required to contain at least two good tracks, to ensure that it is of hadronic origin (jets may be even constituted by a single lepton track). To remove hadronic events produced in $\gamma\gamma$ collisions the ratio R_{ecal} of the total energy measured in the electromagnetic calorimeter and the centre–of–mass energy $\sqrt{s}$ is required to be larger than 0.115 and the invariant mass of the jet pair m_{jj} to be larger than 40 GeV/c^2. In addition R_{ecal} is required to be smaller than 0.5 to reject hadronic events without missing energy. The distribution of R_{ecal} measured in the data collected at $\sqrt{s}$=161–183 GeV is compared with the Monte Carlo prediction in figure 6.1. The excess of events at small values of R_{ecal} in the Monte Carlo is due to $\gamma\gamma \to q\overline{q}$ events and is a feature of the event generator used (PHOJET), whereas another model for this process (PYTHIA)

predicts an event rate smaller than that observed in the data. This discrepancy between data and Monte Carlo is largely reduced by the R_{ecal} cut.

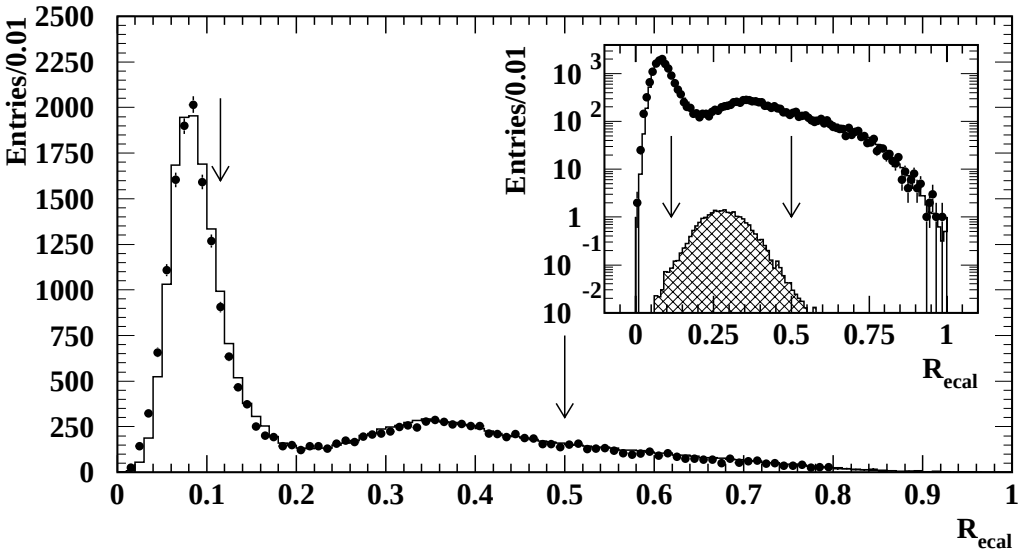

Figure 6.1: Ratio between the total energy measured in the electromagnetic calorimeter and the centre–of–mass energy. The inset shows the same distribution in logarithmic scale. Cut values are indicated by arrows in both plots.

This first step of the preselection has an efficiency of $\sim$ 90% for the $e^+e^- \to q\overline{q}'e^-\overline{\nu}_e$ events where the electron is emitted at $\cos\theta_e > 0.98$, corresponding to 23 events in the data collected at $\sqrt{s}$=161–183 GeV. At this stage of the selection 6645 events are observed in the data, for a Monte Carlo prediction of (7261 ± 28). The predicted composition of the selected sample is given in table 6.1 at page 87 (cut P1).

In $e^+e^- \to q\overline{q}'e^-\overline{\nu}_e$ events produced in the single W reaction the intermediate photon has usually a low four-momentum transfer Q^2 and therefore the electron in the final state is emitted at small polar angles, escaping detection. In principle events could be rejected if there are energy deposits in SW and FD larger than a threshold of few GeV. This tight cut is not applied in the analysis to avoid efficiency losses due to machine backgrounds (section 4.10) and to reduce the sensitivity to the modelling of ISR in the single production. Loose cuts on the energy deposits in SW and FD are instead applied to reduce the background from radiative Z^0 production in the $e^+e^- \to q\overline{q}(\gamma)$ final state. Pair production of *b* quarks in this process represents a potentially dangerous background. The leptonic decays of *b* can be a source of missing transverse momentum, leading at the same time to a reduction of the invariant mass of the jet pair. This could fake the signature of those single W events in which the electron is measured in the forward calorimeters. The energy deposit in the forward calorimeters is however different for the two classes of events. In the case of single W production the electron has a continuous energy spectrum up to 60 GeV, whereas the ISR photon emitted in production of the Z^0 resonance is almost monochromatic. Assuming two body decay kinematics the energy E_γ of this photon is given by:

$$E_\gamma = \frac{s - m_Z^2}{2\sqrt{s}}.$$

Only events with energy deposits smaller than that of the radiative photon peak diminished by twice its standard deviations are further considered in the analysis (cut P2).

The sample of events considered here overlaps with that used for the measurement of the total and differential cross sections of the $e^+e^- \to W^+W^-$ reaction. To avoid double counting of events when setting limits on the TGC's, the events selected in the $W^+W^- \to q\overline{q}'\ell\overline{\nu}_\ell$ and $W^+W^- \to q\overline{q}'q\overline{q}'$ channels using the criteria described in [41] are removed from the sample. Some $W^+W^- \to q\overline{q}'\ell\overline{\nu}_\ell$ may pass the W pair veto either because the lepton is not identified or not isolated or if the lepton momentum is misreconstructed and falls outside the range permitted in W decays. A veto is therefore applied to events with identified leptons. Electrons and muons with energy above 2 GeV are identified using the criteria described in section 4.6. In addition muons are identified using only their energy deposits in the calorimeters and applying tight isolation cuts (less than 5 GeV deposited in a cone of 500 mrad opening angle centered on the lepton) in the region of large polar angles where the tracking efficiency decreases. Events are vetoed if the lepton candidate is isolated and has a high transverse momentum relative to the axis of the nearest jet. The cuts vary as a function of the angle between the lepton and the nearest jet, of the energy and polar angle of the lepton candidate (cut P3).

After these cuts 5404 events remain in the data, for a total Monte Carlo expectation of (5912 ± 25) events. The discrepancy between the Monte Carlo prediction and the data is due mainly to the events in the low two jet invariant mass region ($m_{jj} < 60$ GeV/c^2), where $\gamma\gamma \to q\overline{q}$ collisions dominate the sample. At higher invariant masses ($m_{jj} > 60$ GeV/c^2) the sample is dominated by hadronic events produced through the $e^+e^- \to q\overline{q}(\gamma)$ process. As shown in figure 6.2, both processes are characterised by jets which are dominantly

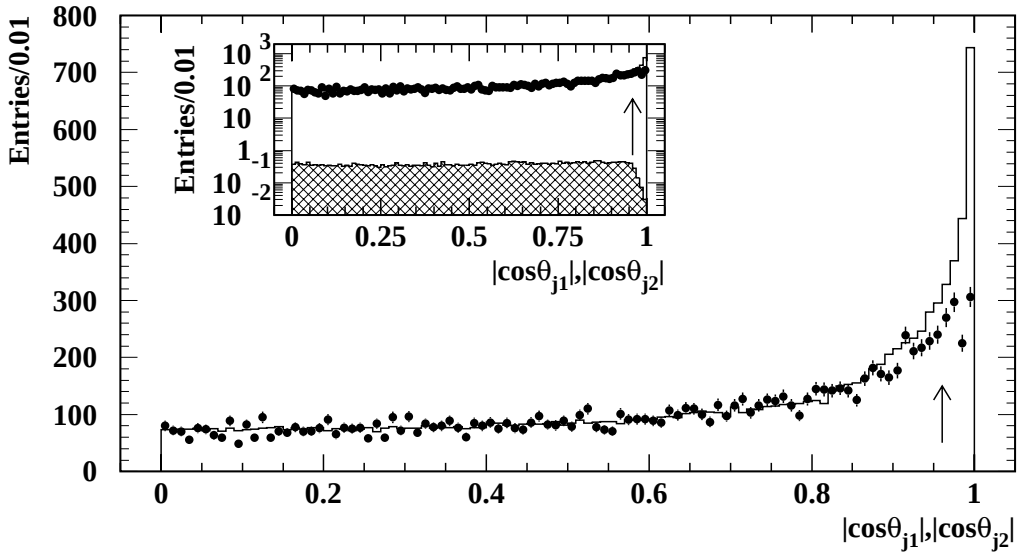

Figure 6.2: Distributions of the cosine of the polar angles of the jets. The inset shows the same distribution in logarithmic scale. The cut value is indicated by arrows.

produced in the forward direction. Given the limited detector acceptance in this region the energy flow in these events cannot be correctly measured. The events in which the reconstructed polar angle of the jets is close to the beam direction are rejected in order to ensure a correct measurement of the missing momentum. Events are rejected if any of the

two jets has a reconstructed polar angle θ_j with $|\cos\theta_j| > 0.96$ (cut P4). This cut improves considerably the quality of the data description provided by the Monte Carlo, causing a large reduction of the background from hadronic events produced in $\gamma\gamma$ collisions.

The sample of events passing this cut on the direction of the jets is dominated by hadronic hadronic events produced in the $e^+e^- \to q\overline{q}(\gamma)$ reaction. Due to the previous cut on R_{ecal} these events are characterised by invariant masses of the jet pair in the region of the Z^0 peak. The veto on energy deposits in the forward calorimeters selects events in which the the ISR photons escape detection at small angles with respect to the beam direction. This type of background can be strongly reduced with a cut on the direction of the missing momentum vector. Events are not further considered in the analysis if any of the following conditions is satisfied (cut P5):

- the sum of the momenta of the two jets points inside a cone of opening angle $|\cos\theta| = 0.96$ centered around the beam direction, or
- the missing momentum vector $\overrightarrow{\not{p}}$, calculated including the energy deposits in the forward detectors, forms an angle $\theta_{\not{p}}$ with the beam direction with $|\cos\theta_{\not{p}}| > 0.975$.

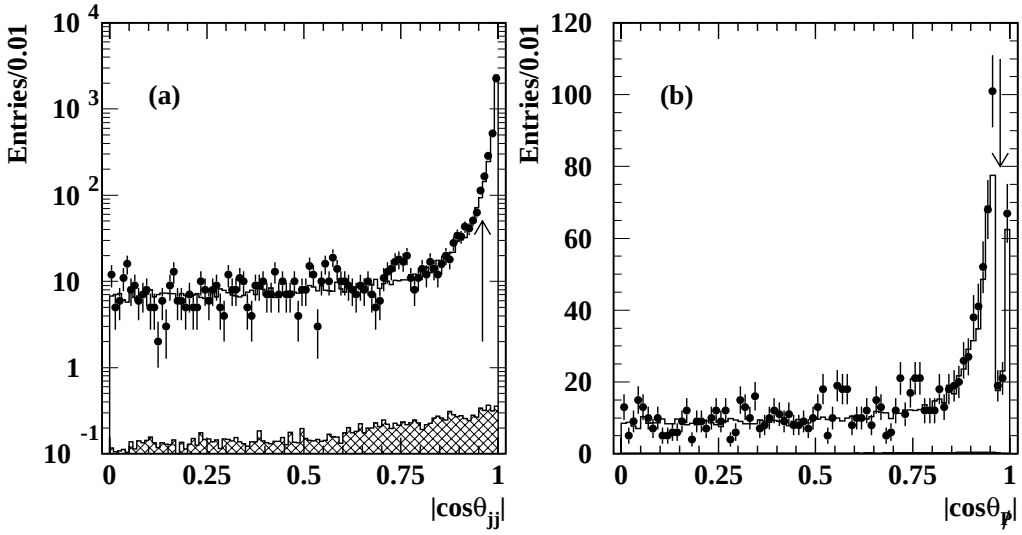

Figure 6.3: Distribution of (*a*) $|\cos\theta_{jj}|$ and (*b*) $|\cos\theta_{\not{p}}|$. The arrows indicate the position of the cuts.

The distribution of the cosine of the polar angle of the total momentum of the two jets $|\cos\theta_{jj}|$ is shown in figure 6.3a. The background peaks at large values of $|\cos\theta_{jj}|$, whereas the $e^+e^- \to q\overline{q}'e^-\overline{\nu}_e$ process is characterised by a flatter distribution. The second cut on $|\cos\theta_{\not{p}}|$ (figure 6.3b) is applied to reject events with two (or more) ISR photons. In these cases the total momentum of the jet pair can point away from the beam direction and be balanced in the transverse plane by a photon which may be observed in one of the forward detectors and pass the veto of cut P2. The cut on $|\cos\theta_{\not{p}}|$ is looser than the one on $|\cos\theta_{jj}|$ to avoid efficiency losses for the signal $e^+e^- \to q\overline{q}'e^-\overline{\nu}_e$ events, given that in some events the electron may be detected in the forward calorimeters.

The distribution of the invariant mass of the jet pair m_{jj} after these cuts is shown in figure 6.4: there is a clear excess in the data in the range from 30 to 90 GeV/c^2. Integrated over

this mass range this excess is three times larger than the statistical error of the data. The excess is due to high multiplicity events where the two jets are emitted at large angles with respect to the beam direction. In all the distributions this excess of events appears to be due to genuine two–jets events which are most probably produced through the $e^+e^- \to q\overline{q}(\gamma)$ process, which still gives the largest contribution to the selected sample. The ratio between the $q\overline{q}'e\overline{\nu}_e$ events in which the electron is scattered at $\cos\theta_e > 0.98$ and the background is $\sim 1/20$ in the region $m_{jj} < 120$ GeV/c^2.

To reduce the $e^+e^- \to q\overline{q}(\gamma)$ background a cut is applied on the acoplanarity ϕ_{acop} of the jet pair: ϕ_{acop} is required to be larger than 7.5° (cut P6). The distribution of ϕ_{acop} is shown in figure 6.5: the excess of events previously observed in the distribution of the invariant mass of the jet pair is concentrated at small values of ϕ_{acop}, whereas at higher values the Monte Carlo provides a good description of the data. Further reduction of background from events without missing energy is obtained with a very loose cut on the missing transverse momentum $\not{p}_T$ scaled to the centre–of–mass energy. The ratio $\not{p}_T/\sqrt{s}$ is required to be larger than $0.035/c$ (cut P7): this corresponds to a cut between 5.6 and 6.4 GeV/c for $\sqrt{s} = 161$–183 GeV. An equal cut is also applied to the missing transverse momentum reconstructed excluding the energy deposits in the hadron calorimeter. This allows to reject events in which a large transverse momentum imbalance is caused by a fluctuation of the energy deposited in

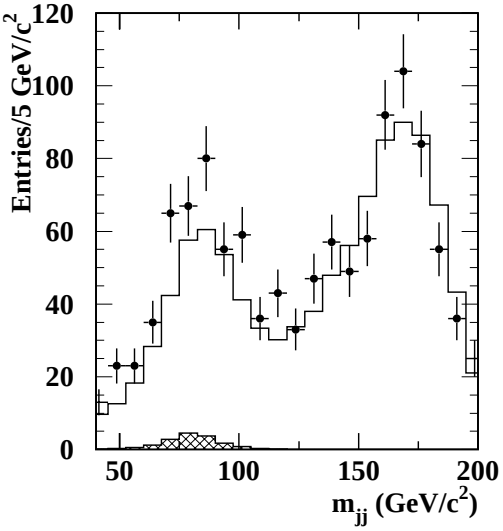

Figure 6.4: Invariant mass of the jet pair for the events selected after cut P5.

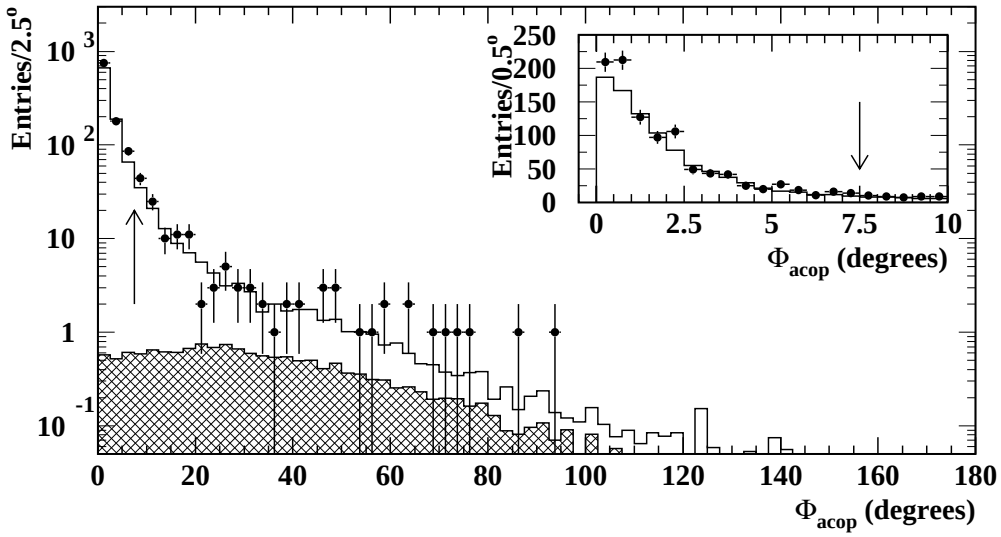

Figure 6.5: Distribution of acoplanarity angle ϕ_{acop}. The inset shows an expanded view of the distribution for small values of ϕ_{acop}. Arrows indicate the cut value in both plots.

the hadron calorimeter. The distribution of the scaled missing transverse momentum is shown in figure 6.6.

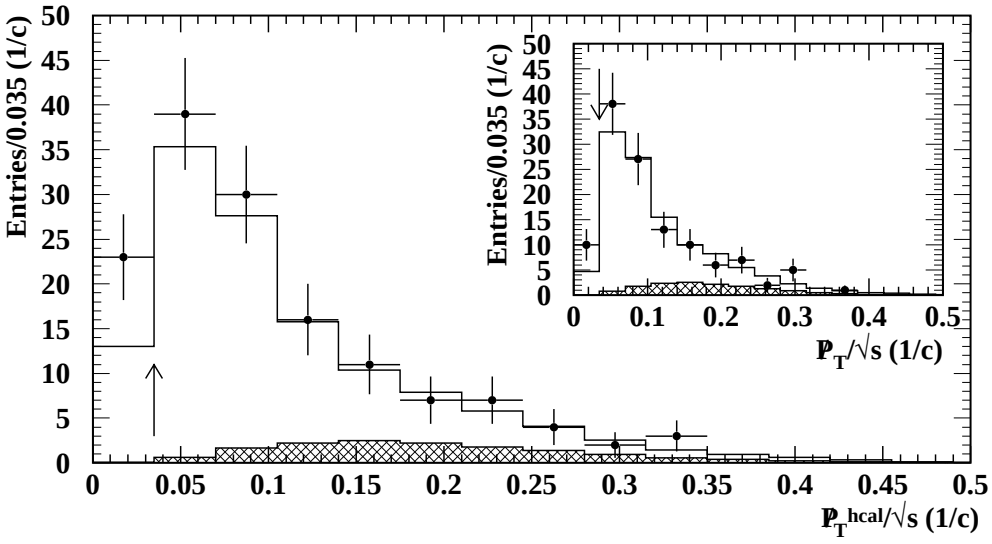

Figure 6.6: Distribution of the scaled missing transverse momentum $\not{p}_T/\sqrt{s}$. The inset shows the distribution of the same quantity after the cut, excluding the clusters in the hadronic calorimeter from the calculation of the missing momentum vector. Cut values are indicated by the arrows.

Finally (cut P8) only events with an invariant mass of the jet pair between 40 and 120 GeV/c^2 are further considered for the likelihood selection described in the next section. At this stage of the analysis 92 events are selected in the data collected at centre–of–mass energies between 161 and 183 GeV, for a Monte Carlo prediction of (82.5 ± 1.7) events. The predicted contribution from $q\overline{q}'e\overline{\nu}_e$ final states in which the electron is scattered at $\cos\theta_e > 0.98$ is of (14.5 ± 0.2) events. This corresponds to an efficiency for selecting these events of approximately 60%. Background processes contribute (68.0 ± 1.7) events. These are mainly $e^+e^- \to q\overline{q}(\gamma)$ events (60%) and $W^+W^- \to q\overline{q}'\ell\overline{\nu}_\ell$ events (30%).

6.4 The likelihood selection

Events satisfying the preselection cuts are classified as signal or background based upon a five variable likelihood selection. Rather than using the product of the individual probability density functions to construct a classic likelihood discriminator, a coordinate transformation technique is used to reduce correlations between the input variables, as discussed in Appendix B.

The following likelihood variables are used since they provide a good separation between the single W signal and the two dominant backgrounds, $e^+e^- \to q\overline{q}(\gamma)$ and $W^+W^- \to q\overline{q}'\ell\overline{\nu}_\ell$:

- the invariant mass of the jet pair, m_{jj};
- the square of the ratio between the missing transverse momentum $\not{p}_T$ and the beam energy E_{beam};

- the total visible energy calculated including the clusters in the forward detectors, E_{vis};

- the logarithm of the ratio of acoplanarity angle and its error, $\sigma_{\phi_{\rm acop}}$, computed through error propagation from a parametrisation of the error on the jet momenta;

- the logarithm of the value of the Durham jet resolution parameter at which an event is reclassified from two to three jets, $\log_{10}(y_{23})$.

The second and the fourth of these variables discriminate between $e^+e^- \to q\overline{q}(\gamma)$ events and four–fermion events with missing energy. The remaining variables are used to separate single W events from $W^+W^- \to q\overline{q}'\ell\overline{\nu}_\ell$ events. The $W^+W^- \to q\overline{q}'\ell\overline{\nu}_\ell$ events which are still contained in the sample are events in which the lepton is not identified and it is close in angle to the jet. These events have on average invariant masses of the jet pair m_{jj} larger than $m_{\rm W}$, and large values of the jet resolution parameter y_{23}.

There is a strong non–linear correlation of kinematic origin between the first three variables used in the likelihood selection. It is caused by the upper bound on the $\not{p}_T$ due to energy conservation: $E_{vis} \geq \sqrt{\not{p}_T{}^2 + m_{jj}^2 c^2}$. The method described in Appendix B is however only capable of handling linear correlations and boundaries on variables which are parallel to the axes. To remove the non–linear correlation, the total visible energy of the event E_{vis} is replaced in the likelihood by the function:

$$\mathcal{F}\left(E_{vis}, m_{jj}, \not{p}_T/E_{beam}\right) \quad = \quad \left| 4\frac{E_{vis} - m_{jj}c^2}{\sqrt{s}} - (\not{p}_T/E_{beam})^2 c^2 \right| .$$

The distribution of the 5 variables used in the likelihood selection is shown for data and Monte Carlo in figure 6.7. Reference distributions for the likelihood selection are built considering only backgrounds from the $e^+e^- \to q\overline{q}(\gamma)$ reaction and from 4–fermion final states, without including the small contribution from the $\gamma\gamma \to q\overline{q}$ process.

Events are selected as candidates if the likelihood discriminant $\mathcal{L}$ is larger than a cut chosen to minimise the expected measurement error on the $\Delta\kappa_\gamma$ coupling, as discussed in section 6.2. The expected measurement error can be also calculated modifying the likelihood discriminant to use a smaller number of variables. This provides a measurement of the relative contribution of the different observables in the likelihood. The quantity giving the largest reduction of the error on $\Delta\kappa_\gamma$ is m_{jj}. The inclusion of this variable in the likelihood causes a 8% relative improvement in the expected error on $\Delta\kappa_\gamma$. All other quantities have smaller impact on the couplings, but help in reducing the $W^+W^- \to q\overline{q}'\ell\overline{\nu}_\ell$ background. The distribution of $\mathcal{F}\left(E_{vis}, m_{jj}, \not{p}_T/E_{beam}\right)$ (figure 6.7c) seems to indicate that this variable has no discriminating power between the single W events and the background. This variable is in fact crucial for controlling the correlations between m_{jj} and $(\not{p}_T/E_{beam})^2$, and is therefore more important than $(\not{p}_T/E_{beam})^2$ itself.

A further improvement of 5% of the expected error on $\Delta\kappa_\gamma$ is obtained by dividing the events in two classes, according to the value of $\phi_{\rm acop}/\sigma_{\phi_{\rm acop}}$. For values of $\phi_{\rm acop}/\sigma_{\phi_{\rm acop}}$ smaller than 5 (region 1) the background is constituted for 80% by events produced in the $e^+e^- \to q\overline{q}(\gamma)$ reaction. At higher values of $\phi_{\rm acop}/\sigma_{\phi_{\rm acop}}$ (region 2) almost 90% of the preselected events come from the semileptonic decay of W pairs. The division of the sample

in two classes allows to take into account properly differences in the correlations between the variables used in the likelihood selection.

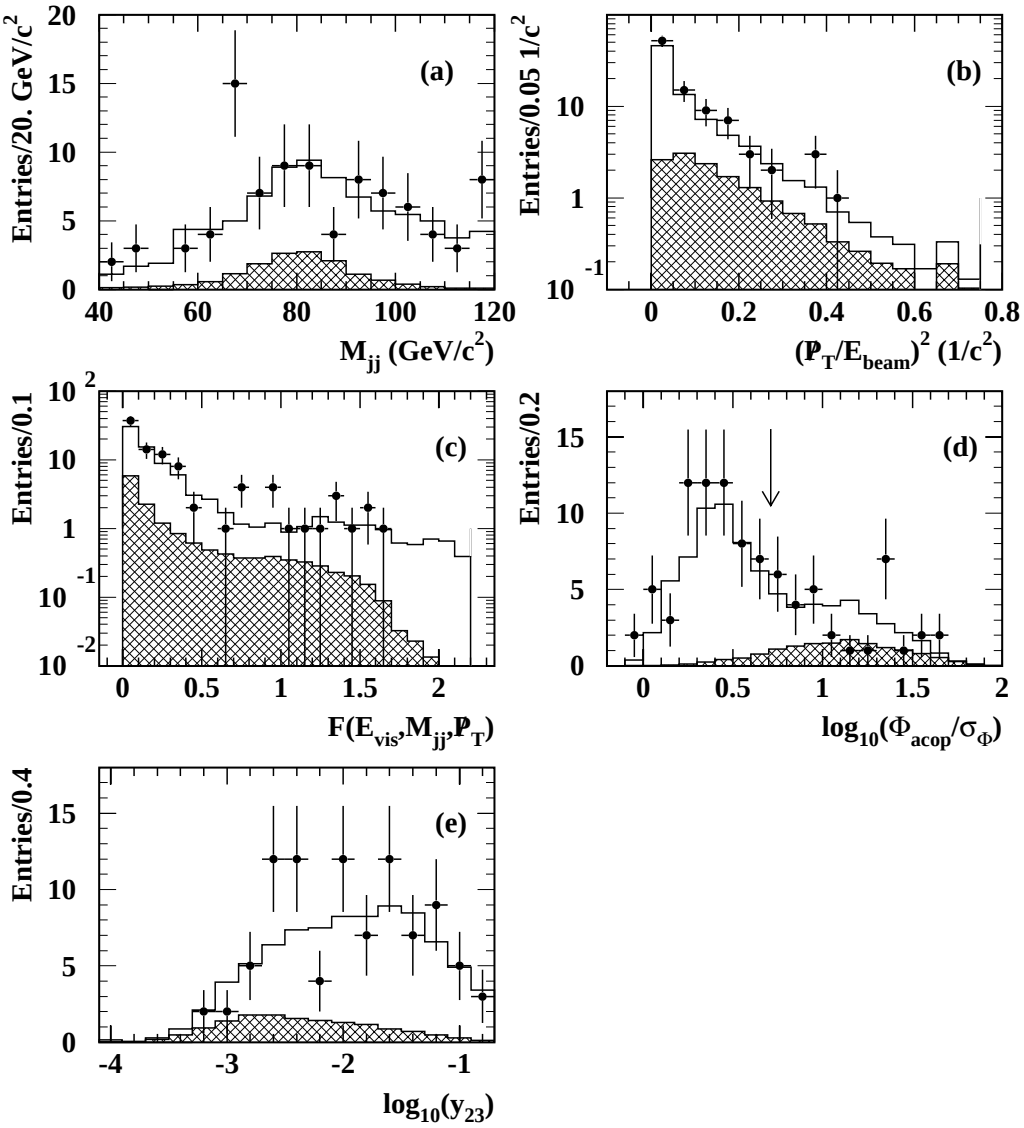

Figure 6.7: Distribution of variables used in the likelihood selection: (*a*) m_{jj}, (*b*) $(\not{p}_T/E_{beam})^2$(*b*), (*c*) $\mathcal{F}$, (*d*) $\log_{10}(\phi_{\rm acop}/\sigma_{\phi_{\rm acop}})$ and (*e*) $\log_{10}(y_{23})$. The value of the cut on $\phi_{\rm acop}/\sigma_{\phi_{\rm acop}}$ separating the two regions for the calculation of the event likelihood is indicated by the arrow in (*d*).

The likelihood selection (cut L) reduces the $e^+e^- \to q\overline{q}(\gamma)$ background by a factor 5 and the contribution from other four–fermion final states by a factor 2. As indicated in table 6.1 (cut L) 23 events events are selected in the (77.05 ± 0.26) pb^{-1} of data collected in 1996–1997 at $\sqrt{s} = 161$–183 GeV for a total Monte Carlo expectation of (24.2 ± 0.5) events. In total (12.4 ± 0.2) events are expected from the $q\overline{q}'e\overline{\nu}_e$ final state in the kinematic region $\cos\theta_e > 0.98$, while other final states give a contribution of (11.8 ± 0.4) events. The most important source of background is the $W^+W^- \to q\overline{q}'\tau\overline{\nu}_\tau$ process (55%), followed by the $q\overline{q}\nu\overline{\nu}$ final state (15%), by the $e^+e^- \to q\overline{q}(\gamma)$ and $W^+W^- \to q\overline{q}'\mu\overline{\nu}_\mu$ processes (10% each). The remainder of the background (9%) is made of $e^+e^- \to q\overline{q}'e^-\overline{\nu}_e$ events, in which the

electron is emitted at $\cos\theta_e < 0.98$, and by other four–fermion final states. All the selected $q\overline{q}'\ell\overline{\nu}_\ell$ background are sensitive to anomalous couplings at the γW^+W^- and $Z^0W^+W^-$ vertices, as they are mainly produced in the $e^+e^- \to W^+W^-$ reaction.

In the selected sample the purity of the $q\overline{q}'e\overline{\nu}_e$ events in which the electron is scattered at $\cos\theta_e > 0.98$ decreases from 65% at the W pair production threshold to 49% at $\sqrt{s} = 183$ GeV. This decrease is due to the faster growth of the $e^+e^- \to W^+W^-$ cross section above threshold compared to the single W process. The growth of the accepted $e^+e^- \to W^+W^-$ cross section (which dominates the 4–fermion processes) from $\sqrt{s} = 161$ to 183 GeV is actually slower than that of the total cross section, due to the increased rejection provided by a better veto for the $W^+W^- \to q\overline{q}'\ell\overline{\nu}_\ell$ final states. Also the second most important background source (the $q\overline{q}\nu\overline{\nu}$ final states) increases rapidly, due to the opening of the Z^0 final state. This background cannot be rejected using the invariant mass of the quark pair, since the invariant mass resolution of the detector (approximately 10 GeV/c^2 as discussed in section 4.8) is not sufficient to distinguish an hadronically decaying Z^0 from a W boson. The accepted cross section for the $e^+e^- \to q\overline{q}(\gamma)$ process increases slightly in the considered energy range, contrary to what happens to the total cross section. This is a result of the optimisation of the analysis, which keeps the relative contribution of the $q\overline{q}$ background approximately constant.

The efficiency for selecting the three different $q\overline{q}'\ell\overline{\nu}_\ell$ final states in this analysis and in the identification of the $W^+W^- \to q\overline{q}'\ell\overline{\nu}_\ell$ final states [41] are shown in figure 6.8 as a

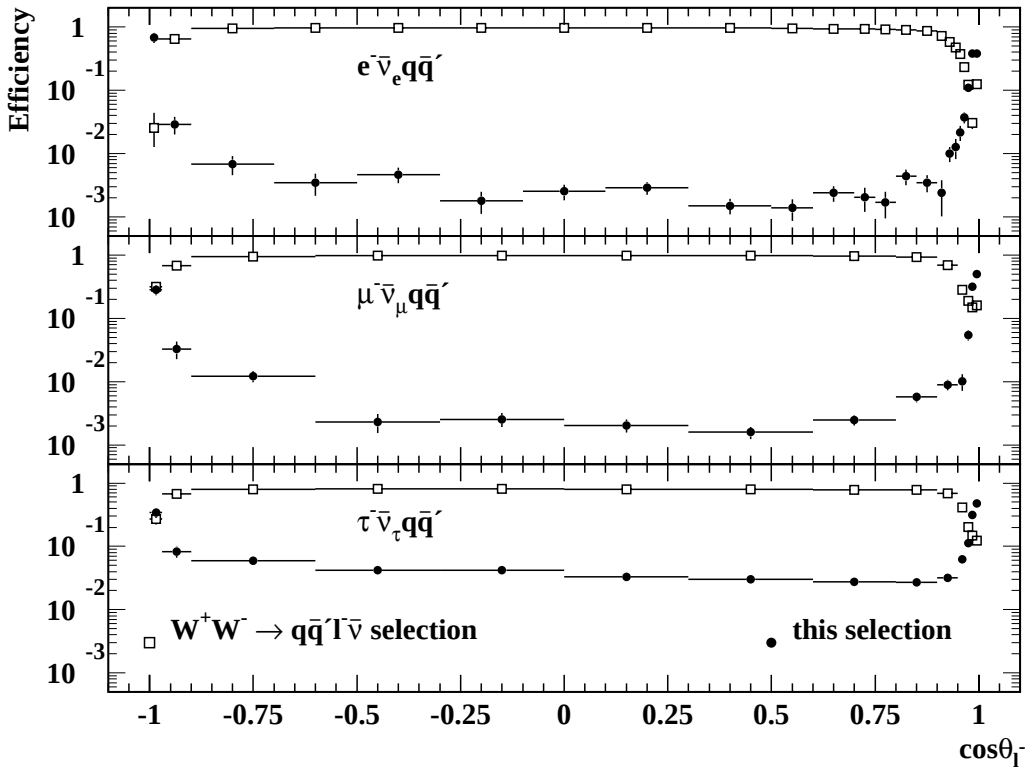

Figure 6.8: Efficiency for selecting the three $e^+e^- \to q\overline{q}'\ell^-\overline{\nu}_\ell$ final states as a function of the lepton angle in the Monte Carlo for the selection described in this chapter (*full dots* •) and for the selection of the $W^+W^- \to q\overline{q}'\ell\overline{\nu}_\ell$ final state (*empty squares* □).

function of the scattering angle of the negative lepton. Due to the presence of the veto for events already identified as $W^+W^- \to q\overline{q}'\ell\overline{\nu}_\ell$ decays (preselection cut P3), the two selection procedures are complementary. Whereas the efficiency of the $W^+W^- \to q\overline{q}'\ell\overline{\nu}_\ell$ selection drops rapidly when the lepton is scattered close to the beam direction, the selection used in this analysis has the opposite behaviour. This happens not only for the $q\overline{q}'e\overline{\nu}_e$ final state, but also for the $q\overline{q}'\mu\overline{\nu}_\mu$ and $q\overline{q}'\tau\overline{\nu}_\tau$ final states, which constitute a large fraction of the background. The three different $q\overline{q}'\ell\overline{\nu}_\ell$ final states cannot be distinguished when the lepton is scattered close to the beam pipe. In all curves the efficiency in the backward direction, $\cos\theta_{\ell^-} < 0$, is larger than in the other hemisphere. This is a combined effect of the angular cuts on the jets directions and the angular distribution of the decay products of W bosons produced in the $e^+e^- \to W^+W^-$ reaction.

A more detailed view of the efficiencies of this analysis and of the $W^+W^- \to q\overline{q}'\ell\overline{\nu}_\ell$ event selection in the kinematic region dominated by single W production is shown in figure 6.9. The efficiency of the $W^+W^- \to q\overline{q}'e\overline{\nu}_e$ selection shows a small rise for $|\cos\theta_e| > 0.99$: these are really single W events which are selected in the $W^+W^- \to q\overline{q}'\tau\overline{\nu}_\tau$ channel, causing a significant loss of efficiency (approximately 9% in absolute terms, or 20% relative) in this analysis. These events are selected in the $W^+W^- \to q\overline{q}'\tau\overline{\nu}_\tau$ channel because one of the tracks is considered as the pion coming from the hadronic decay of the τ, passing the selection criteria of [102]. For the $q\overline{q}'e\overline{\nu}_e$ final state the efficiency of the selection used in this analysis is larger than 10% only for $|\cos\theta_e| > 0.98$, and larger than 1% only for $|\cos\theta_e| > 0.95$. In the barrel only about 0.2–0.3% of the $q\overline{q}'e\overline{\nu}_e$ events are selected. In these events the electron is often close to one of the two jets and therefore it is not identified. A large efficiency is also obtained for events in which the electron is emitted in the backward direction. This does represents however a small background since the cross section for the $e^+e^- \to q\overline{q}'e^-\overline{\nu}_e$ process is forward peaked (figure 2.2). As a function of the invariant mass of the quark pair $m_{q\overline{q}'}$, the analysis is sensitive only for $m_{q\overline{q}'} > 35$ GeV/c^2.

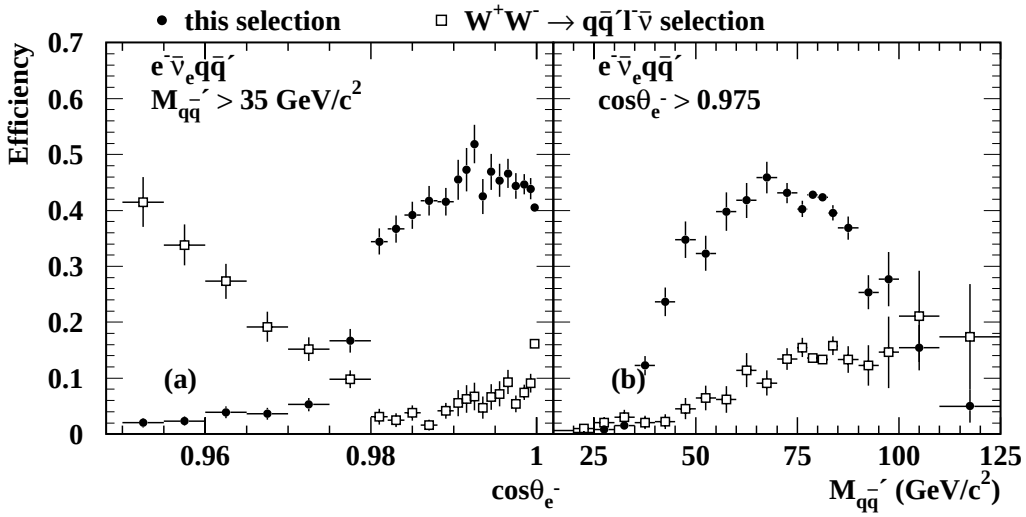

Figure 6.9: Selection efficiencies (*a*) in the forward region and (*b*) as a function of mass.

The efficiency curve for the $q\overline{q}'\mu\overline{\nu}_\mu$ final state (which comes mainly from the decay of two W bosons) is similar to that of the $q\overline{q}'e\overline{\nu}_e$ final state. Due to the absence of the forward peak coming from the single W channel, the $q\overline{q}'\mu\overline{\nu}_\mu$ final state does not constitute a large

	2–fermions	4–fermions	$\gamma\gamma \to q\overline{q}$	Σ_{BG}	We$\overline{\nu}_e$	Monte Carlo	Data
Cut based preselection – $\sqrt{s} = 161$ GeV							
cut P1	883±2	37.4±0.5	161±5	1081±5	1.72±0.02	1083±5	1043
cut P2	792±2	36.3±0.5	153±5	981±5	1.70±0.02	983±5	945
cut P3	675±2	20.5±0.4	149±5	844±5	1.54±0.02	846±5	799
cut P4	613±2	18.8±0.4	13.4±1.3	645±3	1.48±0.02	647±3	664
cut P5	149±1	7.8±0.2	2.7±0.6	159±1	1.36±0.02	160±1	192
cut P6	12.1±0.3	3.8±0.1	0.7±0.3	16.6±0.5	1.20±0.02	17.8±0.5	23
cut P7	10.0±0.3	3.7±0.1	0	13.7±0.3	1.19±0.02	14.9±0.3	20
cut P8	7.1±0.2	2.9±0.1	0	10.0±0.2	1.19±0.02	11.2±0.2	14
region 1	6.8±0.2	1.19±0.07	0	8.0±0.2	0.20±0.01	8.2±0.2	11
region 2	0.2±0.04	1.74±0.07	0	2.0±0.1	0.99±0.01	3.0±0.1	3
Likelihood selection – $\sqrt{s} = 161$ GeV							
cut L	0.06±0.02	0.43±0.03	0	0.49±0.04	0.93±0.02	1.42±0.03	1
region 1	0.06±0.02	0.02±0.01	0	0.08±0.02	0.08±0.01	0.16±0.02	0
region 2	0	0.41±0.03	0	0.41±0.03	0.85±0.01	1.26±0.03	1
Cut based preselection – $\sqrt{s} = 172$ GeV							
cut P1	773±2	79.5±0.6	170±5	1022±6	2.60±0.03	1025±6	1073
cut P2	693±2	78.2±0.6	146±5	917±6	2.57±0.03	920±6	974
cut P3	674±2	28.7±0.5	138±5	841±5	2.18±0.03	843±5	891
cut P4	612±2	26.2±0.5	18±2	656±3	2.11±0.03	658±3	734
cut P5	143±1	10.1±0.2	2.9±0.7	156±1	1.91±0.03	158±1	177
cut P6	10.1±0.2	4.4±0.1	0.2±0.2	14.7±0.3	1.69±0.03	16.4±0.3	21
cut P7	8.1±0.2	4.1±0.1	0.1±0.1	12.3±0.3	1.68±0.03	14.0±0.3	14
cut P8	5.2±0.2	3.1±0.1	0.1±0.1	8.4±0.2	1.67±0.03	10.1±0.2	14
region 1	4.8±0.2	1.0±0.06	0.1±0.1	5.9±0.2	0.20±0.01	6.1±0.2	9
region 2	0.4±0.05	2.1±0.07	0	2.5±0.1	1.47±0.02	4.0±0.6	5
Likelihood selection – $\sqrt{s} = 172$ GeV							
cut L	0.08±0.02	0.91±0.04	0	0.99±0.05	1.36±0.02	2.35±0.05	4
region 1	0.03±0.01	0.02±0.01	0	0.05±0.01	0.06±0.01	0.11±0.02	0
region 2	0.05±0.01	0.89±0.04	0	0.94±0.05	1.30±0.02	2.24±0.05	4
Cut based preselection – $\sqrt{s} = 183$ GeV							
cut P1	3709±15	557±3	851±22	5117±27	18.3±0.2	5135±27	4529
cut P2	3372±14	549±3	767±21	4688±26	17.8±0.2	4706±26	4148
cut P3	3273±14	188±2	747±21	4208±25	15.0±0.2	4223±25	3714
cut P4	2941±13	169±2	85±6	3195±15	14.5±0.2	3209±15	3077
cut P5	637±6	56.8±0.9	21±4	715±7	13.1±0.2	728±7	789
cut P6	49.3±1.8	26.4±0.6	4.5±1.5	80.2±2.4	11.8±0.2	92.0±2.4	98
cut P7	40.0±1.6	25.5±0.6	2.3±1.1	67.8±2.0	11.7±0.2	79.5±2.0	75
cut P8	27.9±1.3	20.2±0.5	1.5±0.9	49.6±1.7	11.6±0.2	61.2±1.7	64
region 1	25.8±1.3	5.4±0.3	1.4±0.9	32.6±1.6	1.32±0.06	33.9±1.6	36
region 2	2.1±0.36	14.8±0.4	0.15±0.12	17.0±0.6	10.32±0.16	27.3±0.6	28
Likelihood selection – $\sqrt{s} = 183$ GeV							
cut L	1.06±0.26	9.26±0.33	0	10.32±0.42	10.11±0.16	20.43±0.45	18
region 1	0.43±0.16	0.26±0.05	0	0.69±0.17	0.46±0.03	1.15±0.18	1
region 2	0.63±0.20	9.00±0.33	0	9.63±0.38	9.65±0.16	19.28±0.41	17

Table 6.1: Number of expected events for signal and backgrounds and number of data events selected for $\sqrt{s} \approx$ 161–183 GeV.

background. On the converse $q\overline{q}'\tau\overline{\nu}_\tau$ events are accepted in this analysis with much higher probability (up to 4% in the barrel region of the detector). Events in which the τ is close in angle to one of the two jets are selected with higher efficiency than the corresponding events with e or μ, given the large hadronic branching fraction of the τ ($\sim 65\%$) and the lower momentum of the decay products. However there is a sizeable efficiency also for events in which the τ is well separated from the two jets. These are events where the τ decays into mostly one low momentum charged hadron (with $p < 1$ GeV/c): it is almost impossible to distinguish such a particle from the softest fragmentation products of the two quarks from the decay of the other W boson.

These backgrounds from semileptonic decays of W pairs where the lepton is either undetected at small angles or mismeasured and/or not identified in the core of a jet are difficult to distinguish from the single W process, as the kinematic properties of the events at these centre–of–mass energies rather similar. The W bosons produced in the $e^+e^- \to W^+W^-$ reaction have a total energy equal to the beam energy, whereas the W bosons produced in the single W process have a broad spectrum (figure 5.4). Unfortunately this difference in the spectrum cannot be exploited to distinguish W bosons produced in the two processes due to the limited resolution on the W momentum and because the ISR and width effect cannot be neglected.

6.5 Analysis of the $\sqrt{s} = 189$ GeV data

The analysis described in the two previous sections has been also applied to the data collected in 1998 at $\sqrt{s} = 189$ GeV with two modifications:

- The energy deposits in the hadronic calorimeters are not considered in the algorithm used for correcting the jet energies and for calculating the missing momentum vector.
- One additional variable is added to the likelihood selection to improve the rejection of the $Z^0Z^0 \to q\overline{q}\nu\overline{\nu}$ background.

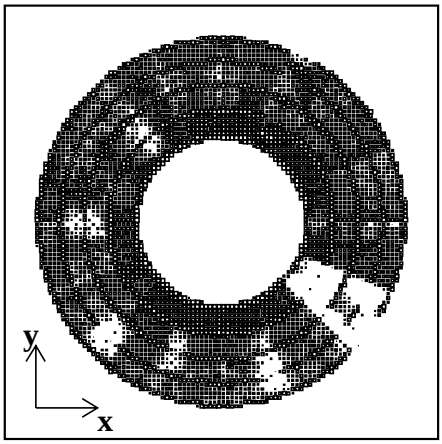

Figure 6.10: Hit map of the right side of HP for the 1998 data.

The first of these modifications is necessary since one tower (a sector of 22.5° in ϕ on the right hand side of the detector) of the hadron pole–tip calorimeter (HP) was not operational during part of the 1998 run, as shown in figure 6.10 by the hit map. Since the pole–tip calorimeter covers the polar angle region $0.91 < |\cos\theta| < 0.99$ this results in a bad measurement of the jet directions and of the missing momentum vector for the $\gamma\gamma \to q\overline{q}$ and $e^+e^- \to q\overline{q}(\gamma)$ processes, which otherwise are suppressed efficiently by the preselection described in section 6.3. The effect of this dead sector is not included in the OPAL detector simulation program, and this does not allow to obtain reliable estimates of the background contribution to the selected sample. If the same analysis procedure adopted to data collected

in 1996 and 1997 at lower centre–of–mass energies is applied to the 1998 data sample, the Monte Carlo underestimates the number of events at the end of the preselection (cut P8) by more than 4 standard deviations, as shown in figure 6.11. The excess is due to hadronic events with small missing transverse momenta, relatively small acoplanarities and at least one jet reconstructed in the forward direction.

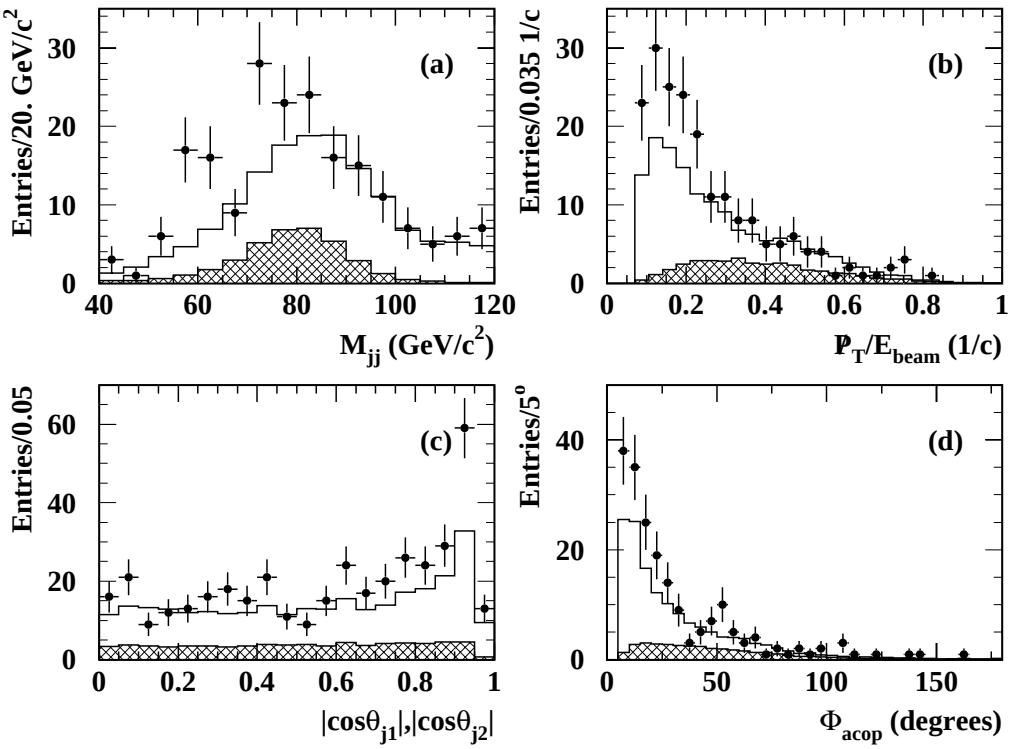

Figure 6.11: Distribution of kinematic variables for the $\sqrt{s} = 189$ GeV data selected with the same analysis procedure applied at lower centre–of–mass energies: (*a*) m_{jj}, (*b*) $\not{p}_T$(*b*), (*c*) $|\cos\theta_j|$ and (*d*) ϕ_{acop}.

It would be necessary to restrict the angular range for jets much below the current requirement $|\cos\theta_j| < 0.96$ (cut P4) to overcome this problem, while still using the hadronic calorimeter information for the energy flow measurement. This would however introduce a large reduction in the selection efficiency for the $q\overline{q}'e\overline{\nu}_e$ events, increasing the expected error on the anomalous couplings. For this reason a different approach is used. The selection cuts are left unchanged and the energy deposits in the hadronic calorimeters are not considered for the reconstruction of the jet energies and the calculation of the missing momentum. The drawback of this approach is that the resolution on the jet directions and on the missing momentum is worse than in the first case. As a result the background of hadronic events without missing energy is rejected with less efficiency by the preselection cuts.

The number of events selected in the data are compared with the Monte Carlo prediction in table 6.2 at page 93 for each step of the preselection and for the final selection cut. At the end of the preselection 271 events are selected in the data collected at $\sqrt{s} = 189$ GeV in 1998, for a Monte Carlo prediction of (247 ± 5) events. In this case the Monte Carlo provides a much better description of the data. The selected sample is constituted for

55% by $e^+e^- \to q\overline{q}(\gamma)$ events, while single W events, $W^+W^- \to q\overline{q}'\ell\overline{\nu}_\ell$ decays and other four–fermion final states (mainly $Z^0Z^0 \to q\overline{q}\nu\overline{\nu}$) contribute each approximately 15% of the events. The amount of $e^+e^- \to q\overline{q}(\gamma)$ background is almost doubled with respect to what could be achieved using also the information from the hadronic calorimeter, whereas contribution from four–fermion final states are unaffected by this change in the analysis. The large increase in the $e^+e^- \to q\overline{q}(\gamma)$ background at the end of the preselection is also visible in the distributions of the variables used for the final event likelihood, shown in figure 6.12, to be compared with figures 6.7 and 6.11. The increased contribution of this background is clearly visible in the missing transverse momentum and in the acoplanarity distributions (figures 6.12b and 6.12d).

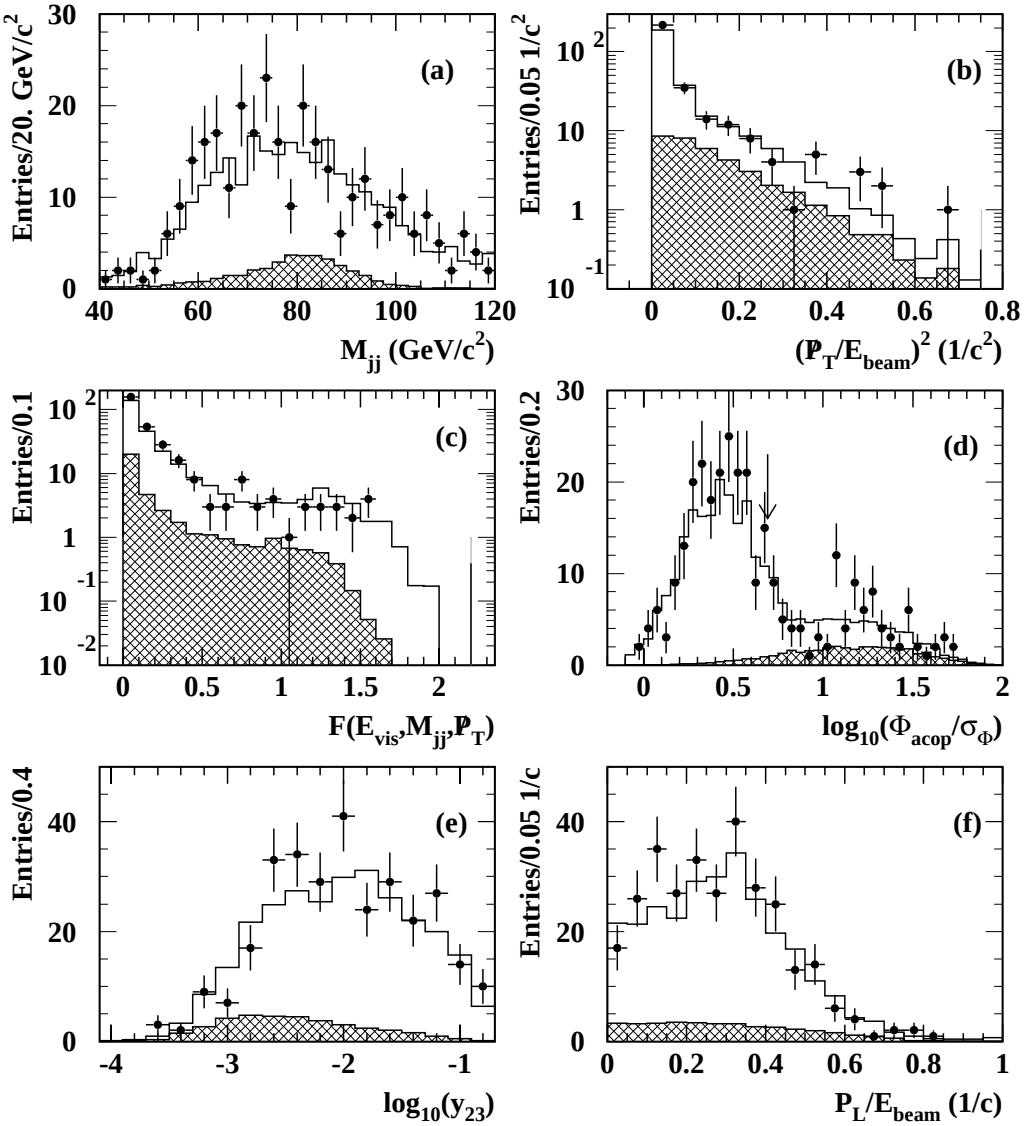

Figure 6.12: Distribution of variables used in the likelihood selection: (*a*) m_{jj}, (*b*) $(\not{p}_T/E_{beam})^2$(*b*), (*c*) $\mathcal{F}$, (*d*) $\log_{10}(\phi_{\rm acop}/\sigma_{\phi_{\rm acop}})$, (*e*) $\log_{10}(y_{23})$ and (*f*) $\not{p}_L/E_{beam}$. The value of the cut on $\phi_{\rm acop}/\sigma_{\phi_{\rm acop}}$ separating the two regions for the calculation of the event likelihood is indicated by the arrow in (*d*).

The reduced rejection power of the preselection is mainly due to the poorer resolution of the jet correction algorithm, when the information from the hadronic calorimeter is not used. The differences between the two jet correction algorithms do not affect the bulk of the distributions, but are clearly visible for events in which the energy deposited in the hadron calorimeter is large. In these events the acoplanarity and the missing transverse momentum can be overestimated when the jet directions are reconstructed using only tracks and clusters in the electromagnetic calorimeter. This reduces the rejection efficiency for the $e^+e^- \to q\overline{q}(\gamma)$ background in which large acoplanarities and large missing transverse momenta are mostly generated through bad measurements.

The second modification of the analysis is necessary to improve the rejection of the $Z^0Z^0 \to q\overline{q}\nu\overline{\nu}$ background. For data collected at centre–of–mass energies below the threshold for the production of Z pairs this background component is negligible. Already at $\sqrt{s} = 183$ GeV the $Z^0Z^0 \to q\overline{q}\nu\overline{\nu}$ process contributes for 10% of the background. At $\sqrt{s} = 189$ GeV the number of events from this process which pass the preselection is half of those coming from the $W^+W^- \to q\overline{q}'\ell\overline{\nu}_\ell$ decays. The $Z^0Z^0 \to q\overline{q}\nu\overline{\nu}$ events are difficult to distinguish from the $q\overline{q}'e\overline{\nu}_e$ events coming from single W production. In both cases only the two jets are visible in the detector, and the distribution of most quantities which can be measured in the final state are similar. One difference between $Z^0Z^0 \to q\overline{q}\nu\overline{\nu}$ and single W production is the distribution of the longitudinal component of the missing momentum. In the case of single W production the final state electron has a longitudinal momentum with an almost flat distribution up to 60 GeV/c. The longitudinal component of the missing momentum, $\not{p}_L$, is dominated by the electron contribution. Therefore the distribution of $\not{p}_L$ (shown in figure 6.12f) is almost flat in the range 0–60 GeV/c. The two Z bosons produced in the $e^+e^- \to Z^0Z^0$ process have small momenta (25 GeV/c at $\sqrt{s} = 189$ GeV), and the two neutrinos from the $Z^0Z^0 \to q\overline{q}\nu\overline{\nu}$ decay are emitted almost back–to–back. The longitudinal component of the missing momentum in these events is therefore small and extends only to 20 GeV/c. This allows to discriminate between single W production and $Z^0Z^0 \to q\overline{q}\nu\overline{\nu}$ decays. For this reason $\not{p}_L$ is used as additional variable in the likelihood selection above the Z pair production threshold.

Apart from these two modifications the analysis of the data collected in 1998 at $\sqrt{s} = 189$ GeV proceeds similarly to that of data taken at lower centre–of–mass energies. After the final likelihood cut 69 events are observed in data, for a Monte Carlo prediction of (63.3 ± 1.3) events, of which (29.9 ± 0.5) events are due to $q\overline{q}'e\overline{\nu}_e$ production in the kinematic region $\cos\theta_e > 0.98$. The detailed composition of the final event sample is given in table 6.2. It is slightly different from that obtained at lower energies. The contribution from the $q\overline{q}\nu\overline{\nu}$ final state increases to 22%, due to the opening of the Z^0Z^0 production channel, while the background from $W^+W^- \to q\overline{q}'\ell\overline{\nu}_\ell$ events is reduced relative to the analysis performed at lower energy. The increase of the $e^+e^- \to q\overline{q}(\gamma)$ background is only due to the less performant energy correction algorithm used for the simulation of the 1998 data.

The distributions of the event selection likelihoods in the two regions $\phi_{\text{acop}}/\sigma_{\phi_{\text{acop}}} < 5$ and $\phi_{\text{acop}}/\sigma_{\phi_{\text{acop}}} > 5$ are shown in figures 6.13a and 6.13b, including all the data collected at $\sqrt{s} = 161$–189 GeV, for a total integrated luminosity of 251 pb^{-1}. In total 92 event satisfy the cuts on the event likelihood $\mathcal{L}$:

- $\mathcal{L}$ must be larger than 0.92 in the region $\phi_{\text{acop}}/\sigma_{\phi_{\text{acop}}} < 5$ and
- $\mathcal{L}$ must be larger than 0.36 in the region $\phi_{\text{acop}}/\sigma_{\phi_{\text{acop}}} > 5$.

The Monte Carlo provides an adequate description of the final event selection, both for the distribution of the likelihood $\mathcal{L}$ and for the two jets invariant mass distribution of the selected events, which is shown in figure 6.13c. The invariant mass distribution shows clearly a peak at $m_{jj} \approx m_W$, as expected since the sample is constituted mainly by single W events and $W^+W^- \to q\overline{q}'\ell\overline{\nu}_\ell$ events in which the lepton (or its decay products for the $W^+W^- \to q\overline{q}'\tau\overline{\nu}_\tau$ process) are not detected.

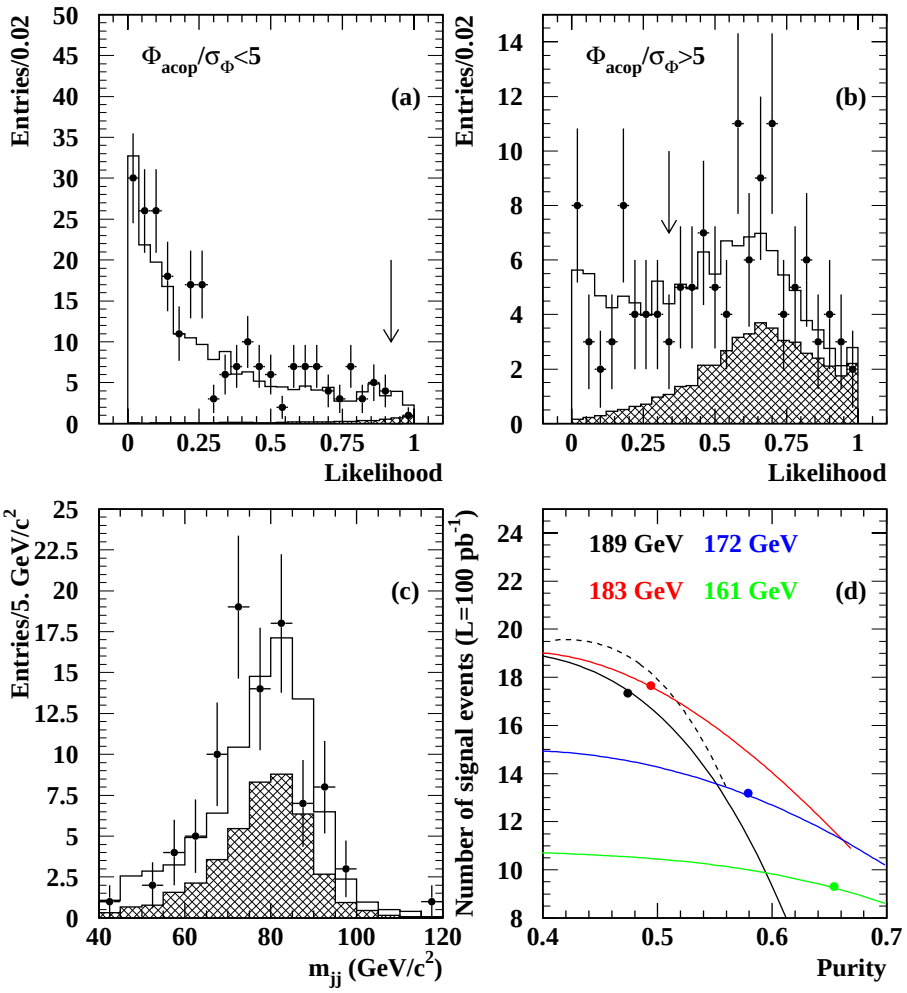

Figure 6.13: The distribution of $\mathcal{L}$ in the two regions defined by the cut $\phi_{\text{acop}}/\sigma_{\phi_{\text{acop}}} < 5$ (> 5) (*a* and *b*). Cuts in the two regions are indicated by the arrows. The two jets invariant mass distribution of the selected sample is shown in (*c*). The number of selected $q\overline{q}'e\overline{\nu}_e$ events as a function of the purity is shown in (*d*) for the samples selected at the four centre–of–mass energies. All samples are normalised to a common luminosity of 100 pb^{-1}. Dots indicate the working point of the selections described in the text. The dashed line indicates the curve which would be obtained at $\sqrt{s} = 189$ GeV using the informations from the hadronic calorimeter in the energy correction algorithm.

To allow a comparison of the event selections at the various centre–of–mass energy the curves giving the number of selected $q\overline{q}'e\overline{\nu}_e$ events in the kinematic region $\cos\theta_e > 0.98$ is plotted in figure 6.13 as a function of the sample purity. All samples are normalised to a common luminosity of 100 pb^{-1}, but no scaling is applied to consider the difference in

cross section. In general the purity of the selected sample decreases as the centre–of–mass increases, and this is mainly due to the fact that the cross sections of the $e^+e^- \to W^+W^-$ and $e^+e^- \to Z^0Z^0$ processes increase with $\sqrt{s}$ much faster than the single W cross section. The selection efficiency for $q\overline{q}'e\overline{\nu}_e$ events with $\cos\theta_e > 0.98$ is instead almost constant in this energy range.

To allow a comparison of the event selections at the various centre–of–mass energy the curves giving the number of selected $q\overline{q}'e\overline{\nu}_e$ events in the kinematic region $\cos\theta_e > 0.98$ is plotted in figure 6.13 as a function of the sample purity. All samples are normalised to a common luminosity of 100 pb^{-1}, but no scaling is applied to consider the difference in cross section. In general the purity of the selected sample decreases as the centre–of–mass increases, and this is mainly due to the fact that the cross sections of the $e^+e^- \to W^+W^-$ and $e^+e^- \to Z^0Z^0$ processes increase with $\sqrt{s}$ much faster than the single W cross section. The selection efficiency for $q\overline{q}'e\overline{\nu}_e$ events with $\cos\theta_e > 0.98$ is instead almost constant in this energy range.

	2–fermions	4–fermions	$\gamma\gamma \to q\overline{q}$	Σ_{BG}	$We\overline{\nu}_e$	Monte Carlo	Data
Cut based preselection – $\sqrt{s} = 189$ GeV							
cut P1	10075±42	1773±5	1337±43	13185±60	70.0±0.8	13255±60	14176
cut P2	9166±40	1752±5	1233±43	12151±58	68.2±0.8	12219±58	13082
cut P3	7794±37	457±3	938±39	9189±53	48.9±0.6	9238±53	9977
cut P4	7128±35	420±3	250±20	7798±40	45.9±0.6	7844±40	8294
cut P5	2226±20	181±2	95±12	2502±23	42.6±0.6	2545±23	2754
cut P6	295±7	86±1	31±6	412±9	38.2±0.6	450±9	483
cut P7	233±6	81±1	6±2	320±7	37.8±0.2	358±7	396
cut P8	147±5	61±1	2.5±0.6	210±5	36.8±0.6	247±5	271
region 1	136±5	16.8±0.5	1.6±0.5	154±5	4.1±0.2	158±5	178
region 2	11±1	44.5±0.6	0.9±0.4	56±2	32.7±0.5	89±2	93
Likelihood selection – $\sqrt{s} = 189$ GeV							
cut L	5.7±1.0	26.7±0.5	1.0±0.4	33.4±1.2	29.9±0.5	63.3±1.3	69
region 1	2.4±0.6	1.0±0.1	0.3±0.2	3.7±0.7	1.0±0.1	4.7±0.7	0
region 2	3.3±0.7	25.7±0.5	0.7±0.3	29.7±1.0	28.9±0.5	58.6±1.1	69

Table 6.2: Number of expected events for signal and backgrounds and number of data events selected for $\sqrt{s} \approx 189$ GeV.

7 Systematic errors

Systematic uncertainties on the Monte Carlo prediction of the number of selected events have been evaluated separately for the $q\overline{q}'e\overline{\nu}_e$ events produced in the single W process, for the remaining 4–fermion events and for the $e^+e^- \to q\overline{q}(\gamma)$ background. The strategy for the evaluation of the systematic errors, based on a separation of detector effects from uncertainties related to the modelling of physical processes, is described in section 7.1. Systematic errors due to uncertainties in the Monte Carlo models are considered in section 7.2, while errors related to the description of the detector response in the simulation program are discussed in section 7.3. Residual differences in the distribution of the quantities used for the preselection and the likelihood are considered as additional sources of systematic errors, which are studied in section 7.4. All systematic uncertainties on the Monte Carlo prediction of the numbers of selected events are summarised at the end of this chapter in table 7.1.

7.1 Control samples

The strategy for estimating systematic errors on the Monte Carlo prediction of the number of selected events is to separate detector effects from uncertainties related to the modelling of physical processes. Uncertainties due to detector effects are studied varying the smearing parameters in the Monte Carlo as discussed in section 4.8. Residual discrepancies between the Monte Carlo and the data in the distributions of the quantities used in the event selection are attributed to a non correct description of the physical processes which contribute to the selected sample of data. Comparisons of data and Monte Carlo are performed on a set of control samples to obtain an estimate of the effects of these residual discrepancies on the event selection.

The differences between data and Monte Carlo distributions observed in the control samples are due either to a difference in the mean values of the distribution or to a difference in shape. In the first case the agreement between the Monte Carlo and the data is improved applying to the simulated events a bias equal to the difference of the mean values of the distributions. The same goal is achieved in the second case weighting the simulated events with the ratio of the data and Monte Carlo distributions. This weight is usually parametrised using only linear or quadratic terms. The effect of the corrections obtained from the study of control samples is applied to the Monte Carlo sample used to estimate the number of events which pass the event selection of chapter 6. Any variation of the number of selected events is taken as estimate of the systematic effects. This procedure is applied in turn to all quantities used for the preselection or to build the event likelihood. Since this procedure may emphasise statistical fluctuations of the Monte Carlo

sample, a normalisation factor is introduced for every event weight, in order to keep the number of events which pass the preselection fixed. Statistical fluctuations of the Monte Carlo samples are included separately in the systematic uncertainty on the selected number of events.

A control sample for the $q\overline{q}'e\overline{\nu}_e$ events in which an electron is scattered at $\cos\theta_{e^-} > 0.98$ can be built starting from the events selected as $W^+W^- \to q\overline{q}'\ell\overline{\nu}_\ell$ using the procedure described in [102]. In the $W^+W^- \to q\overline{q}'e\overline{\nu}_e$ and $W^+W^- \to q\overline{q}'\mu\overline{\nu}_\mu$ decay channels this selection has a purity in excess of 94% and 97% respectively. Multihadronic events produced in the $e^+e^- \to q\overline{q}(\gamma)$ reaction constitute the main background. A sample of single W bosons can be obtained removing the lepton from these $W^+W^- \to q\overline{q}'\ell\overline{\nu}_\ell$ decays. These single W bosons do not have the same kinematical distributions as the W bosons produced in the $e^+e^- \to W^+e^-\overline{\nu}_e$ reaction. The latter have on average a smaller momentum, and the jets produced in their decays tend to be closer in angle to the beam direction. The available statistics of $W^+W^- \to q\overline{q}'\ell\overline{\nu}_\ell$ decays (1071 events in the data collected in 1997 and 1998) does not allow to use these events to build a sample of single W bosons produced in the in the $e^+e^- \to W^+e^-\overline{\nu}_e$ reaction, weighting the angular and momentum distributions. The sample of single W bosons built removing the lepton from $W^+W^- \to q\overline{q}'\ell\overline{\nu}_\ell$ events can be used in any case to check the Monte Carlo modelling of quantities which are not related to angular and momentum distributions, and to check the effects of the lepton veto and of the WW veto used in the preselection. As an example the distributions of y_{23}, of R_{ecal} and of number of tracks obtained from the sample of data $W^+W^- \to q\overline{q}'\ell\overline{\nu}_\ell$ events after the removal of the leptons are compared in figures 7.1a–c with the Monte Carlo distributions given by the KORALW event generator for $q\overline{q}'e\overline{\nu}_e$ events in which the electron is scattered at $\cos\theta_{e^-} > 0.98$.

The same sample of $W^+W^- \to q\overline{q}'\ell\overline{\nu}_\ell$ data with the lepton removed can be used also to check the properties of the $q\overline{q}'\ell\overline{\nu}_\ell$ which satisfy the event selection described in the previous chapter. As discussed in section 6.4 these are mostly $W^+W^- \to q\overline{q}'\ell\overline{\nu}_\ell$ events in which the lepton is emitted in the non–instrumented regions of the detector near the beam pipe or $W^+W^- \to q\overline{q}'\tau\overline{\nu}_\tau$ events in which the τ decays into hadrons which are close to one of the jets from the other W boson. The considerations just made for the $q\overline{q}'e\overline{\nu}_e$ events apply as well to the first class of events. The second class of events is slightly different: in general in these events the invariant mass of the two jets is larger than m_W, since one of the two jets contains also the decay products from the τ. The final likelihood selects mainly the events in which the τ decay products have a very low momentum. Therefore all kinematical distributions, including the invariant mass spectrum, are similar to those obtained from the $W^+W^- \to q\overline{q}'\ell\overline{\nu}_\ell$ events from which the lepton has been removed. The $W^+W^- \to q\overline{q}'\ell\overline{\nu}_\ell$ data with the lepton removed provide therefore an adequate description of the main background to $q\overline{q}'e\overline{\nu}_e$ production in the single W kinematic region. This data sample is compared with a Monte Carlo sample selected in the same way to obtain the corrections which are then applied to the 4–fermion events to asses systematic errors. Data and Monte Carlo are compared in figures 7.1d–f for this category of events.

A control sample used to study the properties of the $e^+e^- \to q\overline{q}(\gamma)$ background is obtained relaxing or inverting the cuts applied in the preselection. This sample is made by the events which satisfy the following list of cuts (the definitions of these quantities are given in section 6.3):

- at least 9 reconstructed tracks which pass the quality criteria of section 4.1,

- a total energy deposited in the forward calorimeters (FD and SW) smaller than 10 GeV,
- a veto on events which are selected as $e^+e^- \to W^+W^-$ candidates,
- $|\cos\theta_j| > 0.96$,
- $|\cos\theta_{jj}| < 0.99$ and $|\cos\theta_{\not p}| < 0.99$,
- $\phi_{\mathrm{acop}} < 15°$,
- $\not p_T/\sqrt{s} < 0.75$ and
- $40 < m_{jj} < 120$ GeV/c^2.

These cuts select a 93% pure sample of $e^+e^- \to q\overline{q}(\gamma)$ events, covering mainly the kinematic region of the preselection cuts. The rest of the sample contains mainly $\gamma\gamma \to q\overline{q}$ events and $Z^0e^+e^- \to q\overline{q}e^+e^-$ final states. The distributions of y_{23}, $\log_{10}(\phi_{\mathrm{acop}}/\sigma_{\phi_{\mathrm{acop}}})$ and $\not p_T/E_{beam}$ in data and Monte Carlo after these cuts are compared in figures 7.1g–i.

7.2 Uncertainties in Monte Carlo models

The limitations of the event generators used to estimate the number of selected events coming from the $e^+e^- \to q\overline{q}'e^-\overline{\nu}_e$ process in the kinematic region dominated by single W production have been discussed in sections 3.2 and 3.3. None of the currently available Monte Carlo programs contains a correct description of the main radiative corrections to the $e^+e^- \to q\overline{q}'e^-\overline{\nu}_e$: initial (ISR) and final state radiation (FSR), and loop corrections in the photon propagator. Uncertainties related to these limitations of the event generators are evaluated as follows:

- All Monte Carlo programs take into account ISR, assuming that the cross section is dominated by the annihilation diagrams. If this assumption is applied to the events produced in the single W kinematic region, the energy carried by ISR photons is overestimated and the effective centre–of–mass energy is too small. This corresponds to an underestimate of the cross section by (7 ± 1)%, as discussed in section 3.3. The uncertainty on this correction is half of the difference of two independent calculations of this effect [80, 81].

- In the Monte Carlo programs ISR photons are either emitted collinear to the beam direction, or with a transverse momentum spectrum better suited to the description of annihilation processes. In the kinematic region of single W production neither of the two descriptions of the p_T^γ spectrum is adequate. Their difference can be anyhow taken as an upper limit on the uncertainties caused the non correct modelling of p_T^γ. The event selection is designed to be insensitive to the correct description of the transverse momentum of ISR photons, and for this reason loose vetoes are applied on the energy deposits in the forward calorimeters. As a result the difference in the number of events selected between Monte Carlo implementing these two different models of ISR is only 1.5%.

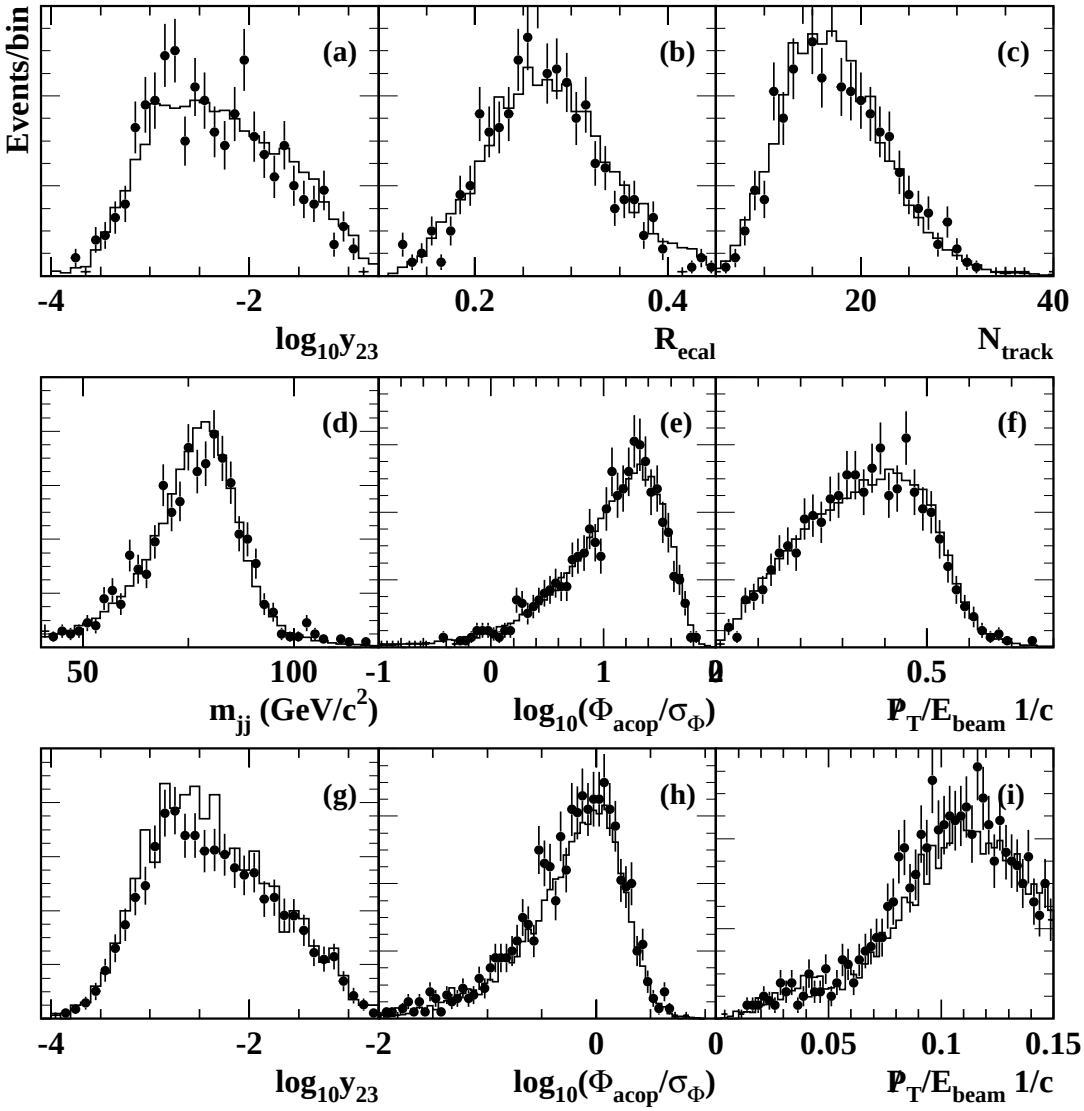

Figure 7.1: Control samples used for the estimation of systematic errors. In (*a–c*) the $q\overline{q}'e\overline{\nu}_e$ Monte Carlo in the single W kinematic region is compared with $W^+W^- \to q\overline{q}'\ell\overline{\nu}_\ell$ data from which the lepton has been removed: (*a*) jet resolution parameter y_{23}, (*b*) ratio of the energy deposited in the electromagnetic calorimeter and of the centre–of–mass energy R_{ecal} and (*c*) number of tracks. Data and Monte Carlo are compared in (*d–f*) for a sample of selected $W^+W^- \to q\overline{q}'\ell\overline{\nu}_\ell$ events from which the lepton is removed: (*d*) invariant mass of the jet pair m_{jj}, (*e*) $\log_{10}(\phi_{\rm acop}/\sigma_{\phi_{\rm acop}})$ and (*f*) $\not{p}_T/E_{beam}$. In (*g–i*) data and Monte Carlo are compared for a sample of events enriched in the $q\overline{q}(\gamma)$ final state: (*g*) y_{23}, (*h*) significance of the acoplanarity $\log_{10}(\phi_{\rm acop}/\sigma_{\phi_{\rm acop}})$ and (*i*) scaled missing transverse momentum $\not{p}_T/E_{beam}$.

- In the Monte Carlo programs, FSR from the electron is either not taken into account or simulated under the assumption that the electron comes from the decay of a W boson. The transverse momentum of the photon relative to the electron may be overestimated, if this second approximation is used for the single W events. The difference in the selected number of events between the two different approaches, 1.7%, is an upper limit on the uncertainties due to FSR modelling.

- To take into account loop corrections in the photon propagator the fine structure constant is set to $\alpha_{em} = 1/135.0$ in the event generators. This value is the average of $\alpha_{em}(Q^2)$ for the generated events. If instead the fine structure constant is fixed to the value it has at the average four–momentum transfer in the events, a value of $\alpha_{em} = 1/135.8$ is obtained. Both approaches are valid approximations of a full calculation which takes into account correctly the loop corrections. The difference between the two values of α_{em} induces a variation of 1.2% in the Monte Carlo prediction of the number of selected events, which is taken as systematic error.

In addition to these theoretical uncertainties related to the inclusion of higher order corrections, two additional sources of systematic errors have to be considered:

- Differences in the technical implementations of the event generators (matrix element calculations, phase space sampling, treatment of the W boson width) cause variations in the number of selected events, which amount to 4.0% at $\sqrt{s} = 161$ GeV and decrease to 2.0% at $\sqrt{s} = 189$ GeV, as shown in table 5.1.

- The scale of hadronisation effects is studied comparing the number of event selected in a single set of four–fermion events which are hadronised once using JETSET and a second time using HERWIG as a hadronisation model. The relative difference in the number of selected events amounts to 1.7%.

The sum of these uncertainties related to the modelling of the $e^+e^- \to q\overline{q}'e^-\overline{\nu}_e$ process in the kinematic region dominated by single W production gives a total systematic error of 5.1% at $\sqrt{s} = 161$ GeV. This error decreases to 3.8% at $\sqrt{s} = 189$ GeV.

For the rest of the 4–fermion final states, dominated by pair production of W and Z bosons, the Monte Carlo calculations are more precise, and the current theoretical predictions have an uncertainty of 2% [120]. Different Monte Carlo programs (KORALW, EXCALIBUR, grc4f and PYTHIA) give predictions of the number of selected events, which are consistent within the statistical errors of the Monte Carlo. Any variation from the prediction of the reference samples is nevertheless taken as an additional source of systematic uncertainty. Added to the 2% theoretical uncertainty on the $e^+e^- \to W^+W^-$ and $e^+e^- \to Z^0Z^0$ production cross section, this gives systematic errors on the 4–fermion contribution to the selected samples of 3.2% at $\sqrt{s} = 161$–189 GeV. This number includes also the uncertainties related to the hadronisation process, estimated as for the $q\overline{q}'e\overline{\nu}_e$ final state.

The comparison of the $\mathcal{KK}$, PYTHIA and HERWIG prediction of the $e^+e^- \to q\overline{q}(\gamma)$ component of the selected sample introduces an additional systematic error of 1.4%, covering also uncertainties related to the hadronisation process.

The statistical uncertainties of the Monte Carlo prediction of the number of selected events are considered as an additional source of systematic errors. These are largest for

the lowest centre–of–mass energies, for which only small Monte Carlo samples were processed through the detector simulation program.

7.3 Detector related systematic uncertainties

Detector resolution effects have been studied using the calibration data taken on the Z^0 peak at the beginning of each year running period. Differences in the kinematical quantities between the data and the Monte Carlo simulations tuned on the high statistics LEP1 data are attributed to inaccuracies in the detector simulation program. It has been shown in section 4.8 that the agreement between the Monte Carlo and the calibration data can be improved applying a smearing procedure to the simulated events. The parameters of this smearing procedure are tuned for each year calibration data and then applied to the Monte Carlo samples used for predicting the number of selected events. Uncertainties related to the simulation of the detector response are estimated varying the parameters of the smearing procedure, within the range allowed by the Z^0 calibration data. This introduces a systematic uncertainty of 1.5% in the number of selected $q\overline{q}'e\overline{\nu}_e$ events which are produced in the single W kinematic region. For the rest of the selected events this uncertainty amounts to 3%.

Additional systematic uncertainties are introduced to take into account possible inefficiencies of the trigger system (0.2%, section 4.5), the error of the luminosity measurement (between 0.2% and 0.6%, section 4.11) and the effect of beam related backgrounds (between 0.1% and 0.4%, section 4.10).

7.4 Uncertainties in the selection procedure

Any residual discrepancy between the Monte Carlo and the data in the event selection is treated as a possible source of systematic error using the method described in section 7.1.

The fraction of $q\overline{q}'e\overline{\nu}_e$ events in the single W kinematic region which are rejected by the W pairs and lepton vetoes is calculated in the control sample built out of $W^+W^- \to q\overline{q}'\ell\overline{\nu}_\ell$ data, from which the lepton has been removed. The Monte Carlo used in the single W kinematic region predicts that the W pairs veto rejects (17.2 ± 0.6)% of the events which otherwise would satisfy the event selection of chapter 6, in perfect agreement with the estimate of (17.0 ± 1.8)% obtained from the single W sample built using the $W^+W^- \to q\overline{q}'\ell\overline{\nu}_\ell$ data. The statistical precision of this test, 1.9%, is taken as systematic uncertainty on the effect of the W pairs veto. This procedure is also applied to the lepton veto, giving a systematic uncertainty of 0.8%. For the data collected at $\sqrt{s} = 172$ and 183 GeV the statistical power of this test is more limited and therefore the assigned error is larger.

For the other four–fermion events the systematic error on the W pairs veto is taken from the the systematic uncertainty of the selection efficiency for the $W^+W^- \to q\overline{q}'\ell\overline{\nu}_\ell$ events which is 1.3% [102]. This number has to be scaled for the relative fraction of $W^+W^- \to q\overline{q}'\ell\overline{\nu}_\ell$ events in the selected sample, giving finally a systematic error of 0.9%. The control samples are used to assess a systematic uncertainty on the efficiency of the lepton veto, obtaining an error of 1.5% at $\sqrt{s} = 189$ GeV.

Good agreement between Monte Carlo and data is found using the control samples for distributions of all the other variables used in the preselection and in the likelihood selection. In most cases the difference of the mean values of the distributions is found to

	$q\overline{q}'e\overline{\nu}_e$ events with $\cos\theta_{e^-} > 0.98$				other 4–fermion events and $e^+e^- \to q\overline{q}(\gamma)$			
$\sqrt{s}$	161 GeV	172 GeV	183 GeV	189 GeV	161 GeV	172 GeV	183 GeV	189 GeV
Uncertainties in Monte Carlo models								
Single W Monte Carlo	5.1	4.8	4.0	3.8				
4–fermion Monte Carlo					3.2	3.2	3.2	2.1
$e^+e^- \to q\overline{q}(\gamma)$ Monte Carlo					1.4	1.4	1.4	1.4
Monte Carlo statistics	1.7	1.7	1.7	1.7	8.2	5.0	4.0	3.6
Detector related systematic uncertainties								
Smearing procedure	1.5	1.5	1.5	1.5	3.0	3.0	3.0	3.0
Trigger efficiency	0.2	0.2	0.2	0.2	0.2	0.2	0.2	0.2
Luminosity measurement	0.5	0.6	0.4	0.2	0.5	0.6	0.4	0.2
Beam related background	0.4	0.4	0.4	0.1	0.2	0.1	0.1	0.3
Uncertainties in the selection procedure								
W pairs veto	0.0	3.8	3.8	1.9	0.0	0.9	0.9	0.9
Lepton veto	1.3	1.3	1.3	0.8	2.6	2.6	2.6	1.5
Track multiplicity and quality	0.5	0.5	0.5	0.5	0.9	0.9	0.9	0.9
R_{ecal} cut	0.3	0.3	0.3	0.3	1.0	1.0	1.0	1.0
Energy deposits in FD and SW	0.3	0.3	0.3	0.3	0.7	0.7	0.7	0.7
Angular cuts on jets	0.8	0.8	0.8	0.8	2.1	2.1	2.1	1.5
$\lvert\cos\theta_{jj}\rvert$ and $\lvert\cos\theta_{\not p}\rvert$ cuts	0.7	0.7	0.7	0.7	2.4	2.4	2.4	1.8
Acoplanarity cut	0.4	0.4	0.4	0.4	1.8	1.8	1.8	1.1
Missing transverse momentum	1.0	1.0	0.5	0.2	3.5	2.2	1.9	1.4
Likelihood variables	1.4	1.2	0.7	0.7	5.1	3.8	2.8	1.7
Total	6.1	7.0	6.3	5.1	12.2	9.4	8.5	6.7
Additional uncertainties for the *t*–channel cross section measurement								
WW / ZZ cross section measurement					20.0	7.8	8.5	4.8
$e^+e^- \to q\overline{q}(\gamma)$ cross section measurement					4.0	3.0	2.0	1.4

Table 7.1: Systematic errors (in %) on the selected number of events for the $q\overline{q}'e\overline{\nu}_e$ signal with a forward going electron and for the 4–fermion and $q\overline{q}(\gamma)$ backgrounds.

be smaller than the resolution of the quantity being measured. For example the difference of the mean values of the polar angles of jets is 0.5°, which is smaller than the average angular resolution for jets 1°. Most systematic uncertainties are dominated by the size of the available control samples. This explains the scaling of the systematic errors when the $\sqrt{s} = 189$ samples are analysed.

The total systematic errors for the $q\overline{q}'e\overline{\nu}_e$ events (5.1% at $\sqrt{s} = 189$ GeV) is dominated by the theoretical uncertainties in the cross section calculation. Another big source of systematic uncertainty is the veto on W pairs.

For the remaining four–fermion events and for the hadrons produced in the $e^+e^- \to q\overline{q}(\gamma)$ process the main systematic error is represented by the uncertainty in the detectors response, and by the statistical errors of the control samples.

8 Single W production cross section

The event selection described in chapter 6 is modified in order to measure the *t*–channel production cross section for the $q\overline{q}'e\overline{\nu}_e$ final state in e^+e^- collisions, in the kinematic region in which the quark pair has an invariant mass $m_{q\overline{q}'} > 40$ GeV/c^2. The reasons for this definition of the single W production cross section, which will be used in the future by all the LEP experiments, have been discusses in section 3.5.

Only small modifications to the event selection of chapter 6 are needed in order to perform this cross section measurement. These modifications are discussed in section 8.1. The measurements of the *t*–channel cross section for the $e^+e^- \rightarrow q\overline{q}'e^-\overline{\nu}_e$ reaction are then presented in section 8.2.

8.1 Modified event selection

The selection of $q\overline{q}'e\overline{\nu}_e$ events produced through the *t*–channel diagrams (diagrams 11–20 in figure 3.1) starts from the events accepted by the preselection described in 6.3. A different event classification is now adopted in which the signal is represented by $q\overline{q}'e\overline{\nu}_e$ events produced through *t*–channel diagrams. All other final states and the $q\overline{q}'e\overline{\nu}_e$ events produced through *s*–channel diagrams are considered background. Using this modified definition the composition of the preselected samples is given at the four different centre–of–mass energies in table 8.1.

The total number of events accepted by the preselection changes in some cases (within the statistical errors of the Monte Carlo) with respect to the numbers given in tables 6.1 and 6.2 since different Monte Carlo programs are used for computing the contribution from the $q\overline{q}'e\overline{\nu}_e$ final state. This contribution is now obtained using the grc4f program to simulate the *t*–channel diagrams, and the KORALW program to simulate the $e^+e^- \rightarrow W^+W^-$ process, with the following approximations:

- the contribution of the *s*–channel diagrams is calculated using only the CC03 diagrams, corresponding to a underestimation of the background of 0.1%;

- the contribution of the interference term between *s* and *t*–channel diagrams, which should be considered as part of the background, is neglected. The size of the interference term is estimated using the first of the two procedures introduced in section 5.3. Using fully simulated samples of $q\overline{q}'e\overline{\nu}_e$ events produced through the full CC20 set of diagrams, or only through the 10 *t*–channel and the CC03 diagrams, this correction is found to be compatible with zero at the 0.5% level. This uncertainty of 0.5%, dominated by the available Monte Carlo statistics, is considered as an additional systematic error on the accepted background cross section.

	2–fermions	4–fermions	$\gamma\gamma \to q\overline{q}$	Σ_{BG}	$q\overline{q}'e\overline{\nu}_e$ (t-channel)	Monte Carlo	Data
Cut based preselection – $\sqrt{s} = 161$ GeV							
cut P8	7.1±0.2	2.9±0.1	0	10.0±0.2	1.23±0.02	11.2±0.2	14
region 1	7.0±0.2	1.67±0.07	0	8.7±0.2	0.33±0.01	9.0±0.2	11
region 2	0.1±0.04	1.3±0.05	0	2.2±0.1	0.90±0.02	3.0±0.1	3
Likelihood selection – $\sqrt{s} = 161$ GeV							
cut L	0.05±0.02	0.46±0.03	0	0.51±0.04	0.97±0.02	1.48±0.04	1
region 1	0.05±0.02	0.08±0.01	0	0.13±0.02	0.14±0.01	0.27±0.02	0
region 2	0	0.38±0.03	0	0.38±0.03	0.83±0.02	1.21±0.03	1
Cut based preselection – $\sqrt{s} = 172$ GeV							
cut P8	5.2±0.2	3.3±0.1	0.1±0.1	8.6±0.2	1.52±0.03	10.1±0.2	14
region 1	5.0±0.2	1.3±0.06	0.1±0.1	6.4±0.2	0.23±0.01	6.6±0.2	10
region 2	0.2±0.05	2.0±0.07	0	2.2±0.1	1.29±0.02	3.5±0.1	4
Likelihood selection – $\sqrt{s} = 172$ GeV							
cut L	0.06±0.02	0.97±0.04	0	1.03±0.05	1.20±0.02	2.23±0.06	3
region 1	0.04±0.01	0.06±0.01	0	0.10±0.02	0.08±0.01	0.18±0.02	0
region 2	0.02±0.01	0.91±0.04	0	0.93±0.04	1.12±0.02	2.05±0.05	3
Cut based preselection – $\sqrt{s} = 183$ GeV							
cut P8	27.9±1.3	20.6±0.5	1.5±0.9	50.0±1.7	10.5±0.2	60.5±1.7	64
region 1	27.8±1.3	11.6±0.4	1.5±0.9	40.9±1.6	3.9±0.1	44.8±1.6	50
region 2	0.1±0.1	9.0±0.3	0	9.1±0.3	6.6±0.1	15.7±0.4	14
Likelihood selection – $\sqrt{s} = 183$ GeV							
cut L	0.88±0.23	6.60±0.27	0	7.48±0.36	8.30±0.16	15.78±0.39	15
region 1	0.81±0.23	2.36±0.17	0	3.17±0.28	2.47±0.08	5.64±0.29	6
region 2	0.07±0.06	4.24±0.22	0	4.31±0.22	5.83±0.13	10.14±0.25	9
Cut based preselection – $\sqrt{s} = 189$ GeV							
cut P8	147±5	63±1	2.5±0.6	212±5	36.3±0.6	248±5	271
region 1	146±5	27.3±0.5	2.1±0.6	175±5	9.5±0.3	185±5	201
region 2	tr1±1	35.7±0.6	0.4±0.3	37±1	26.8±0.5	64±1	70
Likelihood selection – $\sqrt{s} = 189$ GeV							
cut L	5.2±1.0	21.9±0.4	1.0±0.4	28.1±1.1	27.4±0.5	55.5±1.2	64
region 1	4.6±0.6	3.3±0.1	0.7±0.2	8.6±0.7	4.1±0.2	12.7±1.0	13
region 2	0.6±0.7	18.6±0.4	0.3±0.3	19.5±1.0	23.3±0.5	42.8±0.7	51

Table 8.1: Number of expected events for signal and backgrounds and number of data events selected for $\sqrt{s} \approx$ 161–189 GeV.

The likelihood selection uses the same set of discriminating variables introduced in section 6.4, with two minor changes:

- as discussed above a different set of Monte Carlo samples is used for preparing the reference distributions used in the likelihood calculation;
- the value of the $\phi_{\mathrm{acop}}/\sigma_{\phi_{\mathrm{acop}}}$ cut, used to separate the background in two regions dominated respectively by 4–fermion final states and by events produced in the $\mathrm{e^+e^-} \to \mathrm{q\overline{q}}(\gamma)$ reaction, is changed from 5 to 8, leading to an improvement of 2% in the product of signal efficiency times purity.

The Monte Carlo prediction of the number of events accepted by this modified event selection is compared with the data in table 8.1. The expected signal contribution from the *t*–channel diagrams to the $\mathrm{q\overline{q}'e\overline{\nu}_e}$ final state is obtained from the grc4f Monte Carlo. The selection efficiency for the signal varies between 37% at $\sqrt{s} = 161$ GeV and 31% at $\sqrt{s} = 189$ GeV, for expected signal purities close to 50%.

The proposed definition of single W production cross section (section 3.5) contains a cut on the invariant mass of the quark pair, $m_{\mathrm{q\overline{q}'}} > 40$ GeV/c^2, to avoid the kinematic region dominated by multiperipheral diagrams, which is affected by large uncertainties in the QCD corrections. Therefore a correction factor is needed to account for events in which the invariant mass of the jet pair is larger than 40 GeV/c^2, although the invariant mass of the quark pair is smaller than this value. This correction factor is calculated using the grc4f Monte Carlo, and corresponds to an increase of the accepted background cross section of approximately 10 fb.

The selection efficiency, ε, and the accepted background cross section after this correction, σ_{Bkg}, are given in table 8.2, for the different OPAL data sets. The overlap between this selection and the one described in the previous chapter is both in the data and in the Monte Carlo close to 92%.

8.2 Cross section measurements

The *t*–channel cross section for the $\mathrm{e^+e^-} \to \mathrm{q\overline{q}'e^-\overline{\nu}_e}$ process in the kinematic region $m_{\mathrm{q\overline{q}'}} >$ 40 GeV/c^2 is calculated for each centre–of–mass energy using the formula:

$$\sigma = \frac{N_{obs} - \mathcal{L}\sigma_{Bkg}}{\varepsilon\mathcal{L}},$$

where $\mathcal{L}$ is the integrated luminosity and N_{obs} is the number of observed events in data. The measured cross sections are listed in table 8.2. Within the limited statistics available no deviation is observed from the predictions of two different Monte Carlo programs, grc4f and EXCALIBUR, as shown in figure 8.1. Given the limited integrated luminosity of the two data sets collected in 1996, a significative measurement of the cross section is not possible at the two lowest centre–of–mass energies, $\sqrt{s} = 161$ and 172 GeV. The data collected at $\sqrt{s} = 183$ GeV allow to measure a cross section different from zero only for 2.2 standard deviations. The significance of the cross section measurement grows to 5.5 standard deviations at $\sqrt{s} = 189$ GeV.

Systematic errors on the selection efficiency and on the accepted background cross section are calculated using the same procedures of chapter 7. The selection efficiencies are

known with systematic errors varying between 4 and 5%. The systematic errors on the background prediction are much larger (up to 24% at $\sqrt{s} = 161$ GeV), mainly due to the low integrated luminosity of some data sets, which does not allow to measure precisely the cross section for those backgrounds (W pair and Z pair production) which are just above threshold. The final systematic errors on the cross section measurements are anyhow much below the current statistical precision, and vary between 40 and 60 fb.

$\sqrt{s}$(GeV)	161	172	183	189
ε	37.8%	35.7%	36.8 %	31.9 %
$\Delta\varepsilon$	4.7%	6.0%	5.8%	4.4%
σ_{Bkg} (fb)	64	110	140	171
$\Delta\sigma_{Bkg}$	23.8%	12.8%	10.5%	9.7%
N_{obs}	1	3	15	64
Cross section (fb)	100^{+360}_{-100}	510^{+565}_{-385}	340^{+200}_{-170}	615^{+150}_{-135}
Systematic error (fb)	± 40	± 45	± 45	± 60
95% CL limits (fb)	$[0, 1000]$	$[0, 1800]$	$[35, 760]$	$[225, 750]$

Table 8.2: Selection efficiency, accepted background cross section, number of selected events and measured t–channel cross section for the $e^+e^- \to q\overline{q}'e^-\overline{\nu}_e$ process.

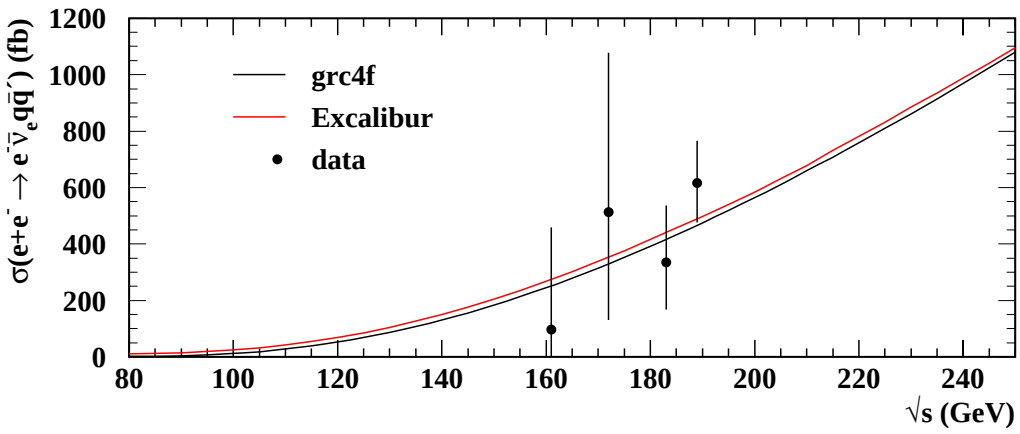

Figure 8.1: Measurements of the t–channel cross section for the $e^+e^- \to q\overline{q}'e^-\overline{\nu}_e$ process in the kinematic region $m_{q\overline{q}'} > 40$ GeV/c^2. OPAL data are compared with Monte Carlo predictions of grc4f (black curve) and EXCALIBUR (red curve).

9 Measurement of gauge couplings

The event selection presented in chapter 6 is used to measure the $\Delta\kappa_\gamma$ and λ_γ parameters of the Lagrangian that describes the γW^+W^- vertex. Fits to the observed event rate are performed in section 9.1 and compared with expectations from Monte Carlo. The use of differential distributions in the TGC's fit is investigated in section 9.2. Systematic uncertainties in the measurement of the couplings are considered in section 9.3. The final results of the analysis are given in section 9.4 and then combined in section 9.5 with measurements performed using $e^+e^- \to W^+W^-$ events.

9.1 TGC's fit to the event rate

The values of the TGC's can be extracted from a fit to the observed event rate, using the event selection presented in chapter 6. The number of events selected in the data is compared in table 9.1 with the Monte Carlo prediction, assuming $\mathcal{SM}$ values for the couplings. At all energies the total number of expected events is consistent with the corresponding number of observed events. There is no evidence for any significant contribution from anomalous couplings. A quantitative study of TGC's from the yield of the event selection is performed comparing the number of observed events with the expected number which is parametrised as a second–order polynomial in the couplings. The coefficients of this polynomial are calculated from the expected number of events at different values of the couplings, obtained using the reweighting technique described in appendix A and assuming the SU(2) $\otimes$ U(1) relations between the couplings at the γW^+W^- and $Z^0W^+W^-$ vertices. This approach based on the direct comparison of an event rate between data and Monte Carlo avoids the need to define a signal cross section and to calculate the dependence of the selection efficiency as a function of the couplings. It also allows to take into account all final states which are sensitive to the anomalous couplings, irrespective of the production process.

$\sqrt{s}$ (GeV)	161	172	183	189
Data	1	4	18	69
Monte Carlo	1.42$\pm$0.10	2.35$\pm$0.17	20.4 $\pm$1.3	63.4 $\pm$3.5

Table 9.1: Number of selected events in data at the different centre–of–mass energies compared with the Monte Carlo expectations assuming $\mathcal{SM}$ values for the TGC's. The Monte Carlo expectations include both statistical and systematic uncertainties.

The dependence of the selected number of events on the $\Delta\kappa_\gamma$ and λ_γ couplings is shown in figure 9.1. The parametrisations obtained using the reweighting technique agree

with estimates obtained using fully simulated Monte Carlo samples generated with values of the TGC's different from the $\mathcal{SM}$ expectations, except possibly for large deviations from the $\mathcal{SM}$. Figure 9.1 shows also the contribution to the selected events from the $e^+e^- \to q\overline{q}'e^-\overline{\nu}_e$ process in the kinematic region $\cos\theta_{e^-} > 0.98$ dominated by single W production, and the contribution from all the remaining four–fermion final states and background processes. A comparison of the dependence of the number of selected events on the couplings with the cross section curves shown in figure 5.2 indicates that the main property of single W production, the increased sensitivity to the $\Delta\kappa_\gamma$ coupling compared to the W^+W^- final state, is not affected by the event selection, nor by the large $W^+W^- \to q\overline{q}'\ell\overline{\nu}_\ell$ background.

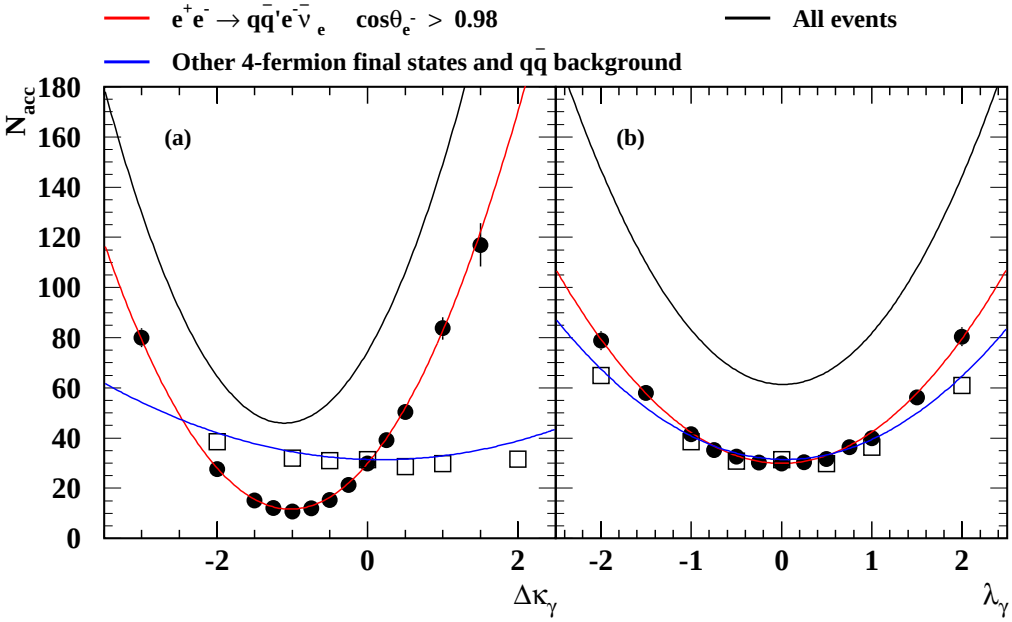

Figure 9.1: Monte Carlo prediction of the total number of selected events as a function of (*a*) $\Delta\kappa_\gamma$ and (*b*) λ_γ(black curves) at $\sqrt{s} = 189$ GeV. The contribution from the $e^+e^- \to q\overline{q}'e^-\overline{\nu}_e$ process in the $\cos\theta_{e^-} > 0.98$ phase space region is given by the red curves, while the contribution from the remainder of the phase space and from all other processes is shown by the blue curves. Dots (•) and empty squares (□) represent the Monte Carlo predictions obtained using fully simulated Monte Carlo samples generated for various values of the couplings.

For each centre–of–mass energy the probability to observe the measured number of candidates is calculated using a Poisson distribution centered around the number of expected events. The product of the four probability distributions corresponding to the four data sets is taken as the event rate likelihood function to be maximised in order to obtain the values of the couplings.

This fit procedure has been tested by treating Monte Carlo samples as data, as already done for studies performed at the generator level (section 5.5) and for the optimisation of the event selection (section 6.2). Fits to samples generated with $\mathcal{SM}$ values of the couplings are performed to predict the expected errors and 95% CL limits and to check that the modelling of the fit errors is correct. In addition fits are also performed to samples gen-

erated with values of the couplings different from the $\mathcal{SM}$ to check that the fit is unbiased and that its response is linear in the couplings.

High statistics samples (1000 times the luminosity of the OPAL data) indicate that the reproduction of the input TGC's values by the fit is excellent for all values of λ_γ and for values of $\Delta\kappa_\gamma$ different from -1. This result is actually in contrast with what has been shown in section 5.5, where a second minimum was always found when performing fits using only the cross section information and the wrong minimum was chosen in approximately half of the simulated experiments. This difference is due to the background of the $W^+W^- \to q\overline{q}'\ell\overline{\nu}_\ell$ events in the selected sample, which was not considered in the analysis of section 5.5. The different dependence on the $\Delta\kappa_\gamma$ coupling of the $W^+W^- \to q\overline{q}'\ell\overline{\nu}_\ell$ final state lifts the degeneracy of the cross section which affects the single W kinematic region. A second minimum usually exists in the likelihood curve, but the probability of it being consistent with the absolute minimum is smaller than 5%. Only for $\Delta\kappa_\gamma \approx -1$ the shape of the likelihood curve is such that this second minimum is consistent with the absolute one at a level smaller than 2 standard deviations in a sizeable fraction (23%) of the simulated experiments. In 7% of all the experiments the wrong minimum, located at $\Delta\kappa_\gamma \approx -0.78$ is selected instead of the correct one.

This kind of problems in the fit are more evident when considering samples with an integrated luminosity equal to that of the OPAL data. Results obtained from these tests of the fit procedure are shown in table 9.2 for samples generated with various values of the couplings. In the fit for the $\Delta\kappa_\gamma$ coupling a second minimum is found in 99% of the simulated experiments and the right minimum is chosen by the likelihood only in 52% of the experiments. Only assuming that the right minimum can be selected with another measurement (like the TGC's measurement in the W^+W^- production), the fit remains unbiased. Another feature evident from table 9.2 is that the expected error depends on the couplings and is maximal for $\Delta\kappa_\gamma = -1$ and $\lambda_\gamma = 0$. Near these two values of the couplings the sensitivity of the analysis to TGC's is minimal.

This procedure based on small samples tests allows also to check whether the errors returned by the maximum likelihood fit have the correct statistical meaning. Two types of checks can be performed:

- The pull, defined as the difference between the measured and the true coupling, divided by the measurement error, should follow a normal distribution. If the variance of distribution is different from 1, then the error needs to be rescaled, which in turn corresponds to dividing the log–likelihood curve by the variance. This technique for checking the statistical error is not of direct applicability in the case of non–gaussian errors, which are expected in the current analysis due to the limited number of events. One possibility is to perform the test of the pull distribution using the positive error if the measured value of the coupling is smaller than the true value, and the negative error viceversa. The positive and negative errors are obtained finding the values of the log–likelihood which differs from the maximum by 0.5. Pull distributions defined in this way have a variance consistent with 1, indicating that the statistical errors given by the fit program are correctly estimated.

- The second check of the correctness of the errors returned by the fit program is based on the distribution of the value of the log–likelihood at the $\mathcal{SM}$ point. If the errors are correctly defined then in 68.3% of these simulated Monte Carlo experiments the

Coupling	Fraction (%) of experiments with			σ	Allowed region
	$2\ \Delta\kappa_\gamma$ minima	$2\ \Delta\kappa_\gamma$ regions	wrong $\Delta\kappa_\gamma$ minimum	$(\Delta\kappa_\gamma)$	at the 95% CL for $\Delta\kappa_\gamma$
$\Delta\kappa_\gamma = -2.0$	100	95	50	0.16	$[-2.29, -1.69]$
$\Delta\kappa_\gamma = -1.0$	43	3	63	0.19	$[-1.67,\ 0.00]$
$\Delta\kappa_\gamma = -0.5$	61	7	63	0.22	$[-1.73,\ 0.00]$
$\Delta\kappa_\gamma = 0.0$	99	67	52	0.19	$[-0.34,\ 0.33]$
$\Delta\kappa_\gamma = 0.5$	100	100	50	0.15	$[\ 0.18,\ 0.75]$
$\Delta\kappa_\gamma = 1.0$	100	100	50	0.12	$[\ 0.78,\ 1.25]$
$\Delta\kappa_\gamma = 2.0$	100	100	50	0.11	$[\ 1.79,\ 2.20]$
	$2\ \lambda_\gamma$ minima	$2\ \lambda_\gamma$ regions	wrong λ_γ minimum	(λ_γ)	for λ_γ
$\lambda_\gamma = -2.0$	100	100	40	0.12	$[-2.25, -1.78]$
$\lambda_\gamma = -1.0$	100	84	47	0.18	$[-1.32, -0.62]$
$\lambda_\gamma = -0.5$	72	13	50	0.21	$[-0.96,\ 0.98]$
$\lambda_\gamma = 0.0$	42	4	50	0.37	$[-0.82,\ 0.85]$
$\lambda_\gamma = 0.5$	65	8	50	0.22	$[-0.92,\ 0.95]$
$\lambda_\gamma = 1.0$	100	78	48	0.19	$[\ 0.61,\ 1.32]$
$\lambda_\gamma = 2.0$	100	100	38	0.13	$[\ 1.81,\ 2.27]$

Table 9.2: Results obtained testing the fit procedure on an ensemble of Monte Carlo experiments generated for various values of the TGC's. Only cross section information are used in the fits.

value of the log–likelihood should be smaller than 0.5 and in 95% of the cases it should be smaller than 1.92. This is actually the case for $\Delta\kappa_\gamma$: $(65.3 \pm 0.9)\%$ and $(94.6 \pm 0.5)\%$ of the experiments satisfy the two requirements. For λ_γ this procedure indicates that the errors are overestimated, but this is due to the non–parabolic shape of the log–likelihood curve near the minimum. The 95% CL limits on λ_γ are however correctly estimated.

The results of the fit to the event rate on the OPAL data are given in table 9.3 and shown graphically in figure 9.4 at page 113. As expected the log–likelihood curves presents two minima in $\Delta\kappa_\gamma$. For λ_γ the fit prefers a value different from the $\mathcal{SM}$ coupling, but still within 1 standard deviation.

	$\Delta\kappa_\gamma$	λ_γ
Fit results	$-0.09^{+0.19}_{-0.17}$	$-0.39^{+1.09}_{-0.31}$
95% CL limits	$[-2.17, -1.46] \cup [-0.33, 0.42]$	$[-0.92, 0.92]$

Table 9.3: Results on $\Delta\kappa_\gamma$ and λ_γ parameters. Each result is obtained setting the other parameter at its Standard Model value of zero. Only statistical errors are included.

9.2 TGC's fit to differential distributions

It has been shown in section 5.5 that the degeneracy between the two minima present in the log–likelihood curve obtained from the fit to the $\Delta\kappa_\gamma$ parameter can be removed by using the differential distributions of the selected events. Two suitable variables have

been identified for the use in the fit to extract the anomalous couplings: the total transverse momentum of the jet pair p_{jj}^T and the difference between the cosine of the polar angles of the two jets $|\cos\theta_{j_1} - \cos\theta_{j_2}|$. The distribution of p_{jj}^T for the data collected at $\sqrt{s} = 189$ GeV is compared with different Monte Carlo expectations for various values of the $\Delta\kappa_\gamma$ and λ_γ parameters in figure 9.2.

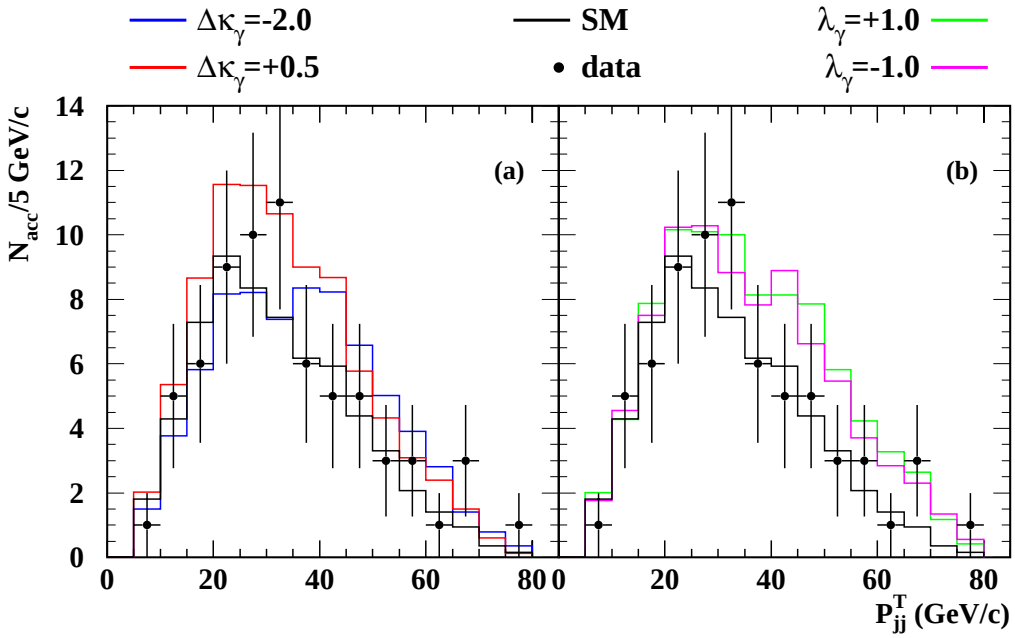

Figure 9.2: Distribution of the accepted events as a function of the total transverse momentum of the jet pair p_{jj}^T for different values of the couplings. The black line shows the Monte Carlo prediction for $\mathcal{SM}$ values of the couplings. The red and blue histograms in (*a*) show the expected distribution for $\Delta\kappa_\gamma = +0.5$ and $\Delta\kappa_\gamma = -2.0$. In (*b*) the green and magenta histograms show the expected distributions for $\lambda_\gamma = \pm 1.0$.

The differential distributions of p_{jj}^T and $|\cos\theta_{j_1} - \cos\theta_{j_2}|$ are included in the fit for the anomalous couplings using a binned maximum likelihood method. Data and Monte Carlo are divided into 30 non uniform bins (6 bins in p_{jj}^T and 5 bins in $|\cos\theta_{j_1} - \cos\theta_{j_2}|$). Bin widths are chosen such that the number of expected events is approximately equal in all bins and that there is a sufficient number of Monte Carlo events for calculating the TGC's dependence of the expected number of events. The fit to differential distributions is only applied to the data collected at $\sqrt{s} = 183$ and 189 GeV. The limited statistics available at lower energies does not justify the use of differential cross sections in the fit.

All the studies performed in the previous section for the fit to the total number of observed events have been repeated to estimate the gain obtained from the use of the differential distributions. It has also been checked that the properties of the fit (linearity, absence of biases, correctness of the error estimates) are not spoiled by the use of additional informations in the fit.

This study confirms the results already obtained in section 5.5, even after taking into account background sources, effects of the event selection and detector resolution. The inclusion of the differential distributions in the TGC's fit removes almost completely the ambiguity concerning the fitted value of $\Delta\kappa_\gamma$ and reduces the expected error for the mea-

surement of the λ_γ parameter. Results obtained from tests on an ensemble of Monte Carlo samples of integrated luminosity equivalent to that of the OPAL data are summarised in table 9.4.

Coupling	Fraction (%) of experiments with			σ	Allowed region
	2 $\Delta\kappa_\gamma$ minima	2 $\Delta\kappa_\gamma$ regions	wrong $\Delta\kappa_\gamma$ minimum	($\Delta\kappa_\gamma$)	at the 95% CL for $\Delta\kappa_\gamma$
$\Delta\kappa_\gamma = -2.0$	40	40	11	0.16	$[-2.29, -1.64]$
$\Delta\kappa_\gamma = -1.0$	68	64	0	0.21	$[-1.61, -0.14]$
$\Delta\kappa_\gamma = -0.5$	53	17	0	0.21	$[-1.47, -0.03]$
$\Delta\kappa_\gamma = 0.0$	25	4	16	0.18	$[-0.38, 0.33]$
$\Delta\kappa_\gamma = 0.5$	51	15	8	0.14	$[0.21, 0.77]$
$\Delta\kappa_\gamma = 1.0$	68	37	5	0.12	$[0.75, 1.24]$
$\Delta\kappa_\gamma = 2.0$	40	40	3	0.11	$[1.79, 2.22]$
	2 λ_γ minima	2 λ_γ regions	wrong λ_γ minimum	(λ_γ)	for λ_γ
$\lambda_\gamma = -2.0$	100	100	14	0.12	$[-2.22, -1.77]$
$\lambda_\gamma = -1.0$	100	84	22	0.18	$[-1.28, -0.65]$
$\lambda_\gamma = -0.5$	72	13	65	0.21	$[-0.89, 0.84]$
$\lambda_\gamma = 0.0$	42	4	–	0.37	$[-0.72, 0.74]$
$\lambda_\gamma = 0.5$	65	8	65	0.22	$[-0.81, 0.89]$
$\lambda_\gamma = 1.0$	100	78	23	0.19	$[0.65, 1.28]$
$\lambda_\gamma = 2.0$	100	100	15	0.13	$[1.77, 2.23]$

Table 9.4: Results obtained testing the fit procedure on an ensemble of Monte Carlo experiments generated for various values of the TGC's. Total and differential cross section informations are used to extract the couplings.

The main differences with respect to the fit which uses only the total cross section information are:

- When high statistics tests are performed the fit has a linear response on the TGC's even for values of $\Delta\kappa_\gamma \approx -1$. The second minimum present in 23% of the simulated experiments at $\Delta\kappa_\gamma = -1$ disappears when using differential cross sections in the TGC's fit.
- For integrated luminosities equivalent to the OPAL data the number of tests in which the log–likelihood curve for $\Delta\kappa_\gamma$ has two minima is largely reduced. For $\Delta\kappa_\gamma = 0$ the probability of finding two minima in the log–likelihood curve is only 25% for the TGC's fit which uses the p_{jj}^T and $|\cos\theta_{j_1} - \cos\theta_{j_2}|$ distribution,
- The λ_γ region allowed at the 95% CL is reduced by 10%.
- For simultaneous fits to the two couplings the region of the $(\Delta\kappa_\gamma, \lambda_\gamma)$ plane allowed at the 68% CL is reduced by 60%, and the 95% CL one is reduced by 40%.

The same procedure has also been tested with fits which use only the p_{jj}^T distribution, using a higher number of bins (9). While for $\Delta\kappa_\gamma$ this fit to a single differential distribution has the same performance as the fit to the two–dimensional (p_{jj}^T,$|\cos\theta_{j_1} - \cos\theta_{j_2}|$) distribution, the results are 10% worse for λ_γ. Therefore it has been decided to use the fit to the two–dimension (p_{jj}^T,$|\cos\theta_{j_1} - \cos\theta_{j_2}|$) distribution to obtain the final results of the analysis.

The improvements given by the use of the p_{jj}^T and $|\cos\theta_{j_1} - \cos\theta_{j_2}|$ distributions in the TGC's fit are most clearly visible in figure 9.3. The distribution of the minima of the log–likelihood curves for 3000 simulated experiments with a luminosity equal to the OPAL data are shown for the three types of fit performed. In $\Delta\kappa_\gamma$ the number of events in which the wrong minimum is chosen by the fit are strongly reduced.

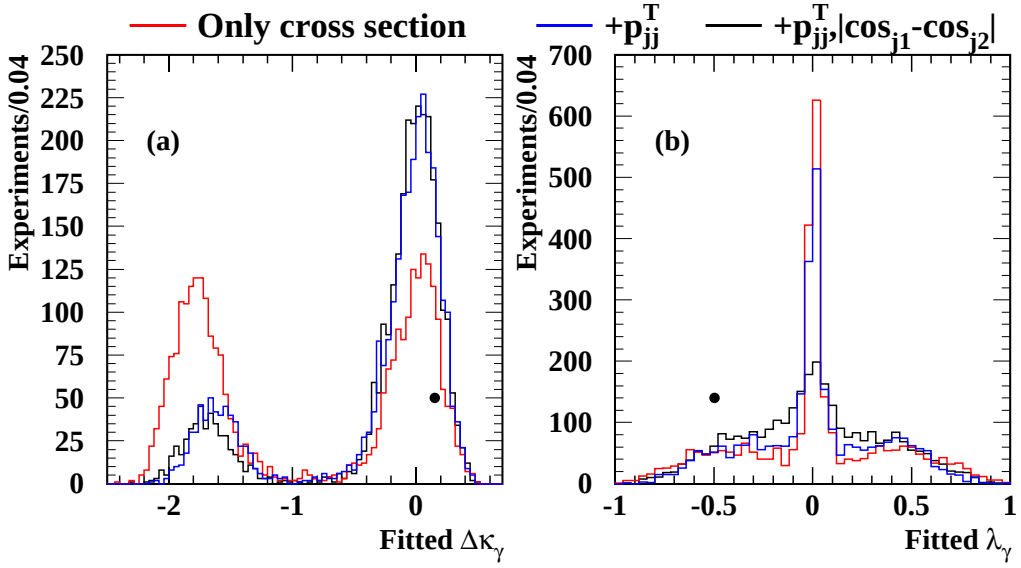

Figure 9.3: Distribution of the fitted values of (*a*) $\Delta\kappa_\gamma$ and (*b*) λ_γ for 3000 simulated experiments each with a luminosity equivalent to the OPAL data. The red histograms show the distribution of the results of fits in which only the total cross section is used to extract the TGC's. The other histograms show the results of fits which also use differential distributions (1d–fit to the p_{jj}^T distribution in blue, 2d–fit to the (p_{jj}^T, $|\cos\theta_{j_1} - \cos\theta_{j_2}|$) distribution in black). Dots indicate the results of the fits on the OPAL data.

In λ_γ the fit which uses only the event rate and the fit which also includes the p_{jj}^T distribution predict similar results. It would appear that the fit which uses the two–dimensional (p_{jj}^T,$|\cos\theta_{j_1} - \cos\theta_{j_2}|$) distribution gives worse results, since there are less events in which the correct value of the coupling $\lambda_\gamma = 0$ is chosen by the fit. However the large peak at $\lambda_\gamma = 0$ does not correspond to better constraints on the couplings, but rather to a complete absence of information in the variables used in the fit. This peak occurs whenever the observed event rate is smaller than the expected one, due to a statistical fluctuation. In all these cases λ_γ takes the value which gives a minimum for the cross section, but there is no distinction between experiments which have an event rate below the expectation by 0.1 standard deviations and those in which this difference amounts to 3 standard deviations. The use of the $|\cos\theta_{j_1} - \cos\theta_{j_2}|$ distribution distinguishes among these cases, improving in the end the overall sensitivity of the fit. As a consequence the 95% CL limits on λ_γ are expected to improve by 10% when the two–dimensional distribution of p_{jj}^T and $|\cos\theta_{j_1} - \cos\theta_{j_2}|$ is used to measure the couplings.

The effect of the use of the p_{jj}^T and $|\cos\theta_{j_1} - \cos\theta_{j_2}|$ distributions in the TGC's fit is clearly visible in figure 9.4 which shows for the OPAL data the log–likelihood curves of the one parameter fits to $\Delta\kappa_\gamma$ and λ_γ, and of the simultaneous fit to the two couplings. For $\Delta\kappa_\gamma$ the differential distributions are essential in reducing the probability of the second minimum

to 2.9%. If both couplings are allowed to vary simultaneously, the effect of the differential information in the fit is to exclude a large portion of the parameter space, mainly for $\Delta\kappa_\gamma < -1$.There is only a small region with a probability of 6% or smaller which signals the presence of the second minimum in the log–likelihood curve. The results obtained with this fit on the OPAL data are summarised in table 9.5.

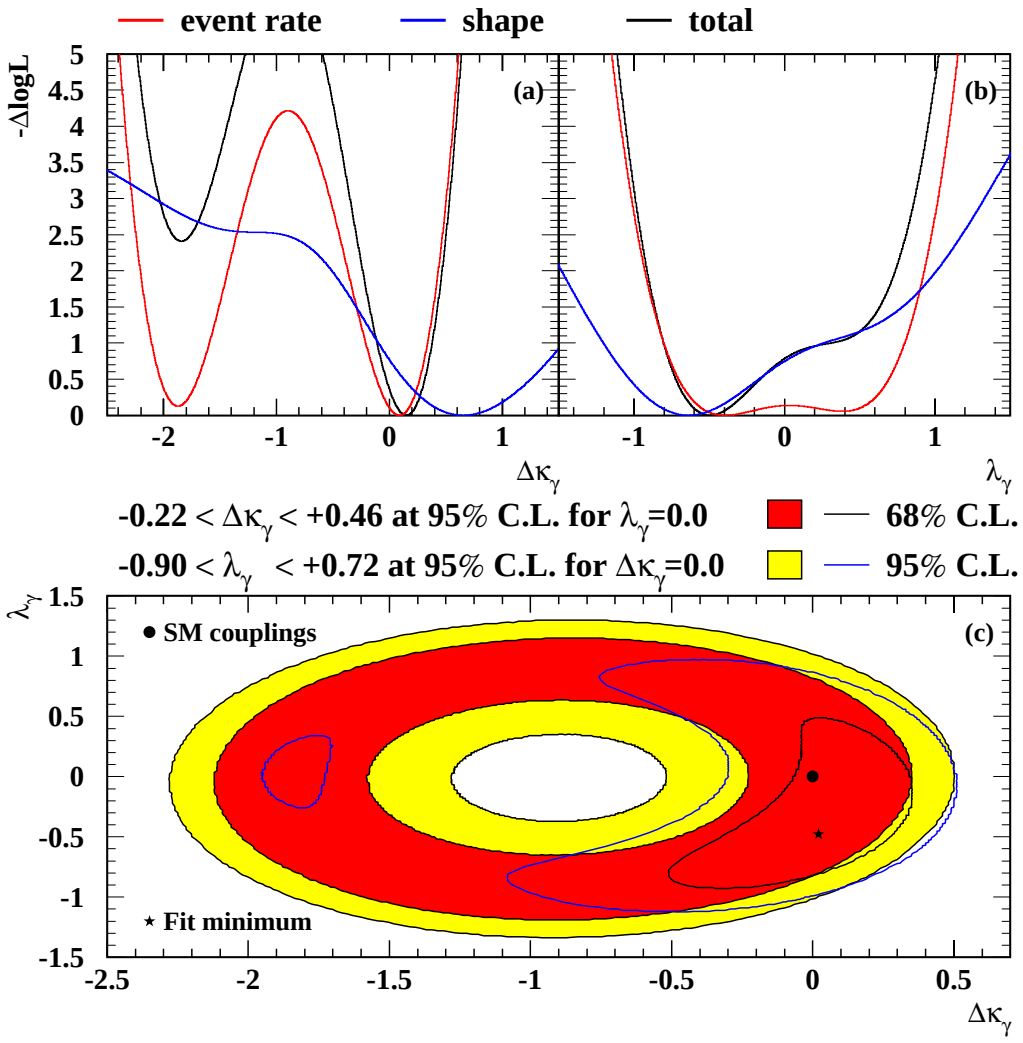

Figure 9.4: Log–likelihood difference curves (in black) for fits allowing one anomalous coupling to vary at a time: (*a*) $\Delta\kappa_\gamma$ and (*b*) λ_γ. The blue and red curves are obtained using only the cross section and shape information respectively. Projection (*c*) of the two–dimensional log–likelihood: the red and yellow areas show the regions allowed at the 68% CL and at the 95% CL by the fit which uses only the cross section information. The black and blue curves enclose the regions allowed by the fit which also uses the differential distributions of the selected events.

9.3 Systematic errors

Systematic errors on the Monte Carlo prediction for the number of selected events have been discussed in chapter 7. Each of the systematic uncertainties listed in table 7.1 is prop-

	$\Delta\kappa_\gamma$	λ_γ
Fit results	$-0.15^{+0.16}_{-0.17}$	$-0.50^{+0.33}_{-0.22}$
95% CL limits	$[-0.22, 0.46]$	$[-0.90, 0.72]$

Table 9.5: Results on $\Delta\kappa_\gamma$ and λ_γ parameters obtained with the fit using the event rate information and the p_{jj}^T and $|\cos\theta_{j_1} - \cos\theta_{j_2}|$ differential distributions. Each result is obtained setting the other parameter at its Standard Model value of zero. Only statistical errors are included.

agated to the measurement of anomalous couplings. All the systematic errors on $\Delta\kappa_\gamma$ and λ_γ are then added and convoluted with the log–likelihood functions to obtain the final results of the analysis, presented in the next section.

To estimate the effect of a systematic uncertainty in the predicted number of selected events the following likelihood is maximised:

$$\mathcal{L} \;=\; \int \mathcal{G}(f,\sigma)\mathcal{P}(N,n)\,df$$

where the Poisson distribution to observe N events in the data is expressed in terms of the expected number of events n as:

$$\mathcal{P}(N,n) \;=\; \frac{(f\,n(\Delta\kappa_\gamma,\lambda_\gamma))^N}{N!}\,e^{-f\,n(\Delta\kappa_\gamma,\lambda_\gamma)}.$$

The multiplicative factor f is introduced to take into account the systematic error on the expected number of events. It is allowed to vary from the central value of 1 with a Gaussian distribution $\mathcal{G}$ of width σ.

The likelihood actually used is slightly more complicated, since the systematic uncertainties estimated in chapter 7 are divided in two categories depending on the final state, and several correlations, between different centre–of–mass energies and between different final states, are taken into account. Two estimates of the systematic error on each coupling are obtained for a given uncertainty σ on the expected number of events:

- the difference between the value of the coupling which maximises the modified likelihood and the value obtained from the fit considering only statistical errors, and
- the value of the error which added in quadrature to the statistical uncertainty of the coupling reproduces the error obtained from the modified likelihood.

The largest of these two quantities is then taken as systematic error on the coupling parameter due to the uncertainty on the number of expected events.

The systematic errors are estimated with this procedure using for simplicity only the total cross section information in the fit for the anomalous couplings. Systematic uncertainties related to the use of the distributions of p_{jj}^T and of $|\cos\theta_{j_1} - \cos\theta_{j_2}|$ are considered separately. This approximation does not lead to a wrong estimation of the systematic error on the couplings, since the use of differential distributions does not improve the expected error resulting from the fit, but only restricts the region allowed at the 95% CL in λ_γ, making the likelihood curve more parabolic than the fit which uses only the event rate.

The systematic errors on $\Delta\kappa_\gamma$ and λ_γ obtained with this procedure from the uncertainties on the selected number of events are given in table 9.6.

Two additional sources of systematic errors are considered for the TGC's fit which uses the p_{jj}^T and $|\cos\theta_{j_1} - \cos\theta_{j_2}|$ distributions:

- The fit is repeated using a different parametrisation of the number of accepted events as a function of the TGC's. The EXCALIBUR program is used for the reweighting procedure instead of grc4f. The coefficients of the parametrisation produced by the two programs are all consistent within errors. The shift obtained in the fit to the OPAL data is much smaller than the statistical error, but it is nevertheless considered as a possible systematic error.

- The distributions of p_{jj}^T and $|\cos\theta_{j_1} - \cos\theta_{j_2}|$ are consistent between data and Monte Carlo. The effects of possible differences are studied repeating the fit after changing the bin boundaries of an amount corresponding to the difference in the mean values of the distributions of data and Monte Carlo. The resulting shifts of the couplings are taken as additional source of systematic uncertainty.

Source of systematic uncertainty	Systematic error on	
	$\Delta\kappa_\gamma$	λ_γ
Monte Carlo modelling of single W	0.029	0.054
Monte Carlo modelling of 4–fermions	0.012	0.030
Monte Carlo modelling of $q\overline{q}$	0.013	0.023
Monte Carlo statistics	0.025	0.030
detector response	0.027	0.029
trigger efficiency	0.004	0.007
luminosity	0.006	0.010
beam related backgrounds	0.003	0.004
W^+W^- veto	0.017	0.028
lepton veto	0.013	0.024
track multiplicity and quality	0.013	0.016
R_{ecal}	0.009	0.014
forward energy deposits	0.009	0.020
jet directions	0.013	0.027
missing momentum direction	0.013	0.027
acoplanarity	0.013	0.023
missing transverse momentum	0.014	0.023
likelihood variables	0.028	0.044
W^+W^- cross section	0.017	0.024
TGC's dependence	0.030	0.033
p_{jj}^T scale	0.007	0.025
$\|\cos\theta_{j_1} - \cos\theta_{j_2}\|$ scale	0.007	0.025
Total	0.079	0.124

Table 9.6: Systematic uncertainties on $\Delta\kappa_\gamma$ and λ_γ.

The total systematic error is obtained summing all possible sources in quadrature. The error amounts to 0.079 for $\Delta\kappa_\gamma$ and 0.124 for λ_γ. The difference between the two systematic errors is due to the shape of the likelihood curve near the minimum. The smaller sensitivity to the λ_γ parameter compared to $\Delta\kappa_\gamma$ has the consequence that equal changes in the expected number of events cause larger deviations.

The systematic errors are dominated for both measurements by the uncertainties in the Monte Carlo models of the $e^+e^- \to q\overline{q}'e^-\overline{\nu}_e$ process in the region dominated by single W production. These errors can be reduced with a correct treatment of the radiative corrections discussed in section 3.3 in the event generators. The other large systematic uncertainties are related either to the simulation of the detector response or to the Monte Carlo description of the variables used in the event selection. The estimates of these errors are dominated by the data statistics and should decrease once additional data are analysed.

9.4 Results

To obtain the final results of the analysis, the total systematic errors calculated in the previous section are incorporated into the log–likelihood functions of section 9.2. The corrected likelihood functions which result from the convolution with the distribution of the systematic errors, assumed to be Gaussian, are used to obtain new values for the TGC's, with modified errors which include the systematic uncertainties. These new values of the couplings are different from those obtained before the convolution due to the asymmetric nature of the likelihood functions. Since systematic uncertainties are currently smaller than the statistical errors, the changes in the log-likelihood curves, and therefore in the measured values of the couplings, in the errors and in the allowed region at the 95% CL, are small. For example, the size of the $\Delta\kappa_\gamma$ region allowed at the 95% CL, assuming that λ_γ is fixed at its $\mathcal{SM}$ value $\lambda_\gamma = 0$, increases by only 10% when systematic errors are convoluted with the log–likelihood.

The final results of the analysis are listed in table 9.7 and shown graphically in figure 9.5. They are consistent within two standard deviations with the expectation of the $\mathcal{SM}$. The largest deviation is observed for the λ_γ parameter. It is mostly due to the slight excess of data observed at $\sqrt{s} = 189$ GeV.

The final log–likelihood curves can be also used to interpret these measurements of the couplings in terms of the magnetic dipole μ_W and of the electric quadrupole q_W of the W boson, using the relations of section 1.3, which correspond to a coordinate transformation of the log–likelihood curve. The results for μ_W and q_W are listed in table 9.7.

Quantity	$\mathcal{SM}$ value	Measurement	95% CL limits
$\Delta\kappa_\gamma$	0	$0.15^{+0.18}_{-0.20}$	$[-0.26,0.50]$
λ_γ	0	$-0.47^{+0.39}_{-0.27}$	$[-0.97,0.75]$
μ_W	2	$2.20^{+0.30}_{-0.40}$	$[0.21,2.77]$
q_W	-1	$-0.69^{+0.29}_{-0.30}$	$[-1.43,-0.18]$

Table 9.7: Results on anomalous couplings, allowing only one of the couplings to vary in the fit, after the inclusion of systematic errors. The magnetic dipole moment μ_W and the electric quadrupole moment q_W are shown in units of $e\hbar/2m_W$ and $e\hbar/m_W^2$ respectively.

A thorough comparison of the results of this analysis with those obtained by the other LEP experiments, summarised in section 3.4, is not possible, since the expected errors are available only for the L3 analysis. The measurement of $\Delta\kappa_\gamma$, the coupling to which this analysis is mostly sensitive, is compared anyhow in table 9.8 and in figure 9.6 with the measurements obtained by the LEP experiments and the DØ collaboration. The measurement of λ_γ obtained in this analysis is of a quality similar to those obtained by the other

LEP experiments in the same channel, shown in table 3.3. All of these λ_γ measurements have anyhow a lower precision of those obtained from the study of the $e^+e^- \to W^+W^-$ process.

The errors on the $\Delta\kappa_\gamma$ coupling obtained in the analysis of the single W final state performed by the ALEPH [86] and by the L3 [45] collaborations are quite similar to the errors obtained in this analysis. However in the ALEPH analysis the region $\Delta\kappa_\gamma \approx -2$ is not excluded at the 95% CL, whereas in this analysis it is excluded at 2.4 standard deviations. This difference is due to the use in this analysis of the the transverse momentum and angular distribution of jets in the TGC's fit. The L3 analysis considers only data collected

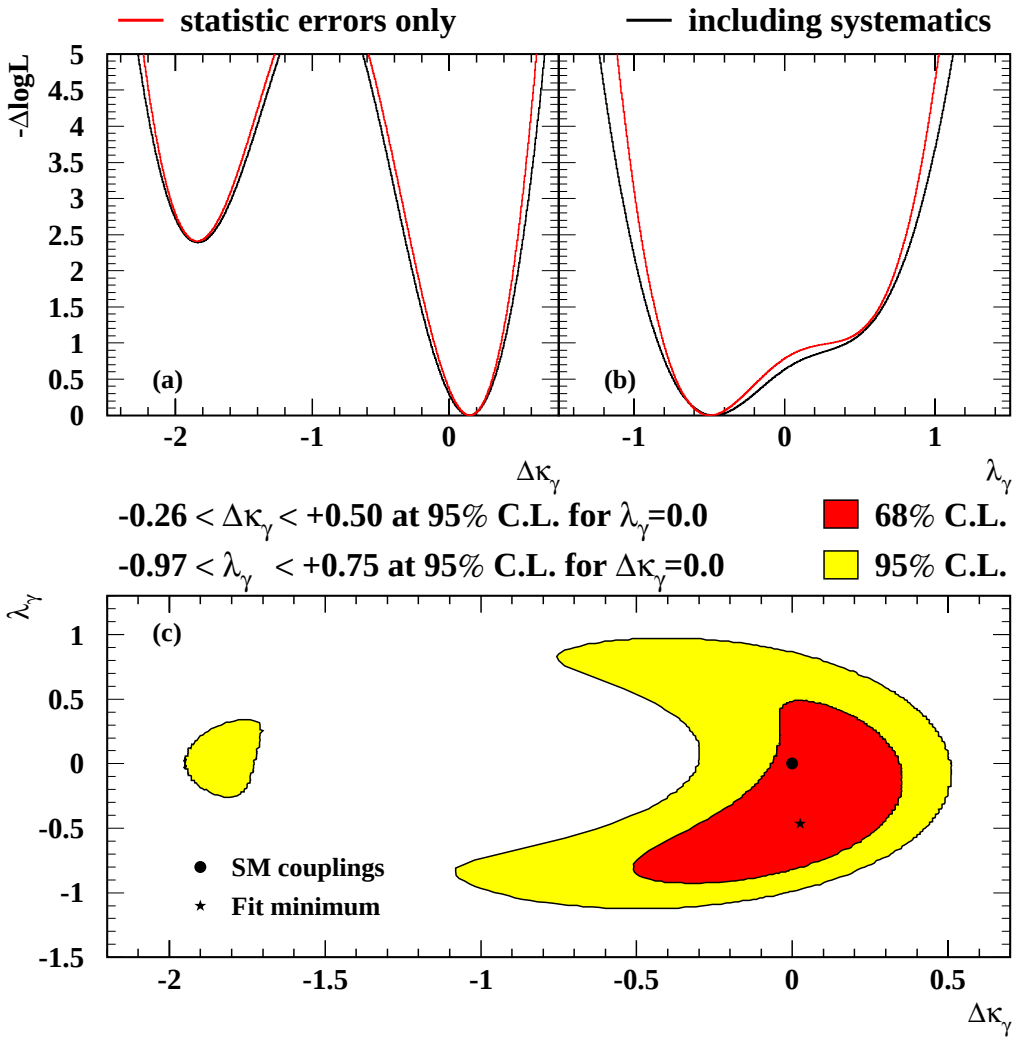

Figure 9.5: Log–likelihood difference curves for fits allowing one anomalous coupling to vary at a time: (*a*) $\Delta\kappa_\gamma$ and (*b*) λ_γ. Black curves are obtained after inclusion of the systematic errors, while for the red curves only statistical errors are considered. Projection (*c*) of the two–dimensional log–likelihood: red and yellow areas show the regions allowed at the 68% CL and at the 95% CL. The maximum of the log–likelihood is indicated by the $\star$.

in 1996 and 1997 at centre–of–mass energies between 161 and 183 GeV. Including also the leptonic decay channel they obtain an expected error for the $\Delta\kappa_\gamma$ parameter of 0.34, which is 10% larger than the expected error for this analysis, when applied to a data set of similar

integrated luminosity. The error on $\Delta\kappa_\gamma$ obtained in the DELPHI analysis [44] is by a factor 1.5 larger than the error obtained in this analysis. This is the consequence of the lower selection efficiency for the $q\overline{q}'e\overline{\nu}_e$ final state in the single W kinematic region.

Contrary to the precision reached in the λ_γ parameter, all measurements of the $\Delta\kappa_\gamma$ coupling obtained from the study of the $e^+e^- \to W^+W^-$ process give results which are worse than the one obtained in this analysis. An exception is represented by the L3 measurement [45], which is currently the best measurement of $\Delta\kappa_\gamma$. Also the measurements of $\Delta\kappa_\gamma$ performed at Tevatron by the DØ collaboration have a precision lower than that obtained from the analyses of single W production.

Experiment	Channel	Measurement	95% CL limits
This analysis	Single W	$0.15^{+0.18}_{-0.20}$	$[-0.26, 0.50]$
ALEPH [86]	Single W	$-0.24^{+0.18}_{-0.24}$	$[-2.12, 0.23]$
DELPHI [44]	Single W	$0.25^{+0.28}_{-0.38}$	
L3 [45]	Single W	$0.12^{+0.37}_{-0.40}$	$[-0.83, 0.62]$
OPAL [41]	W pairs	$-0.00^{+0.27}_{-0.19}$	$[-0.36, 0.83]$
ALEPH [43]	W pairs	$0.11^{+0.36}_{-0.19}$	$[-0.19, 0.82]$
DELPHI [44]	W pairs	$0.27^{+0.27}_{-0.31}$	$[-0.14, 0.82]$
L3 [45]	W pairs	$-0.12^{+0.16}_{-0.14}$	$[-0.38, 0.22]$
DØ [56]	All channels	$-0.08^{+0.34}_{-0.34}$	$[-0.67, 0.56]$

Table 9.8: Summary of results on the $\Delta\kappa_\gamma$ coupling.

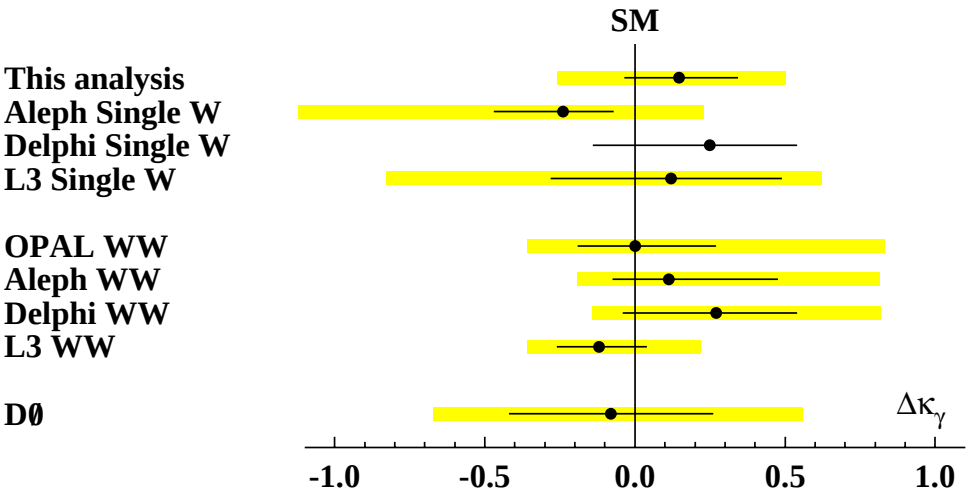

Figure 9.6: Comparison of results on $\Delta\kappa_\gamma$ obtained from the analysis of single W and W pair final states at LEP and of pair production of weak bosons at Tevatron. The 95% CL limits are not available for the DELPHI single W analysis. The L3 single W analysis is based only on the $\sqrt{s} = 161$–183 GeV data set. Yellow bands indicate regions allowed at the 95% CL. The vertical line indicates the $\mathcal{SM}$ prediction $\Delta\kappa_\gamma = 0$.

9.5 Combination of results on anomalous couplings

The measurements of the $\Delta\kappa_\gamma$ and λ_γ couplings obtained in the previous section are compatible with those obtained from the analysis of the $e^+e^- \to W^+W^-$ process (section 2.2, [41]) and do not show any deviation from the $\mathcal{SM}$ predictions. The two results are obtained at different energy scales: in single W production the couplings are measured at a Q^2 scale close to zero, whereas in the $e^+e^- \to W^+W^-$ process the couplings are measured at $Q^2 = s$. Assuming that any variation of the couplings with the energy scale is not observable with the current precisions, the two measurements can be combined to obtain better constraints on the TGC's. This assumption on the scale dependence of the couplings is equivalent to state that any possible deviation of the couplings from their $\mathcal{SM}$ values is

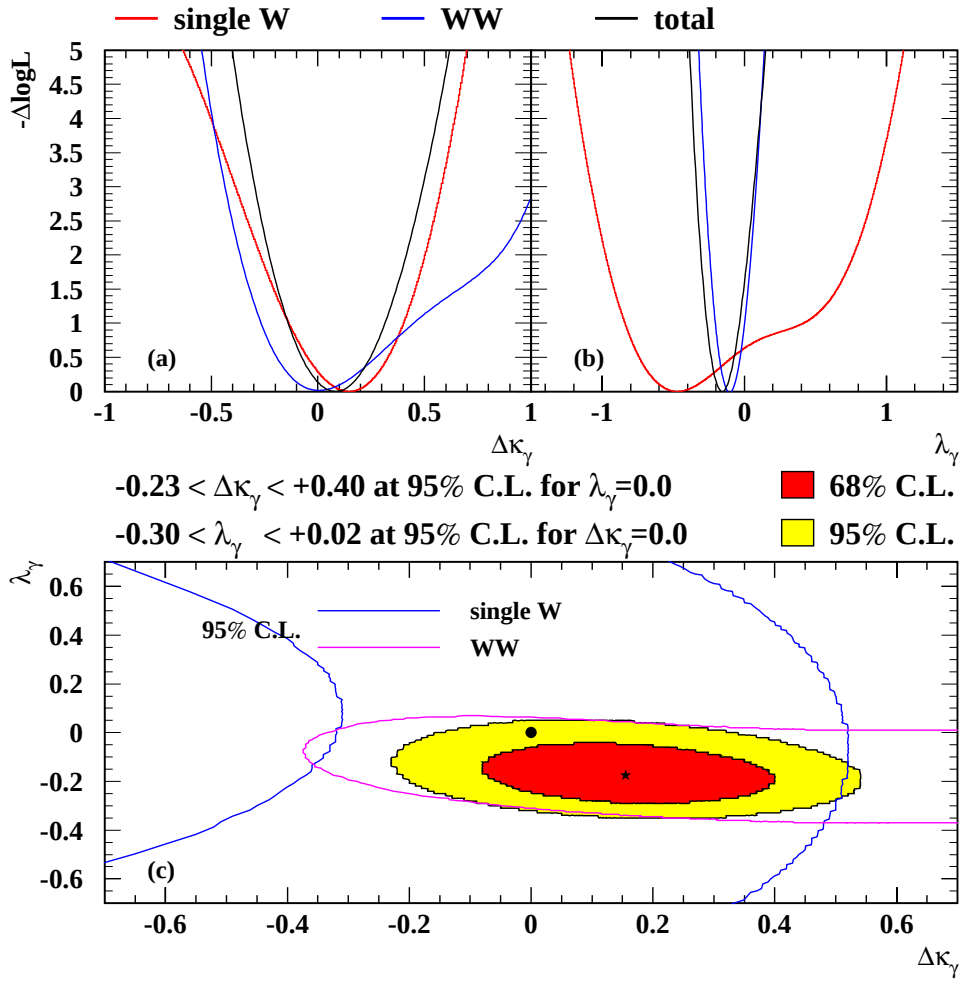

Figure 9.7: Combination of the log–likelihood curves with the analysis of [41]. Log–likelihood difference curves for fits allowing one anomalous coupling to vary at a time: (*a*) $\Delta\kappa_\gamma$ and (*b*) λ_γ. Projection (*c*) of the two–dimensional log–likelihood: red and yellow areas show the regions allowed at the 68% CL and at the 95% CL. The maximum of the log–likelihood is indicated by the $\star$.

induced by effects which occur at scales much higher than the current LEP centre–of–mass energy (sections 1.5 and 1.6).

The combination of the results is simply performed by adding the log–likelihood curves of the two analyses and searching for the new maxima, and neglecting any correlation between the results of the two analyses. The veto on events which are already selected for the measurement of the gauge couplings in the $e^+e^- \to W^+W^-$ process (section 6.3) ensures that the two samples are statistically independent. Therefore a correlation between the two analyses can result only from common systematic errors, which for the currently available data sets are smaller than statistical uncertainties. As discussed in section 2.2 the main systematic errors in the $e^+e^- \to W^+W^-$ process come from hadronisation uncertainties in the $W^+W^- \to q\overline{q}'\ell\overline{\nu}_\ell$ channel and Bose–Einstein and colour reconnection effects in the $W^+W^- \to q\overline{q}'q\overline{q}'$ channel. For the analysis of the $q\overline{q}'e\overline{\nu}_e$ final state in the kinematic region dominated by single W production the main sources of uncertainties are instead the differences between Monte Carlo models and detector effects. Any possible correlation of systematic uncertainties is therefore negligible at the current level of precision.

The results of the combination of the two measurements of the $\Delta\kappa_\gamma$ and λ_γ are given in table 9.9 and displayed graphically in figure 9.7. As discussed in chapter 5 the two analyses are complementary. The analysis of the W^+W^- final states has a much higher sensitivity to the λ_γ coupling, whereas the $q\overline{q}'e\overline{\nu}_e$ final state in the kinematic region dominated by single W production is better suited to measure the $\Delta\kappa_\gamma$ parameter. As a consequence, when the results of this analysis are combined with those of the W^+W^- final state the error on $\Delta\kappa_\gamma$ is approximately halved. This brings the combined result of the OPAL experiment in line with the results of other experiments given in table 2.1. It should be noted that this combination of results actually leads to an increase of the final error on λ_γ. This is due to the statistical fluctuation towards negative values of λ_γ present in the analysis of the $q\overline{q}'e\overline{\nu}_e$ final state in the single W kinematic region.

Quantity	$\mathcal{SM}$ value	Measurement	95% CL limits
$\Delta\kappa_\gamma$	0	$0.08^{+0.16}_{-0.16}$	$[-0.23,0.40]$
λ_γ	0	$-0.16^{+0.08}_{-0.08}$	$[-0.30,0.02]$
μ_W	2	$1.82^{+0.16}_{-0.12}$	$[1.58,2.14]$
q_W	-1	$-0.65^{+0.15}_{-0.16}$	$[-0.99,-0.38]$

Table 9.9: Combined results on TGC's of the $e^+e^- \to W^+W^-$ analysis (table 2.1) and of the $q\overline{q}'e\overline{\nu}_e$ final state in the single W kinematic region (table 9.7), allowing only one of the couplings to vary at a time. The magnetic dipole moment μ_W and the electric quadrupole moment q_W are shown in units of $e\hbar/2m_W$ and $e\hbar/m_W^2$ respectively.

Conclusions

Single W production in the $e^+e^- \to q\overline{q}'e^-\overline{\nu}_e$ reaction has been studied using a data sample with an integrated luminosity of 251 pb^{-1} collected between 1996 and 1998 with the OPAL detector at LEP2. The Standard Model predicts for this process a cross section which rises from 200 fb at $\sqrt{s} = 161$ GeV to 480 fb at $\sqrt{s} = 189$ GeV. Signal events are characterised by two acoplanar jets and missing transverse momentum, while the electron is scattered mostly along the beam pipe. An event selection has been developed which has an efficiency of 35% for the signal, for a purity close to 50%. A total of 92 events is selected in data, for a Monte Carlo prediction of (87.6 ± 3.7) events. The Monte Carlo provides an adequate description of all the kinematic properties of the selected sample.

The selected events are used to measure the κ_γ and λ_γ parameters describing the triple gauge boson vertex γW^+W^-. A new method, which uses also the kinematic distributions of the selected events to constrain the coupling parameters, has been applied for the first time in this analysis to this channel, allowing a reduction of the errors in κ_γ and λ_γ. The results and 95% CL limits, including statistical and systematic errors, are:

$$\begin{aligned} \kappa_\gamma &= 1.15^{+0.18}_{-0.20} \qquad & \kappa_\gamma &\in [0.74, 1.50] \quad \text{at } 95\%\ \text{CL}\ , \\ \lambda_\gamma &= -0.47^{+0.39}_{-0.27} \qquad & \lambda_\gamma &\in [-0.97, 0.75] \quad \text{at } 95\%\ \text{CL}\ , \end{aligned}$$

in agreement with the Standard Model prediction $\kappa_\gamma = 1$ and $\lambda_\gamma = 0$. This represents the second best measurement of the κ_γ parameter using a single analysis. These measurements of the couplings have been combined with those obtained from the study of the $e^+e^- \to W^+W^-$ reaction to obtain:

$$\begin{aligned} \kappa_\gamma &= 1.08^{+0.16}_{-0.16} \qquad & \kappa_\gamma &\in [0.77, 1.40] \quad \text{at } 95\%\ \text{CL}\ , \\ \lambda_\gamma &= -0.16^{+0.08}_{-0.08} \qquad & \lambda_\gamma &\in [-0.30, 0.02] \quad \text{at } 95\%\ \text{CL}\ . \end{aligned}$$

This represent an improvement of a factor 2 in the κ_γ error with respect to the measurement performed by the OPAL collaboration using only the W^+W^- final state.

These measurements of the triple gauge boson couplings can be also interpreted as measurements of the magnetic dipole moment μ_W and of the electric quadrupole moment q_W of the W boson:

$$\begin{aligned} \mu_W &= (1.82^{+0.16}_{-0.12})\frac{e\hbar}{2m_W} \qquad & \mu_W &\in [1.58, 2.14]\frac{e\hbar}{2m_W} \quad \text{at } 95\%\ \text{CL}\ , \\ q_W &= (-0.65^{+0.15}_{-0.16})\frac{e\hbar}{m_W^2} \qquad & q_W &\in [-0.99, -0.38]\frac{e\hbar}{m_W^2} \quad \text{at } 95\%\ \text{CL}\ . \end{aligned}$$

While the measurement of μ_W agrees with the Standard Model prediction $\mu_W = 2e\hbar/2m_W$,

the measurement of q_W deviates by two standard deviations from the $\mathcal{SM}$ value $q_W = -e\hbar/m_W^2$.

An improvement of the precision of these measurements by a factor 1.5 should be possible in the future by applying this analysis to the data collected in 1999 (250 pb^{-1} at $\sqrt{s}$ = 192–202 GeV) and to the data which will be collected during the final year of LEP running. This will bring the statistical error on κ_γ close to the current systematic error. However since the determination of most systematic uncertainties is dominated by the statistics of the available control samples, also the systematic errors should decrease by a similar amount. Measurements of the triple gauge couplings of higher precision will only be possible at future colliders like the LHC or the proposed e^+e^- linear collider.

The event selection has also been used to measure the *t*–channel cross section for the $e^+e^- \to q\overline{q}'e^-\overline{\nu}_e$ reaction at $\sqrt{s} = 183$ and 189 GeV, for invariant masses of the quark pair, $m_{q\overline{q}'}$, larger than 40 GeV/c^2, obtaining the following results:

$$\begin{aligned}\sigma(\sqrt{s} = 183\,\mathrm{GeV}) &= (340^{+200}_{-170} \pm 45)\,\mathrm{fb}\ ,\\ \sigma(\sqrt{s} = 189\,\mathrm{GeV}) &= (615^{+150}_{-135} \pm 60)\,\mathrm{fb},\end{aligned}$$

where the first error is statistical and the second systematic.

These results are in agreement with the Standard Model predictions of approximately 400 fb and 480 fb at the two centre–of–mass energies. Other measurements of the $e^+e^- \to q\overline{q}'e^-\overline{\nu}_e$ cross section of similar precision have been performed also by the other LEP collaborations. This is the first measurement which adopts a new signal definition which will be in the future used by all experiments to provide combined results for this channel.

Bibliography

[1] S.L. Glashow, Nucl. Phys. **22** (1961) 579,
A. Salam in *"Proceedings 8^{th} Nobel Symposium"*, edited by Aspenaegarden, Almqvist and Wicksel (Stockholm), (1967) 367,
S. Weinberg, Phys. Rev. Lett. **46** (1973) 138,
G. 't Hooft, Phys. Lett. **B37** (1971) 195,
N. Cabibbo, Phys. Rev. Lett. **10** (1963) 531,
S.L. Glashow, J. Iliopoulos, L. Maiani, Phys. Rev. **D2** (1970) 1285,
M. Kobayashi and T. Maskawa, Prog. Theor. Phys. **49** (1973) 652.

[2] A nice review of most current measurements in this field and of proposals for new experiments is: C.K. Jung, *"Neutrino masses and oscillations"*, talk given at the *"International Europhysics Conference High Energy Physics 99"*, Tampere, Finland, 15–21 July 1999, to be published in the proceedings. An exhaustive list of references can be found at the following WWW address: http://www.hep.anl.gov/ndk/longbnews/index.html.

[3] A rather complete account of the crucial experimental discovery and theoretical innovations can be found in the book by R.N. Cahn and G. Goldhaber, *"The experimental foundations of particle physics"*, Cambridge University Press (1989).

[4] F.J. Hasert *et al.*, Phys. Lett. **B46** (1973) 138.

[5] UA1 Collaboration, G. Arnison *et al.*, Phys. Lett. **B122** (1983) 103,
UA1 Collaboration, G. Arnison *et al.*, Phys. Lett. **B126** (1983) 398,
UA2 Collaboration, M. Banner *et al.*, Phys. Lett. **B122** (1983) 476,
UA2 Collaboration, P. Bagnaia *et al.*, Phys. Lett. **B129** (1983) 130.

[6] The CDF Collaboration, F. Abe *et al.*, Phys. Rev. Lett. **73** (1994) 225,
The CDF Collaboration, F. Abe *et al.*, Phys. Rev. **D50** (1994) 2966,
The CDF Collaboration, F. Abe *et al.*, Phys. Rev. Lett. **74** (1995) 2626,
The DØ Collaboration, S. Abachi *et al.*, Phys. Rev. Lett. **74** (1995) 2632.

[7] NA31 Collaboration, G.D. Barr *et al.*, Phys. Lett. **B317** (1993) 1203,
KTeV Collaboration, A. Alavi–Harati *et al.*, Phys. Rev. Lett. **83** (1999) 22,
NA48 Collaboration, V. Fanti *et al.*, Phys. Lett. **B465** (1999) 335.

[8] CDF Collaboration, T. Affolder *et al.*, *"A measurement of sin2β from $B \to J/\psi K^0_S$ with the CDF detector"*, preprint FERMILAB–PUB/99–225–E, September 1999, submitted for publication in Phys. Rev. **D**.

[9] The most recent lower limit at the 95% CL on the mass of the Higgs boson is $m_{\rm H} > 102.6$ GeV/c^2, P. McNamara, *"LEP Higgs working group status report"* talk given at the 52^{nd} session of the *"LEP Experiments Committee"*,, 16 September 1999.

[10] A complete account of the current precision predictions of the $\mathcal{SM}$ can be found in: D. Bardin and G. Passarino, *"The standard model in the making. Precision study of the electroweak interactions"*, Oxford Science Publications (1999).

[11] F.J.M. Farley and E. Picasso, *"The muon g−2 experiment"* in *"Quantum electrodynamics"*, edited by T.Kinoshita, World Scientific (1990) 479.

[12] Final results of the data collected during the LEP1 phase are not yet available from all the experiments. A comprehensive review of these measurements is: M. Martinez *et al.*, Rev. Mod. Phys. **71** (1999) 575. The last updated results can be found in: J. Mnich, *"Tests of the standard model"*, talk given at the *"International Europhysics Conference High Energy Physics 99"*, Tampere, Finland, 15–21 July 1999, preprint CERN–EP/99–143, October 1999, to be published in the proceedings. Most recent results and some older references can be found on the WWW site: http://www.cern.ch/LEPEWWG/.

[13] The LEP Electroweak Working Group and the SLD Heavy Flavour and Electroweak Groups, *"A combination of preliminary electroweak measurements and constraints on the Standard Model"*, preprint CERN–EP/99–15, February 1999.

[14] The most up–to–date value of m_t can be found in: M. Lancaster, *"Precision electroweak physics at hadron machines"*, talk given at the *"Lepton–Photon '99, XIX International Symposium on Lepton and Photon Interactions at High Energies"*,, Stanford University, California, 9–14 August 1999, to be published in the proceedings, preprint hep-ex/9912031, December 1999.

[15] This result is usually shown using the *S*, *T* and *U* variables proposed by M. Peskin and T. Takeuchi, Phys. Rev. Lett. **65** (1990) 964, or the ε parameters of G. Altarelli, R. Barbieri and S. Jadach, Nucl. Phys. **B369** (1992) 3.

[16] Physics at LEP2, G. Altarelli, T. Sjöstrand and F. Zwirner, CERN 96–01.

[17] The most recent value for $m_{\rm W}$ can be found in [12] and [14]: $m_{\rm W} = 80.394 \pm 0.062$ GeV/c^2.

[18] P.W. Higgs, Phys. Lett. **12** (1964) 132, Phys. Lett. **13** (1964) 508, Phys. Rev. **145** (1966) 1156.

[19] D.A. Ross and M. Veltman, Nucl. Phys. **B95** (1975) 135,
M. Veltman, Nucl. Phys. **B123** (1977) 89.

[20] S. Weinberg, Phys. Rev. **D19** (1979) 1266,
L. Susskind, Phys. Rev. **D20** (1979) 2619,
P.Sikivie *et al.*, Nucl. Phys. **B173** (1980) 189.

[21] S. Dawson, A. Likhoded, G. Valencia and O. Yushchenko, *"Probing quartic couplings through three gauge boson production at an e^+e^- linear collider"*, proceedings of the *"1996 DPF/DPB Summer Study on New Directions for High–Energy Physics (Snowmass '96)"*,

Snowmass, Colorado, 25 June–12 July 1996, preprint hep-ph/9610299, July 1996,
W.J. Stirling and A. Werthenbach, *"Anomalous quartic couplings in $W^+W^-\gamma, Z^0Z^0\gamma$ and $Z^0\gamma\gamma$ production at present and future e^+e^-colliders"*, preprint hep–ph/9903315, March 1999, to be published in Eur. Phys. J. **C**,
W.J. Stirling and A. Werthenbach, *"Anomalous quartic couplings in $\nu\overline{\nu}\gamma\gamma$ production via WW fusion at LEP2"*, preprint hep-ph/9907235, July 1999, to be published in Phys. Lett. **B**,
G. Bélanger, F. Boudjema, Y. Kurihara, D. Perret–Gallix and A. Semenov, *"Bosonic quartic couplings at LEP2"*, preprint hep-ph/9908254, August 1999.

[22] The OPAL Collaboration, G. Abbiendi *et al.*, *"Measurement of the $W^+W^-\gamma$ cross-section and first direct limits on anomalous electroweak quartic couplings"*, preprint CERN-EP/99-130, September 1999, submitted for publication in Phys. Lett. **B**,
The OPAL Collaboration, *"Constraints on anomalous quartic gauge boson couplings from acoplanar photon pair events"*, OPAL Physics Note PN410, August 1999,
L3 Collaboration, M. Acciarri *et al.*,*"Measurement of the $e^+e^- \rightarrow Z^0\gamma\gamma$ cross section and determination of quartic gauge boson couplings at LEP"*, preprint CERN–EP/2000-006, January 2000, submitted for publication in Phys. Lett. **B**.

[23] K.J.F. Gaemers and G.J. Gounaris, Zeit. Phys. **C1** (1979) 256,
K. Hagiwara, R.D. Peccei, D. Zeppenfeld and K. Hikasa, Nucl. Phys. **B282** (1987) 253.

[24] C.H. Llewellyn Smith, Phys. Lett. **B46** (1973) 233,
J.M. Cornwall, D.N. Levin and G.Tiktopoulos, Phys. Rev. **D10** (1974) 1145,
U. Baur and D. Zeppenfeld, Phys. Lett. **B201** (1988) 383.

[25] J. Ellison and J. Wudka, Ann. Rev. Nucl. Part. Sci. **48**(1998)38.

[26] see for example the references [4]–[7] of [29].

[27] A. De Rújula, M.B. Gavela, P. Hernandez and E. Massó, Nucl. Phys. **B384** (1992) 3.

[28] W. Buchmüller and D. Wyler, Nucl. Phys. **B288** (1986) 621.

[29] K. Hagiwara, S. Ishihara, R. Szalapski and D. Zeppenfeld, Phys. Lett. **B283** (1992) 353, Phys. Rev. **D48** (1993) 2182.

[30] M. Bilenky, J.L. Kneur, F.M. Renard and D. Schildknecht, Nucl. Phys. **B409** (1993) 22, Nucl. Phys. **B419** (1994) 240.

[31] F. Boudjema, *"Tests on the hierarchy of trilinear and quadrilinear weak bosons couplings at the NLC and comparison with the LHC/SSC"*, proceedings of the *"2nd International Workshop on Physics and Experiments with e^+e^- Linear Colliders"*, Waikoloa, Hawaii, 26–30 April 1993, p. 712, preprint hep–ph/9308343.
F. Boudjema, *"Aspects of W physics at the linear collider"*, proceedings of the *"3rd Workshop on Physics and Experiments with e^+e^- Linear Colliders (LCWS 95)"*, Iwate, Japan, 8–12 September 1995, p. 199, preprint hep–ph/9701409, January 1997.

[32] J. Bagger, S. Dawson and G. Valencia, Nucl. Phys. **B399** (1993) 364,
S. Dawson and G. Valencia, Phys. Rev. **D49** (1994) 2188.

[33] T. Applequist and C. Bernard, Phys. Rev. **D22** (1980) 200,
A. Longhitano, Phys. Rev. **D22** (1980) 1166, Nucl. Phys. **B188** (1981) 118,
T. Applequist and Guo–Hong Wu, Phys. Rev. **D48** (1993) 3235.

[34] J. Fleischer, J.–L. Kneur, K. Kolodziej, M. Kuroda and D. Schildknecht, Nucl. Phys. **B378** (1992) 443, Nucl. Phys. **B426** (1994) 246,
E.N. Argyres, G.Katsilieris, A.B. Lahanas, C.G. Papadopoulos and V. Spanos, Nucl. Phys. **B391** (1993) 23,
J. Papavassiliou and K.Philippides, Phys. Rev. **D48** (1993) 4255.

[35] A.B. Lahanas and V.C. Spanos, Phys. Lett. **B334** (1994) 378,
E.N. Argyres, A.B. Lahanas, C.G. Papadopoulos and V.C. Spanos, Phys. Lett. **B383** (1996) 63,
A. Arhrib, J.–L. Kneur and G. Moultaka, Phys. Lett. **B376** (1996) 127.

[36] A. Arzt, M.B. Einhorn and J. Wudka, Phys. Rev. **D49** (1994) 1370, Nucl. Phys. **B433** (1995) 41.

[37] R. Kleiss and W.J. Stirling, Nucl. Phys. **B262** (1985) 235,
K. Hagiwara and D. Zeppenfeld, Nucl. Phys. **B274** (1986) 1

[38] R.D. Field and R.P. Feynman, Nucl. Phys. **B136** (1978) 1.

[39] M.Diehl and O Nachtmann, Zeit. Phys. **C62** (1994) 397, Eur. Phys. J. **C1** (1998) 177,
C.G. Papadopoulos, Phys. Lett. **B386** (1996) 442,
G.K. Fanourakis *et al.*, Nucl. Instr. Meth. **A414** (1998) 399, Nucl. Instr. Meth. **A430** (1999) 455, Nucl. Instr. Meth. **A430** (1999) 474.

[40] G. Gounaris, J. Layssac, G.Moutalka and F.M. Renard, Int. J. Mod. Phys. **A19** (1993) 3285.

[41] The OPAL Collaboration, K. Ackerstaff *et al.*, Phys. Lett. **B397** (1997) 315,
The OPAL Collaboration, K. Ackerstaff *et al.*, Eur. Phys. J. **C2** (1998) 597,
The OPAL Collaboration, G. Abbiendi *et al.*, Eur. Phys. J. **C8** (19999) 191,
The OPAL Collaboration, G. Abbiendi *et al.*, *"Measurement of triple gauge boson couplings from W^+W^- production at LEP energies up to 189 GeV"*, OPAL Physics Note PN375, march 1999.

[42] L3 Collaboration, *"Direct observation of longitudinally polarised $W^{\pm}$ bosons"*, preprint CERN-EP/99-176, November 1999, submitted for publication in Phys. Lett. **B**,

[43] ALEPH Collaboration, R. Barate *et al.*, Phys. Lett. **B422** (1998) 369,
ALEPH Collaboration, R. Barate *et al.*, *"Measurements of triple gauge boson couplings at 183–189 GeV"*, ALEPH–CONF 99–072, July 1999.

[44] DELPHI Collaboration, P. Abreu *et al.*, Phys. Lett. **B423** (1998) 194,
DELPHI Collaboration, P. Abreu *et al.*, Phys. Lett. **B459** (1999) 382,
DELPHI Collaboration, P. Abreu *et al.*, *"Measurement of trilinear gauge couplings in e^+e^- collisions at 189 GeV"*, DELPHI 99–63 CONF 250, June 1999.

[45] L3 Collaboration, M. Acciarri *et al.*, Phys. Lett. **B413** (1997) 176,
L3 Collaboration, M. Acciarri *et al.*, Phys. Lett. **B467** (1999) 171, L3 Collaboration, M. Acciarri *et al.*, *"Preliminary results on the measurement of triple gauge boson couplings of the W boson at LEP"*, L3 Note 2378, March 1999.

[46] The combination of results from single experiments is performed as explained in: The LEP TGC combination group *"A combination of preliminary measurements of triple gauge boson coupling parameters measured by the LEP experiments"*, internal note LEPEWWG/TGC/97–01, September 1997. The most recent results can be found on the WWW page: http://www.cern.ch/LEPEWWG/tgc/.

[47] The notes describing the preliminary results used for this table can be found on the WWW server: http://www.physics.helsinki.fi/ abstract/papers/papers0.html.

[48] A.Jacholkowaska, J. Kalinowski and Z. Wąs, Eur. Phys. J. **C6** (1999) 485.

[49] ALEPH Collaboration, R. Barate *et al.*, Phys. Lett. **B445** (1998) 445,
ALEPH Collaboration, R. Barate *et al.*, *"Single– and multi–photon production in e^+e^- collisions at a centre–of–mass energy of 188.6 GeV"*, ALEPH–CONF 99–046, June 1999.

[50] U. Baur, T. Han and J. Ohnemus, Phys. Rev. **D48** (1993) 5140, Phys. Rev. **D51** (1995) 3381, Phys. Rev. **D53** (1996) 1098.

[51] CDF Collaboration, F. Abe *et al.*, Phys. Rev. Lett. **74** (1995) 1936.

[52] DØ Collaboration, S. Abachi *et al.*, Phys. Rev. Lett. **75** (1995) 1034, Phys. Rev. Lett. **78** (1997) 3634, Phys. Rev. **D56** (1997) 6742.

[53] CDF Collaboration, F. Abe *et al.*, Phys. Rev. Lett. **78** (1997) 4536.

[54] CDF Collaboration, F. Abe *et al.*, Phys. Rev. Lett. **75** (1995) 1017.

[55] DØ Collaboration, S. Abachi *et al.*, Phys. Rev. Lett. **75** (1995) 1023, Phys. Rev. Lett. **77** (1996) 3303, Phys. Rev. **D56** (1997) 6742, Phys. Rev. Lett. **79** (1997) 1441, Phys. Rev. **D58** (1998) 051101, Phys. Rev. **D60** (1999) 072002.

[56] DØ Collaboration, S. Abachi *et al.*, Phys. Rev. **D58** (1998) 031102, Phys. Rev. **D60** (1999) 072002.

[57] D. Amidei *et al.*, *"Future electroweak physics at the Fermilab Tevatron: report of the TEV-2000 study group"*, FERMILAB–PUB–96–082, April 1996, available from the WWW page: http://www-theory.fnal.gov/TeV2000.html.

[58] P. Molnár and M. Grünewald, Phys. Lett. **B461** (1999) 149.

[59] J.J. van der Bij and B. Kastening, Phys. Rev. **D57** (1998) 2903.

[60] S. Alam, S. Dawson and R. Szalapski, Phys. Rev. **D57** (1998) 1577,
F.M. Renard and C. Verzegnassi, Phys. Lett. **B345** (1995) 500, O.J.P. Eboli, S.M.Lietti, M.C. Gonzalez–Garcia and S.F.Novaes, Phys. Lett. **B339** (1994) 119,
O.J.P. Eboli, M.C. Gonzalez–Garcia and S.F.Novaes, *"Indirect constraints on the triple gauge boson couplings from $Z^0 \to b\bar{b}$ partial width: an update"*, preprint hep–ph/9811388, November 1998.

[61] G. Burdman, Phys. Rev. **D59** (1999) 035001,
Xiao–Gang He, Phys. Lett. **B460** (1999) 405.

[62] P. Méry, S.E. Moubarik, M. Perrottet and F.M. Renard, Zeit. Phys. **C46** (1990) 229,
F. Boudjema, K. Hagiwara, C. Hamzaoui and K. Numata, Phys. Rev. **D43** (1991) 2223.

[63] ATLAS Collaboration, "ATLAS *detector and physics performance. Technical design report*", ATLAS TDR 14, CERN / LHCC 99–14, Volume 2, p. 553, May 1999, available from the WWW page: http://atlasinfo.cern.ch/Atlas/GROUP/PHYSICS/TDR/access.html.

[64] Studies on the achievable precision in TGC measurements at high energy e^+e^- colliders can be found in the proceedings of "*Workshop on Physics and Experiments with e^+e^- Linear Colliders*" conference series (held at Saariselka, Finland, 9–14 April 1991, proceedings edited by R. Orava, P. Eerola and M. Nordberg, published by World Scientific, River Edge, New Jersey (1992), Waikoloa, Hawaii, 26–30 April 1993, proceedings edited by F.A. Harris, S.L. Olsen, S. Pakvasa and X. Tata, published by World Scientific, River Edge, New Jersey (1993), Iwate, Japan, 8–12 September 1995, proceedings edited by A. Miyamoto, Y. Fujii, T. Matsui and S. Iwata, published by World Scientific, Singapore (1996), Sitges, Spain, 28 April–5 May 1999, proceedings to be published by World Scientific), and in the proceedings of the "*Joint ECFA/DESY Study on Physics and Detectors for a Linear Electron–Positron Collider*" (proceedings are published as DESY reports numbers: DESY 92–123A / B / C, DESY 96–123D and DESY 97-123E).

[65] E. Boos and T. Ohl, Phys. Rev. Lett. **83** (1999) 480.

[66] C.G. Papadopoulos, Phys. Lett. **B263** (1991) 298, Phys. Lett. **B333** (1994) 202.

[67] T. Tsukamato and Y. Kurihara, Phys. Lett. **B389** (1996) 162.

[68] G. Passarino, "*The single W production case*", preprint hep–ph/9810416, October 1998,
G. Passarino, "*Single W production and fermion loop scheme: numerical results*", preprint hep–ph/0001212, January 2000.

[69] F.A. Berends, R. Kleiss and R. Pittau, Nucl. Phys. **B424** (1994) 308.

[70] W. Beenakker, A. Denner, S. Dittmaier, J. Hoogland, R. Kleiss, C.G. Papadopoulos and G. Passarino , Nucl. Phys. **B500** (1997) 255,
G. Passarino, "*Unstable particles and nonconserved currents: a generalisation of the fermion loop scheme*", preprint hep–ph/9911482, November 1999.

[71] Y. Kurihara, D. Peret–Gallix and Y. Shimizu, Phys. Lett. **B349** (1995) 367.

[72] Informations concerning the "*LEP2 Monte Carlo Workshop*", can be found at the WWW page: http://www.to.infn.it/ giampier/lep2.html. Proceedings of the Workshop will be published as a CERN Yellow Report in June 2000.

[73] grc4f program (version 2.1.38), J. Fujimoto *et al.*, Comp. Phys. Comm. **100** (1997) 74, available from ftp://ftp.kek.jp/kek/minami/grc4f.

[74] KORALW program (version 1.42), S.Jadach, W. Placzek, M. Skrzypek, B.F.L. Ward and Z. Wąs, Comp. Phys. Comm. **119** (1999) 272. Internally this program uses the matrix element calculator of [73].

[75] EXCALIBUR program, F.A. Berends, R. Pittau, R.Kleiss, Comp. Phys. Comm. **85** (1995) 437.

[76] ERATO program, C.G. Papadopoulos, Comp. Phys. Comm. **101** (1997) 183.

[77] PYTHIA program (version 5.7), T. Sjöstrand, Comp. Phys. Comm. **82** (1994) 74.

[78] WPHACT program, E. Accomando and A. Ballestrero, Comp. Phys. Comm. **99** (1997) 270.

[79] COMPHEP program, A. Pukhov, E. Boos, M. Dubinin, V. Edneral, V. Ilyin, D. Kovalenko, A. Kryukov, V. Savrin, S. Shichanin and A. Semenov, "COMPHEP*: a package for evaluation of Feynman diagrams and integration over multiparticle phase space"*, preprint hep–ph/9808288, August 1998.

[80] G. Montagna, M. Moretti, O. Nicrosini, A. Pallavicini and F. Piccinini, *"Photon radiation in the single W process"*, talk given at the *"LEP2 Monte Carlo workshop"*, CERN, Geneva, Switzerland, 12 October 1999, [72], and private communication.

[81] Y.Kurihara, J. Fujimoto, Y. Shimizu, K. Kato, K. Tobimatsu and T. Munehisa, *"QED radiative corrections to the non–annihilation processes using the structure function and the parton shower"*, hep–ph/9912520, December 1999.

[82] T. Munehisa, J. Fujimoto, Y. Kurihara and Y. Shimizu, Prog. Theor. Phys. **95** (1996) 375,
Y. Kurihara, J. Fujimoto, T. Munehisa and Y. Shimizu, Prog. Theor. Phys. **96** (1996) 1223.

[83] D.R. Yennie, S. Frautschi and H. Suura, Annals Phys. **13** (1961) 379,
M. Skrzypek, S. Jadach, M. Martinez, W. Placzek and Z. Wąs, Phys. Lett. **B372** (1996) 289.

[84] E. Barberio and Z. Wąs, Comp. Phys. Comm. **79** (1994) 291.

[85] K. Hagiwara, H. Iwasaki, A. Miyamoto, H. Murayama and D. Zeppenfeld, Nucl. Phys. **B365** (1991) 544.

[86] ALEPH Collaboration, R. Barate *et al.*, Phys. Lett. **B462** (1999) 389,
ALEPH Collaboration, R. Barate *et al.*, *"Single W production at energies up to $\sqrt{s} = 189$ GeV and search for monojet events"*, ALEPH–CONF 99–052, July 1999.

[87] DELPHI Collaboration, P. Abreu *et al.*, *"Measurement of the single W production cross section at LEP2"*, DELPHI 99-67 CONF 254, June 1999.

[88] L3 Collaboration, M. Acciarri *et al.*, Phys. Lett. **B403** (1997) 168,
L3 Collaboration, M. Acciarri *et al.*, Phys. Lett. **B436** (1998) 417,
L3 Collaboration, M. Acciarri *et al.*, *"Preliminary results on single W boson production at $\sqrt{s} = 189$ GeV"*, L3 Note 2367, March 1999.

[89] OPAL Technical Proposal, CERN / LEPC / 83–4.

[90] The OPAL Collaboration, K. Ahmet *et al.*, Nucl. Instr. Meth. **A305** (1991) 275.

[91] P.P. Allport *et al.*, Nucl. Instr. Meth. **A346** (1994) 476,
S. Anderson *et al.*, Nucl. Instr. Meth. **A403** (1998) 326.

[92] B.E. Anderson *et al.*, IEEE Trans. on Nucl. Sci. **41** (1994) 845.

[93] The OPAL Collaboration, G. Abbiendi *et al.*, *"Precision luminosity for Z^0 lineshape measurements with a silicon–tungsten calorimeter"*, preprint CERN–EP/99-136, September 1999, submitted for publication in Eur. Phys. J. **C**.

[94] G. Aguillon *et al.*, Nucl. Instr. Meth. **A417** (1998) 266.

[95] J.T.M. Baines *et al.*, Nucl. Instr. Meth. **A325** (1993) 271.
The DAQ system used for the 1996–1998 runs is based on the same components described in this paper. Improvements have been made during the years to cope with higher luminosities and trigger rates, and with increased backgrounds at LEP2. The main changes consist in the use of faster processors in the local system crates and in the event builder.

[96] D.G. Charlton *et al.*, Nucl. Instr. Meth. **A325** (1993) 129.
The current implementation of the filter uses faster computers, but still performs the same tasks.

[97] M. Arignon *et al.*, Nucl. Instr. Meth. **A313** (1993) 103,
M. Arignon *et al.*, Nucl. Instr. Meth. **A333** (1993) 330.

[98] R. Bürgin, *"Trigger efficiency for untagged inclusive two–photon events at $\sqrt{s} = 161$ and 172 GeV"*, OPAL Technical Note TN496, July 1997.

[99] C. Hawkes *et al.*, *"ROPE Users Guide"*, OPAL–Offline note 16 / OFFL-0487 (unpublished).

[100] J. Allison *et al.*, Nucl. Instr. Meth. **A317** (1992) 47.

[101] R. Brun *et al.*, *"GEANT Users Guide"*, CERN Program Library Long Writeup W5013.

[102] The OPAL Collaboration, K. Ackerstaff *et al.*, Phys. Lett. **B389** (1996) 416,
M.A. Thomson and M.F. Watson, *"$W^+W^- \to q\overline{q}'\ell\overline{\nu}_\ell$ event selection at $\sqrt{s} = 161$ GeV"*, OPAL Technical Note TN386, July 1996,
M.A. Thomson, *"The OPAL $W^+W^- \to q\overline{q}'\ell\overline{\nu}_\ell$ event selection"*, OPAL Technical Note TN635, January 2000.

[103] The OPAL Collaboration, R. Akers *et al.*, Zeit. Phys. **C70** (1996) 357,
The OPAL Collaboration, G. Abbiendi *et al.*, Eur. Phys. J. **C8** (1999) 217.

[104] The OPAL Collaboration, P.D. Acton *et al.*, Zeit. Phys. **C58** (1993) 523,
The OPAL Collaboration, R. Akers *et al.*, Zeit. Phys. **C65** (1995) 17.

[105] M. Kolrep, *"Tau tagging with a neural network"*, OPAL Technical Note TN334, November 1995,
D. Glenzinski and A. Hocker, *"An artificial neural network algorithm for τ identification at LEP2"*, OPAL Technical Note TN559, August 1998.

[106] The OPAL Collaboration, K. Ackerstaff *et al.*, Eur. Phys. J. **C1** (1998) 395.

[107] T. Omori, S. Asai, I. Nakamura and S. Yamashita, *"A matching algorithm: MT package"*, OPAL Technical Note TN381, July 1996.

[108] T. Omori, S. Asai and I. Nakamura, *"Attempt to compensate energy in OPAL calorimeter complex based on MT package"*, OPAL Technical Note TN447, December 1996.

[109] The OPAL Collaboration, G. Alexander *et al.*, Zeit. Phys. **C52** (1991) 175.

[110] S. Brandt, Ch. Peyrou, R. Sosnowski and A. Wroblewski, Phys. Lett. **12** (1964) 57,
E. Farhi, Phys. Rev. Lett. **39** (1977) 1587.

[111] N. Brown and W.J. Stirling, Phys. Lett. **B252** (1990) 657,
S. Bethke, Z. Kunszt, D. Soper and W.J. Stirling, Nucl. Phys. **B370** (1992) 310,
S. Catani *et al.*, Phys. Lett. **B269** (1991) 432,
N. Brown and W.J. Stirling, Zeit. Phys. **C53** (1992) 629.

[112] C.P. Ward and D.R. Ward, *"Measurement of the mass of the W boson at 183 GeV using an analytic Breit–Wigner fit"*, OPAL Technical Note TN564, September 1998.

[113] The LEP Energy Working Group, R. Assmann *et al.*, Eur. Phys. J. **C6** (1999) 187,
The LEP Energy Working Group, A. Blondel *et al.*, Eur. Phys. J. **C11** (1999) 573,
The LEP Energy Working Group, R. Assmann *et al.*, *"Evaluation of the LEP centre–of–mass energy for data taken in 1998"*, internal note LEP Energy Working Group 99/01, March 1999.

[114] M. Verzocchi, *"4–fermion effects in the W mass measurement"*, talk given at the *"WW'99 Workshop on WW Physics at LEP200"*, 20–23 October 1999, Kolymbari-Chania, Greece.

[115] The OPAL Collaboration, G. Alexander *et al.*, Zeit. Phys. **C69** (1996) 543.

[116] G. Marchesini *et al.*, Comp. Phys. Comm. **67** (1992) 465.

[117] S. Jadach, B.F.L. Ward and Z. Wąs, *"The precision Monte Carlo event generator KK for two–fermion final states in e^+e^- collisions"*, preprint hep–ph/9912214, December 1999, submitted for publication in Comp. Phys. Comm..

[118] R. Engel and J. Ranft, Phys. Rev. **D54** (1996) 4244;
R. Engel, Zeit. Phys. **C66** (1995) 203.

[119] A. Buijs, W.G.J. Langeveld, M.H. Lehto and D.J. Miller, Comp. Phys. Comm. **79** (1994) 523.

[120] GENTLE program (version 2.02), J. Biebel and T. Riemann, Eur. Phys. J. **C8** (1999) 655.

[121] ALPHA program, F. Caravaglios and M. Moretti, Zeit. Phys. **C74** (1997) 291.

[122] RACOONWW program, A. Denner *et al.*, "Predictions for all processes $e^+e^- \to 4$ fermions $+\gamma$", preprint hep–ph/9904472, submitted to Nucl. Phys. **B**.

[123] M. Verzocchi, "REW99*: a library of routines for reweighting four fermion Monte Carlo samples based on the* grc4f *matrix elements"*, OPAL Technical Note TN618, August 1999.

[124] D. Charlton, WVCXME routine, available from http://opalinfo.cern.ch/opal/group/ww/TgcWorkPage/wvcdoc.html#wvcxme.

[125] The OPAL Collaboration, K. Ackerstaff *et al.*, Eur. Phys. J. **C2** (1998) 441,
The OPAL Collaboration, K. Ackerstaff *et al.*, Eur. Phys. J. **C6** (1999) 1,
The OPAL Collaboration, G. Abbiendi *et al.*, *"Tests of the Standard Model and Constraints on New Physics from Measurements of Fermion-pair Production at 189 GeV at LEP"*, preprint CERN–EP/99–097, July 1999, to be published in Eur. Phys. J. **C**.

[126] The OPAL Collaboration, G. Abbiendi *et al.*, *"Z Boson Pair Production in e^+e^- Collisions at $\sqrt{s}$ =183 and 189 GeV"*, preprint CERN–EP/99–1XX, December 1999, submitted to Phys. Lett. **B**.

[127] J. Fujimoto *et al.*, GRACE manual version 2.0, in preparation, S. Kawabata *et al.*, GRACE manual version 1.0, preprint KEK 92–19, available from ftp://ftp.kek.jp/kek/minami/grace.

[128] References to artificial neural network are numerous. One source with a focus on applications in high energy physics is: http://www.cern.ch/NeuralNets/nnwInHep.html. A good introductory book is: L. Fausett, *"Fundamentals of neural networks: architectures, algorithms, and applications"*, Prentice Hall, Englewood Cliffs, NJ (1994), ISBN 0-13-334186-0.

[129] C. Peterson, T.Rögnvaldsson and L. Lönnblad, Comp. Phys. Comm. **81** (1994) 185. The most recent version of the program and the user manual can be found at the WWW address: ftp://ftp.thep.lu.se/LundPrograms/Jetnet.

[130] A. Zell *et al.*, *"SNNS – Stuggart neural network simulator User Manual, version 4.0"*, University of Stuggart, Institute for parallel and distributed high performance computing (IPVR), Fakultät für Informatik, Bericht 6/95, 1995. The program and the manual can be downloaded from the WWW address: http://www.informatik.uni-stuttgart.de/ipvr/bv/projekte/snns/snns.html.

[131] D. Karlen, *"An improved likelihood selection technique for correlated variables"*, OPAL Technical Note TN459, February 1997,
D. Karlen, *"Approximation of probability distributions by their projections and correlations"*, OPAL Technical Note TN483, May 1997,
D. Karlen and E. Torrence, *"PC102 Manual"*, OPAL software manual, December 1997,
D. Karlen, Computers in Physics **12** (1998) 380.

A Reweighting methods

There are two possible approaches for extracting the predicted TGC dependence of the selected events (or of the accepted cross section) which is needed in the maximum likelihood fit to the observed number of data events to extract the value of the couplings. The first approach consists in generating many samples of Monte Carlo events for a finite set of TGC's different from the $\mathcal{SM}$ values. In principle only $1 + 2n + n(n-1)/2$ different Monte Carlo sample with different sets of TGC's are needed to extract the dependence of the accepted cross section on n independent parameters, given the bilinear dependence of the cross section on the couplings. Already for small values of n this number can be extremely large, making this procedure unpracticable from the point of view of CPU requirements. Moreover this number is valid only if the selected cross section in each Monte Carlo sample has a negligible error. Otherwise to extract the parameters of the second degree polynomial that describes the dependence of the selected number of events on the TGC's it is preferable to have an even larger number of reference samples with different couplings and to perform a fit.

The second possible approach consists instead generating only one (possibly very large) Monte Carlo sample in which all the TGC's are set to their $\mathcal{SM}$ value and applying a reweighting technique. The basis of the reweighting technique is the following equation giving the differential cross section, $\mathrm{d}\sigma$, as a function of the matrix element squared, $|\mathcal{M}|^2$, and of a phase space term, dLips:

$$\mathrm{d}\sigma \;=\; \kappa\,|\mathcal{M}|^2\,\mathrm{dLips},$$

where κ is a constant multiplicative factor. At a fixed centre–of–mass energy all the dependency of the differential cross section on the TGC's (but also from m_{W} or the diagrams used to calculate the cross section) is contained in the matrix element squared, whereas the phase space term depends only on the four–fermion momenta. To obtain the differential distribution for different values of the TGC's it is enough to start from one fully simulated Monte Carlo sample and to apply a weight, $\mathcal{W}$, for each event given by the ratio of matrix elements. The event generator used to produce the original distributions provides the correct sampling of the phase space. Unfortunately analytical formulas are not available for the calculation of the matrix element $|\mathcal{M}|^2$ (these exists only for the double resonating process $\mathrm{e^+e^-} \to \mathrm{W^+W^-}$, and for the CC11 class of final states $\mathrm{q\overline{q}'}\mu\overline{\nu}_\mu$, $\mathrm{q\overline{q}'}\tau\overline{\nu}_\tau$, $\mu^+\nu_\mu\tau^-\overline{\nu}_\tau$ and $\mathrm{u\overline{d}s\overline{c}}$ [120]). In the case of single W production it is necessary to use a matrix element calculator based on the complete set of 4–fermion diagrams.

In OPAL two matrix elements calculators based on the complete set of 4–fermion diagrams are commonly used: EXCALIBUR [75] and grc4f [73]. Other full four–fermion matrix element calculators have not been tested yet or do not include yet the dependence on

TGC's (ALPHA [121], RACOONWW [122]). This appendix contain a brief description of the interface to the grc4f matrix element calculator contained in the REW99 library [123], which was originally developed for this thesis and then extended to cover also other topics (mainly in the area of reweighting four–fermion events according to the set of Feynman diagrams considered). For cross–checks the interface to the EXCALIBUR matrix element calculator [124] has also been used. The grc4f calculator described here is generally slower than the EXCALIBUR one by at least one order of magnitude, but it has some advantages:

- Fully massive matrix elements: this allows to apply the reweighting technique also in some phase space regions where the EXCALIBUR calculator may not give reliable results due to the massless treatments of fermions (for example in the single–W kinematic region).
- More flexibility in the choice of diagrams: in grc4f it is (relatively) easy to compute matrix elements using only subsets of the full four–fermion diagrams, and therefore to study interference effects between diagrams which are considered signal (as the *s*– and the *t*–channel sets of diagrams considered in sections 3.1 and 5.3) and the remaining ones. The REW99 matrix element calculator has also been used to compute the fraction of four–fermion events which are considered as signal or background in the measurement of the $e^+e^- \to f\bar{f}$ reaction at LEP2 [125] and to correct the accepted four–fermion cross section back to the NC02 cross section in the Z^0Z^0 production analysis [126].
- It allows to study the effect of beam polarisation. This is not relevant for the LEP2 program, but has a very wide range of application for physics simulations for a high energy e^+e^- linear collider.

This appendix starts with a description of the interface to the grc4f matrix element calculator in section A.1. Then in sections A.2 and A.3 applications of this technique to the calculation of the TGC dependence of the accepted cross section, to the calculation of interference effects in the $q\overline{q}'e\overline{\nu}_e$ final states and to the extraction of the *t*–channel cross section are described. A more detailed and technical description of the REW99 library and of its applications can be found in [123]. There are also described applications of this library in other OPAL analyses.

A.1 The interface to the grc4f matrix element

The interface to the grc4f matrix element calculator is completely contained inside two FORTRAN routines. The first of this routines uses the Monte Carlo information concerning the primary four–fermions of the event to identify the relevant physics process inside grc4f, performs, when necessary, some reordering and charge conjugation operations and boost the 4–fermions into their effective centre–of–mass system, in which the matrix element calculation is performed. Finally some kinematically invariant quantities (like momentum–transfers, invariant masses) are computed. These quantities are all what is needed by grc4f to calculate the matrix element squared $|\mathcal{M}|^2$, which is the task of the second routine, that essentially just calls the relevant grc4f routine for calculating the amplitudes and then squaring them.

The standard calling sequence of the REW99 library is therefore the following:

1. Read in the PDG code and the 4-momenta of the four–fermion for one event.
2. Extract the relevant kinematic quantities describing the event.
3. Set the grc4f default parameters.
4. Calculate $|\mathcal{M}|^2_{def} = |\mathcal{M}|^2$ a first time.
5. Change one or more of the grc4f parameters.
6. Calculate $|\mathcal{M}|^2_{rew} = |\mathcal{M}|^2$ a second time.
7. The event weight is then given by the ratio of matrix elements: $\mathcal{W} = |\mathcal{M}|^2_{rew}/|\mathcal{M}|^2_{def}$.

Steps 5–7 of this procedure can be repeated many times. Care should be taken when using this method. If the statistics of the original sample is poor in certain bins of a distribution, then it is not appropriate to use the reweighting procedure. The same is true also if the weights become too large. This reweighting procedure is generally slow and therefore not suited for direct use inside fitting programs for TGC's measurements. Therefore tables of weights $\mathcal{W}$ are computed for fixed values of the parameters, and then interpolation methods are used.

A.2 Extracting the TGC dependence of the cross section

The method described in the previous section is applied for the extraction of the TGC dependence of the accepted cross section. Results on the anomalous couplings are presented in chapter 9 using the SU(2) $\otimes$ U(1) relations among the couplings and the additional assumption $\Delta g_1^Z = 0$. This allows then to combine results with the ones obtained from the study of the $e^+e^- \to W^+W^-$ reaction. Only two parameters are free in the TGC's fit, $\Delta\kappa_\gamma$ and λ_γ. The dependence of the accepted cross section on the couplings is obtained calculating a set of 50 weights $\mathcal{W}$ (though in principle only 5 additional points with couplings different from the $\mathcal{SM}$ ones are sufficient) using the procedure outlined in the previous section. The dependence of the selected number of events on the couplings $(\Delta\kappa_\gamma, \lambda_\gamma)$ is then obtained through a fit in the form of a second degree polynomial.

A.3 Changing the set of Feynman diagrams

The main feature of the REW99 calculator is the possibility of selecting the diagrams used for the calculation of the matrix element. This possibility has been used in section 5.3 to investigate interference effects between the $e^+e^- \to W^+W^-$ and the $e^+e^- \to W^+e^-\overline{\nu}_e$ processes, and to calculate the *t*–channel cross section.

By default $|\mathcal{M}|^2$ is calculated using all the four–fermion diagrams for a given process. At step number 5 of the procedure outlined in section A.1 instead of changing one parameter (like the couplings or a mass) the set of diagrams used for the calculation of $|\mathcal{M}|^2$ can be changed. It is therefore possible, starting from a sample of events generated using a full 4–fermion description of a process, to obtain the differential and total cross section corresponding only to a subset of diagrams. In the grc4f library the amplitude for each diagram of a given four–fermion process is contained into a separate subroutine. The selection of the diagrams is therefore performed by giving to the REW99 library the list of

diagrams which should be used for the calculation of $|\mathcal{M}|^2$. Once all Feynman diagrams for a given process are drawn, the only difficulty of this process resides in making the correspondence between single diagrams and the FORTRAN routine which calculates the amplitude of a process. This task is simplified by using the GRACEFIG program contained in the GRACE package [127] which displays interactively all Feynman diagrams for each four–fermion process and the correspondence to the FORTRAN routines which perform the amplitude calculation.

Assuming that the weight $\mathcal{W}$ for the reference set of diagrams has a value of 1, if the new weight is close to 1 this indicates that the chosen set of diagrams for a particular event dominates the cross section. If the new weight is close to 0, then the probability that the event is produced through those diagrams is small. The weight $\mathcal{W}$ is not restricted between 0 and 1. Values larger than 1 indicate that negative interference effects between the chosen set of diagrams and the remaining ones cannot be neglected. The interference term between two sets of diagrams can be calculated directly with the help of the REW99 library. Introducing the weight $\mathcal{W}_{CC20} = 1$ for the complete set of diagrams leading to the $\mathrm{q\overline{q}'e\overline{\nu}_e}$ final state, and the weights $\mathcal{W}_{s,t}$ calculated assuming that only the s– or t–channel diagrams contribute to the cross section, the interference $\mathcal{I}$ can be obtained as $\mathcal{I} = \mathcal{W} - \mathcal{W}_s - \mathcal{W}_t$ on a event by event basis. This is the procedure adopted for deriving the interference curves shown in figure 5.1.

B Multivariate analysis methods

The aim of an event selection is to classify events into two or more classes by analysing a set of n observables. Visualisation of multi–dimensional distributions is often performed by examining the one–dimension projections and linear correlation coefficients amongst the variables. This method is adequate when the sample size is small, the distribution consists of essentially uncorrelated variables, or when the correlations between the variables are approximately linear.

Multivariate analysis methods which exploit the non–linear correlations amongst the observables result often in a better separation power between different classes of events. Artificial neural networks [128] are often used in particle physics for event classification purposes. This method suffers from the drawback of being almost a "black–box" which comes in the form of a computer program (like JETNET [129] or SNNS [130]). For a large set of observables it is often difficult to understand in detail how the correlations amongst the different observables are exploited by the network to achieve an optimal separation power. This method moreover relies entirely on the availability of a Monte Carlo simulation of the different classes of events containing a good description of the correlations between the observables. This constitutes a weakness of the method, as systematic errors arising from possible inaccuracies in the simulations of the correlations are difficult to estimate. Systematic errors are usually considered only in terms of the one–dimensional projections of the full n–dimensional distribution.

This appendix contains a description of another multivariate method, the Projection and Correlation Approximation (PCA) [131], which has been used for the selection of the single W signal events described in chapter 6. This method represents an improvement over the standard likelihood method described in section B.1. The differences and advantages of the PCA method are discussed in section B.2.

B.1 The likelihood method

In the likelihood method the decision to classify an event as signal or background candidate is made on the basis of a single quantity called the *likelihood probability* which has values peaking near 1 for the majority of the signal, and values peaking near 0 for most of the background(s), with tails for both channels between 0 and 1. This quantity is given by:

$$\mathcal{L} = \frac{P_{signal}(\mathbf{x})}{P_{signal}(\mathbf{x}) + P_{background}(\mathbf{x})} \tag{B.1}$$

where P_{signal} and $P_{background}$ are to be proportional to the probability that a signal and a background event would have produced a set of observables $\mathbf{x}$. The method can be easily

extended to two or more background sources.

In the standard likelihood method the probability density functions $P_{signal}(\mathbf{x})$ and $P_{background}(\mathbf{x})$ are determined from the product of Monte Carlo one–dimensional distributions functions. This method provides optimal discrimination between two or several classes of events if the statistics on the Monte Carlo samples used to generate the one–dimensional distribution functions is sufficient to allow fine binning and if the all the input variables are uncorrelated. If this is the case the likelihood becomes a *real* probability for the considered event being signal or background. The only drawback in comparison to neural network methods is that some statistical power is lost through the binning process.

In presence of strong or nonlinear correlations amongst the observables $\mathbf{x}$, the approximation of the likelihood selection method is not valid. As a consequence the separation power becomes worse that that of a neural network. A signal of the failure of the likelihood method is the presence of a peak at 0 (1) in the signal (background) distribution of the quantity $\mathcal{L}$. In this case the likelihood method suffers from the same limitation of a neural network method concerning systematic errors arising from the Monte Carlo description of the correlations among observables.

B.2 The improved likelihood method

An improved likelihood method has been recently proposed in the literature [131] and adopted in other OPAL analyses [41]. The main improvement with respect to the standard likelihood method consists in taking into account explicitly the correlations among the different measured quantities $\mathbf{x}$.

The basis for the new method is the n–dimensional Gaussian probability distribution centered in the origin with a $n \times n$ covariance matrix V, given by:

$$G(\mathbf{y}) = (2\pi)^{-n/2}|V|^{-1/2}e^{-\frac{1}{2}\mathbf{y}^T V^{-1}\mathbf{y}}, \tag{B.2}$$

where $|V|$ is the determinant of V. The observables $\mathbf{x}$ are not in general Gaussian distributed, so this formula would be a poor approximation of the n–dimensional probability density function if used directly. The PCA method uses a parameter transformation on each variable $y_i = y_i(x_i)$, such that the individual distributions for y_i are Gaussian. As a result the n–dimensional distribution for $\mathbf{y}$ may be well approximated by the Gaussian distribution $G(\mathbf{y})$. One possible choice of a monotonic function $y = y(x)$ which transforms a variable x having a distribution function $p(x)$ to the variable y which follows a normal distribution is

$$y(x) = \sqrt{2}\,\mathrm{erf}^{-1}(2\mathrm{F}(x) - 1), \tag{B.3}$$

where erf^{-1} is the inverse error function and $\mathrm{F}(x)$ is the cumulative distribution of x,

$$\mathrm{F}(x) = \frac{\int_{x_{min}}^{x} p(x')dx'}{\int_{x_{min}}^{x_{max}} p(x')dx'}. \tag{B.4}$$

The resulting n–dimensional distribution for $\mathbf{y}$ will not be usually a n–dimensional Gaussian distribution. It is only guaranteed that the projections of this distribution on each axis y_i are Gaussian. The PCA approximation consists in assuming that the probability density

function of **y** is Gaussian. Although not exact this represents a much better approximation compared to the method where the correlations are ignored. The approximation will be best when the correlations amongst the observables **x** are as simple as possible.

The improved likelihood selection variable $\mathcal{L}'$ uses the improved probability distributions P' given by:

$$P'_{signal}(\mathbf{x})d^n\mathbf{x} = G(\mathbf{y})d^n\mathbf{y}, \tag{B.5}$$

where $G(\mathbf{y})$ is the n–dimensional Gaussian distribution.

The Jacobian of the transformation B.3 for the i^{th} observable is given by $p_{signal}(x_i)/g(y_i)$, where $p_{signal}(x_i)$ is the 1–dimensional probability distribution of x_i for the signal events and g is a normal distribution. For the set of **x** observables the Jacobian **J** of the transformation is therefore given by:

$$\mathbf{J} = \prod_{i=1}^{n} \frac{p_{signal}(x_i)}{g(y_i)}. \tag{B.6}$$

The improved probability distributions can therefore be written as a correction to the standard signal distributions in the form

$$P'_{signal}(\mathbf{x}) = c(\mathbf{x})P_{signal}(\mathbf{x}) \tag{B.7}$$

where P_{signal} is the estimated probability function used in the standard method without taking into account correlations amongst the observables

$$P_{signal}(\mathbf{x}) = \prod_{i=1}^{n} p_{signal}(x_i), \tag{B.8}$$

and $c(\mathbf{x})$ is the ratio of the Gaussian distributions,

$$c(\mathbf{x}) = \frac{G(\mathbf{y})}{\prod_{i=1}^{n} g(y_i)}, \tag{B.9}$$

with $G(\mathbf{y})$ given by Eqn. B.2.

The improved signal probability distribution is therefore

$$P'_{signal}(\mathbf{x}) = \frac{\mathrm{e}^{-\frac{1}{2}\mathbf{y}^T(V_s^{-1}-\mathrm{I})\mathbf{y}}}{|V_s|^{1/2}} \prod_{i=1}^{n} p_{signal}(x_i) \tag{B.10}$$

where V_s is the covariance matrix for **y** and I is the identity matrix. A similar formula gives the probability distribution for the background $P'_{background}(\mathbf{x})$. However in this case a different set of transformations $z_i(x_i)$ are necessary to transform the observables x_i into normally distributed quantities z_i. The correlations amongst the transformed variables z_i are described by a different covariance matrix V_b.

In terms of the transformed variables the improved likelihood selection variable $\mathcal{L}'$ is

given by

$$\mathcal{L}' = \frac{P'_{signal}(\mathbf{x})}{P'_{signal}(\mathbf{x}) + P'_{background}(\mathbf{x})}. \tag{B.11}$$

Improvements in the efficiency vs. purity curve of the selection are generally obtained with this modified likelihood method, particularly in cases where the correlation amongst the observables are different for the signal and background samples. A signal of this improvement is the disappearance of the signal (background) peak at 0 (1) in the distribution of the selection variable $\mathcal{L}'$.

With this method it is possible to evaluate the systematic uncertainties arising from inaccurate simulations of correlations by the Monte Carlo. The covariance matrices V can be adjusted and the purity / efficiency of the selection can be re–estimated. This procedure would leave the 1–dimensional x_i distributions untouched, and thus would single out the contribution to the systematic error due to uncertainties in the correlations.

It is also interesting to check whether the transformed probability distribution provide a good estimate of the true n–dimensional probability distribution. In such cases the approximated distribution can be used in a likelihood fit to mostly accurately determine the signal fraction with correctly estimated statistical uncertainties and without introducing biases in the measurement. When approximating a multidimensional distribution from a sample of Monte Carlo events it can be difficult to derive a goodness of fit statistic, like a χ^2 statistics, to check if the approximation is sufficient. This is because the required multidimensional binning can reduce the average number of events per bin to a very small number. A statistic that is sensitive to the correlation amongst variables and which does not require slicing the variable space in bins is easily defined for the transformed variables y which have a probability density function approximated by a n–dimensional Gaussian. For each event the value X^2 defined as

$$X^2 = \mathbf{y}^T V^{-1} \mathbf{y} \tag{B.12}$$

can be calculated. If the events follow the approximate probability density function the X^2 variable has a χ^2 distribution with n degrees of freedom, where n is the dimension of the Gaussian. A probability weight w can therefore be formed

$$w = \int_{X^2}^{\infty} \chi^2(t,n)dt, \tag{B.13}$$

which will have a uniform distribution between 0 and 1 if the events follow the probability distribution function.

When the goodness of fit test shows that the event sample is not well described by the projection and correlation approximation, further steps may be necessary before applying the method to an analysis. To identify correlations which are poorly described the goodness of test fit can be repeated for each pair of variables. If the test fails it may be possible to improve the approximation by modifying the choice of variables used in the analysis, or by treating different regions of the observables space by separate approximations.